Spreading gravity currents with temperature-dependent viscosity

By Ahmos Sansom

Thesis submitted to the University of Nottingham for the degree of Doctor of Philosophy, February 2000

ABSTRACT

The spreading of a fluid under gravity has many important industrial and geophysical applications and has been the focus of much research. Variations in the thermal properties of the fluid have often been neglected. This thesis introduces a series of models incorporating fluids having temperature-dependent viscosity and vertical cross-sectional profile of small aspect ratio to show the important effects that cooling can have on the flow field. The numerical results show features that are commonly observed in experiments and lava dome growth, such as plateauing and fingering.

ACKNOWLEDGMENTS

I would like to thank my supervisors, Professors David Riley and John King for their guidance during my period of research, the postgraduates in the department for an enjoyable environment to work in, especialy, Caroline Noakes, Duncan Williams for his amazing Latex wizardry and Manchester City football team which has been the inspirational drive behind my thesis.

I gratefully acknowledge the research scholarship which has been provided by the University of Nottingham and especially thank my parents.

CONTENTS

CHAPTER ONE

Introduction

1.1. Gravity currents

The spreading of gravity currents, which is a phenomenon associated with a wide range of problems involving the transfer of mass, usually in the horizontal direction, has many applications in industry and nature, ranging from spreading of radioactive material to lava flowing from a volcano. For a descriptive overview of gravity currents see Simpson (1997).

The spreading flows in this thesis are assumed to be laminar, to be governed by a buoyancy-viscous balance and to have a small aspect ratio. The effects of capillary forces are assumed to be negligible. The lubrication equations used to determine the evolution equation for the free surface appear to have been first derived by Mei (1966) who considered laminar flow down an incline. The analysis was simplified by Smith (1969), who considered the flow of a fluid on a horizontal substrate. Later studies of thin films by López & Miller (1976) included the effects of intermolecular forces (which are also neglected in this thesis) when the fluid has a thickness of the $O(10^{-7})$ and similarly by Greenspan (1978), who included surface tension forces. Neglecting the intermolecular and capillary forces, the governing evolution equation simplifies to the form used by Huppert (1982b), who considered gravity currents from line and point sources. Huppert used the similarity solutions first obtained by Barenblatt (1952) to describe isothermal flow over a smooth horizontal substrate and his results agree with the earlier model by Smith (1969). The theoretical model gives good agreement with measurements of lava dome growth on the island of Saint Vincent for the first 90 days, see Huppert *et al.* (1982). At large times the actual lava dome growth is influenced by other factors such as cooling and the collection of rubble at the flow front and deviates from the isothermal model predictions.

On assuming a no-slip boundary condition, a non-integrable shear stress singularity is introduced at the contact line (three-phase line) in the continuum formulation of the problem. The boundary condition at the contact-line usually needs to be modified if surface tension is significant. This is done by allowing slipping of fluid near the contact line and this introduces a boundary condition at the contact line which is usually formulated as a relation between the contact angle and the speed of the moving contact line. Experimental data is often used to find this relationship between the contact angle and the contact-line speed. For example, Dussan (1979) found the contact line speed to be a monotonically increasing function of the contact angle. To simplify the analysis, Greenspan (1978) and Davis (1983) used a linear relationship between the contact angle and the speed of the contact line for a spreading droplet. Haley & Miksis (1991) discuss the effects of slip at the contact line using slip to speed relationships which are quadratic and cubic in the contact angle. More complicated relationships for the problem of spreading molten material on a cold substrate were proposed by Schiaffino & Sonin (1997b), who discuss

a theoretical relationship for the slip velocity which they validated using the experimental data of Schiaffino & Sonin (1997a). Such slip conditions do not need to be addressed here since, as stated earlier, we are concerned with gravity dominated spreading. The relative importance of gravitational to capillary forces can be characterised by the Bond number:

$$B = \frac{\rho g l_0^2}{\sigma},$$

where ρ is the density, g is gravity, l_0 is a typical horizontal length scale and σ is the surface tension. A large Bond number implies that gravity is dominant and a small Bond number implies that the spreading is dominated by capillarity. The paper by Hocking (1983) discusses the effects of capillarity and gravity on a thin film for all values of the Bond number. The paper concludes that, for large Bond numbers, there are regions near the flow front where capillarity is of equal importance to, or even dominant to gravity. The subsequent analysis in the paper nevertheless shows that the overall spreading behaviour is governed by gravity, so that similarity solutions given in Smith (1969) apply; in other words surface tension can be assumed negligible in treating the bulk flow behaviour if the spreading has not reached a large radius and the time scale is of order B. In summary, a spreading fluid usually needs a boundary condition on the contact line to account for the slipping of the fluid; the above paper by Hocking (1983) states that for a gravity dominated spreading of fluid, then the forces at the contact line have a negligible effect on the dynamics if the attained radius of the spreading liquid at the contact line is small; otherwise the inclusion of a boundary condition at the contact line is important, where some relationships are discussed above.

The flow of gravity currents has been widely researched. For example, a viscous fluid flowing down an incline from point and line sources is discussed both theoretically and experimentally by Lister (1992). His similarity solutions show good agreement with the experimental data. For large time, the flows are observed to be unstable in the experiments, with the formation of capillary rivulets on the flow front. Similar instabilities have been observed in the two-dimensional constant mass case, Huppert (1982a), where a series of small amplitude rivulets of fairly constant wavelength begin to grow across the slope at critical distances down the inclined plane. The inclined model is discussed further by Liu & Mei (1989), who consider a Bingham plastic flowing down an incline to model the dynamics of fluid mud with a high concentration of cohesive clay. Huang & Garcia (1998) discuss a Herschel-Bulkley model for nonlinear viscoplastic flow down a slope. The viscoplastic model is also applied to spreading of lava domes with a small aspect ratio in Balmforth *et al.* (2000). Gravity currents spreading into a hot vapour-saturated porous rock are considered by Woods (1998). Other noteworthy studies include: spreading problems in porous layers by Huppert & Woods (1995), the spreading of thin films down a vertical wall by Moriarty *et al.* (1991) and hanging drops by Ehrhard (1994). Non-Newtonian liquids are discussed in more detail by Tanner (1985). More recent work involving thin films are: the study of the formation of dry spots by Zhang & Lister (1999), who found similarity solutions to a model which incorporated van der Waals forces, the study by Davis & Hocking (1999) of the problem of a viscous liquid spreading on an absorbing substrate, with applications to ink-jet printing and

spin coating (where a fluid is placed onto a rotating substrate subject to centrifugal forces) and the effects on the fluid of a jet of air are considered by McKinley *et al.* (1999).

The problems considered in this thesis are concerned with the effects of cooling on the dynamics of a gravity current with temperature-dependent viscosity. There are a few temperature-dependent viscosity models of gravity currents in the literature. For example, Sakimoto & Zuber (1995) investigated the influence of a variable-viscosity relationship on the profile of the free surface and apply their model to Venusian 'pancake' domes. The flow from a point source of a material with a radial variation in viscosity is investigated by Bercovici (1994), who finds profiles that develop a steep flow front followed by a plateau (see Chapter 4). This is in agreement with experiments performed by Stasiuk *et al.* (1993), discussed in the next section. The same viscosity model is used to discuss the cooling of mantle plume heads by Bercovici & Lin (1996). Other related work, not involving gravity currents includes: Wylie & Lister (1995), who investigate instabilities in channel flows, Wall & Wilson (1996), who extend this study by considering a broad range of viscosity models, and Wylie & Lister (1998), who discuss the straining flow of a fluid with temperature-dependent viscosity subjected to surface cooling by radiation.

Non-isothermal spreading behaviour of gravity currents has also been investigated theoretically by Ehrhard & Davis (1991); subject to capillary, thermocapillary and gravity forces, and experimentally by Ehrhard (1993). The theoretical model, which assumes constant viscosity and a temperature-dependent surface tension, shows good agreement with the experiments, which involved silicone and paraffin oil drops spreading on glass plates. The theory and experiments show that cooling retards the spreading rate, as expected, and that the free surface of the drop has a lens shaped profile, similar to the isothermal model discussed by Huppert (1982b). A similar model with a diffusion-dominated temperature field is considered by Oron *et al.* (1997). The model is extended by the addition of an internal heat source by Oron & Peles (1998), who find that destabilising thermocapillary effects can be mitigated by a volumetric heat source in the thin film. A further extension to the non-isothermal spreading model involving surface tension is discussed by López *et al.* (1996) who include the effect of an inclined plane.

1.2. Lava flow morphologies and experimental models

An important application of spreading gravity currents is that of lava flow, which has been the subject of much research, both theoretically and experimentally. The importance of fluid dynamics has increased over the years in geological problems, see the review by Huppert (1986).

There are three important factors which influence the spreading rate of erupted lava, see Guest *et al.* (1987); the first of these is the rate at which the magma erupts at the surface; secondly the advance of a flow front is strongly influenced by the topographic profile of the substrate so that, for example, increasing its declination causes a related increase in the flow rate. Finally, thermal conditions affect the lava flow. As lava cools, its viscosity can increase by orders of magnitude and impede the spreading of the melt.

FIG. 1.1. Lava dome growth on Mount St. Helens taken on 18th October 1980 with dimensions 34 metres high by 300 metres wide. Photograph is courtesy of the USGS/Cascades Volcano observatory; http://vulcan.wr.usgsgov/home.html.

One possible application of the theoretical modelling described in this thesis is to the growth of lava domes. Volcanic domes are mounds that form as magma is erupted slowly over a vent. The lava is very viscous, causing the development of a dome profile. The sides of most domes are very steep and as the dome cools the outer surface hardens, and sometimes shatters to produce debris around the flow. Some domes are produced as a result of many eruptions and are termed composite domes, as observered at Mount St. Helens. Lava dome growth is often observed to form lobes (as in the eruption on Mount Unzen for example, see Nakada & Fujii (1993)) which are believed to be caused by a slow effusion rate and large yield strengths. The new lava dome growth in Figure 1.1 is from the volcanic activity at Mount St. Helens. Lava dome growth has been subject to much research and experimental simulations, as discussed below.

Laboratory experiments have been performed to investigate the morphology of lava flow as a function of various parameters, including temperature and extrusion rates. For example, Fink & Griffiths (1990) investigated the surface morphology of viscous gravity currents using molten polythylene glycol (PEG) from point and line sources and considered the effects of a solidifying crust on the dynamics. If the liquid does not cool quickly, the spreading of the liquid is described by the isothermal model discussed by Huppert (1982b). Further experiments using PEG to simulate lava flow from volcanoes are discussed by Fink & Griffiths (1992). The experiments show that the variations of surface morphology depend upon the extrusion rate, thermal conditions and the substrate type, which is either smooth or rough. The typical morphologies observed as the cooling rate increases are: no crust (isothermal case), levees (where the flow front solidifies), folds, rifts and pillows, as shown in Figure 1.2. Under certain conditions, it is observed that the majority of the fluid remains at its initial temperature but develops a surrounding 'skin'. This 'skin' can become wrinkled by the liquid flow, and lava flow instabilities, such as developing lobes and clefts at the flow front, can be observed.

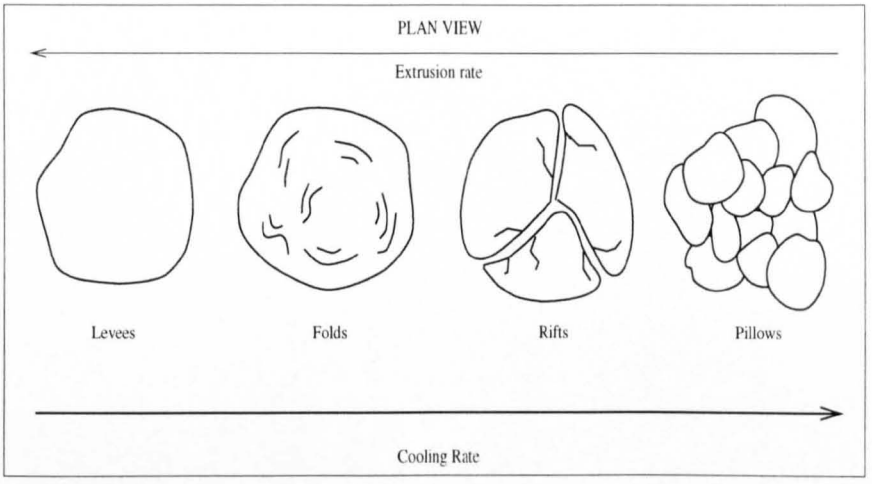

FIG. 1.2. Lava Morphologies

Similar morphologies are observed in submarine-lava flows; see Gregg & Fink (1995) where the effect of a substrate gradient is investigated. It is shown that increasing the substrate gradient has the same effect as increasing the extrusion rate and leads to the transition from pillows to levees. Note that increasing the flow rate causes the morphological transition from pillows to levees, whereas increasing the cooling rate has the opposite effect whereby a transition from levees to pillows is instigated. A Bingham-type fluid was studied by Griffiths & Fink (1997) using a PEG and kaolin powder mixture extruded onto a substrate, whereby there is a stronger yield stress on the surface than their earlier experiments. A similar range of flow regimes to that depicted in Figure 1.2 for the earlier experiments are observed, the small bulbous 'pillows' now being replaced by lobes or spines. The paper by Fink & Griffiths (1998) discusses the above laboratory simulations and, together with comparisons of lava dome growth, leads to a classification of various lava dome growth regimes in terms of their morphology.

The above studies were primarily motivated by geological applications. Another important motivation lies in safety studies of nuclear power plants. Plant operators are required to show that adequate safety margins exist even under severe accident conditions. This means that the relevant physical processes need to be sufficiently understood that corrective actions can be implemented effectively. For example, one extreme hypothetical situation is where it is supposed that the shutdown systems have failed to arrest some event that has led to the fuel in a particular channel overheating, causing the fuel inventory of that channel to melt and pour onto the floor below. In this application, the material generates internal heat as the radioactivity decays. As a contribution to such safety studies, Hallot *et al.* (1994) carried out an experimental programme in which two different solidifying fluids, PEG and gum rosin, were extruded over a solid horizontal base (PEG features a sharp transition at the solidification temperature, whereas the properties of the rosin vary more gradually). The qualitative features of the PEG results were consistent with those found by Fink and Griffiths, described above. Hallot *et al.* also found, however, that there was a substantial contribution to the energy budget from an exothermic reaction

between PEG and sucrose solution. Such internal energy sources therefore need to be considered when comparing experimental results with theoretical models; this does not seem to have been undertaken previously. Hallot *et al.* circumvented this complication by using ethylene glycol, which does not react with PEG, as the coolant and reported excellent agreement between their results from experiments and from scaling arguments.

Experiments carried out by Stasiuk *et al.* (1993) examine the effect of cooling of an initially warm glucose syrup extruded from a point source onto a horizontal substrate of a tank filled with a cold aqueous solution. Their results show that the majority of the spreading material attains a constant temperature, where the majority of the cooling takes place near the flow front. For certain eruption rates, the cooling effect produces a nearly horizontal free surface and a steep flow front, rather than the lens shaped profiles of the isothermal experiments, see the Discussion in Chapter 3. Further experiments by Snyder & Tait (1998) examine flow-front instability of laminar gravity currents intruding into a miscible, viscous ambient fluid. Instabilities cause the current to segment into fingers, which is said to be caused predominantly by two mechanisms. The first arises because of the no-slip condition on the substrate, which causes the nose of the current to elevate above the substrate and entrap the bouyant ambient fluid. The second mechanism is said to be analogous to the Saffman-Taylor instability (observed when low viscosity fluid displaces an ambient fluid of higher viscosity in a Hele-Shaw cell, see Saffman & Taylor (1958)). Homsy (1987) considers viscous fingering in a porous media and discusses the Hele-Shaw cell. Further experiments by Stasiuk & Jaupart (1997) consider the morphological characteristics, as influenced by a magma chamber and conduit system. Monaghan *et al.* (1999) consider experimental data for gravity currents flowing down an incline into a tank stratified in two layers. The experiments show that waves with large amplitudes can be generated where the initial gravity current splits into a gravity current along the bottom of the tank and a gravity current along the interface between the layers. The experimental results are accompanied with numerical simulations which show good agreement. Experiments by Johnson *et al.* (1999) study the formation of rivulets on a moving contact line down an incline, similar to the work considered by Huppert (1982a). Further fingering patterns are discussed by Matar & Trojan (1999) on the spreading of surfactant coated films.

1.3. Physical parameters and temperature-dependent viscosity relationships

This section discusses the physical parameters in modelling the spreading of liquid under gravity as the liquid cools. The parameters which can vary with temperature are: thermal conductivity (k), density (ρ), specific heat (c) and viscosity (μ); see the table in Figure 1.3 compiled from Raznjevic (1995), Stasiuk *et al.* (1993) and Fink & Griffiths (1990). Note that all values are given in SI units.

Density is assumed constant in this thesis, where most fluids can be assumed to be incompressible. Similarly, the specific heat changes little with temperature; for example the values of

Table of physical properties					
Liquid	θ/ °C	k/ $\mathrm{Wm^{-1}K^{-1}}$	ρ/ $\mathrm{kgm^{-3}}$	c/ $\mathrm{JKg^{-1}K^{-1}} \times 10^{-3}$	μ/ $\mathrm{Nsm^{-2}} \times 10^{-3}$
Castor oil	20	0.181	960	1.926	987
	80	0.175			32
Olive oil	20	0.169	914	1.633	80.8
	80	0.165			11.6
Paraffin oil	20	0.124	810	2.135	
	80	0.120			
Lubrication oil	20	0.144	871	1.851	13.05
	80	0.141	832	2.102	2.83
Water	20	0.598	998	4.183	1.0046
	80	0.669	958	4.199	0.3556
PEG	18	0.218	1128	2.500	204
	25		1122		146
Glucose syrup	-20				$O(10^7)$
	30				$O(10^2)$
Andesitic lava	800				$O(10^9)$
	1200				$O(10^3)$
Basaltic lava	1150		2800	1.200	$O(10^5)$
Silicic lava	800	1.260	2600	1.150	$O(10^{12})$

FIG. 1.3. Physical properties of various liquids.

lubricating oil and water seen in the above table. The values of thermal conductivity are seen to have a limited increase as the liquid cools. The most dramatic change is in the viscosity, as discussed below. Clearly when modelling the cooling of liquids, viscosity is an important parameter and is assumed temperature-dependent in the formulation of the governing equations in this thesis. In some liquids viscosity varies little with temperature and for example, density, is strongly temperature-dependent. This would lead to a different model being required where the effects of bouyancy would need to be considered; in the model in this thesis this is not the case, here viscosity is considered to be the only parameter that is temperature-dependent. To simplify the modelling, the density, thermal conductivity, specific heat are treated as constant; from the table this can be seen to be an appropriate simplification given the much larger changes in viscosity.

Generally, the viscosity of a liquid increases as it cools. For example, the viscosities of magmas increase roughly by an orders of magnitude over a 100K drop in temperature and the increase is much greater near the liquidus/ solidus boundary, see Ryan & Blevins (1987). This is seen in the above table for the different types of lava. The PEG mixture used in the Fink & Griffiths (1990) experiments show a relatively small change in viscosity when compared to the viscosity values of golden syrup used in the experiments by Stasiuk *et al.* (1993). The simplest viscosity

relationship capturing this behaviour, based upon the Arrhenius law, is

$$\mu(\theta) = \mu_0 \exp(-\alpha\theta), \tag{1.3.1}$$

where α and μ_0 are positive constants and θ is the temperature; this relationship was used by Wall & Wilson (1996) in their model of a channel flow. In the simple temperature models used in Chapter 2, the exponential relationship is compared with a linear relationship, which can be derived from the exponential model using a truncated Taylor series expansion, namely

$$\mu(\theta) = \mu_0(1 - \alpha\theta). \tag{1.3.2}$$

An equivalent model ($\alpha = \ln\beta$), used by Wylie & Lister (1995), is

$$\mu(\theta) = \mu(\theta_h)\beta^{1-\theta},$$

where $\beta \equiv \mu(\theta_c)/\mu(\theta_h)$, θ_c is the ambient temperature and θ_h is the influx temperature of the liquid. The relationship gives good experimental agreement, over a large temperature range, for a variety of liquids, including lubricating oils and many viscous syrups. A step function for non-dimensionalisied temperature T and viscosity, $\bar{\mu}$, is also considered by Wylie & Lister (1995) of the form

$$\bar{\mu} = \begin{cases} 1 & \text{if} \quad T > M, \\ \beta & \text{if} \quad T < M, \end{cases} \tag{1.3.3}$$

where M is a constant such that $0 < M \leq 1$ and β is as previously defined. Generally, the variation in viscosity is greatest close to the liquidus/solidus transition and can be represented by

$$\mu(\theta) = \mu_0 \left(a - (1-a)\tanh(l(\theta - \theta_m))\right), \tag{1.3.4}$$

as shown in Figure 1.4 with $\theta_m = 0.5$, $a = 0.505$ and $l = 100$, θ_m being the temperature

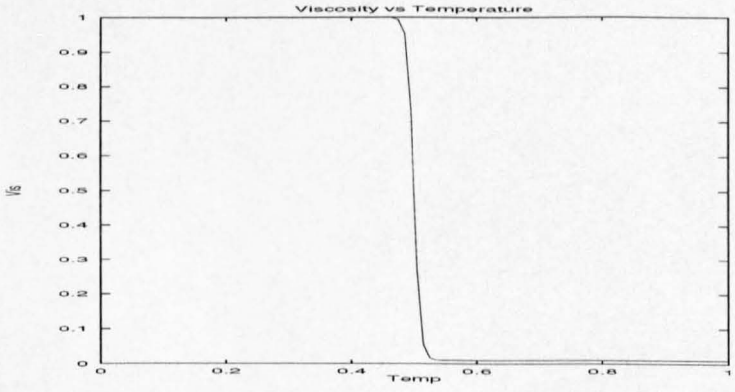

FIG. 1.4. Viscosity relationship with temperature for tanh profile.

about which where the change in viscosity occurs. The above tanh viscosity relationship can be approximated by a step function

$$\bar{\mu} = \begin{cases} 2a - 1 & \text{if} \quad T > T_m, \\ 1 & \text{if} \quad T < T_m, \end{cases} \tag{1.3.5}$$

where T and $\bar{\mu}$ are, respectively, the non-dimensionalised temperature and viscosity. Here T_m and a are positive constants, such that $0 < T_m \leq 1$; setting a close to 0.5 gives the greatest viscosity contrast between the two regions. Another class of temperature-viscosity relationship is the inverse temperature relationships. For example, Kafoussias & Williams (1995) use

$$\mu(\theta) = \frac{\mu_\infty}{1 + \gamma(\theta - \theta_\infty)} \tag{1.3.6}$$

to study steady laminar boundary layer flow over a vertical flat plate, where μ_∞ and γ are constants depending upon the properties of the liquid. The non-dimensionalised formula for temperature-dependent viscosity used by Mehta & Sood (1992) in a study of transient free convection along a non-isothermal vertical surface was

$$\mu(\theta) = (1 + k_1\theta + k_2\theta^2)^{-1}, \tag{1.3.7}$$

where k_1 and k_2 are constants. A table of viscosity-temperature relationships based on experimental data for a variety of liquids is given in Reid *et al.* (1987). The relationships have the forms

$$\mu(\theta) = A\theta^B, \tag{1.3.8}$$

$$\ln(\mu(\theta)) = A + B/\theta, \tag{1.3.9}$$

$$\ln(\mu(\theta)) = A + B/\theta + C\theta + D\theta^2, \tag{1.3.10}$$

where A, B, C and D are constants which depend upon the liquid properties.

1.4. Outline of thesis

In the following chapters the importance of cooling on the dynamics of gravity currents is investigated theoretically and numerically, by considering various temperature models, in order to determine the profiles of two-dimensional, axisymmetric and three-dimensional gravity currents spreading over a horizontal smooth substrate. The viscosity relationships in this thesis use the non-dimensionalised forms of the exponential, linear and the bi-viscosity relationships (equations (1.3.1), (1.3.2) and (1.3.5), respectively). In Chapters 2, 3 and 4 the problems of a spreading fluid with constant mass are considered in two-dimensional and axisymmetric geometries, the two-dimensional and axisymmetric models being extended to include an influx of liquid from a line source and point source, respectively. In Chapter 5, the two-dimensional model is extended to a three-dimensional model governing the free surface and instabilities at the flow front are discussed.

The temperature field is governed by advection, diffusion and a heat source. The diffusion term is synonymous with conduction and physically is a slow process to transmit heat; for example, to transport temperature changes of geological importance, over kilometres, by conduction takes thousands of years. Considering spreading melts, the heat transport is much more rapid, where heat is flowing from one point to another, depending on the type of flow and liquid. This type of heat transfer is known as convective heat transport, which is associated with (for example) melts

undergoing some kind of flow. The heat source term is included to model the effects of internal heating from a distributed source of energy.

Physically, the layer of melt adjacent to the cooler boundary becomes cool by conduction. Since the melt is spreading, the layer of cooled melt is removed and replaced by a layer of hot melt brought up to the boundary from the interior. Hence the heat flux through the boundary is sustained by the flow, rather than decaying as soon as the region near the boundary has been warmed. This is known as advective heat flux, where heat is brought up to the boundary by the convecting flow and transmitted through the boundary by conduction. The advective heat flux is maintained until either the whole body of the melt has cooled to the ambient temperature, by recycling it through the layer against the boundary, or the melt has stopped spreading by solidifying.

The assumptions for the temperature modelling in Chapter 2 assumes that the $\mathrm{Pe}_r \to 0$, where Pe_r is the reduced Peclet number (which is a heat transfer parameter) and that the aspect ratio is small in order to derive a simple temperature relationship. In Chapter 3, the Peclet number is now considered important ($\mathrm{Pe}_r = O(1)$) to give the conduction limited model and in Chapter 4 and 5, an asymptotic formulation for the temperature model is derived to give a conduction dominated temperature model such that $\mathrm{Pe} = O(1)$.

In summary, the spreading occurs under the action of two forces, the hydrostatic pressure due to the weight of the fluid and viscous forces, the viscosity being a function of temperature. It is assumed that the conditions at the head of the viscous current play no role in determining the current's motion or profile. This is valid when the Reynolds number and the effects of surface tension are small.

CHAPTER TWO

Isothermal and simple non-isothermal temperature models

2.1. Introduction

This chapter introduces a few simple models in which the viscosity is temperature-dependent. The non-isothermal models are developed from the isothermal model discussed by, for example, Huppert (1982b).

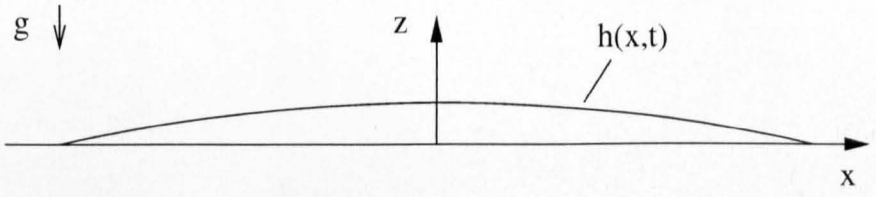

FIG. 2.1. Coordinate system.

Two-dimensional (and axisymmetric) spreading under gravity, $\mathbf{g}$, of a Newtonian liquid drop, with constant mass, temperature-dependent viscosity, $\mu(\theta)$, horizontal velocity, u, in the x-direction and vertical velocity, w, in the z-direction is initially considered. The height profile of the drop is given by $z = h(x,t)$, where t is time; see Figure 2.1. The initial temperature of the liquid drop is θ_i, the ambient temperature is θ_a and the temperature on the smooth horizontal substrate is taken to be θ_s. In order to simplify the equations governing the spreading process, assumptions are made to reduce the number of terms for specific types of problem. The asymptotic expansions which follow show how the so-called lubrication equations are derived for fluid problems with small aspect ratios. The two-dimensional and axisymmetric models are extended to include an influx boundary condition to model liquid spreading from a line source and a point source, respectively.

2.1.1. *Governing equation and derivation in two dimensions*

The Navier-Stokes equations for a Newtonian liquid of constant density, ρ, and variable viscosity, μ, are given in two dimensions by

$$\rho\left(\frac{\partial u}{\partial t}+u\frac{\partial u}{\partial x}+w\frac{\partial u}{\partial z}\right)=-\frac{\partial p}{\partial x}+\frac{\partial}{\partial x}\left(\mu\frac{\partial u}{\partial x}\right)+\frac{\partial}{\partial z}\left(\mu\frac{\partial u}{\partial z}\right)+\frac{d\mu}{d\theta}\left(\frac{\partial\theta}{\partial x}\frac{\partial u}{\partial x}+\frac{\partial\theta}{\partial z}\frac{\partial w}{\partial x}\right), \quad (2.1.1)$$

$$\rho\left(\frac{\partial w}{\partial t}+u\frac{\partial w}{\partial x}+w\frac{\partial w}{\partial z}\right)=-\frac{\partial p}{\partial z}+\frac{\partial}{\partial x}\left(\mu\frac{\partial w}{\partial x}\right)+\frac{\partial}{\partial z}\left(\mu\frac{\partial w}{\partial z}\right)+\frac{d\mu}{d\theta}\left(\frac{\partial\theta}{\partial x}\frac{\partial u}{\partial z}+\frac{\partial\theta}{\partial z}\frac{\partial w}{\partial z}\right)-\rho g, \quad (2.1.2)$$

where p denotes pressure, and the continuity equation is

$$\frac{\partial u}{\partial x}+\frac{\partial w}{\partial z}=0. \quad (2.1.3)$$

The energy equation governing the temperature evolution is

$$\rho c\left(\frac{\partial\theta}{\partial t}+u\frac{\partial\theta}{\partial x}+w\frac{\partial\theta}{\partial z}\right)=k\left(\frac{\partial^2\theta}{\partial x^2}+\frac{\partial^2\theta}{\partial z^2}\right)+\dot{q}, \tag{2.1.4}$$

where c is the constant specific heat of the drop, k is the constant thermal conductivity, $\dot{q}$ is the strength of a heat source and θ is the temperature. We define $\epsilon = h_0/l_0$ (the aspect ratio), where l_0 and h_0 are typical length scales in the x and z-directions, respectively, and take U_0 to be a typical horizontal velocity scale and μ_0 to be a typical viscosity scale. The equations are non-dimensionalised by introducing

$$\begin{aligned} &x=l_0x^*, \quad z=h_0z^*, \quad u=U_0u^*, \quad w=\epsilon U_0w^*, \quad \mu=\mu_0\mu^*, \\ &T=\frac{\theta-\theta_1}{\Delta\theta}, \quad \dot{q}=\frac{\Delta\theta k}{h_0^2}\dot{q}^*, \quad t=\frac{l_0}{U_0}t^*, \quad \text{and} \quad p=\frac{U_0\mu_0l_0}{h_0^2}p^*. \end{aligned} \tag{2.1.5}$$

The temperature is thus measured relative to θ_1 in units $\Delta\theta$, where θ_1 and $\Delta\theta$ are discussed next.

There are four scenarios considered for the temperature models in this thesis. The first involves a model with a hot substrate and cold free surface, such that $\theta_s > \theta_a$, and we take $\theta_1 = \theta_a$, $\theta_i = 0$ and $\Delta\theta = \theta_s - \theta_a$. The second is the reverse of first scenario, where we now have a cold substrate with a hot free surface. This gives $\theta_a > \theta_s$, $\theta_1 = \theta_s$, $\theta_i = 0$ and $\Delta\theta = \theta_a - \theta_s$. The next case, which is studied in Chapters 3, 4 and 5, we have $\theta_a = \theta_s$, and we take $\theta_1 = \theta_a = \theta_s$ and $\Delta\theta = \theta_i$. This case is simplified for the heat generation model in this Chapter in Section 2.4, where we take $\theta_i = \theta_a = \theta_s = 0$. In Chapter 6, the hot substrate model is extended to include a variable temperature along the substrate (in three dimensions) and is discussed in more detail there.

Dropping the star notation for clarity, the above scales transform the Navier-Stokes equations and the energy equation to

$$\begin{aligned} \epsilon^2R\left\{\frac{\partial u}{\partial t}+u\frac{\partial u}{\partial x}+w\frac{\partial u}{\partial z}\right\} &= -\frac{\partial p}{\partial x}+\epsilon^2\frac{\partial}{\partial x}\left(\mu\frac{\partial u}{\partial x}\right)+\frac{\partial}{\partial z}\left(\mu\frac{\partial u}{\partial z}\right) \\ &\quad +\epsilon^2\frac{d\mu}{dT}\left(\frac{\partial T}{\partial x}\frac{\partial u}{\partial x}+\frac{\partial T}{\partial z}\frac{\partial w}{\partial x}\right), \end{aligned} \tag{2.1.6}$$

$$\begin{aligned} \epsilon^4R\left\{\frac{\partial w}{\partial t}+u\frac{\partial w}{\partial x}+w\frac{\partial w}{\partial z}\right\} &= -\frac{\partial p}{\partial z}+\epsilon^4\frac{\partial}{\partial x}\left(\mu\frac{\partial w}{\partial x}\right)+\epsilon^2\frac{\partial}{\partial z}\left(\mu\frac{\partial w}{\partial z}\right) \\ &\quad +\epsilon^2\frac{d\mu}{dT}\left(\frac{\partial T}{\partial x}\frac{\partial u}{\partial z}+\frac{\partial T}{\partial z}\frac{\partial w}{\partial z}\right)-\frac{\rho\epsilon^3gl_0^2}{\mu_0U_0}, \end{aligned} \tag{2.1.7}$$

$$\frac{\partial u}{\partial x}+\frac{\partial w}{\partial z}=0, \tag{2.1.8}$$

$$\epsilon^2\mathrm{Pe}\left\{\frac{\partial T}{\partial t}+u\frac{\partial T}{\partial x}+w\frac{\partial T}{\partial z}\right\}=\epsilon^2\frac{\partial^2T}{\partial x^2}+\frac{\partial^2T}{\partial z^2}+\dot{q}. \tag{2.1.9}$$

Three further dimensionless parameters arise. These are the Prandtl number, defined by

$$\mathrm{Pr}=\frac{c\mu_0}{k},$$

the Peclet number, Pe, defined by

$$\mathrm{Pe}=R\mathrm{Pr}=\frac{\rho cU_0l_0}{k}$$

and the Reynolds number, R, defined by

$$R = \frac{\rho U_0 l_0}{\mu_0}.$$

On assuming $\epsilon^2 \ll 1$ (small aspect ratio), $\epsilon^2 R \ll 1$ (small reduced Reynolds number) and $\epsilon^2 \mathrm{Pe} \ll 1$ (small reduced Peclet number) the equations reduce to

$$-\frac{\partial p}{\partial x} + \frac{\partial}{\partial z}\left(\mu \frac{\partial u}{\partial z}\right) = 0, \tag{2.1.10}$$

$$\frac{\partial p}{\partial z} = -1, \tag{2.1.11}$$

$$\frac{\partial u}{\partial x} + \frac{\partial w}{\partial z} = 0 \tag{2.1.12}$$

and

$$\frac{\partial^2 T}{\partial z^2} = -\dot{q} \tag{2.1.13}$$

where the horizontal velocity scale has been defined as

$$U_0 = \frac{\rho h_0^3 g}{\mu_0 l_0}; \tag{2.1.14}$$

see Acheson (1990), for example, for a similar derivation of the lubrication equations. In this chapter, when taking $\dot{q}$ to be constant and non zero, equation (2.1.13) is rescaled again using

$$T = \dot{q} T^*. \tag{2.1.15}$$

This transformation does not affect the boundary conditions since the corresponding ambient temperatures of the fluid and the substrate are set to zero ($\theta_a = \theta_s = 0$, see Section 2.4). Dropping the star notation gives the governing temperature field as

$$\frac{\partial^2 T}{\partial z^2} = -1. \tag{2.1.16}$$

In the absence of internal heating, the temperature equation (2.1.13) simplifies to

$$\frac{\partial^2 T}{\partial z^2} = 0. \tag{2.1.17}$$

The reduced Navier-Stokes equations are coupled to the temperature field by viscosity relationships defined in the following sections (as first mentioned in the introduction) with specific boundary conditions for the temperature. The boundary conditions on the velocities and stresses at the substrate and the free surface are used in deriving the governing equation for the free surface and are discussed next.

Along the impermeable, non-slip substrate, the velocities u, w are zero. On the free surface the kinematic condition states that fluid particles on the surface remain on the surface. Thus the material derivative of $F(x, z, t) = z - h(x, t) = 0$, is zero i.e.

$$\frac{\partial F}{\partial t} + (\mathbf{u}.\nabla)F = 0,$$

or

$$\frac{\partial h}{\partial t} + u\frac{\partial h}{\partial x} - w = 0. \tag{2.1.18}$$

The components of stress σ on the free surface are given by

$$\sigma_i = T_{ij} n_j, \tag{2.1.19}$$

where T_{ij} is the stress tensor and the free surface has normal $\mathbf{n}$. For a Newtonian fluid T_{ij} is given by

$$T_{ij} = -p\delta_{ij} + \mu\left(\frac{\partial u_i}{\partial x_j} + \frac{\partial u_j}{\partial x_i}\right), \tag{2.1.20}$$

where δ_{ij} is the Kronecker delta. The normal to the free surface is

$$\begin{aligned} \boldsymbol{n} &= \frac{1}{|\boldsymbol{\nabla} F(x,z,t)|}\boldsymbol{\nabla} F(x,z,t), \\ &= \left(1 + \left(\frac{\partial h}{\partial x}\right)^2\right)^{-\frac{1}{2}} \left(-\frac{\partial h}{\partial x}, 1\right), \end{aligned} \tag{2.1.21}$$

where $F(x,z,t)$ is as defined above. On rescaling using (2.1.5), and noting that

$$\begin{aligned} \left(1 + \left(\epsilon\frac{\partial h^*}{\partial x^*}\right)^2\right)^{-\frac{1}{2}} &\sim 1 - \frac{1}{2}\epsilon^2\left(\frac{\partial h^*}{\partial x^*}\right)^2 + \frac{1}{8}\epsilon^4\left(\frac{\partial h^*}{\partial x^*}\right)^4 + \cdots \\ &\sim 1, \end{aligned} \tag{2.1.22}$$

on assuming $\epsilon^2 \ll 1$ we have

$$\boldsymbol{n} \sim (-\epsilon\frac{\partial h^*}{\partial x^*}, 1). \tag{2.1.23}$$

The normal component of stress in the x-direction is

$$\sigma_1 \sim \frac{U_0\mu_0}{h_0}\frac{\partial h^*}{\partial x^*}p^* - \frac{2\mu_0 U_0 h_0}{l_0^2}\mu^*\frac{\partial u^*}{\partial x^*}\frac{\partial h^*}{\partial x^*} + \mu_0\mu^*\left(\frac{U_0}{h_0}\frac{\partial u^*}{\partial z^*} + \frac{h_0 U_0}{l_0^2}\frac{\partial w^*}{\partial x^*}\right) \tag{2.1.24}$$

and, similarly, in the z-direction

$$\sigma_3 \sim -\frac{\mu_0 h_0}{l_0}\mu^*\frac{\partial h^*}{\partial x^*}\left(\frac{h_0 U_0}{l_0^2}\frac{\partial w^*}{\partial x^*} + \frac{U_0}{h_0}\frac{\partial u^*}{\partial z^*}\right) - \frac{U_0\mu_0 l_0}{h_0^2}p^* + \frac{2\mu_0 h_0 U_0}{l_0^2}\mu^*\frac{\partial w^*}{\partial z^*}. \tag{2.1.25}$$

Writing $\sigma_1^* = \frac{U_0\mu_0}{h_0}\sigma_1$ and $\sigma_3^* = \frac{U_0\mu_0 l_0}{h_0^2}\sigma_3$, where the star notation is again subsequently dropped, the leading order terms in (2.1.24) and (2.1.25) are

$$\sigma_1 = \frac{\partial h}{\partial x}p + \mu\frac{\partial u}{\partial z}, \tag{2.1.26}$$

$$\sigma_3 = -p. \tag{2.1.27}$$

Assuming that stress is continuous on the interface and that $\mu_{air} \ll \mu_{liquid}$ (and neglecting surface tension) requires $\sigma_1 = \sigma_3 = 0$ at $z = h$, giving

$$p = 0, \quad \mu\frac{\partial u}{\partial z} = 0. \tag{2.1.28}$$

The reduced equations (2.1.10) and (2.1.11), known as the lubrication equations, can now be used to derive an evolution equation governing the free surface of the liquid drop with temperature-dependent viscosity in conjunction with the boundary conditions on the surface (the kinematic condition (2.1.18) and tangential and normal stress components (2.1.28)) and along the substrate. To interpret the dynamics of the spreading viscous liquid, the stream function, ψ,

is used, where

$$u = \frac{\partial \psi}{\partial z} \quad \text{and} \quad w = -\frac{\partial \psi}{\partial x}.$$

ψ is constant along the streamlines and is calculated from the Cartesian horizontal velocity, u, as derived in equation (2.1.37) below, by

$$\psi = \int_0^z u dz. \tag{2.1.29}$$

The lubrication equations are now used to derive the equation governing the evolution of a spreading liquid with a temperature-dependent viscosity, $\mu = \mu(T)$ and temperature $T = T(x, z, t)$. The equations are:

$$-\frac{\partial p}{\partial x} + \frac{\partial}{\partial z}\left(\mu \frac{\partial u}{\partial z}\right) = 0, \tag{2.1.30}$$

$$\frac{\partial p}{\partial z} = -1, \tag{2.1.31}$$

$$\frac{\partial u}{\partial x} + \frac{\partial w}{\partial z} = 0, \tag{2.1.32}$$

subject to

$$u = 0, \quad w = 0 \tag{2.1.33}$$

on $z = 0$.

$$p = 0, \quad \mu \frac{\partial u}{\partial z} = 0, \quad \frac{\partial h}{\partial t} + u \frac{\partial h}{\partial x} - w = 0, \tag{2.1.34}$$

on $z = h$. From (2.1.31) and (2.1.34) we have

$$p = h(x, t) - z \tag{2.1.35}$$

and on substituting this in (2.1.30) gives

$$\frac{\partial}{\partial z}\left(\mu \frac{\partial u}{\partial z}\right) = \frac{\partial h}{\partial x}.$$

Integrating with respect to z and using (2.1.34) gives

$$\frac{\partial u}{\partial z} = \frac{1}{\mu}(z - h)\frac{\partial h}{\partial x}, \tag{2.1.36}$$

and another integration and satisfying the no-slip condition gives

$$u = \int_0^z \frac{(z' - h)}{\mu} dz' \frac{\partial h}{\partial x}. \tag{2.1.37}$$

From the equation of continuity (2.1.32) we obtain

$$\frac{\partial w}{\partial z} = \frac{\partial h}{\partial x} \int_0^z \left(\frac{1}{\mu}\frac{\partial h}{\partial x} + \frac{(z' - h)}{\mu^2}\frac{\partial \mu}{\partial x}\right) dz' - \frac{\partial^2 h}{\partial x^2} \int_0^z \frac{(z' - h)}{\mu} dz',$$

which subject to $w = 0$ on $z = 0$ gives

$$w = \frac{\partial h}{\partial x} \int_0^z \int_0^{z''} \left(\frac{1}{\mu}\frac{\partial h}{\partial x} + \frac{(z' - h)}{\mu^2}\frac{\partial \mu}{\partial x}\right) dz' dz'' - \frac{\partial^2 h}{\partial x^2} \int_0^z \int_0^{z''} \frac{(z' - h)}{\mu} dz' dz''. \tag{2.1.38}$$

(2.1.38) can be simplified by changing the order of the integration: the integral is of the form:-

$$\int_0^z \int_0^{z''} f(x,z,t)dz'dz'', \tag{2.1.39}$$

which on interchanging the order of integration becomes

$$\int_0^z \int_{z'}^z f(x,z,t)dz''dz' = \int_0^z f(x,z,t)(z-z')dz'. \tag{2.1.40}$$

Hence equation (2.1.38) may be written,

$$w = \frac{\partial h}{\partial x}\int_0^z \left(\frac{(z-z')}{\mu}\frac{\partial h}{\partial x} + \frac{(z'-h)(z-z')}{\mu^2}\frac{\partial \mu}{\partial x}\right)dz' - \frac{\partial^2 h}{\partial x^2}\int_0^z \frac{(z'-h)(z-z')}{\mu}dz'. \tag{2.1.41}$$

Finally substituting (2.1.37) and (2.1.41) into the kinematic condition (2.1.34) gives

$$\frac{\partial h}{\partial t} + \left(\frac{\partial h}{\partial x}\right)^2 \int_0^h \frac{(z-h)}{\mu}dz - \frac{\partial h}{\partial x}\int_0^h \left(\frac{1}{\mu}\frac{\partial h}{\partial x} + \frac{(z-h)}{\mu^2}\frac{\partial \mu}{\partial x}\right)(h-z)dz$$
$$-\frac{\partial^2 h}{\partial x^2}\int_0^h \frac{(z-h)^2}{\mu}dz = 0, \tag{2.1.42}$$

which simplifies to

$$\frac{\partial h}{\partial t} = \frac{\partial}{\partial x}\left(D\frac{\partial h}{\partial x}\right), \tag{2.1.43}$$

where D is the 'diffusivity' given by

$$D = \int_0^{h(x,t)} \frac{(z-h(x,t))^2}{\mu(T)}dz. \tag{2.1.44}$$

Equation (2.1.43) is the partial differential equation governing the evolution of a drop of liquid with temperature-dependent viscosity in two dimensions.

2.1.2. *Influx boundary condition from a line source*

Considering a liquid flowing from a line source gives rise to an influx model; we assume the fluid to be released at a rate $2Q_c\beta t^{\beta-1}$ from a line source along $x = 0$ in the two-dimensional coordinate system. The flow front of the viscous liquid on the horizontal substrate is taken to be at $x = s(t)$, so that $h = 0$ for $x \geq s(t)$. The global continuity equation is thus

$$\int_0^{s(t)} h(x,t)dx = Q_c t^{\beta}. \tag{2.1.45}$$

To formulate the influx boundary condition at $x = 0$, equation (2.1.45) is differentiated with respect to t, giving

$$\frac{ds}{dt}h(s,t) + \int_0^s \frac{\partial h}{\partial t}dx = \beta Q_c t^{\beta-1}. \tag{2.1.46}$$

Substituting equation (2.1.43) into the above expression, with $h(s,t) = 0$ gives,

$$\int_0^s \left(\frac{\partial}{\partial x}\left(\int_0^h \frac{(z-h)^2}{\mu}dz\frac{\partial h}{\partial x}\right)\right)dx = \beta Q_c t^{\beta-1},$$

hence

$$\left[\int_0^h \frac{(z-h)^2}{\mu} dz \frac{\partial h}{\partial x}\right]_{x=0}^{x=s} = \beta Q_c t^{\beta-1}. \tag{2.1.47}$$

The integral evaluated at $x = s$ is zero; integrating the contribution from $x = 0$ and rearranging gives

$$\frac{\partial h}{\partial x} + \frac{\beta Q_c t^{\beta-1}}{D} = 0, \tag{2.1.48}$$

where D is the diffusivity evaluated at $x = 0$, such that

$$D = \int_0^h \frac{(z-h)^2}{\mu} dz \bigg|_{x=0}.$$

2.1.3. *Governing equations in cylindrical polar coordinates*

The Navier-Stokes equations for a Newtonian liquid of constant density, ρ, and variable viscosity, μ, are given in the axisymmetric case by

$$\rho\left(\frac{\partial u}{\partial t} + u\frac{\partial u}{\partial r} + w\frac{\partial u}{\partial z}\right) = -\frac{\partial p}{\partial r} + \frac{1}{r}\frac{\partial}{\partial r}\left(\mu r \frac{\partial u}{\partial r}\right) + \frac{\partial}{\partial z}\left(\mu \frac{\partial u}{\partial z}\right) + \frac{d\mu}{d\theta}\left(\frac{\partial \theta}{\partial r}\frac{\partial u}{\partial r} + \frac{\partial \theta}{\partial z}\frac{\partial w}{\partial r}\right), \tag{2.1.49}$$

$$\rho\left(\frac{\partial w}{\partial t} + u\frac{\partial w}{\partial r} + w\frac{\partial w}{\partial z}\right) = -\frac{\partial p}{\partial z} + \frac{1}{r}\frac{\partial}{\partial r}\left(\mu r \frac{\partial w}{\partial r}\right) + \frac{\partial}{\partial z}\left(\mu \frac{\partial w}{\partial z}\right) + \frac{d\mu}{d\theta}\left(\frac{\partial \theta}{\partial r}\frac{\partial u}{\partial z} + \frac{\partial \theta}{\partial z}\frac{\partial w}{\partial z}\right) - \rho g, \tag{2.1.50}$$

where p again denotes pressure, and the continuity equation is

$$\frac{1}{r}\frac{\partial (ru)}{\partial r} + \frac{\partial w}{\partial z} = 0. \tag{2.1.51}$$

The energy equation governing the temperature evolution is

$$\rho c\left(\frac{\partial \theta}{\partial t} + u\frac{\partial \theta}{\partial r} + w\frac{\partial \theta}{\partial z}\right) = k\left(\frac{1}{r}\frac{\partial}{\partial r}\left(r\frac{\partial \theta}{\partial r}\right) + \frac{\partial^2 \theta}{\partial z^2}\right) + \dot{q}, \tag{2.1.52}$$

where c, k and $\dot{q}$ are as defined previously, and that l_0 is now a typical length scale in the r-direction. Non-dimensionalising using (2.1.5), where x is now r, and dropping the star notation for clarity gives the transformed Navier-Stokes equations as

$$\epsilon^2 R\left\{\frac{\partial u}{\partial t} + u\frac{\partial u}{\partial r} + w\frac{\partial u}{\partial z}\right\} = -\frac{\partial p}{\partial r} + \frac{\epsilon^2}{r}\frac{\partial}{\partial r}\left(\mu r \frac{\partial u}{\partial r}\right) + \frac{\partial}{\partial z}\left(\mu \frac{\partial u}{\partial z}\right) + \epsilon^2 \frac{d\mu}{dT}\left(\frac{\partial T}{\partial r}\frac{\partial u}{\partial r} + \frac{\partial T}{\partial z}\frac{\partial w}{\partial r}\right), \tag{2.1.53}$$

$$\epsilon^4 R\left\{\frac{\partial w}{\partial t} + u\frac{\partial w}{\partial r} + w\frac{\partial w}{\partial z}\right\} = -\frac{\partial p}{\partial z} + \frac{\epsilon^4}{r}\frac{\partial}{\partial r}\left(\mu r \frac{\partial w}{\partial r}\right) + \epsilon^2 \frac{\partial}{\partial z}\left(\mu \frac{\partial w}{\partial z}\right) + \frac{d\mu}{dT}\left(\frac{\partial T}{\partial r}\frac{\partial u}{\partial z} + \frac{\partial T}{\partial z}\frac{\partial w}{\partial z}\right) - \frac{\rho \epsilon^3 g l_0^2}{\mu_0 U_0}, \tag{2.1.54}$$

$$\frac{1}{r}\frac{\partial (ru)}{\partial r} + \frac{\partial w}{\partial z} = 0, \tag{2.1.55}$$

$$\epsilon^2 \mathrm{Pe}\left\{\frac{\partial T}{\partial t} + u\frac{\partial T}{\partial r} + w\frac{\partial T}{\partial z}\right\} = \frac{\epsilon^2}{r}\frac{\partial}{\partial r}\left(r\frac{\partial T}{\partial r}\right) + \frac{\partial^2 T}{\partial z^2} + \dot{q}. \tag{2.1.56}$$

On assuming $\epsilon^2 \ll 1$ (small aspect ratio), $\epsilon^2 R \ll 1$ (small reduced Reynolds number) and $\epsilon^2 \mathrm{Pe} \ll 1$ (small reduced Peclet number) the equations reduce to

$$-\frac{\partial p}{\partial r} + \frac{\partial}{\partial z}\left(\mu \frac{\partial u}{\partial z}\right) = 0, \tag{2.1.57}$$

$$\frac{\partial p}{\partial z} = -1, \tag{2.1.58}$$

$$\frac{1}{r}\frac{\partial (ru)}{\partial r} + \frac{\partial w}{\partial z} = 0 \tag{2.1.59}$$

and

$$\frac{\partial^2 T}{\partial z^2} = -\dot{q} \tag{2.1.60}$$

where the horizontal velocity scale has been defined as

$$U_0 = \frac{\rho h_0^3 g}{\mu_0 l_0}.$$

The temperature field can be rescaled as shown in the two-dimensional derivation and gives the same governing equations for temperature field in equations (2.1.16) and (2.1.17).

The reduced equations (2.1.57) and (2.1.58) are used to derive an evolution equation governing the free surface of the liquid drop with temperature-dependent viscosity using the same form of boundary conditions on the surface (the kinematic condition (2.1.18) and tangential and normal stress components (2.1.28)) and along the substrate (the condition of no-slip) as the two-dimensional case, but with x replaced by r. To interpret the dynamics of the spreading viscous liquid, the Stokes stream function, Ψ, is used such that $\mathbf{u} = \nabla \wedge (\frac{\Psi}{r}\mathbf{e}_\phi)$, where $\mathbf{e}_\phi$ is the unit vector in the azimuthal direction, hence

$$u = -\frac{1}{r}\frac{\partial \Psi}{\partial z} \quad \text{and} \quad w = \frac{1}{r}\frac{\partial \Psi}{\partial r}. \tag{2.1.61}$$

Ψ is constant along the streamlines and is calculated using the horizontal velocity, u, given in (2.1.63) below, by

$$\Psi = -r\int_0^z u dz. \tag{2.1.62}$$

By a similar derivation to the two-dimensional case we obtain the velocity field which is governed by

$$u = \int_0^z \frac{(z^{'} - h)}{\mu} dz^{'} \frac{\partial h}{\partial r}, \tag{2.1.63}$$

where (referenced for the next chapter)

$$\frac{\partial u}{\partial z} = \frac{1}{\mu}(z-h)\frac{\partial h}{\partial r}, \tag{2.1.64}$$

$$w = \left(\frac{\partial^2 h}{\partial r^2} + \frac{1}{r}\frac{\partial h}{\partial r}\right)\int_0^z \frac{(z^{'} - h)(z^{'} - z)}{\mu} dz^{'} - \frac{\partial h}{\partial r}\int_0^z \left(\frac{(z^{'} - z)}{\mu}\frac{\partial h}{\partial r} + \frac{(z^{'} - h)(z^{'} - z)}{\mu^2}\frac{\partial \mu}{\partial r}\right) dz^{'}. \tag{2.1.65}$$

and the free surface is given by

$$\frac{\partial h}{\partial t} = \frac{1}{r}\frac{\partial}{\partial r}\left(rD\frac{\partial h}{\partial r}\right), \tag{2.1.66}$$

where D is the same as in the two-dimensional case and is given by (2.1.44). Equation (2.1.66) is the partial differential equation governing the evolution of the profile of an axisymmetric spreading drop of liquid with temperature-dependent viscosity.

The vector formulation which encapsulates both (2.1.43) and (2.1.66) is shown in Chapter 5 to be

$$\frac{\partial h}{\partial t} = \nabla.\left(D\nabla h\right), \tag{2.1.67}$$

where, in Cartesian coordinates, $h = h(x, y, t)$ and ∇ is the gradient operator in the horizontal coordinates (x, y). In the following sections we solve the nonlinear diffusion equation governing the free surface for specific viscosity relationships.

2.1.4. *Influx boundary condition from a point source*

An influx boundary condition similar to that of the two-dimensional case is now derived for a point source of axisymmetric spreading. A variable flux of fluid is released at at rate $\beta Q_p t^{\beta-1}$ from $r = 0$. If the flow front is at $r = s(t)$ and radial symmetry is assumed, the global continuity equation is

$$2\pi \int_0^{s(t)} rh(r,t)dr = Q_p t^{\beta}. \tag{2.1.68}$$

To formulate the influx boundary condition at $r = 0$, equation (2.1.68) is differentiated with respect to t, giving

$$2\pi\frac{ds}{dt}rh(s,t) + 2\pi\int_0^s r\frac{\partial h}{\partial t}dr = \beta Q_p t^{\beta-1}. \tag{2.1.69}$$

and hence

$$\frac{\partial h}{\partial r} + \frac{\beta Q_c t^{\beta-1}}{2\pi rD} = 0 \tag{2.1.70}$$

at $r = 0$ where D is the diffusivity, (2.1.44), evaluated at $r = 0$.

The boundary condition (2.1.70) has a singularity at $r = 0$ and has to be modified when implementing the condition numerically. This can be done by applying the boundary condition at $r = \varepsilon$, where ε is a small value, to avoid the singularity, as discussed in the numerical result sections.

2.2. The isothermal model

On assuming viscosity is constant ($\mu = 1$), the governing equations (2.1.43) and (2.1.66) for the drop height profiles simplify to

$$\frac{\partial h}{\partial t} = \frac{\partial}{\partial x}\left(\frac{h^3}{3}\frac{\partial h}{\partial x}\right) \tag{2.2.1c}$$

and

$$\frac{\partial h}{\partial t} = \frac{1}{r}\frac{\partial}{\partial r}\left(r\frac{h^3}{3}\frac{\partial h}{\partial r}\right), \tag{2.2.1p}$$

the isothermal 'diffusivity' being given by

$$D = \frac{h^3}{3}. \tag{2.2.2}$$

The letter extensions to the equation number indicate the two-dimensional (Cartesian) equation (c) and the axisymmetric (polar) equation (p). The above nonlinear diffusion equations have been studied by Huppert (1982b) using similarity and numerical methods. We now recap some of the details.

2.2.1. *Similarity solutions*

Similarity methods, techniques based on invariance under continuous Lie group transformations, can be used to simplify ordinary and partial differential equations. Similarity transformations reduce either the order of ordinary differential equations, or the number of independent variables, in a partial differential equation. A particular similarity reduction is sought by substituting

$$h = t^{-a} f(\eta), \tag{2.2.3}$$

where $\eta = x/t^b$ into equation (2.2.1c):

$$-t^{-a-1}\left(af + b\eta\frac{df}{d\eta}\right) = \frac{1}{3}t^{-4a-2b}\frac{d}{d\eta}\left(f^3\frac{df}{d\eta}\right). \tag{2.2.4}$$

To eliminate t in equation (2.2.4) we require

$$3a + 2b = 1 \tag{2.2.5}$$

and the same requirement applies as the axisymmetric case with $\eta = r/t^b$. A second relation is needed to fix the exponents a and b. In the two-dimensional constant mass case we have

$$\int_{-\infty}^{\infty} h dx = 2Q_c \quad \text{(constant)}, \quad \text{say}, \tag{2.2.6}$$

or

$$t^{b-a}\int_{-\infty}^{\infty} f d\eta = 2Q_c. \tag{2.2.7}$$

Thus $a = b$ and, using equation (2.2.5), we have $a = b = \frac{1}{5}$. Hence the similarity solution is

$$h = t^{-\frac{1}{5}} f(\eta), \tag{2.2.8}$$

where $\eta = xt^{-\frac{1}{5}}$ and equation (2.2.4) simplifies to

$$-\frac{1}{5}\left(f + \eta\frac{df}{d\eta}\right) = \frac{1}{3}\frac{d}{d\eta}\left(f^3\frac{df}{d\eta}\right).$$

Integrating and using $\frac{df}{d\eta} = 0$ at $\eta = 0$ (from symmetry at $x = 0$) gives

$$-\frac{3}{5}f\eta = f^3\frac{df}{d\eta};$$

integrating again, we obtain

$$f = \left(c^2 - \frac{9}{10}\eta^2\right)^{\frac{1}{3}}, \tag{2.2.9}$$

where c is a positive constant. The resulting height profile is given by

$$h = \begin{cases} \left(\frac{9}{10}\right)^{\frac{1}{3}} t^{-1/5} \left(d^2 - x^2 t^{-2/5}\right)^{\frac{1}{3}}, & |x| < dt^{1/5}, \\ 0, & |x| \geq dt^{1/5}, \end{cases} \tag{2.2.10}$$

where d is a positive constant which can be expressed in terms of Q_c via (2.2.6).

Similarly, in the axisymmetric constant mass case, the global continuity equation is

$$2\pi \int_0^\infty rh dr = Q_p \tag{2.2.11}$$

or

$$2\pi t^{2b-a} \int_0^\infty \eta f d\eta = Q_p. \tag{2.2.12}$$

Thus $a = 2b$ and, using (2.2.5), we obtain $a = \frac{1}{4}$ and $b = \frac{1}{8}$. Hence the similarity solution can be shown to be

$$h = \begin{cases} \left(\frac{9}{16}\right)^{\frac{1}{3}} t^{-1/4} \left(d^2 - r^2 t^{-1/4}\right)^{\frac{1}{3}}, & r < dt^{1/8}, \\ 0, & r \geq dt^{1/8}. \end{cases} \tag{2.2.13}$$

The similarity solution for the two-dimensional case shows that the drop height, h, at $x = 0$ varies like $O(t^{-\frac{1}{5}})$ and the horizontal position of the front like $O(t^{\frac{1}{5}})$, cf. Lacey *et al.* (1982). In the axisymmetric case the drop height, h, at $r = 0$ varies like $O(t^{-\frac{1}{4}})$ and the front like $O(t^{\frac{1}{8}})$. Similarity solutions of this type have been obtained for a more general form of the nonlinear diffusion equation by King (1990).

The solution for a drop spreading from a line source with a total injected volume $2Q_c t^\beta$ at time t is now considered. The global continuity equation is

$$\int_{-\infty}^{\infty} h(x,t) dx = 2Q_c t^\beta, \tag{2.2.14}$$

or

$$t^{b-a} \int_{-\infty}^{\infty} f d\eta = 2Q_c t^\beta. \tag{2.2.15}$$

From (2.2.15) and (2.2.5) we obtain

$$a = \frac{1-2\beta}{5} \quad \text{and} \quad b = \frac{3\beta+1}{5}. \tag{2.2.16}$$

From (2.2.3), as $t \to \infty$, the maximum height $h_{max} \sim t^{\frac{2\beta-1}{5}}$ and the front location $s \sim t^{\frac{3\beta+1}{5}}$, as shown in Huppert (1982b). Similarly from a point source with a total injected volume $Q_p t^\beta$ at time t, the axisymmetric global continuity equation is

$$2\pi \int_0^\infty rh(r,t) dx = Q_p t^\beta, \tag{2.2.17}$$

or

$$2\pi t^{2b-a} \int_0^\infty \eta f d\eta = Q_p t^\beta. \tag{2.2.18}$$

Similarly, from (2.2.18) and (2.2.5), we obtain

$$a = \frac{1-\beta}{4}, \quad \text{and} \quad b = \frac{3\beta+1}{8} \tag{2.2.19}$$

and from (2.2.3), as $t \to \infty$, at $r = 0$, $h_{max} \sim t^{\frac{\beta-1}{4}}$ and the front location $s \sim t^{\frac{3\beta+1}{8}}$. The similarity solutions describe the behaviour as $t \to \infty$ for any finite mass initial conditions. Note that the theory is valid only when the viscous forces are much greater than the inertial forces. In Huppert (1982b) it is shown that the inertia terms become important for large time when $\beta > 7/4$. Similarly for axisymmetric spreading from a point source the inertia terms become important when $\beta > 3$.

2.2.2. *Numerical results for the two-dimensional spreading of a drop of fixed mass*

The partial differential equation (2.2.1c) is solved numerically using the NAG routine D03PGF. This NAG routine uses the method of lines technique, where the partial differential equation is discretised in finite difference form in space and solved as a system of coupled time-dependent ordinary differential equations. The following initial drop profile and boundary conditions are applied, where the solution has compact support (i.e. $h \equiv 0$ for all sufficiently large values of $|x|$),

$$\begin{aligned} &\text{at} \quad t = 0 \quad h = (1-x^2)_+, \\ &\text{as} \quad |x| \to \infty \quad h \to 0, \end{aligned} \tag{2.2.20}$$

where the boundary condition as $|x| \to \infty$ is applied numerically at the edge of the numerical domain (and similarly for the axisymmetric profiles). The spatial range shown in the following results represents the numerical domain. Illustrations of the resulting evolution of the drop shape and streamlines are shown in Figure 2.2. Note that the scales are different in the figures.

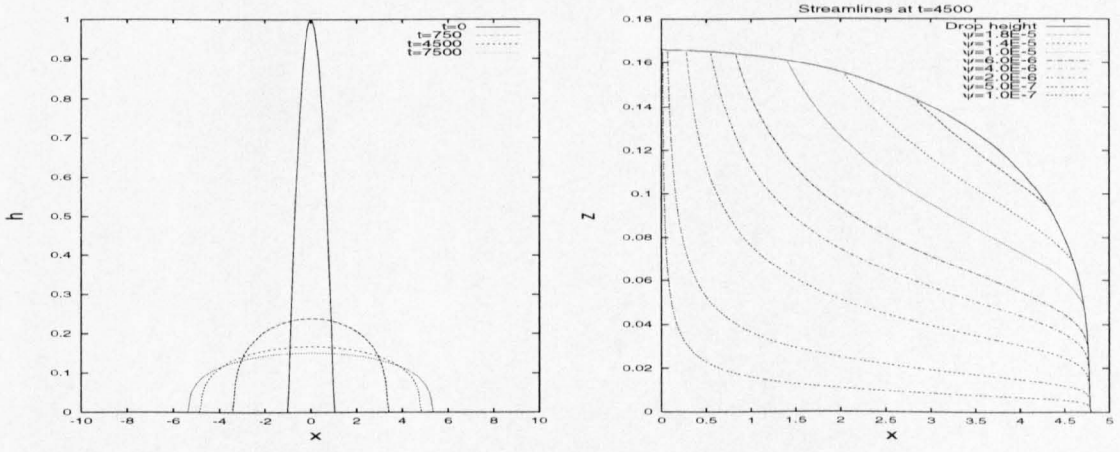

(a) Free surface profiles. (b) Streamlines at $t = 4500$.

FIG. 2.2. Two-dimensional spreading of a constant mass of fluid: isothermal case.

The resulting profiles show the drop clearly spreading under gravity, as expected, with the streamlines showing the contact line being fed by fluid from the free surface. In the isothermal case

(2.1.37) simplifies to

$$u = z\left(\frac{z}{2} - h\right)\frac{\partial h}{\partial x} \tag{2.2.21}$$

and (2.1.29) becomes

$$\psi = \frac{z^2}{2}\left(\frac{z}{3} - h\right)\frac{\partial h}{\partial x} \tag{2.2.22}$$

which is used to determine the streamlines in Figure 2.2(b). Similarly the Stokes stream function has the form in the axisymmetric case, from (2.1.62), as

$$\Psi = -r\frac{z^2}{2}\left(\frac{z}{3} - h\right)\frac{\partial h}{\partial r}. \tag{2.2.23}$$

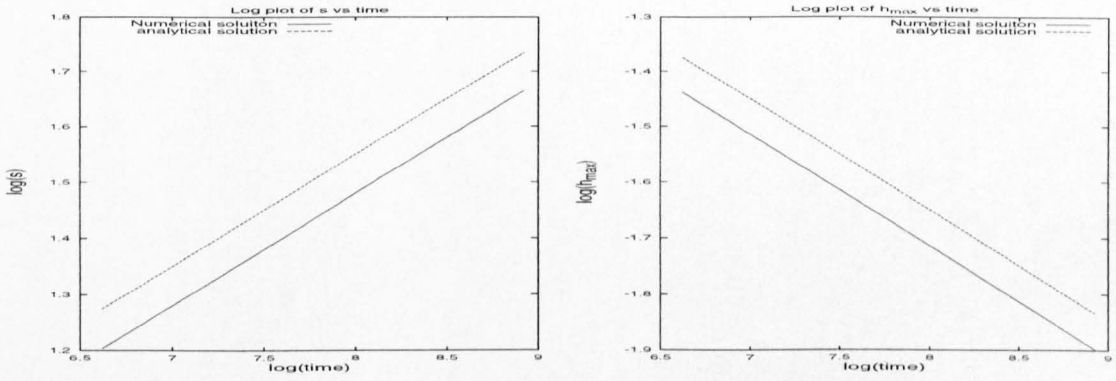

(a) Log-log plot of front location *vs* time. (b) Log-log plot of drop height *vs* time.

FIG. 2.3. Isothermal spreading rates: two-dimensional with constant mass.

The corresponding log-log plots of the front location, s, and maximum height of the drop, h_{max}, against time are shown in Figures 2.3(a) and 2.3(b), and are compared against the analytical result by plotting the exponent of the similarity solution from (2.2.10) as the gradient. The front location $s(t)$ is determined from the numerical solution as the minimum value of x for which h is smaller than 10^{-4}. The two graphs confirm that $s \sim t^{\frac{1}{5}}$ and $h_{max} \sim t^{-\frac{1}{5}}$, as $t \to \infty$, in agreement with the known similarity solution, Huppert (1982b). Note that, whatever the initial condition, the drop profile will ultimately evolve into the similarity form (given by (2.2.10), say). For example, using the initial profile, $h = 1$ for $-1 \leq x \leq 1$, $h = 0$ for $|x| > 1$, the NAG routine gives the height profiles shown in Figure 2.4. Note that the method of lines is usually only applied to data that is smooth, unless a loss of accuracy is permitted; the above initial profile is allowed by lowering the tolerences for the absolute errors in the NAG routine with an acceptable small loss in accuracy, where the results show the behaviour of the expected similarity solution.

2.2.3. *Numerical results for the two-dimensional spreading of a drop fed by a line source*

The inflow boundary condition (2.1.48) using (2.2.2), for the isothermal model simplifies to

$$\frac{\partial h}{\partial x} + \frac{3\beta Q_c t^{\beta-1}}{h^3} = 0. \tag{2.2.24}$$

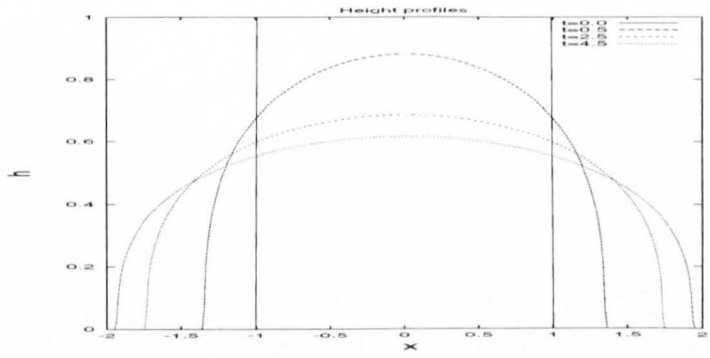

FIG. 2.4. Free surface profiles resulting from an initial rectangular profile.

The governing equation for the free surface, (2.2.1c), is again solved using the NAG routine D03PGF. In this case a small amount of mass is assumed to be present initially in order to avoid numerical problems. The initial and boundary conditions are taken to be:

$$\begin{aligned} &\text{at} \quad t = 0 \quad h = 10(0.01 - x^2)_+, \\ &\text{as} \quad x \to \infty \quad h \to 0. \end{aligned} \tag{2.2.25}$$

The resulting surface profiles and streamlines are shown in Figure 2.5 for $\beta = 1.5$ and $Q_c = 0.009$.

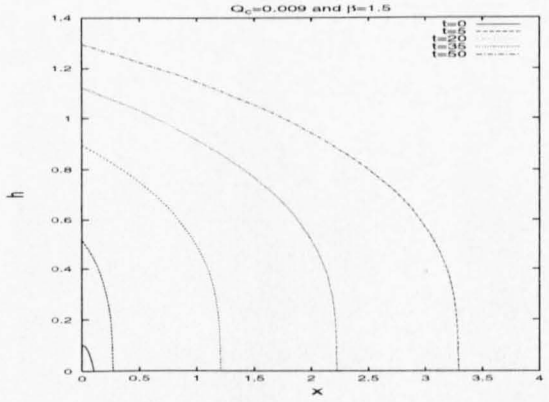

(a) Free surface profiles.

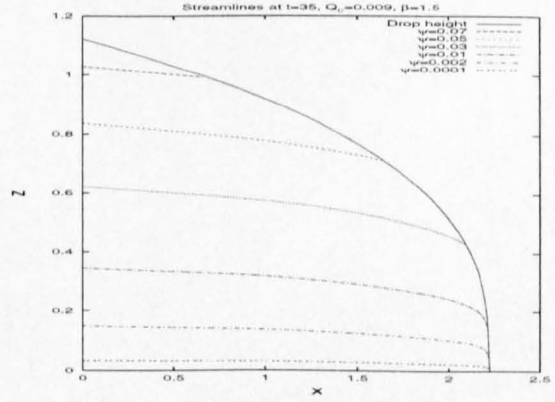

(b) Streamlines at $t = 35$.

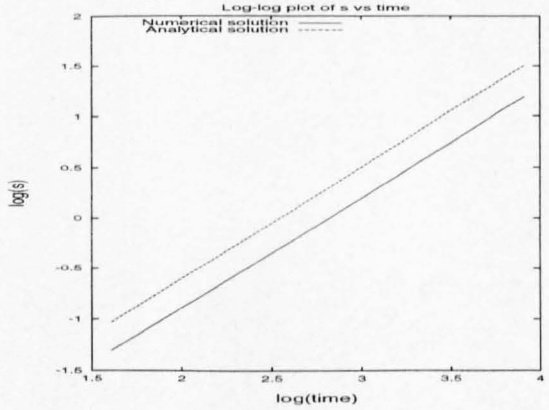

(c) Log-log plot of front location.

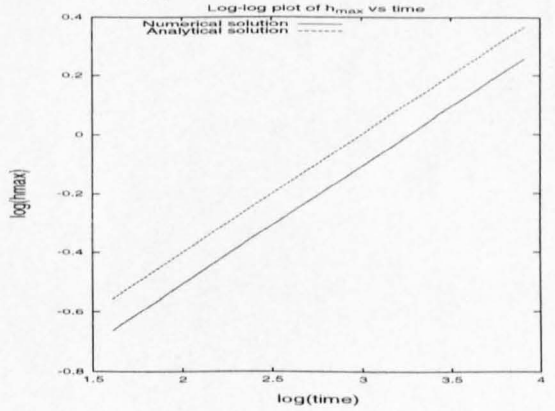

(d) Log-log plot of drop height at $x = 0$.

FIG. 2.5. Two-dimensional spreading from a line source with $\beta = 1.5$ and $Q_c = 0.009$: isothermal case.

The streamlines in Figure 2.5(b) show that the contact line is fed by the fluid from the influx boundary rather than the free boundary as in the constant mass case. Figures 2.5(c) and 2.5(d) confirm, as expected, that $s \sim t^{\frac{11}{10}}$ and $h_{max} \sim t^{\frac{2}{5}}$ as $t \to \infty$ by comparing the numerical log-log plots with the respective exponents in the analytical solutions from (2.2.16).

2.2.4. *Numerical results for the axisymmetric spreading of a drop of fixed mass*

The final set of isothermal numerical results considers the axisymmetric geometry. Solving (2.2.1p) numerically, subject to the initial and boundary conditions

$$\begin{aligned} \text{at} \quad & t = 0 \quad h = (1 - r^2)_+, \\ \text{as} \quad & r \to \infty \quad h \to 0, \end{aligned} \tag{2.2.26}$$

together with radial symmetry at $r = 0$,

$$\frac{\partial h}{\partial r} = 0. \tag{2.2.27}$$

gives the drop evolution and streamlines shown in Figure 2.6.

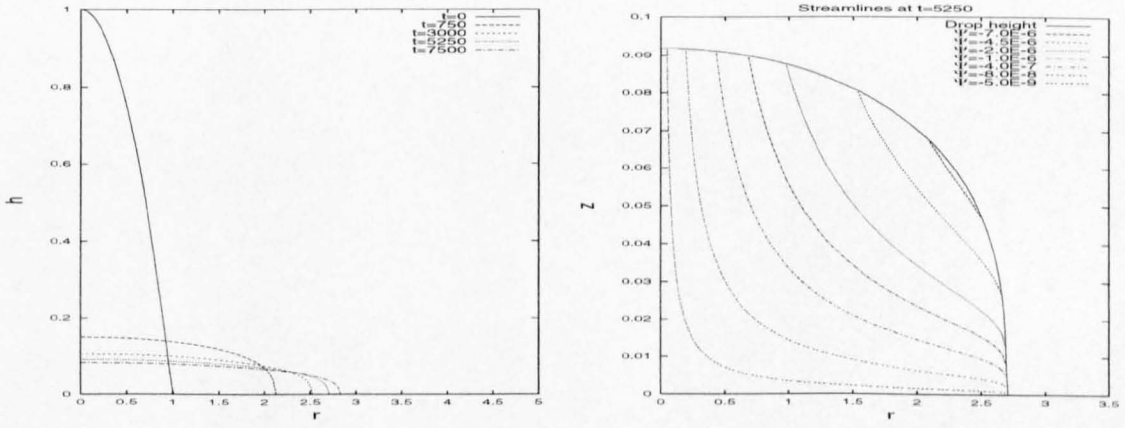

(a) Free surface profiles. (b) Streamlines at $t = 5250$.

FIG. 2.6. Axisymmetric spreading of a constant mass of fluid: isothermal case.

As in the two-dimensional case the effect of gravity is clearly observed on the free surface profiles. The log-log plots of the front location, s, and maximum height of the drop, h_{max}, against time are shown in Figure 2.7 and are again compared with the analytical solution given by (2.2.13). The graphs show that $s \sim t^{\frac{1}{8}}$ and $h_{max} \sim t^{-\frac{1}{4}}$ as $t \to \infty$. This again agrees with known similarity solutions, López & Miller (1976) and Huppert *et al.* (1982).

2.2.5. *Numerical results for the axisymmetric spreading of a drop fed by a point source*

The inflow boundary condition (2.1.70) using (2.2.2), simplifies for the isothermal model to

$$\frac{\partial h}{\partial r} + \frac{3\beta Q_c t^{\beta-1}}{2\pi r h^3} = 0. \tag{2.2.28}$$

The governing equation for the free surface, (2.2.1p), is now solved using the NAG routine D03PGF. The singularity at $r = 0$ causes complications in imposing the boundary condition

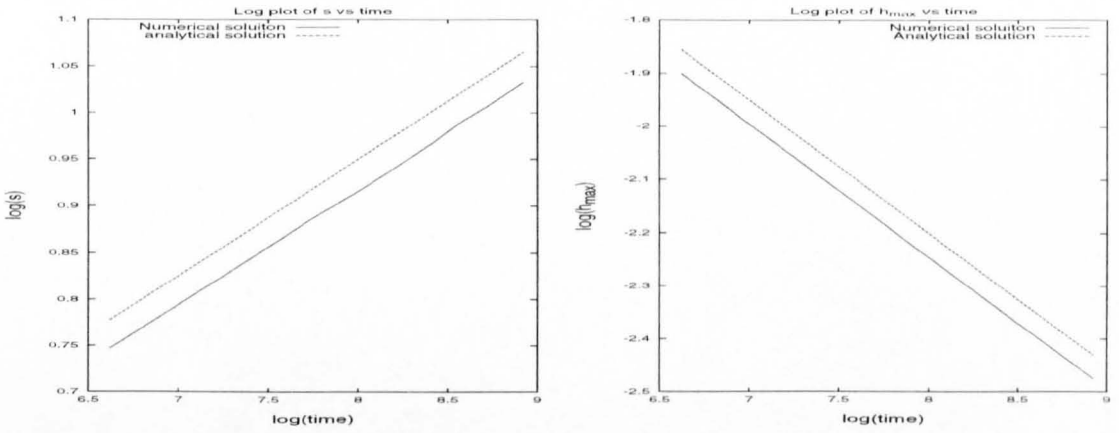

(a) Log-log plot of front location. (b) Log-log plot of drop height at $r = 0$.

FIG. 2.7. Isothermal spreading rates: axisymmetric with constant mass.

(2.2.28). To get round this, the boundary condition is applied at $r = \varepsilon$, where $\varepsilon = 0.01$ in the following numerical results. Again, as in the two-dimensional case, a small initial amount of mass is present at $t = 0$, the initial and boundary conditions being taken to be

$$\begin{aligned} &\text{at} \quad t = 0 \quad h = 10(0.01 - r^2)_+, \\ &\text{as} \quad r \to \infty \quad h \to 0. \end{aligned} \tag{2.2.29}$$

The resulting surface profiles and streamlines are shown in Figure 2.8 for $\beta = 1.4$ and $Q_p = 0.07$. The streamlines are similar to the two-dimensional case, showing that the contact line is fed by

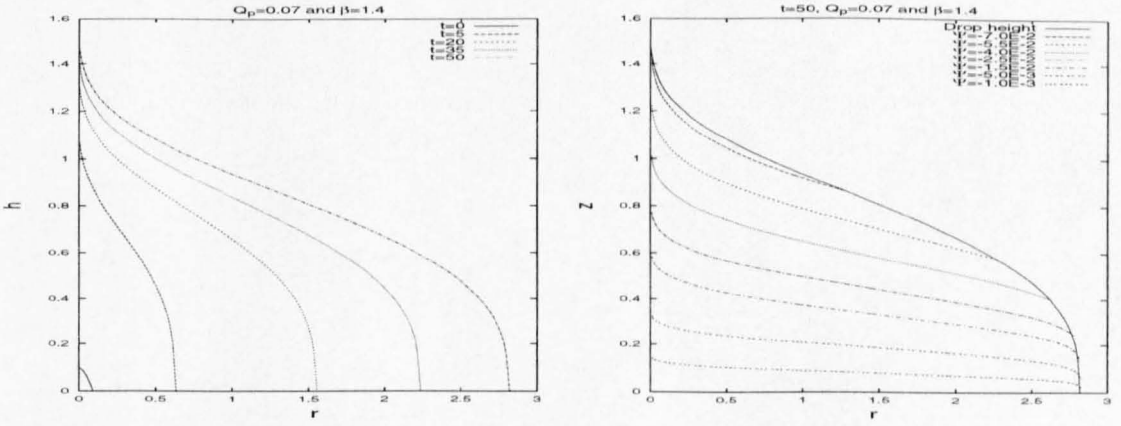

(a) Free surface profiles. (b) Streamlines at $t = 50$.

FIG. 2.8. Axisymmetric spreading from a point sourced with $\beta = 1.4$ and $Q_p = 0.07$.

the fluid from the point source. Figure 2.9 confirms, as expected, $s \sim t^{\frac{13}{20}}$ as $t \to \infty$ for $\beta = 1.4$ by comparing the numerical spreading rates with the analytical solution from (2.2.19). The height at $r = 0$ cannot be found because it is in fact unbounded and numerically the boundary condition is set at $r = \varepsilon$.

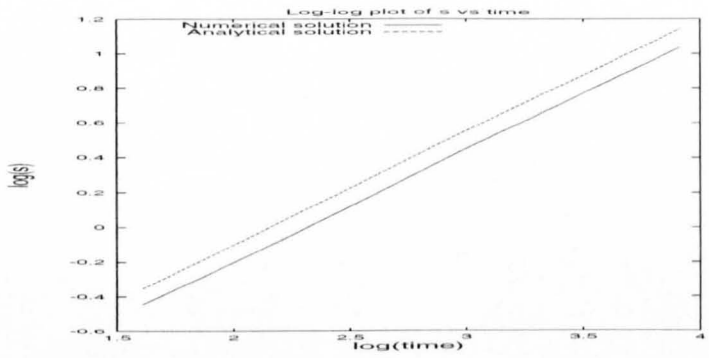

FIG. 2.9. Log-log plot of front location *vs* time.

2.2.6. *Numerical validation*

To complete the comparison of the numerical results with the similarity solutions, the constant d in (2.2.10) and (2.2.13) is needed. For the two-dimensional case, substituting (2.2.10) into the global continuity equation (2.2.6) gives

$$\left(\frac{9}{10}\right)^{\frac{1}{3}} \int_{-d}^{d} (d^2 - \eta^2)^{\frac{1}{3}} d\eta = \left(\frac{9}{10}\right)^{\frac{1}{3}} d^{\frac{5}{3}} \int_{0}^{\pi} \sin^{\frac{5}{3}} \theta d\theta = 2Q_c, \tag{2.2.30}$$

using the substitution $\eta = d\cos\theta$. This simplifies to

$$d \propto \left(\frac{9}{10}\right)^{-\frac{1}{5}} \left(\frac{2Q_c}{1.6826}\right)^{\frac{3}{5}} \tag{2.2.31}$$

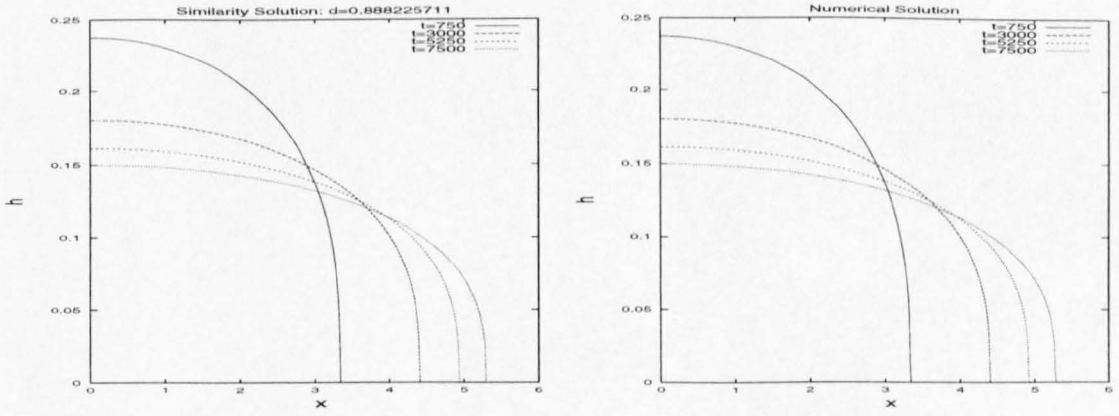

(a) Similarity solutions. (b) Numerical solutions.

FIG. 2.10. Two-dimensional spreading of a constant mass of fluid: analytical *vs* numerical.

For the axisymmetric constant mass case, substituting (2.2.13) into the global continuity equation gives

$$2\pi \int_{0}^{\infty} rh(r,t)dr = 2\pi \left(\frac{9}{16}\right)^{-\frac{1}{8}} \int_{0}^{d} \eta(d^2 - \eta^2)d\eta = Q_p, \tag{2.2.32}$$

hence

$$d = \left(\frac{9}{16}\right)^{-\frac{1}{8}} \left(\frac{4}{3\pi} Q_p\right)^{\frac{3}{8}}. \tag{2.2.33}$$

The values of Q_c and Q_p are the mass of the fluid in two-dimensional and axisymmetric geometries, respectively, and are calculated from the initial conditions. Comparisons between the similarity and numerical solutions are shown in Figures 2.10-2.11 in the two-dimensional and axisymmetric cases, respectively. The agreement is excellent, the figures being graphically indistinguishable.

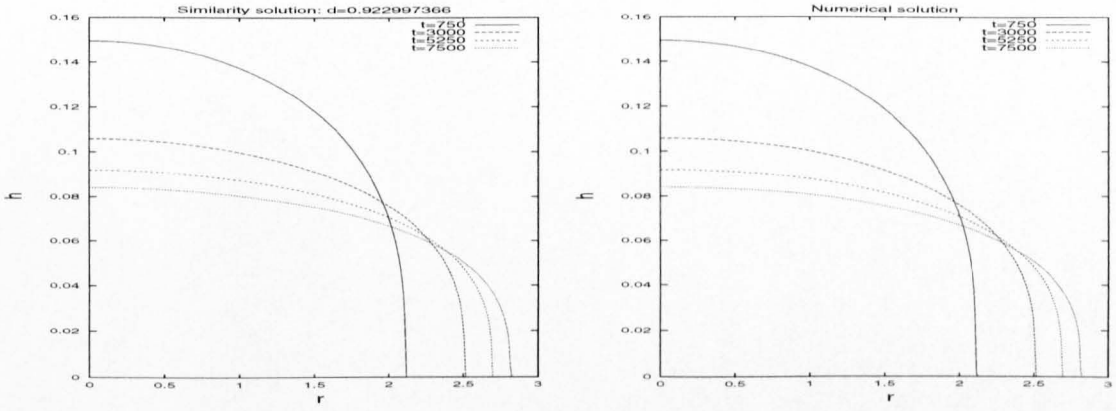

(a) Similarity solutions. (b) Numerical solutions.

FIG. 2.11. Axisymmetric spreading of a constant mass of fluid: analytical *vs* numerical.

Another check is to plot $t^a h$ *vs* rt^{-b}, which should show the profiles converge as $t \to \infty$. The results shown in Figure 2.12 are for the two-dimensional case with influx ($t^{\frac{1-2\beta}{5}} h$ *vs* $xt^{-\frac{3\beta+1}{5}}$) and axisymmetric spreading from a point source ($t^{\frac{1-\beta}{4}} h$ *vs* $rt^{-\frac{3\beta+1}{8}}$). As expected, the solutions

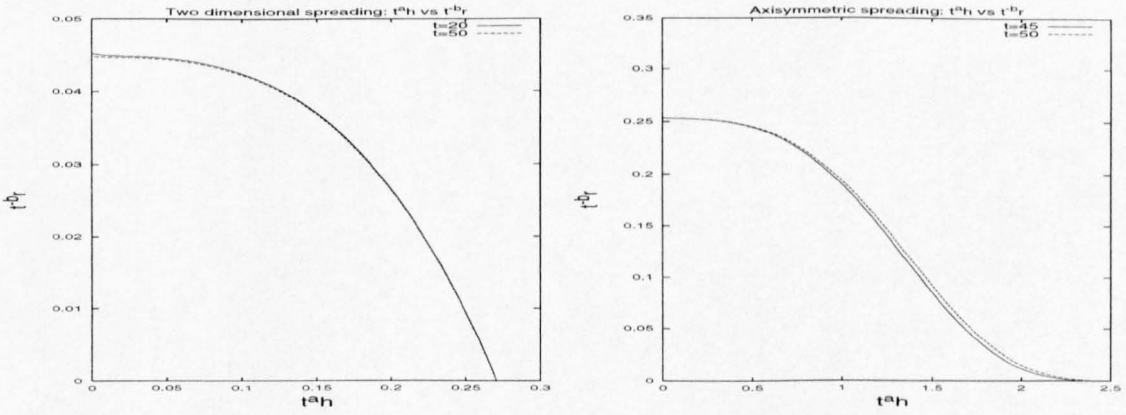

(a) Two-dimensional inflow model with $Q_c = 0.009$ and $\beta = 1.5$.

(b) Axisymmetric inflow model with $Q_c = 0.05$ and $\beta = 1.4$.

FIG. 2.12. Convergence check for fluid spreading from a line and point source.

to both models converge as $t \to \infty$. Notice that the convergence for the axisymmetric model is not as rapid as the two-dimensional model. The reason for this is probably that the boundary condition at $r = 0$ for the point source boundary condition is shifted numerically to $r = \varepsilon$. Such checks can also be used on the constant mass numerical results.

2.3. Hot and cold substrate models

We now consider the situation where there is no internal heating and the surface of the drop and the substrate are at different constant temperatures. First we take, from (2.1.17),

$$\frac{\partial^2 T}{\partial z^2} = 0,$$

with $T = 0$ on $z = 0$ and $T = 1$ on $z = h$. Hence the temperature field is given by

$$T = \frac{z}{h}. \tag{2.3.1}$$

In the second case we consider the reverse case in which the drop surface is cold ($T = 0$) and the substrate hot ($T = 1$). In this case

$$T = \frac{h - z}{h}. \tag{2.3.2}$$

2.3.1. *Linear viscosity model*

Considering the linear viscosity law in the cold substrate model, we have

$$\begin{aligned} \mu &= 1 - \alpha T \\ &= 1 - \alpha z/h, \end{aligned} \tag{2.3.3}$$

with $\alpha < 1$ so that $\mu > 0$. Substituting (2.3.3) into (2.1.43) and (2.1.66) gives

$$\frac{\partial h}{\partial t} = \bar{k}_{lc} \frac{\partial}{\partial x}\left(h^3 \frac{\partial h}{\partial x}\right) \tag{2.3.4c}$$

and

$$\frac{\partial h}{\partial t} = \frac{\bar{k}_{lc}}{r} \frac{\partial}{\partial r}\left(r h^3 \frac{\partial h}{\partial r}\right), \tag{2.3.4p}$$

respectively, where the constant

$$\bar{k}_{lc} = \alpha^{-3}\left(\frac{3}{2}\alpha^2 - \alpha - (\alpha - 1)^2 \ln(1 - \alpha)\right).$$

The subscript notation lc denotes the linear viscosity model on a cold substrate and a similar notation is used for the different viscosity models and the hot substrate cases. As $\alpha \to 0$

$$\bar{k}_{lc} = \frac{1}{3} + \frac{1}{12}\alpha + \frac{1}{30}\alpha^2 + \frac{1}{60}\alpha^3 + O(\alpha^4) \tag{2.3.5}$$

and the isothermal forms, equations (2.2.1c) and (2.2.1p), are recovered when $\alpha = 0$. This can also be shown more generally by using the substitution $z = h\zeta$ in the diffusivity term in equation (2.1.43),

$$D = \int_0^h \frac{(z - h)^2}{\mu(z/h)} dz = h^3 \int_0^1 \frac{(\zeta' - 1)^2}{\mu(\zeta')} d\zeta'. \tag{2.3.6}$$

Thus, whenever T depends only on ζ and t, (2.3.4) can be mapped to the isothermal ($\mu = 1$) problem by introducing the new time variable

$$t^* = 3 \int_0^t \int_0^1 \frac{(1 - \zeta')^2}{\mu(T(\zeta', t'))} d\zeta' \, dt'. \tag{2.3.7}$$

In particular, the isothermal case is recovered by rescaling time with $3\bar{k}_{lc}$ for the cold substrate model. This is by no means obvious a priori; in particular, the streamlines differ between isothermal and non-isothermal cases, as shown in Figure 2.15 in the next section for an exponential viscosity model. The range for positive α is restricted in the linear viscosity case to $\alpha < 1$ and there is little variation in the streamline pattern.

The linear viscosity model for the hot substrate is

$$\mu = 1 - \alpha(h - z)/h. \tag{2.3.8}$$

Again substituting into (2.1.43) and (2.1.66), gives the governing diffusion equations for the free surface as

$$\frac{\partial h}{\partial t} = \bar{k}_{lh} \frac{\partial}{\partial x}\left(h^3 \frac{\partial h}{\partial x}\right) \tag{2.3.9c}$$

and

$$\frac{\partial h}{\partial t} = \frac{\bar{k}_{lh}}{r} \frac{\partial}{\partial r}\left(r h^3 \frac{\partial h}{\partial r}\right), \tag{2.3.9p}$$

with

$$\bar{k}_{lh} = \alpha^{-3}\left(-\frac{\alpha^2}{2} - \alpha - \ln(1-\alpha)\right),$$

and

$$\bar{k}_{lh} = \frac{1}{3} + \frac{1}{4}\alpha + \frac{1}{5}\alpha^2 + \frac{1}{6}\alpha^3 + O(\alpha^4) \tag{2.3.10}$$

as $\alpha \to 0$.

Increasing α is equivalent to decreasing the viscosity, so the drop spreads more quickly. Figure 2.13 shows that as α increases, $\bar{k}$ increases for both the hot and cold substrate models. The increase in $\bar{k}$ is less than that in the hot substrate model and implies that the cold substrate restricts the flow of spreading drop, as expected. Note again that rescaling time with $3\bar{k}$ recovers the isothermal case, (2.2.1).

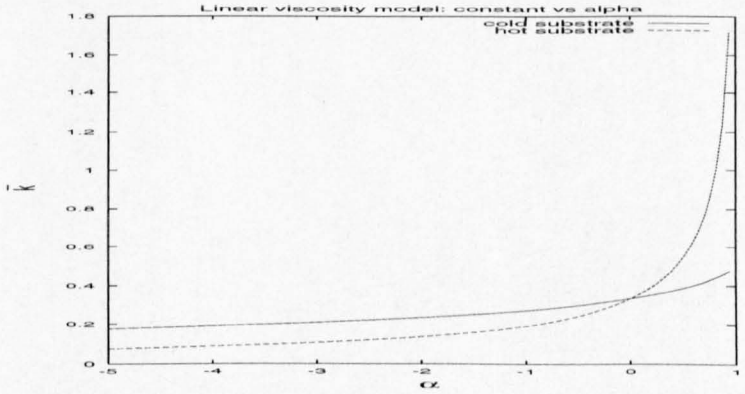

FIG. 2.13. Hot and cold substrate models of $\bar{k}$ *vs* α: linear viscosity relationship.

2.3.2. *Exponential viscosity model*

Considering the viscosity model

$$\begin{aligned}\mu &= e^{-\alpha T} \\ &= e^{-\alpha z/h},\end{aligned} \tag{2.3.11}$$

and evaluating the diffusivity integral in (2.1.43) and (2.1.66), the cold substrate model has the governing height evolution equations

$$\frac{\partial h}{\partial t} = \bar{k}_{ec}\frac{\partial}{\partial x}\left(h^3\frac{\partial h}{\partial x}\right) \tag{2.3.12c}$$

and

$$\frac{\partial h}{\partial t} = \frac{\bar{k}_{ec}}{r}\frac{\partial}{\partial r}\left(rh^3\frac{\partial h}{\partial r}\right), \tag{2.3.12p}$$

with

$$\bar{k}_{ec} = \alpha^{-3}\left(2e^{\alpha} - (\alpha^2 + 2\alpha + 2)\right),$$

and

$$\bar{k}_{ec} = \frac{1}{3} + \frac{1}{12}\alpha + \frac{1}{60}\alpha^2 + \frac{1}{360}\alpha^3 + O(\alpha^4) \tag{2.3.13}$$

as $\alpha \to 0$.

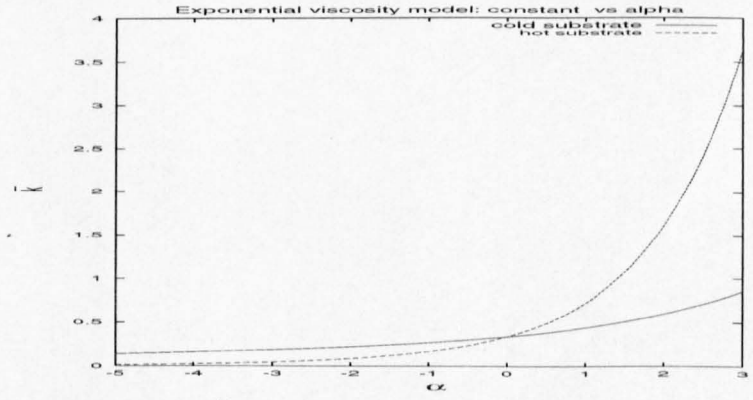

FIG. 2.14. Hot and cold substrate models of $\bar{k}$ *vs* α: exponential viscosity relationship.

The viscosity relationship for the hot substrate model is

$$\mu = e^{-\alpha(h-z)/h}, \tag{2.3.14}$$

which leads to the evolution equations

$$\frac{\partial h}{\partial t} = \bar{k}_{eh}\frac{\partial}{\partial x}\left(h^3\frac{\partial h}{\partial x}\right) \tag{2.3.15c}$$

and

$$\frac{\partial h}{\partial t} = \frac{\bar{k}_{eh}}{r}\frac{\partial}{\partial r}\left(rh^3\frac{\partial h}{\partial r}\right), \tag{2.3.15p}$$

with

$$\bar{k}_{eh} = \alpha^{-3}\left(e^{\alpha}(\alpha^2 - 2\alpha + 2) - 2\right)$$

and

$$\bar{k}_{eh} = \frac{1}{3} + \frac{1}{4}\alpha + \frac{1}{10}\alpha^2 + \frac{1}{36}\alpha^3 + O(\alpha^4), \tag{2.3.16}$$

as $\alpha \to 0$. Figure 2.14 shows the relationship between $\bar{k}$ and α, and (as for the linear viscosity relationship) the cold substrate model shows a slower increase in $\bar{k}$ with increasing α than the hot substrate model. As discussed in the linear model, rescaling time in equations (2.3.12) and (2.3.15) with $3\bar{k}$ gives the isothermal case ($\mu = 1$).

The results for the spreading of a fluid with constant mass in a two-dimensional geometry, illustrated in Figure 2.15, show the effect that the hot and cold substrate models have on the flow dynamics. The initial conditions are given by (2.2.20) and the governing equation (2.3.12) and (2.3.15) are solved using the NAG routine D03PGF. The times in Figures 2.15(a) and 2.15(b)

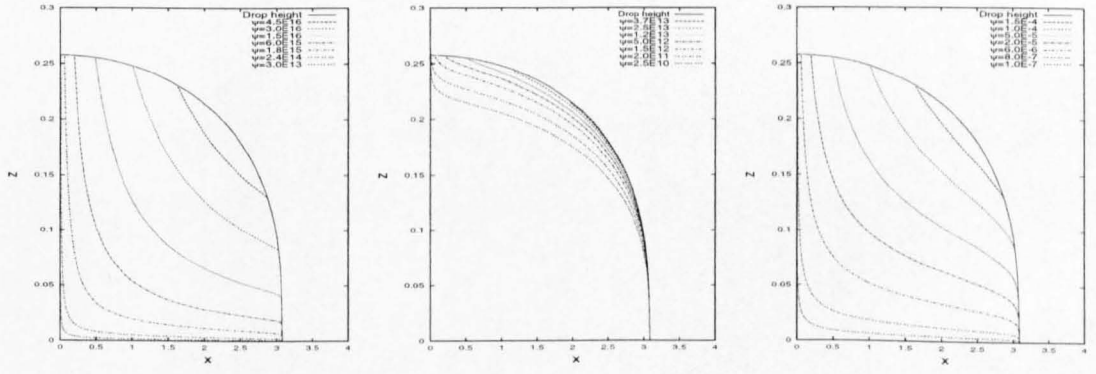

(a) (b) (c)

FIG. 2.15. Streamlines for the two-dimensional spreading of a constant mass of fluid with $\alpha = 50$. a) Hot substrate model, $t = 1.7 \times 10^{-18}$. b) Cold substrate model, $t = 2.0 \times 10^{-15}$ c) Isothermal model, $t = 500$.

are rescaled by $t = t_{iso}/3\bar{k}_{eh}(\alpha)$ and $t = t_{iso}/3\bar{k}_{ec}(\alpha)$ respectively, where t_{iso} is the value of time in Figure 2.15(c); similarly the streamlines in Figures 2.15(a) and 2.15(b) are rescaled by $\psi = 3\bar{k}_{eh}(\alpha)\psi_{iso}$ and $\psi = 3\bar{k}_{ec}(\alpha)\psi_{iso}$ respectively, where ψ_{iso} are the streamline values in Figure 2.15(c). As to be expected, most of the flow in Figures 2.15(a) and 2.15(b) occurs where the fluid is hottest and the viscosity therefore lowest.

2.3.3. *Bi-viscosity model*

The last case we consider involves a bi-viscosity model:

$$\mu = \begin{cases} 2a - 1 & \text{if } T > T_m, \\ 1 & \text{if } T < T_m, \end{cases} \tag{2.3.17}$$

where T_m and a are constants such that $0 < T_m < 1$; setting a close to 0.5 gives the greatest viscosity contrast between the two regions. The piecewise constant approximation for the diffusivity

in equation (2.1.43) and (2.1.66) for the cold substrate model is

$$D = \int_0^{hT_m} \frac{(z-h)^2}{1} dz + \int_{hT_m}^{h} \frac{(z-h)^2}{2a-1} dz. \tag{2.3.18}$$

This leads to

$$\frac{\partial h}{\partial t} = \bar{k}_{bc} \frac{\partial}{\partial x}\left(h^3 \frac{\partial h}{\partial x}\right) \tag{2.3.19c}$$

and

$$\frac{\partial h}{\partial t} = \frac{\bar{k}_{bc}}{r} \frac{\partial}{\partial r}\left(r h^3 \frac{\partial h}{\partial r}\right), \tag{2.3.19p}$$

where

$$\bar{k}_{bc} = \frac{2T_m(a-1)(T_m^2 - 3T_m + 3) + 1}{3(2a-1)}.$$

Solving (2.3.19c) numerically using NAG routine D03PGF, subject to (2.2.20), the two-dimensional spreading of a constant mass, has height profiles and streamlines shown in Figure 2.16.

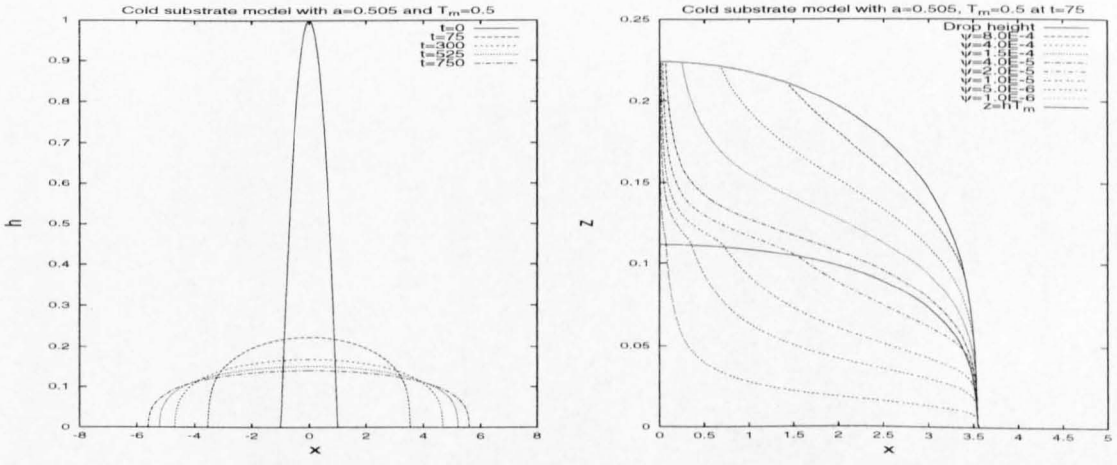

(a) Free surface profiles. (b) Streamlines at $t = 75$.

FIG. 2.16. Two-dimensional spreading of a constant mass of liquid: cold substrate results.

The free surface profiles are given by those for the isothermal model, (2.2.1c), on rescaling time with $3\bar{k}_{bc}$, see (2.3.19c) and (2.3.7). The streamlines show the effect that the viscosity variation has on the spreading dynamics: the fluid immediately above the cold substrate is more viscous and the flow is restricted compared to the region above the hot substrate. The boundary across which the viscosity changes is given by $z = hT_m$ and is shown in Figure 2.16(b).

Solving (2.3.19p) numerically using NAG routine D03PGF, subject to (2.2.26)-(2.2.27), the axisymmetric spreading of a constant mass has height profiles and streamlines shown in Figure 2.17.

The height profiles in Figure 2.17(a) are given by the isothermal model, (2.2.1p) on rescaling time with $3\bar{k}_{bc}$, as in the two-dimensional constant mass case. The streamlines in Figure 2.17(b) are similar to the two-dimensional constant mass ones. Comparing with Figure 2.16(b) shows the effect that the viscosity variation has on the spreading dynamics.

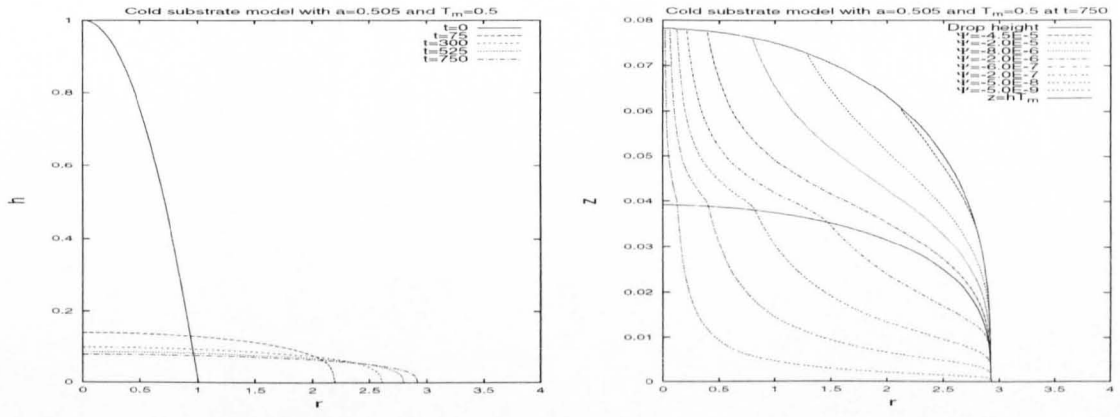

(a) Free surface profiles. (b) Streamlines at $t = 750$.

FIG. 2.17. Axisymmetric spreading of a constant mass of fluid: cold substrate results.

The two-dimensional model is now extended to include a line source at $x = 0$, such that the influx boundary condition from (2.1.48) simplifies for the cold substrate model to

$$\frac{\partial h}{\partial x} + \frac{\mu\beta Q_c t^{\beta-1}}{\bar{k}_{bc} h^3} = 0. \tag{2.3.20}$$

The initial conditions for the influx model are given by (2.2.25) and result in the height profiles and streamlines given in Figure 2.18.

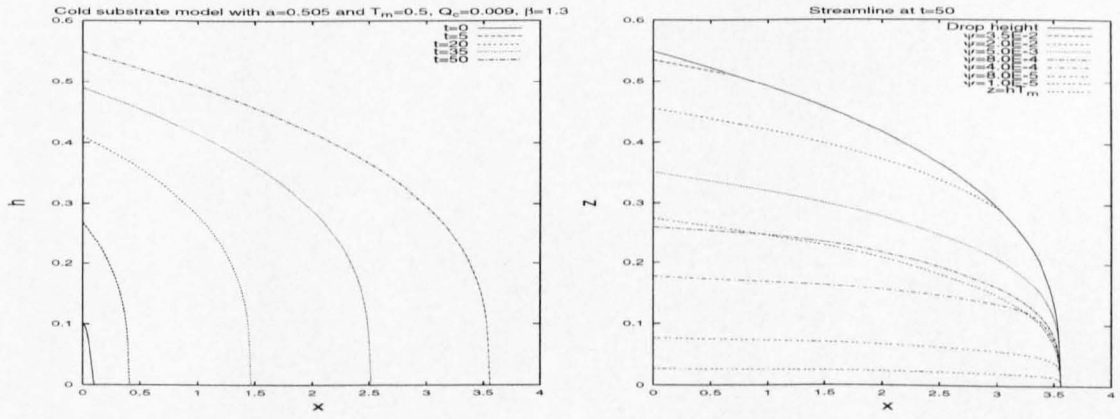

(a) Free surface profiles. (b) Streamlines at $t = 50$.

FIG. 2.18. Two-dimensional spreading from a line source with $\beta = 1.3$ and $Q_c = 0.009$: cold substrate results.

The height profiles are again equivalent to the isothermal case on rescaling time with $3k_{bc}$, see Figure 2.18(a). The streamlines do not show the effects of the cold substrate as clearly as the constant mass case, because the streamlines run in a similar direction to the boundary across which the viscosity changes.

Finally, the axisymmetric case is extended to include a point source condition at $r = \varepsilon$, where $\varepsilon = 0.01$. The influx boundary condition from (2.1.70) simplifies for the cold substrate model to

$$\frac{\partial h}{\partial r} + \frac{\mu\beta Q_p t^{\beta-1}}{2\pi r \bar{k}_{bc} h^3} = 0. \tag{2.3.21}$$

The initial conditions for the point source model are given by (2.2.29), resulting in height profiles and streamlines shown in Figure 2.19.

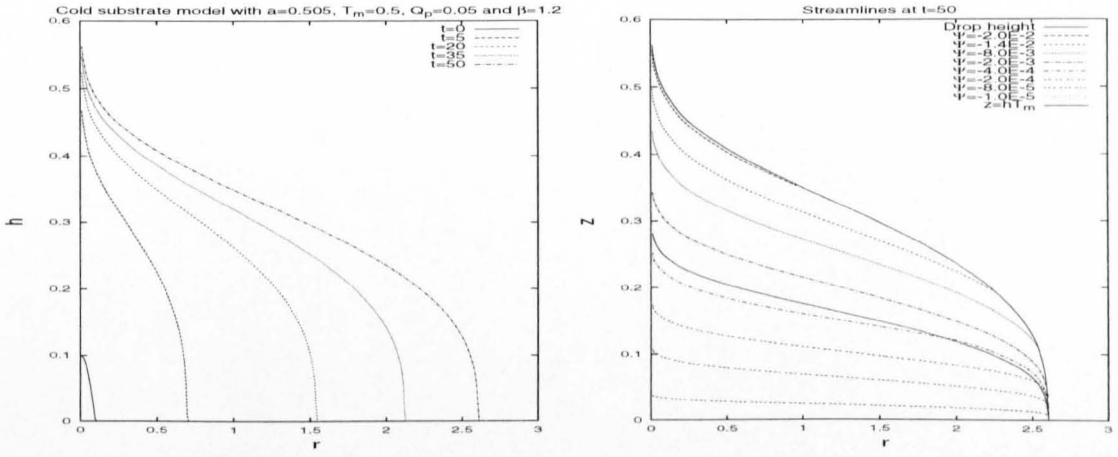

(a) Free surface profiles. (b) Streamlines at $t = 50$.

FIG. 2.19. Axisymmetric spreading from a point source with $\beta = 1.2$ and $Q_p = 0.05$: cold substrate results.

The height profiles are again equivalent to the isothermal case on rescaling time with $3k_{bc}$; the streamlines do not show the effects of the cold substrate as clearly as in the constant mass case.

In the case of a hot substrate, the piecewise constant approximation for the diffusivity is

$$D = \int_0^{h(1-T_m)} \frac{(z-h)^2}{2a-1}\,dz + \int_{h(1-T_m)}^{h} \frac{(z-h)^2}{1}\,dz. \tag{2.3.22}$$

Hence the height evolution equation is

$$\frac{\partial h}{\partial t} = \bar{k}_{bh}\frac{\partial}{\partial x}\left(h^3\frac{\partial h}{\partial x}\right) \tag{2.3.23c}$$

and

$$\frac{\partial h}{\partial t} = \frac{\bar{k}_{bh}}{r}\frac{\partial}{\partial r}\left(rh^3\frac{\partial h}{\partial r}\right), \tag{2.3.23p}$$

where

$$\bar{k}_{bh} = \frac{2T_m^3(a-1)+1}{3(2a-1)}.$$

Solving equation (2.3.23c) subject to (2.2.20) numerically gives the results shown in Figure 2.20 for planar spreading of a fluid of constant mass.

Solving equation (2.3.23p) numerically subject to (2.2.26)-(2.2.27), results in the height profiles and streamlines shown in Figure 2.21.

The height profiles for the two-dimensional and axisymmetric cases with constant mass, as shown in Figures 2.20(a) and 2.21(a), respectively, are again equivalent to the isothermal case on rescaling time with $3\bar{k}_{bh}$. The fluid spreads at a much quicker rate compared to the respective results with a cold substrate; this is due to the fluid near the hot substrate being less viscous

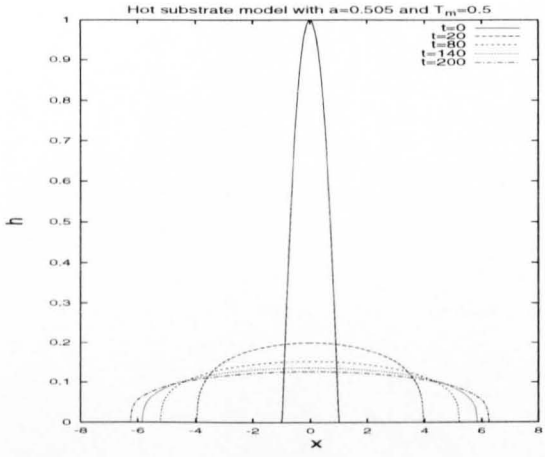

(a) Free surface profiles.

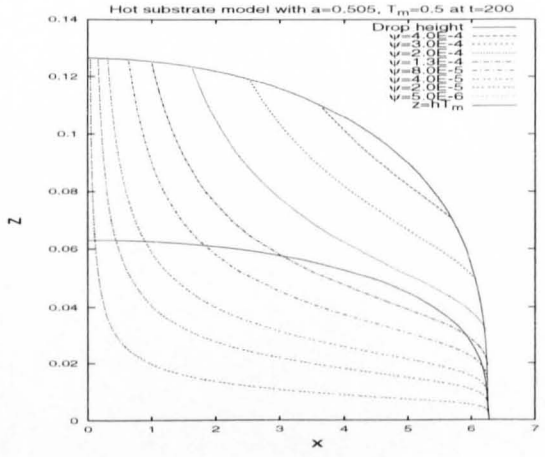

(b) Streamlines at $t = 200$.

FIG. 2.20. Two-dimensional spreading of a constant mass of fluid: hot substrate results.

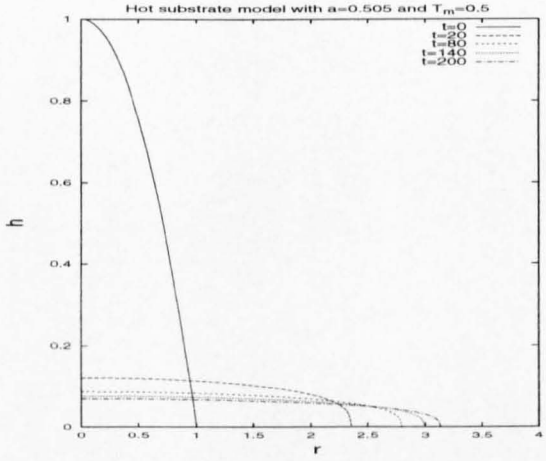

(a) Free surface profiles.

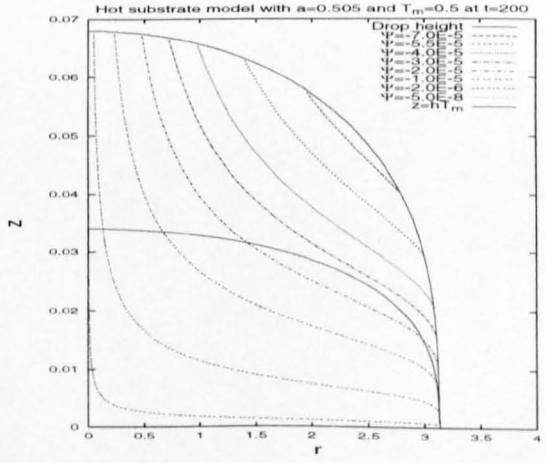

(b) Streamlines at $t = 200$.

FIG. 2.21. Axisymmetric spreading of a constant mass of fluid: hot substrate results.

than that near to a cold substrate. The streamlines show no noticeable effects of the change of viscosity at $z = hT_m$, Figures 2.20(b) and 2.21(b) compared with Figures 2.16(b) and 2.17(b).

Extending the hot substrate two-dimensional model to include the influx boundary condition, (2.1.48) simplifies to

$$\frac{\partial h}{\partial x} + \frac{\mu\beta Q_c t^{\beta-1}}{\bar{k}_{bh} h^3} = 0. \tag{2.3.24}$$

The initial and boundary conditions (2.2.25) are applied and result in the free surface profiles and streamlines shown in Figure 2.22.

The height profiles in Figure 2.22(a) are again equivalent to the isothermal case following a rescaling of time with $3\bar{k}_{bh}$; the fluid spreads at a quicker rate than that in the cold substrate case, see Figure 2.18(a). The streamlines show no effect of the viscosity change on crossing $z = hT_m$, see Figure 2.22(b).

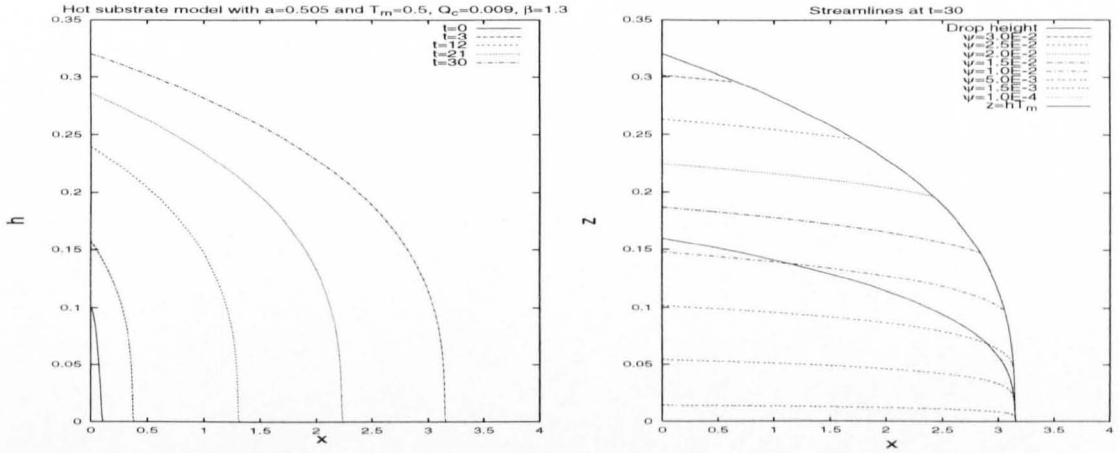

(a) Free surface profiles. (b) Streamlines at $t = 30$.

FIG. 2.22. Axisymmetric spreading from a point source with $\beta = 1.3$ and $Q_c = 0.009$: hot substrate results.

Finally, we extend the hot substrate model to include a point source, so the influx boundary condition applied at $r = \varepsilon$ ($\varepsilon = 0.01$) is

$$\frac{\partial h}{\partial r} + \frac{\mu\beta Q_c t^{\beta-1}}{2\pi r \bar{k}_{bh} h^3} = 0. \tag{2.3.25}$$

On applying the initial and boundary conditions from (2.2.29), the NAG routine D03PGF gives the free surface profiles and streamlines shown in Figure 2.23.

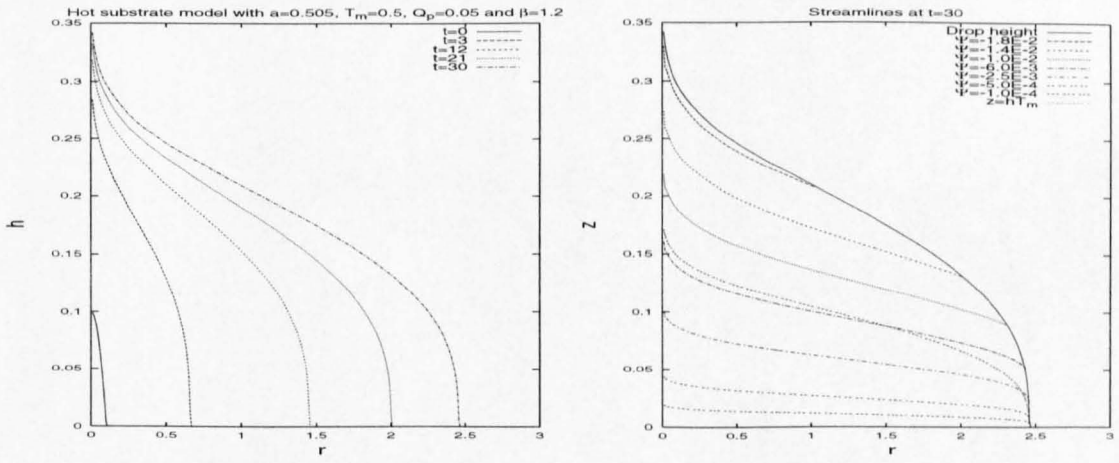

(a) Free surface profiles. (b) Streamlines at $t = 30$.

FIG. 2.23. Axisymmetric spreading from a point source with $\beta = 1.2$ and $Q_p = 0.05$: hot substrate results.

The results are similar to the two-dimensional model with influx: the height profiles in Figure 2.23(a) are given by the isothermal ones on rescaling time with $3\bar{k}_{bh}$ and the fluid spreads at a quicker rate than in the cold substrate case, Figure 2.19(a). The streamlines again show no effect of the viscosity change on crossing $z = hT_m$, see Figure 2.23(b).

Note that the streamlines are found numerically by using the trapezium rule for the integrals in

equations (2.1.29) and (2.1.62). The stream function depends upon T_m and is found numerically. The viscosity dependence on T_m is given by

$$\mu = \begin{cases} 2a - 1 & \text{if } z \leq hT_m, \\ 1 & \text{if } z > hT_m, \end{cases} \tag{2.3.26}$$

for the cold substrate model, and by

$$\mu = \begin{cases} 2a - 1 & \text{if } z \geq hT_m, \\ 1 & \text{if } z < hT_m, \end{cases} \tag{2.3.27}$$

for the hot substrate model.

The overall results show that the cold substrate inhibits the spreading of the droplet as compared with the hot substrate. This is expected because the viscosity is larger near the cold substrate and retards the flow compared to the smaller viscosity associated with the hot substrate. The simple model showed no thermal effect on the free surface profile, but did so on the timescale on which this evolution occurs, as highlighted by equation (2.3.7) which maps the free surface profiles to the isothermal case.

2.4. Simple internal heat generation model

In situations of practical interest, heat may be generated internally as the material spreads. Such heat generation may be caused by viscous dissipation, for example in turbulently convecting lavas (not applicable to this model), or radioactive decay, for example in nuclear reactor accidents. We now consider a very simple model in order to investigate such thermal effects on the spreading characteristics of liquids with temperature-dependent viscosity. We assume that the temperature on the surface of the fluid and on the solid surface is uniform and that there is a constant rate of heat generation throughout the drop.

The temperature equation, from (2.1.16), is

$$\frac{\partial^2 T}{\partial z^2} = -1,$$

which is solved, subject to $T = 0$ on $z = 0$ and $z = h$, to give

$$T = \frac{1}{2} z(h - z). \tag{2.4.1}$$

This simple form will now be substituted into the three viscosity models introduced in Section 2.3 in turn.

2.4.1. *Linear viscosity model*

Here

$$\mu = 1 - \frac{\alpha}{2} z(h - z), \tag{2.4.2}$$

and evaluating the integrals in (2.1.43) and (2.1.66) gives

$$\frac{\partial h}{\partial t} = \frac{\partial}{\partial x}\left(D \frac{\partial h}{\partial x}\right) \tag{2.4.3c}$$

and

$$\frac{\partial h}{\partial t} = \frac{1}{r} \frac{\partial}{\partial r}\left(rD \frac{\partial h}{\partial r}\right). \tag{2.4.3p}$$

For $\alpha > 0$,

$$D = \frac{2\varphi h + (4h^2\alpha - 16) \tan^{-1}(\alpha h/\varphi)}{\alpha\varphi} \tag{2.4.4}$$

in both Cartesian and polar coordinates, where $\varphi = \sqrt{8\alpha - \alpha^2 h^2}$ and $0 \leq \alpha < 8$ (the non-dimensionalisation is chosen such that $h_{max} = 1$ at $t = 0$; since h_{max} decreases with time, the constraint $\alpha < 8$ ensures that μ is positive for the constant mass case). When $\alpha < 0$ or when $\alpha h^2 > 8$, for the influx case say, the free surface profile is calculated from equation (2.4.3) with

$$D = \frac{2\varphi h + (16 - 4h^2\alpha) \tanh^{-1}(\alpha h/\varphi)}{\alpha\varphi}, \tag{2.4.5}$$

where $\varphi = \sqrt{-8\alpha + \alpha^2 h^2}$. In practice, viscosity is typically a decreasing function of temperature, in which the case $\alpha < 0$ corresponds to an internal heat *sink*. Expanding the 'diffusivity', using

a Taylor series expansion about α gives

$$\frac{1}{3}h^3 + \frac{1}{40}\alpha h^5 + \frac{1}{420}\alpha^2 h^7 + \frac{1}{4032}\alpha^3 h^9 + O(\alpha^4).$$

Hence for small α the spreading drop may be expected to behave isothermally.

Results from solving (2.4.3c), (2.4.4) and (2.4.5) subject to (2.2.20), for the constant mass case in two dimensions (using the NAG routine D03PGF) are shown in Figures 2.24-2.25.

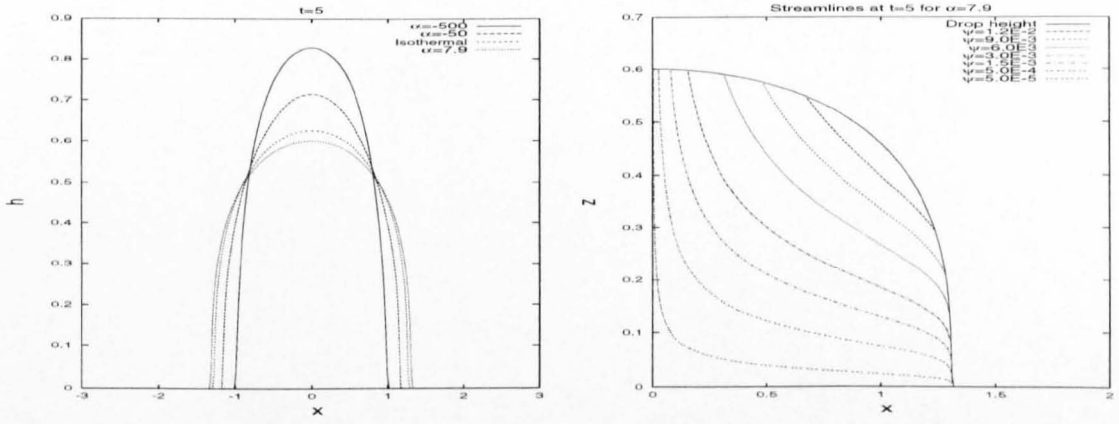

(a) Height profiles at $t = 5$, various α.

(b) Streamlines at $t = 5$, $\alpha = 7.9$.

FIG. 2.24. Results for linear viscosity model: two-dimensional spreading with constant mass.

Figure 2.24 shows a set of height profiles for $\alpha = 7.9$, $\alpha = -50$, $\alpha = -500$ at a fixed time, $t = 5$, together with the equivalent isothermal profile ($\alpha = 0$). The profiles for negative α show that the motion of the drop is retarded, as expected, because the drop is initially very viscous. On the other hand, at $t = 5$, the spreading has progressed further for $\alpha = 7.9$ than in the isothermal case. This is to be expected because the diffusivity is higher than the isothermal value as illustrated by the above Taylor expansion. Note the numerics fail when $\alpha > 7.9$. The streamlines for $\alpha = 7.9$ in Figure 2.24(b) are similar to the isothermal ones.

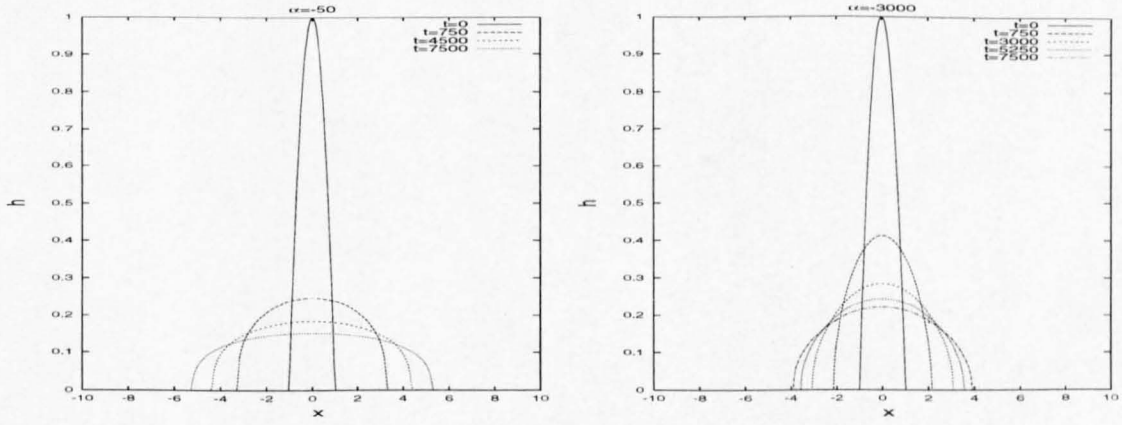

(a) Height profile with $\alpha = -50$.

(b) Height profile with $\alpha = -3000$.

FIG. 2.25. Results for linear viscosity model: planar spreading with constant mass and negative α.

Comparing the results for $\alpha = -50$, Figure 2.25(a), with those for $\alpha = -3000$, Figure 2.25(b),

shows for small time that the evolution is retarded by decreasing α. This is expected since the initial viscosity of the drop increases on decreasing α (cf. Figure 2.24(a) for $\alpha = -50$ and $\alpha = -500$).

Next, we consider the results for the linear viscosity model with the influx boundary condition (2.1.48) where the diffusivity, D, is given by (2.4.4) for positive α and (2.4.5) for negative α. Using the initial and boundary conditions given in (2.2.25), the computed height profiles and streamlines are as shown in Figure 2.26 for $Q_c = 0.01$, $\beta = 1.5$ and $\alpha = 7.9$.

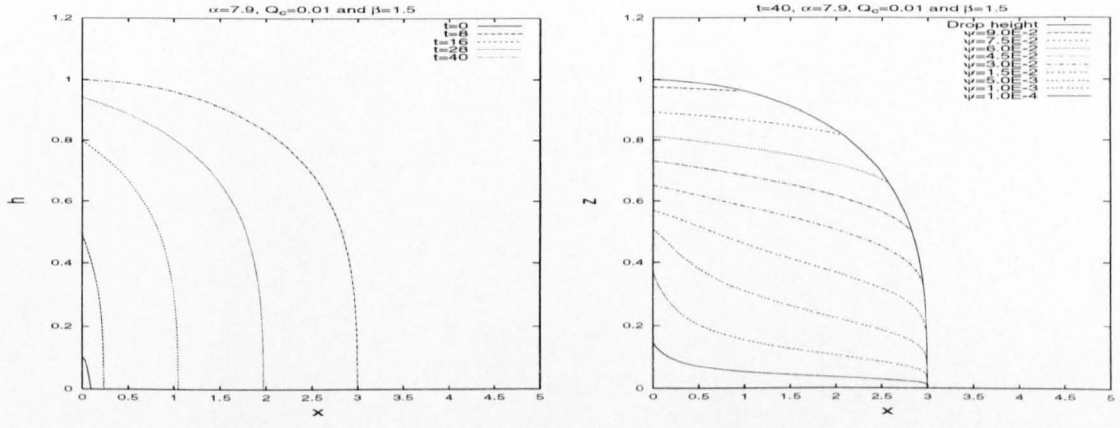

(a) Free surface profiles. (b) Streamlines at $t = 40$.

FIG. 2.26. Results for linear viscosity model: two-dimensional spreading from a line source.

These may be compared with the isothermal results in Figure 2.27. The height profiles for the non-isothermal model are flattened compared to the equivalent isothermal profiles and the streamlines are clearly affected by the temperature gradient. In particular, the contact line region is fed by the more mobile fluid from the centre of the drop in the non-isothermal case. Note that the maximum height is restricted in order to keep viscosity positive. Height profiles and streamlines for negative α are shown in Figure 2.28.

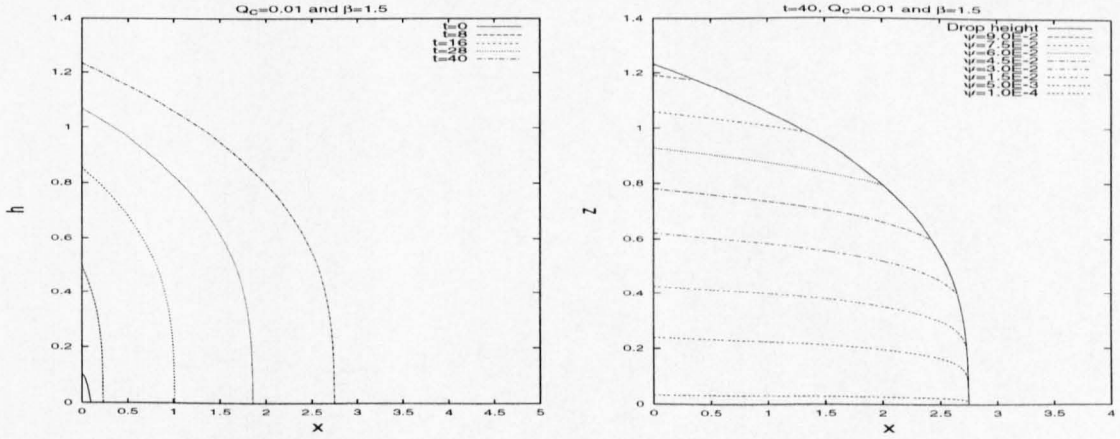

(a) Free surface profiles. (b) Streamlines at $t = 40$.

FIG. 2.27. Two-dimensional spreading with $Q_c = 0.01$ and $\beta = 1.5$: isothermal results.

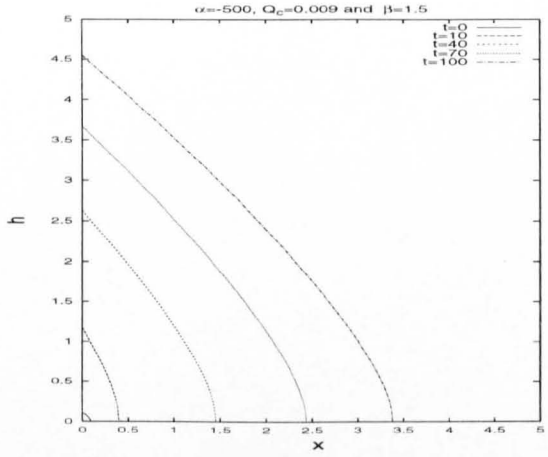

(a) Free surface profiles for $\alpha = -500$.

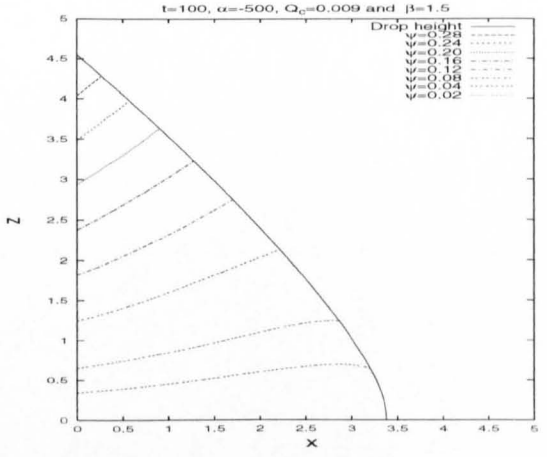

(b) Streamlines at $t = 100$ corresponding to Figure 2.28(a).

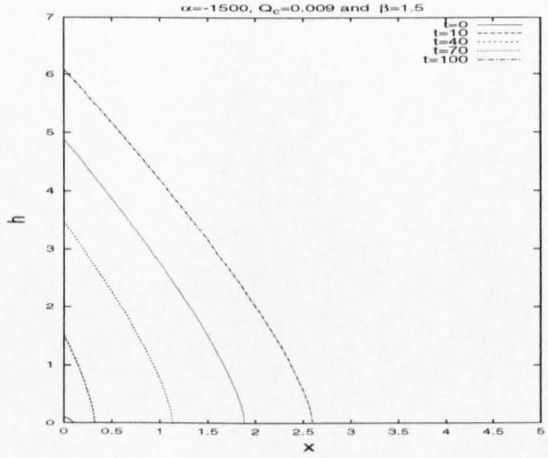

(c) Free surface profiles for $\alpha = -1500$.

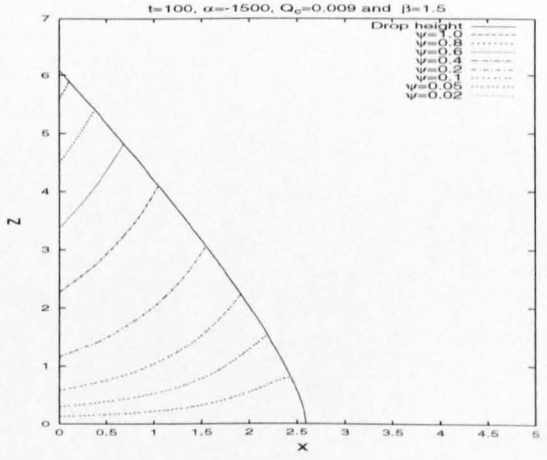

(d) Streamlines at $t = 100$ corresponding to Figure 2.28(c).

FIG. 2.28. Results for linear viscosity model: two-dimensional spreading from a line source for negative α.

The height profiles are shown to develop an almost triangular profile. Physically, the large initial value of the viscosity means that the drop is restricted in movement along the substrate, but the influx rate causes a build up of fluid, resulting in such profiles (see Figure 2.28(b)). The height at $x = 0$ and the front location appear to satisfy $h_{max} \propto t^{0.6}$ and $s \propto t^{0.9}$, respectively, for times t up to 20. As $\alpha \to -\infty$, the results in Section (2.4.3) show that the horizontal velocity component is independent of z, when z is not zero; and is the cause of the triangular profiles, where the evolution equation is simplified and shown to agree with the spreading rates stated above.

The final sets of results are for axisymmetric spreading. Solving (2.4.3p) with (2.4.4) and (2.4.5) using the NAG routine D03PGF, subject to the constant mass case conditions (2.2.26)-(2.2.27), gives the results in Figure 2.29.

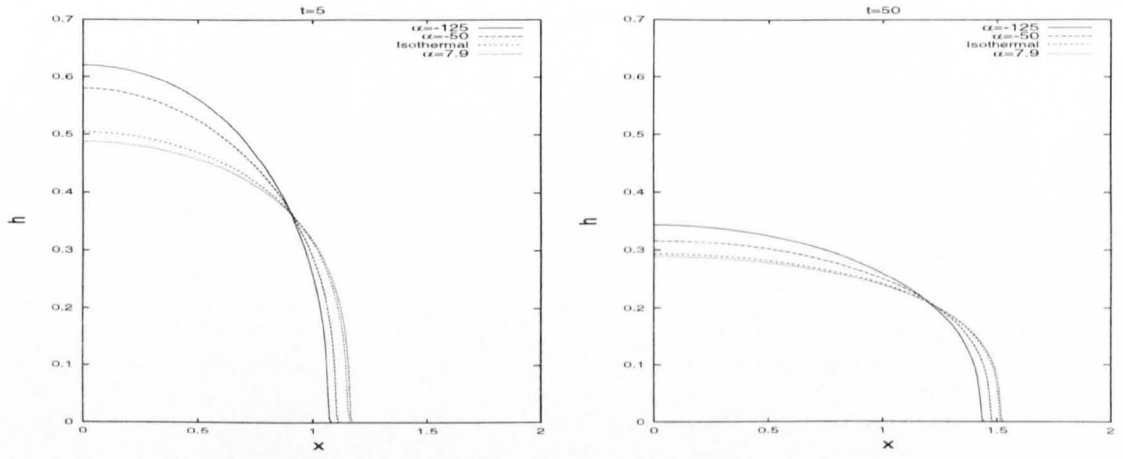

(a) Height profiles at $t = 5$, various α. (b) Height profiles at $t = 50$, various α.

FIG. 2.29. Results for linear viscosity model: axisymmetric spreading of a constant mass of fluid.

As for planar spreading, the free surface profiles for $\alpha = 7.9$ show that there is little difference from the isothermal profile and the profile for $\alpha = 7.9$ at $t = 5$ (Figure 2.29(a)) can be seen to be falling slightly faster than for the isothermal case. For larger time, $t = 50$ being shown in Figure 2.29(b), the profiles can be seen to be approaching the isothermal case. For negative α, the profiles again show that as α is decreased, the rate at which the drop spreads is reduced, caused by the increase in the initial viscosity.

The axisymmetric model is now extended to include an influx of fluid from a point source. This is done using the NAG routine D03PGF, subject to (2.2.29) and the boundary condition at $r = \varepsilon$ given by (2.1.70) with the diffusivities for positive and negative α given respectively by (2.4.4) and (2.4.5). First considering the positive α case gives the results in Figure 2.30.

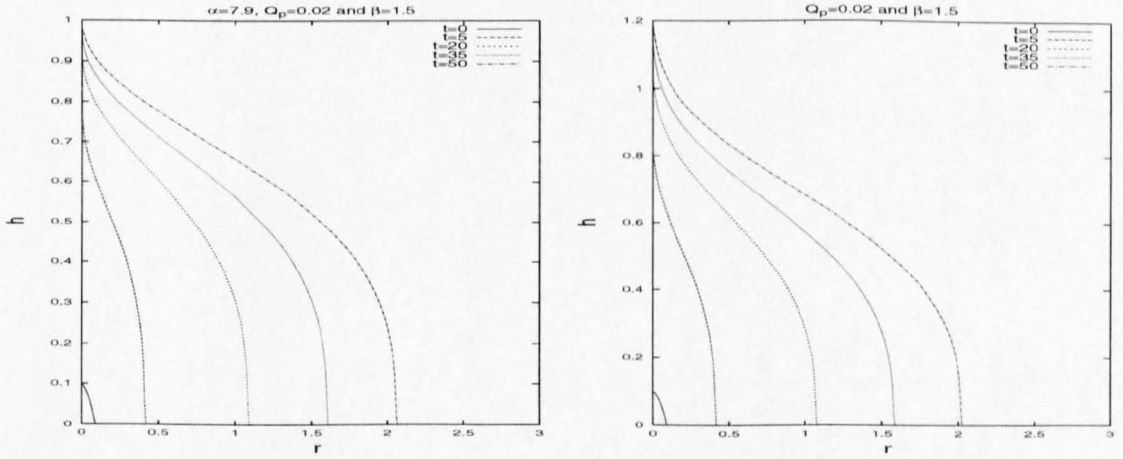

(a) Non-isothermal free surface profiles. (b) Isothermal free surface profiles.

FIG. 2.30. Comparisons of results for linear viscosity model and isothermal model: axisymmetric spreading from a point source.

As in the planar spreading case, the fluid's free surface profile is flattened due to the temper-

ature field. This can be seen by comparing the non-isothermal result in Figure 2.30(a) with the equivalent isothermal case in Figure 2.30(b).

The results for negative α for a point source are shown in Figure (2.31). As in the planar

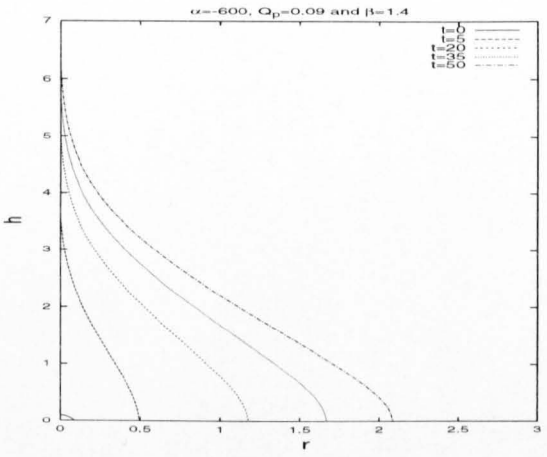

(a) Free surface profiles with $\alpha = -600$.

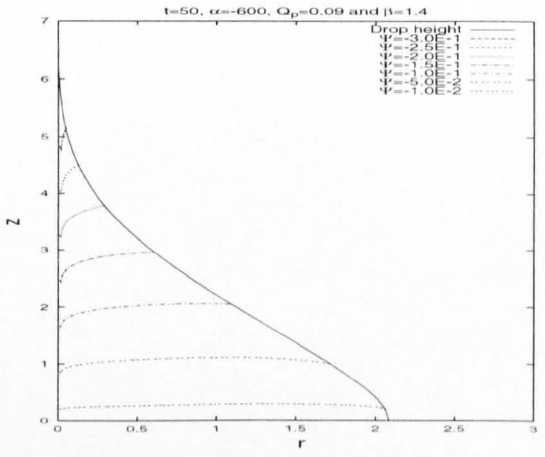

(b) Streamlines at $t = 50$ corresponding to Figure 2.28(a).

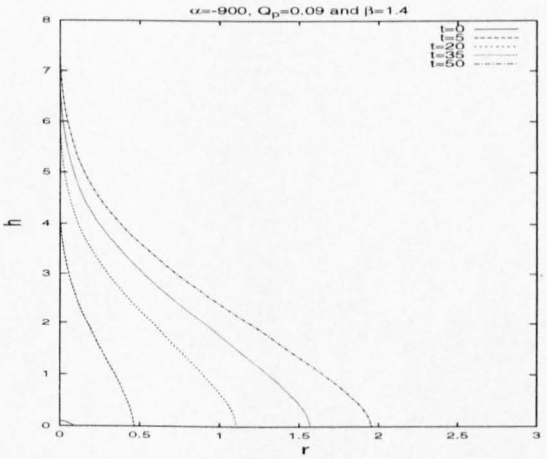

(c) Free surface profiles with $\alpha = -900$.

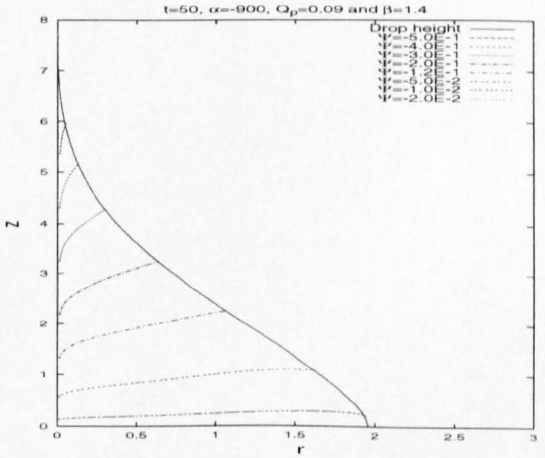

(d) Streamlines at $t = 50$ corresponding to Figure 2.28(c).

FIG. 2.31. Results for linear viscosity model: axisymmetric spreading from a point source for negative α.

spreading profiles from a line source, the free surface profiles develop a triangular profile. The front location appears to satisfy $s \propto t^{0.22}$ in Figure 2.31(a) and $s \propto t^{0.21}$ in Figure 2.31(c). Again the profile is caused by the large initial viscosity, which restricts the flow along the substrate and causes a build up of fluid to give the triangular profile.

The diffusivities are plotted as functions of h for $\alpha = 7.9$, $\alpha = 6.5$, $\alpha = -10$ and $\alpha = -50$, and are compared with the isothermal diffusivity, (2.2.2), in Figure 2.32. For positive α, the non-isothermal diffusivity can be seen to be greater, implying that the fluid will spread much quicker. Conversely for negative α, the non-isothermal diffusivity is smaller, implying that the

spreading of the fluid is retarded. This is in agreement with the behaviour seen in the free surface profiles for the above results.

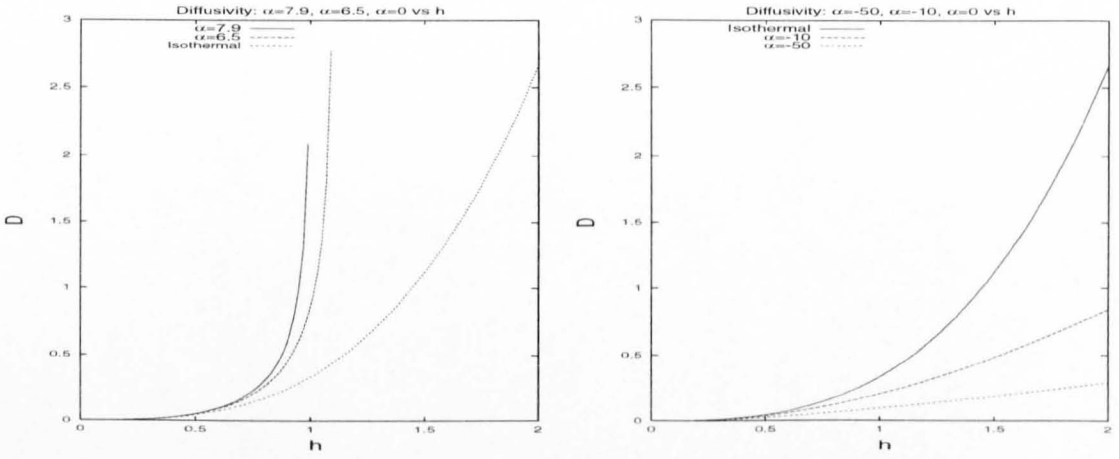

(a) Isothermal *vs* $\alpha = 7.9$. (b) Isothermal *vs* $\alpha = -10$.

FIG. 2.32. Diffusivity plots for the linear viscosity model with positive and negative α *vs* the isothermal case.

In summary, the results for positive α show little difference from the isothermal results, largely due to the restricted range of positive α permitted. For positive α, the height profiles are seen to be falling faster than in the isothermal case and is best exemplified in the line and point source models. The spreading fluid is increasingly retarded for the negative α case as α is decreased. This is as expected because decreasing α increases the initial viscosity.

2.4.2. *Exponential viscosity model*

In this case we have

$$\mu = e^{-\frac{\alpha}{2}z(h-z)}. \tag{2.4.6}$$

The diffusion equation governing the height profile is again given by (2.4.3), where the diffusivity, D, for positive α is now

$$D = \left(\frac{-h}{\alpha} + \sqrt{\frac{2\pi}{\alpha}} e^{\omega^2} \operatorname{erf}(\omega) \left(\frac{1}{\alpha} + \frac{h^2}{4} \right) \right), \tag{2.4.7}$$

$$\operatorname{erf}(\omega) = \frac{2}{\sqrt{\pi}} \int_0^{\omega} e^{-\tau^2} d\tau \quad \text{and} \quad \omega = \frac{\sqrt{2\alpha}h}{4}.$$

For negative α the diffusivity is best rewritten (using symmetry relations for the error function) in the form

$$D = \left(\frac{h}{|\alpha|} - \sqrt{\frac{2\pi}{|\alpha|}} I_D(\omega) \left(\frac{1}{|\alpha|} + \frac{h^2}{4} \right) \right), \tag{2.4.8}$$

where I_D is known as Dawson's integral, defined by

$$I_D(\omega) = e^{-w^2} \int_0^{\omega} e^{\tau^2} d\tau, \tag{2.4.9}$$

and $\omega = \sqrt{2|\alpha|}h/4$. Expanding either (2.4.7) or (2.4.8) about $\alpha = 0$ gives

$$D = \frac{1}{3}h^3 + \frac{1}{40}\alpha h^5 + \frac{1}{840}\alpha^2 h^7 + \frac{1}{24192}\alpha^3 h^9 + O(\alpha^4),$$

and the partial differential equation again reduces to that in the isothermal case when $\alpha = 0$.

The next set of results are for planar spreading with constant mass. Solving (2.4.3c) with (2.4.7) using the NAG routine D03PGF, (the error function is evaluated using NAG routine S15AEF) subject to (2.2.20) gives the results in Figures 2.33-2.34.

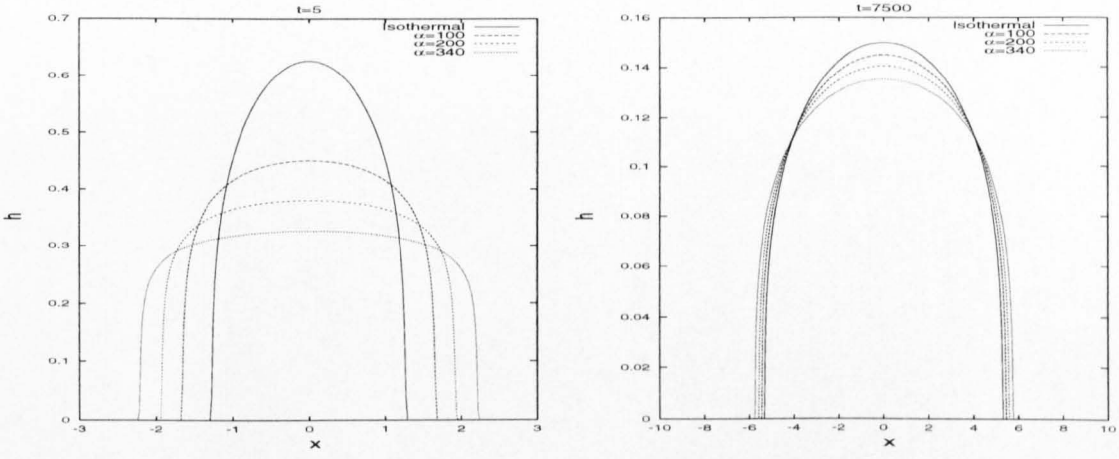

(a) Height profiles at $t = 5$. (b) Height profiles at $t = 7500$.

FIG. 2.33. Results for the exponential viscosity model: two-dimensional spreading with constant mass.

In Figure 2.33 the height profiles are shown at fixed times $t = 5$ and $t = 7500$ for the isothermal model ($\alpha = 0$) and for $\alpha = 100$, $\alpha = 200$ and $\alpha = 340$. The height profiles show that as α is increased, the profile develops a plateau caused by the temperature field. For larger time, Figure 2.33(b) shows that the temperature field has a smaller effect than for small time. This is because the temperature field is governed by a quadratic profile in the vertical direction which is dependent on h, and as the fluid spreads, h decreases for the constant mass case and $T \to 0$. Note that $\alpha = 340$ is the maximum attainable value before the numerics fail because of overflow resulting from the exponential term. The streamlines shown in Figure 2.34 for $\alpha = 100$ and $\alpha = 340$ show no effects of the temperature field and are qualitatively similar to the isothermal streamlines.

The next set of results in Figure 2.35 considers negative α. The governing equations (2.4.3c) and (2.4.8) are solved using the NAG routine D03PGF subject to the boundary and initial conditions described by (2.2.20), for constant mass in two dimensions. The integral in (2.4.8) is evaluated numerically using the NAG routine D01AHF, which encodes a Gaussian quadrature method.

Comparing the results for $\alpha = -300$ with those for $\alpha = -650$ in Figure 2.35, we see that for time $t = 750$ the spreading is retarded by decreasing α, as in the linear viscosity model. The streamlines show no noticeable effects of the temperature field (Figure 2.35(b) and 2.35(d)). The restricted flow can be seen more clearly in Figure 2.36(a) at the fixed time $t = 750$ with $\alpha = -150$,

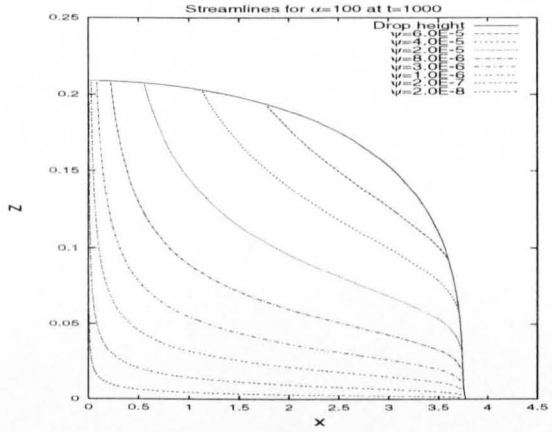

(a) Streamlines at $t = 1000$ with $\alpha = 100$.

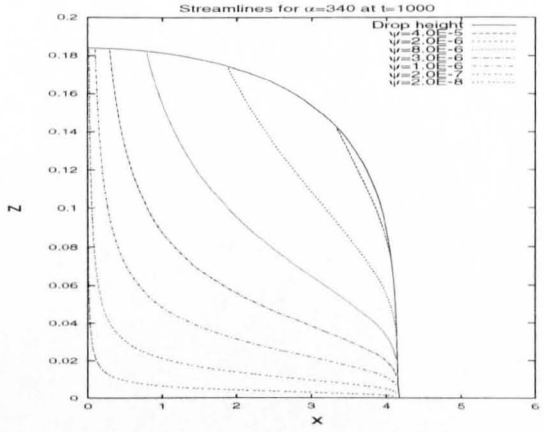

(b) Streamlines at $t = 1000$ with $\alpha = 340$.

FIG. 2.34. Results for the exponential viscosity model: two-dimensional spreading with constant mass.

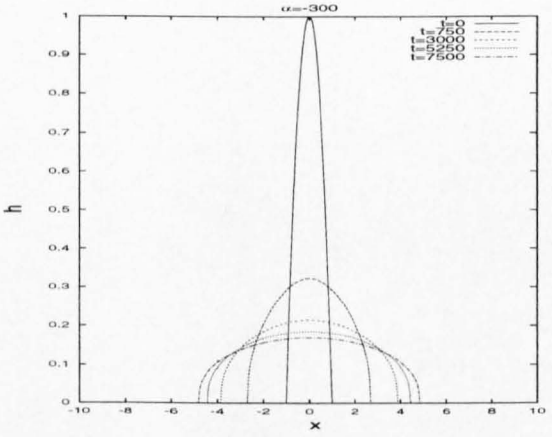

(a) Height profiles for $\alpha = -300$.

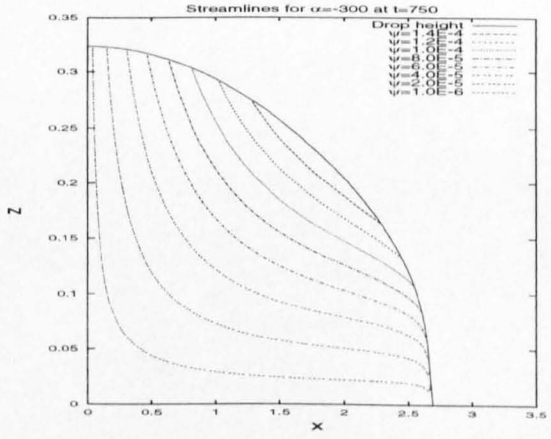

(b) Streamlines at $t = 750$ corresponding to Figure 2.35(a).

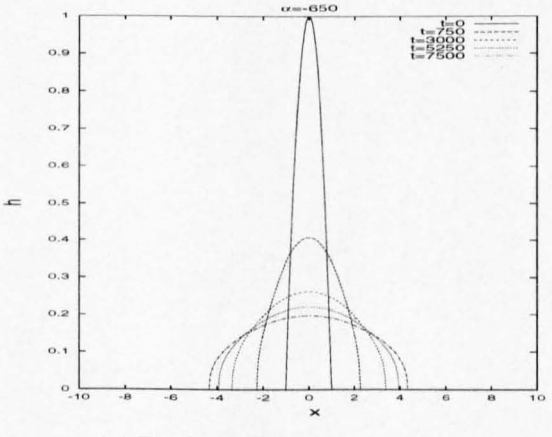

(c) Height profiles for $\alpha = -650$.

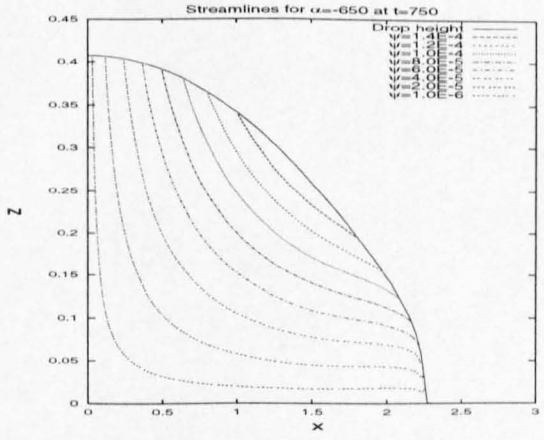

(d) Streamlines at $t = 750$ corresponding to Figure 2.35(c).

FIG. 2.35. Results for the exponential viscosity model: two-dimensional with constant mass for negative α.

$\alpha = -300$, $\alpha = -450$ and $\alpha = -650$, as well as the isothermal profile. The results show that decreasing α retards the flow, as expected. For larger time, $t = 7500$, over the same range of α (Figure 2.36(b)), the height profiles tending to behave isothermally.

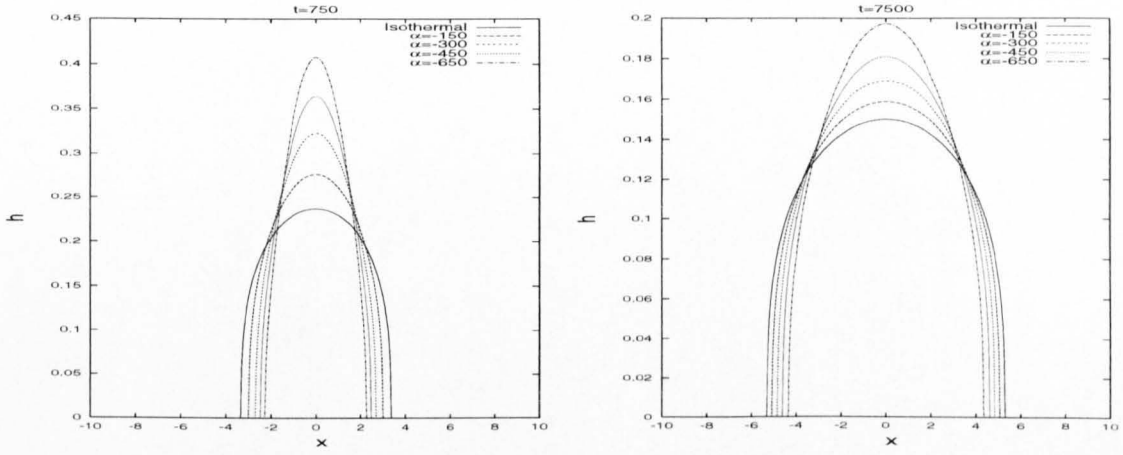

(a) Height profiles at $t = 750$. (b) Height profiles at $t = 7500$.

FIG. 2.36. Results for the exponential viscosity model: two-dimensional spreading with constant mass for negative α.

We now consider the exponential viscosity model in an axisymmetric geometry with constant mass. The results from solving (2.4.3p) with the diffusivity, (2.4.7), using the NAG routine D03PGF subject to (2.2.26) and (2.2.27) are given in Figures 2.37-2.38.

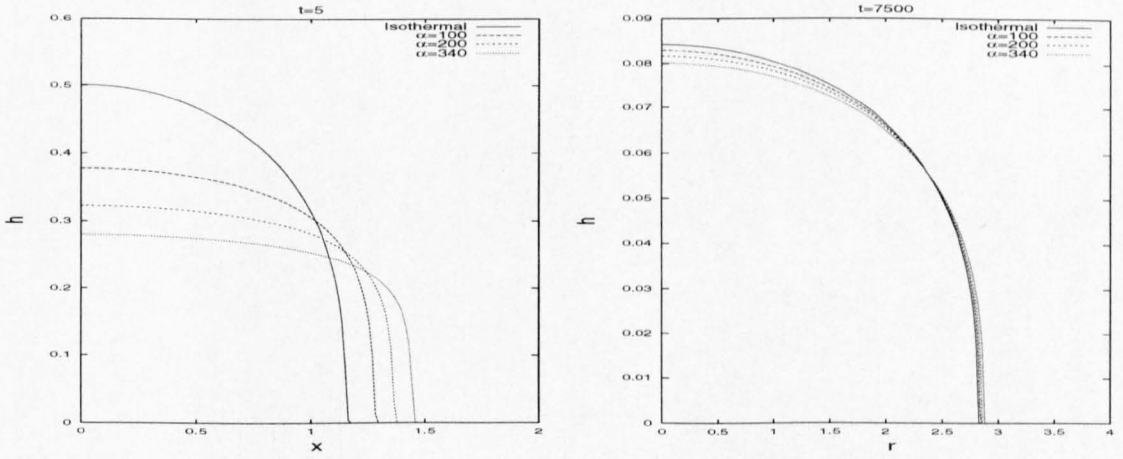

(a) Height profiles at $t = 5$. (b) Height profiles at $t = 7500$.

FIG. 2.37. Results for the exponential viscosity model: axisymmetric spreading with constant mass.

Figure 2.37 shows height profiles for constant mass at times $t = 5$ and $t = 7500$ for $\alpha = 0$, $\alpha = 100$, $\alpha = 200$ and $\alpha = 340$. The axisymmetric results for the constant mass model show that as α increases the fluid develops a plateau and a steep flow front, as in the two-dimensional case. For large time, $t = 7500$, the spreading behaviour tends to the isothermal case (as h becomes small), as discussed in the two-dimensional case. Note that $\alpha = 340$ is again the maximum value

before the numerics fail. The streamlines in Figure 2.38 for $\alpha = 340$ at time $t = 1000$ show no noticeable effects of the temperature field.

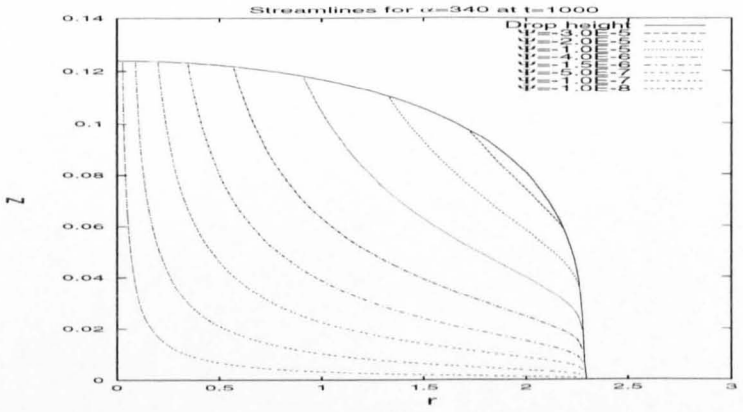

FIG. 2.38. Streamlines at $t = 1000$ with $\alpha = 340$.

Next we consider the case when α is negative. The governing equation is (2.4.3p) with (2.4.8), subject to the axisymmetric constant mass initial conditions (2.2.26)-(2.2.27). This leads to the results in Figure 2.39.

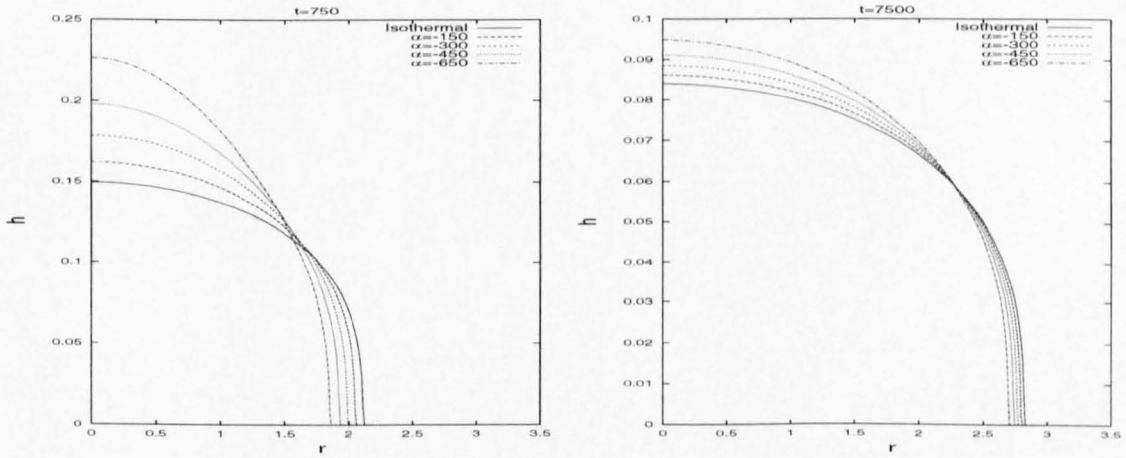

(a) Height profiles at $t = 750$. (b) Height profiles at $t = 7500$.

FIG. 2.39. Results for the exponential viscosity model: axisymmetric spreading with constant mass for negative α.

The results in Figure 2.39 are shown at times $t = 750$ and $t = 7500$ for $\alpha = 0$, $\alpha = -150$, $\alpha = -350$, $\alpha = -450$ and $\alpha = -650$. Again, as in the two-dimensional case, the height profiles show that for time $t = 750$ the flow is restricted as α is decreased. Figure 2.39(b) shows the height profiles tending towards the isothermal results as the maximum height decreases. The streamlines show no interesting behaviour caused by the temperature field and are omitted here.

We now consider a line source with the boundary condition at $x = 0$ given by (2.1.48) with the diffusivity for positive α defined by (2.4.7). Using the NAG routine D03PGF, subject to the initial conditions (2.2.25), gives the height profiles and streamlines shown in Figures 2.40-2.41.

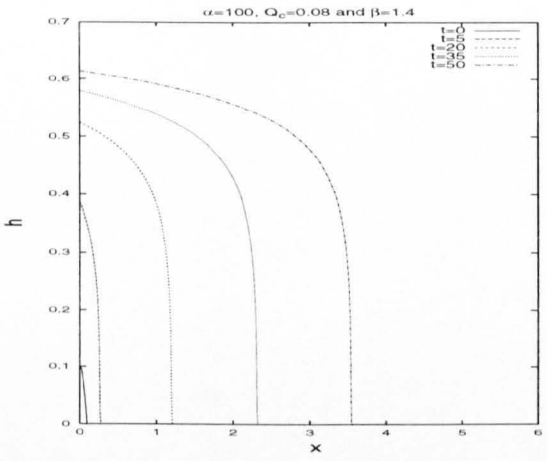

(a) Height profiles with $\alpha = 100$.

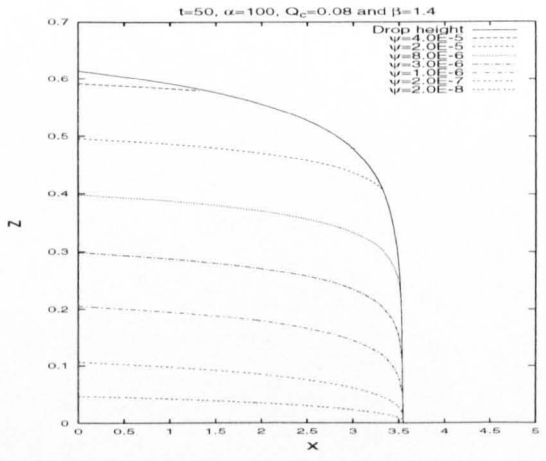

(b) Streamlines at $t = 50$ corresponding to Figure 2.40(a).

FIG. 2.40. Results for the exponential viscosity model: two-dimensional spreading from a line source with $\alpha = 100$.

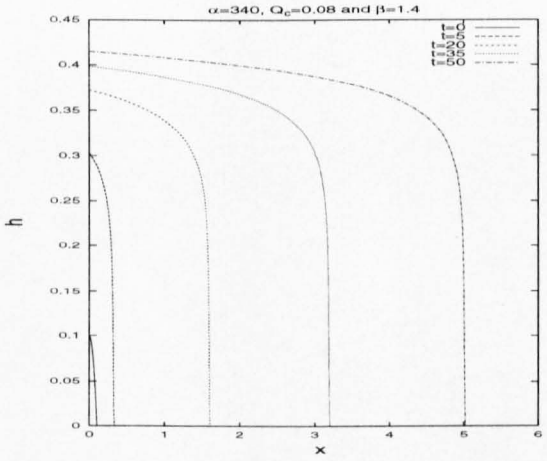

(a) Height profiles with $\alpha = 340$.

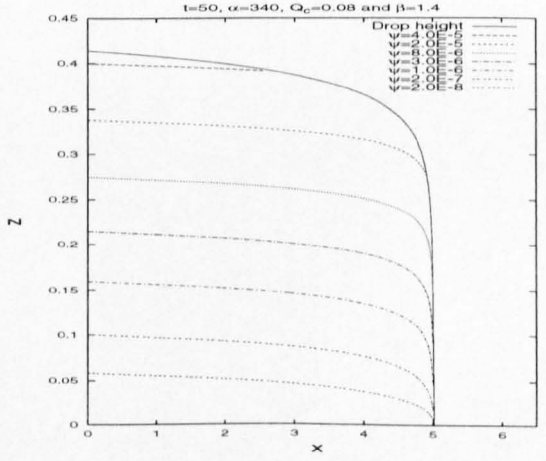

(b) Streamlines at $t = 50$ corresponding to Figure 2.41(a).

FIG. 2.41. Results for the exponential model: two-dimensional spreading from a line source with $\alpha = 340$.

Increasing α leads to the fluid developing a steep flow front followed by a plateau, as observed in the numerical results with constant mass ($\alpha = 340$ is again the maximum value before errors in the code develop, caused by overflow). The streamlines show the fluid flowing from the line source boundary, as opposed to the constant mass streamlines where the fluid is fed from the free boundary.

In laboratory experiments, fluid is often injected from a point source at a constant rate, $\beta = 1$, to model the flow of lava dome growth (see Stasiuk *et al.* (1993), for example). The following numerical results of axisymmetric spreading impose the boundary condition (2.1.70) at $r = \varepsilon$ (with $\varepsilon = 0.01$), with diffusivity (2.4.7) for positive α; the NAG routine D03PGF is used, with the initial conditions (2.2.29), giving the results in Figures 2.42-2.45 for spreading from a point

source.

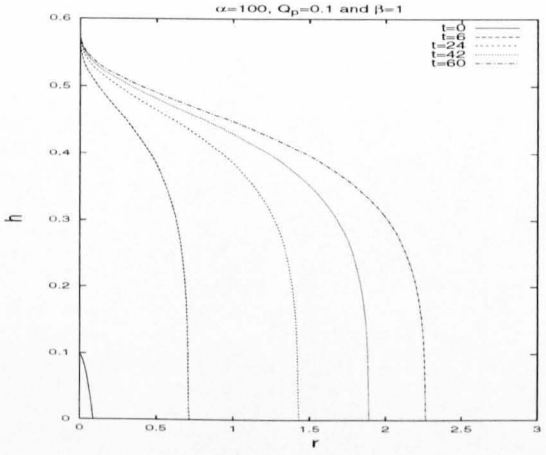

(a) Height profiles with $\alpha = 100$.

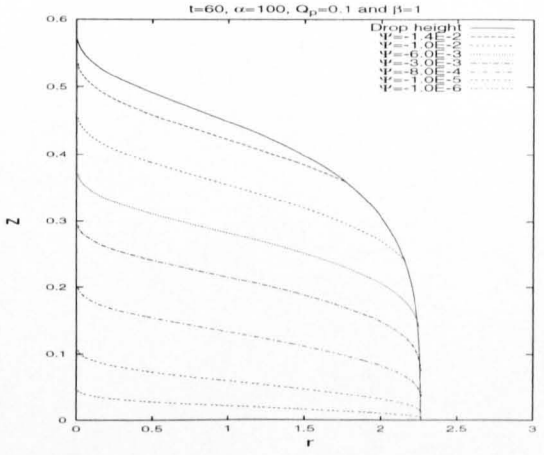

(b) Streamlines at $t = 50$ corresponding to Figure 2.44(a).

FIG. 2.42. Results for the exponential viscosity model: axisymmetric spreading from a constant point source with $\alpha = 100$.

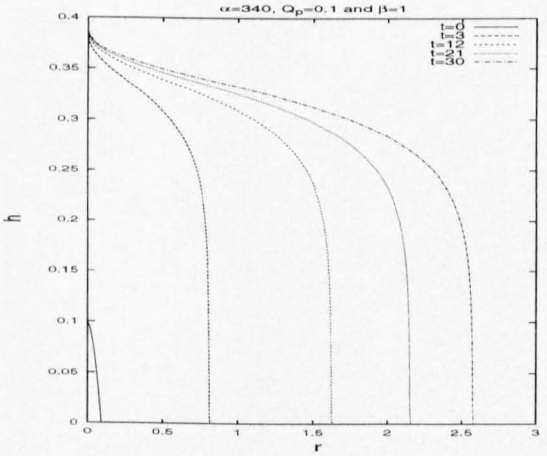

(a) Height profiles with $\alpha = 340$.

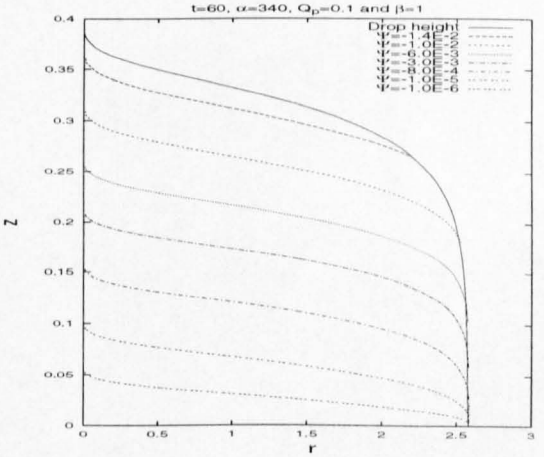

(b) Streamlines at $t = 50$ corresponding to Figure 2.45(a).

FIG. 2.43. Results for the exponential model: axisymmetric spreading from a constant point source with $\alpha = 340$.

As in the two-dimensional case with a line source, increasing α shows the fluid developing a steep flow front followed by a plateau, consistent with experiments performed by Stasiuk *et al.* (1993). The internal heating model is just one mechanism that causes the steep flow front, where the experimental study by Stasiuk *et al.* (1993) does not involve internal heating. The rate at which the fluid is injected has little effect on the flow morphology, plateauing being observed for both constant and variable injection rates. Note that as α increases, the rate at which the fluid spreads also increases, due to the increase in the diffusivity.

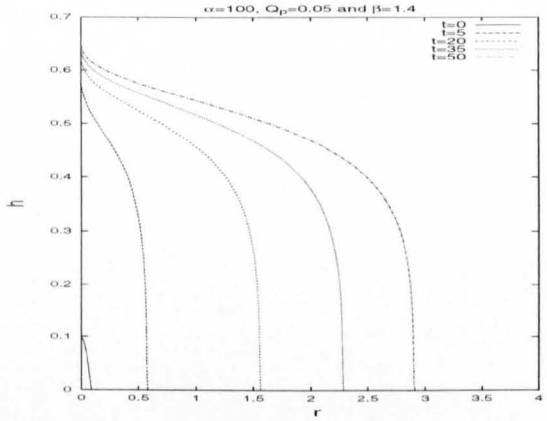

(a) Height profiles with $\alpha = 100$.

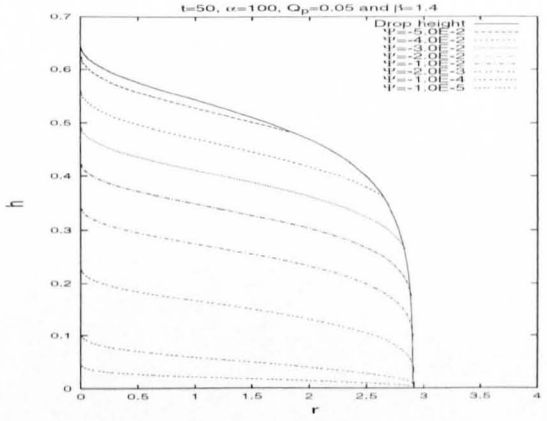

(b) Streamlines at $t = 50$ corresponding to Figure 2.44(a).

FIG. 2.44. Results for the exponential viscosity model: axisymmetric spreading from a variable point source with $\alpha = 100$.

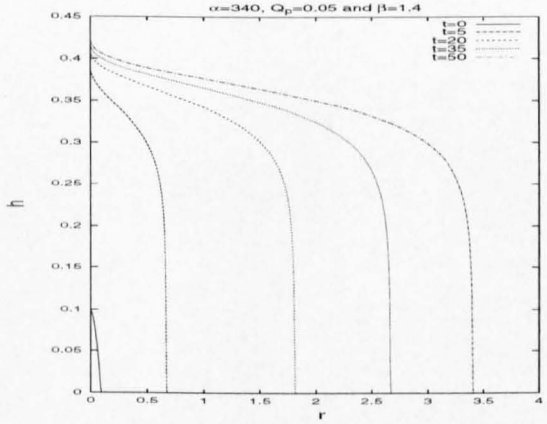

(a) Height profiles with $\alpha = 340$.

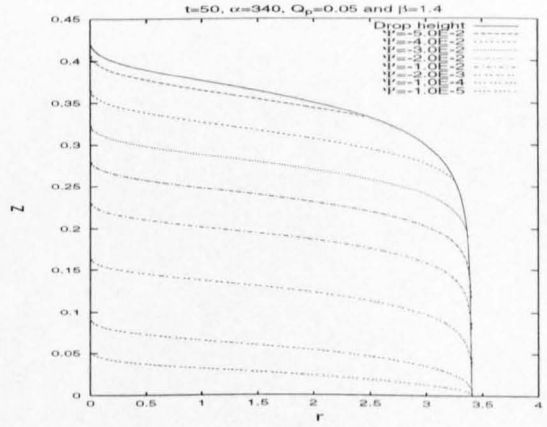

(b) Streamlines at $t = 50$ corresponding to Figure 2.45(a).

FIG. 2.45. Results for the exponential model: axisymmetric spreading from a variable point source with $\alpha = 340$.

Finally we consider the case of negative α from a line and point source boundary. The line source boundary condition at $x = 0$ is given by (2.1.48) where the diffusivity is given by (2.4.8). The NAG routine D03PGF subject to (2.2.25) gives the results in Figures 2.46-2.47 for $\alpha = -50$ and $\alpha = -150$.

The resulting height profiles in Figures 2.46(a) and 2.47(a) are seen to develop a triangular profile, as with the linear viscosity model. The corresponding streamlines in Figures 2.46(b) and 2.47(b) show that the contact line is being fed by the line source, this flow being restricted by the large initial viscosity. The height at $x = 0$ and the front location have the approximate behaviour $h \propto t^{0.65}$ and $s \propto t^{0.90}$ for time less than about 100 in Figure 2.46(a). Decreasing α to -150, leads to the drop height at $x = 0$ varying roughly like $h \propto t^{0.66}$, and the front location like $s \propto t^{0.89}$, for the results illustrated in Figure 2.47(a). The triangular profiles and spreading rates are explained in Section 2.4.3.

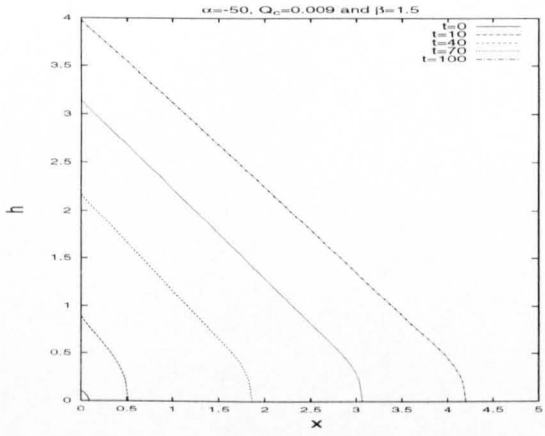

(a) Height profiles with $\alpha = -50$.

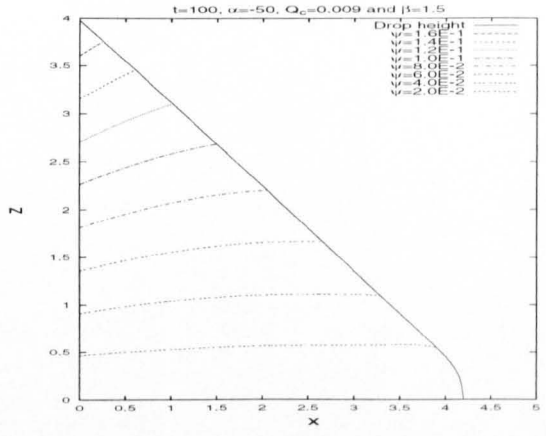

(b) Streamlines at $t = 100$ corresponding to Figure 2.46(a).

FIG. 2.46. Results for the exponential viscosity model: two-dimensional spreading from a line source with $\alpha = -50$.

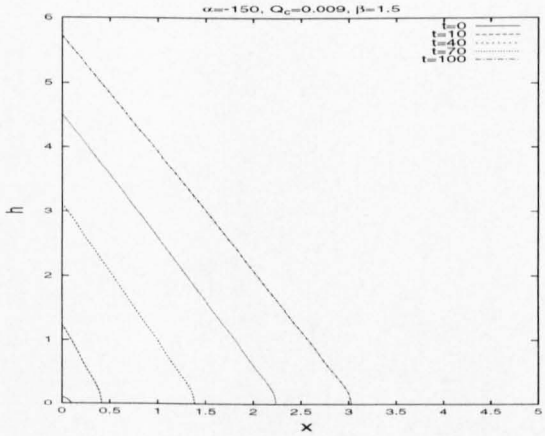

(a) Height profiles with $\alpha = -150$.

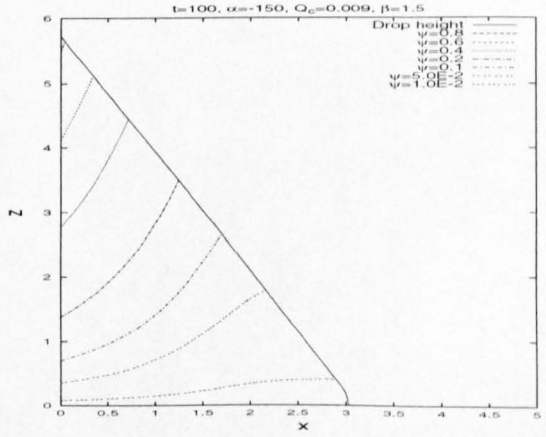

(b) Streamlines at $t = 100$ corresponding to Figure 2.47(a).

FIG. 2.47. Results for the exponential viscosity model: two-dimensional spreading from a line source with $\alpha = -150$.

For small α the spreading should behave in a similar way to the isothermal model ($\alpha = 0$). Setting $\alpha = -5$ leads to the height profiles and streamlines shown in Figure 2.48 which behave in a way characteristic of isothermal spreading. This is as expected from inspection of Taylor series expansion of the diffusion term (2.4.8) and gives further confidence in the numerical solution technique.

We now consider the case of axisymmetric spreading from a point source, the boundary condition at $r = \varepsilon$ ($\varepsilon = 0.01$) being given by (2.1.70) and the diffusivity for negative α by (2.4.8). The NAG routine D03PGF subject to the initial conditions by (2.2.29) gives the free surface and streamlines shown in Figures 2.49-2.50.

As in the two-dimensional (line source) case, the free surface profiles develops a triangular profile, caused by the large initial viscosity. This can be seen in the streamlines, which feed the 'triangu-

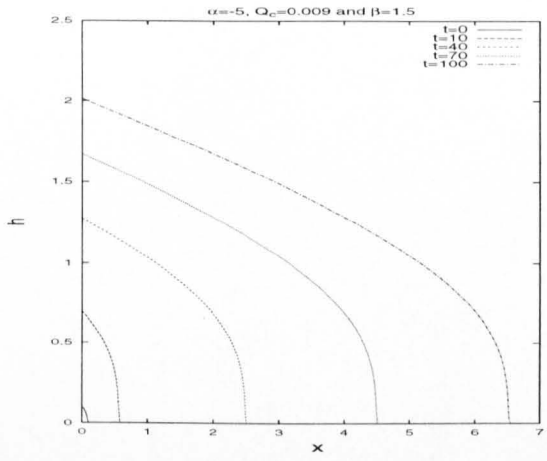

(a) Height profiles with $\alpha = -5$.

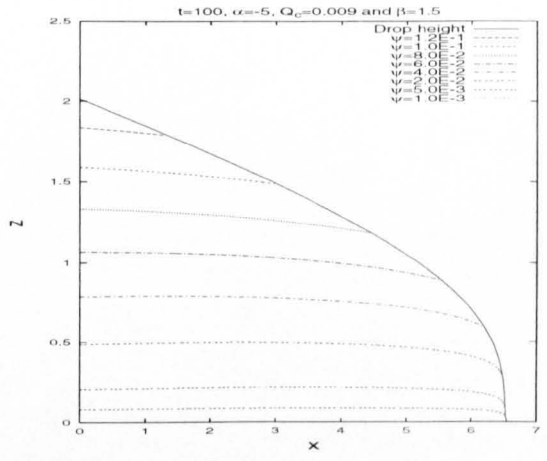

(b) Streamlines at $t = 100$.

FIG. 2.48. Results for the exponential viscosity model: two-dimensional spreading from a line source with $\alpha = -5$.

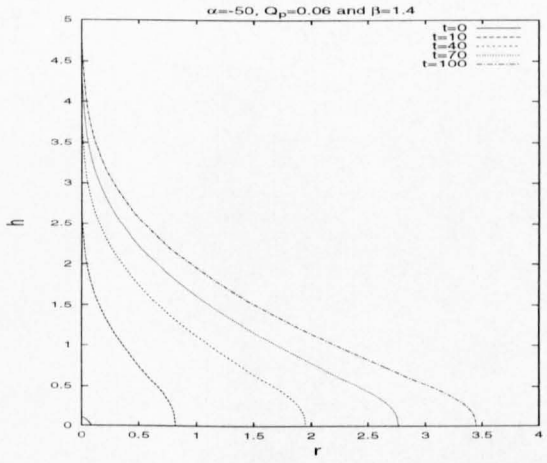

(a) Height profiles with $\alpha = -50$.

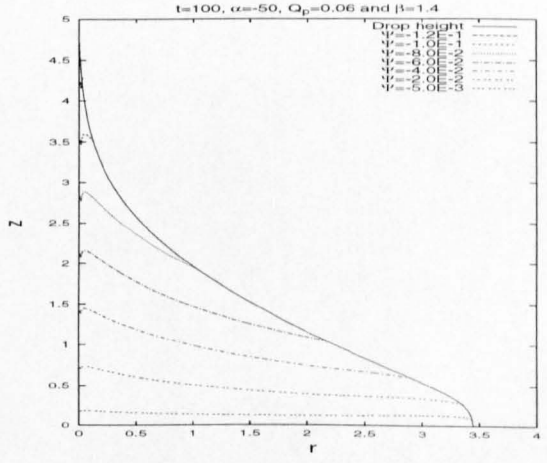

(b) Streamlines at $t = 100$ corresponding to Figure 2.49(a).

FIG. 2.49. Results for the exponential viscosity model: axisymmetric spreading from a point source with $\alpha = -50$.

lar' profile by flowing in an upwards direction. The front location has an approximate behaviour $s \propto t^{0.62}$ for times less than about 100 in Figure 2.49(a) ($\alpha = -50$) and $s \propto t^{0.61}$ in Figure 2.50(a) ($\alpha = -100$).

Another check is to plot the diffusion terms (2.4.7) and (2.4.8), as a function of h. The diffusivities are plotted for $\alpha = 5$ and $\alpha = -10$ in Figure 2.51. We see that, for positive α, the diffusivity is greater than the isothermal diffusivity implying that the fluid will spread at a quicker rate. For negative α, the diffusivity is less than the isothermal case, restricting the flow. This is in agreement with the linear viscosity model and is observed in the above results with the exponential viscosity relationship.

The results for positive α in the exponential relationship show, that for small time, the height

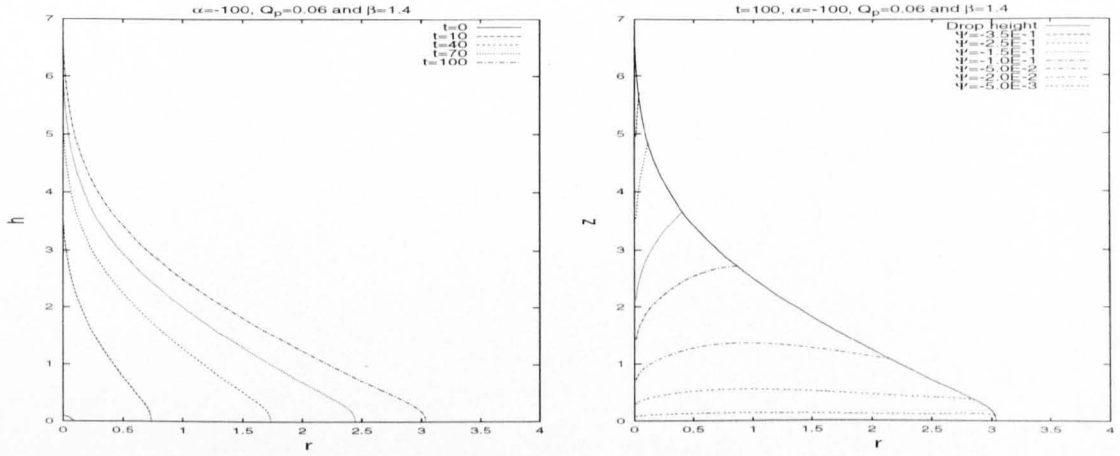

(a) Height profiles with $\alpha = -150$.

(b) Streamlines at $t = 100$ corresponding to Figure 2.50(a).

FIG. 2.50. Results for the exponential viscosity model: axisymmetric spreading from a point source with $\alpha = -150$.

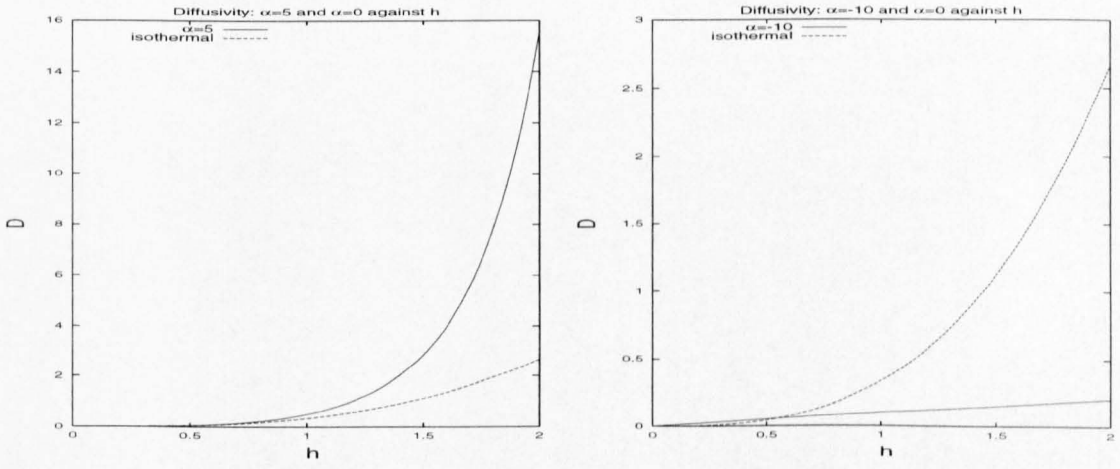

(a) Isothermal *vs* $\alpha = 5$.

(b) Isothermal *vs* $\alpha = -10$.

FIG. 2.51. Diffusivity plots for the exponential viscosity model with positive and negative α *vs* the isothermal case.

profiles develop a flat plateau with steep sides (note that the isothermal results have relatively steep sides). This is most noticeable with the influx boundary results, where a steep flow front and a flattening of the free surface is shown, as the coupling between the spreading dynamics and temperature field is strengthened (by increasing α). The negative α results show, for small time, that the spreading is retarded, as expected since the fluid is initially very viscous. The influx model with negative α produces the interesting 'triangular' profiles caused by the initially large viscosity restricting the flow along the substrate. For large time, for both positive and negative α, the flow is observed to behave isothermally for the constant mass cases. This is not seen with the influx models, where the injected fluid acts as a constant source of heat.

2.4.3. *The limit* $|\alpha| \to \infty$

First we consider the exponential viscosity case with large positive α. For the diffusion term from (2.4.7), we have

$$\operatorname{erf}(\sqrt{2\alpha}h/4) \to 1 \quad \text{as} \quad \alpha \to +\infty.$$

This simplifies the diffusivity, the first two terms being

$$D = \sqrt{\frac{2\pi}{\alpha}} e^{\alpha h^2/8} \left(\frac{h^2}{4} + \frac{1}{\alpha} \right). \tag{2.4.10}$$

Hence the diffusivity grows rapidly with h.

Next, we consider the case of negative α, when $|\alpha|$ is large. An asymptotic series formulated using integration by parts from Dawson's integral, defined by (2.4.9), gives

$$I_D \left(\frac{\sqrt{2|\alpha|}h}{4} \right) \to 0 \quad \text{as} \quad |\alpha| \to \infty.$$

The diffusivity (2.4.8) thus simplifies to

$$D = \frac{h}{|\alpha|}. \tag{2.4.11}$$

The resulting partial differential equations show that as $\alpha \to -\infty$, the free surface profile satisfies, to leading order,

$$\frac{\partial h}{\partial t} \sim \frac{\partial}{\partial x} \left(\frac{h}{|\alpha|} \frac{\partial h}{\partial x} \right) \tag{2.4.12c}$$

and

$$\frac{\partial h}{\partial t} \sim \frac{1}{r} \frac{\partial}{\partial r} \left(r \frac{h}{|\alpha|} \frac{\partial h}{\partial r} \right). \tag{2.4.12p}$$

Similarity solutions can, as discussed earlier, be used to obtain the power laws for the rate at which the front location and height at $x = 0$ change with time. Hence equation (2.2.5) is now replaced by

$$a + 2b = 1, \tag{2.4.13}$$

for both Cartesian and axisymmetric spreading. Considering the influx model in two dimensions, the global continuity equation gives, from equation (2.2.15), the relationship $b - a = \beta$; (2.4.13) then gives

$$a = \frac{1 - 2\beta}{3} \quad \text{and} \quad b = \frac{\beta + 1}{3}. \tag{2.4.14}$$

It thus follows that as $t \to \infty$, the height at $x = 0$ satisfies $h \sim t^{\frac{2\beta-1}{3}}$ and the drop width spreads at $s \sim t^{\frac{\beta+1}{3}}$. Similarly, in axisymmetric geometry it follows from the global continuity equation (2.2.18) and (2.4.13) that the drop height varies like $h \sim t^{\frac{\beta-1}{2}}$ and the front location varies like $s \sim t^{\frac{\beta+1}{4}}$. Note that the height is unbounded as $r \to 0$.

From the numerical results in Figures 2.46(a) and 2.47(a) for $\alpha = -50$ and $\alpha = -150$, the drop height at $x = 0$ varies like $h_{max} \propto t^{0.65}$ and $h_{max} \propto t^{0.66}$ for $\beta = 1.5$, while the front location

varies like $s \propto t^{0.90}$ and $s \propto t^{0.89}$. This shows very good agreement to the expected asymptotic results of $h_{max} \sim t^{\frac{2}{3}}$ and $s \sim t^{\frac{5}{6}}$. Such agreement is also exhibited by the axisymmetric results in Figures 2.49(a) and 2.50(a), where s varies like $t^{0.62}$ and $t^{0.61}$ for $\alpha = -50$ and $\alpha = -150$, respectively, with $\beta = 1.4$, while the asymptotic result gives $s \sim t^{\frac{3}{5}}$.

The stream function for the exponential viscosity law can be written using (2.1.29) and (2.4.6) as

$$\psi = \frac{\partial h}{\partial x} \int_0^z \exp(\alpha z^{'}(h - z^{'})/2)(z^{'} - h)(z - z^{'})dz^{'} \tag{2.4.15}$$

or in the axisymmetric geometry as

$$\Psi = -r\frac{\partial h}{\partial r} \int_0^z \exp(\alpha z^{'}(h - z^{'})/2)(z^{'} - h)(z - z^{'})dz^{'}. \tag{2.4.16}$$

For $\alpha \to -\infty$, writing $z^{'} = Z^{'}/(-\alpha)$ and $z = Z/(-\alpha)$ with $Z = O(1)$ gives

$$\psi \sim \frac{1}{\alpha^2}\frac{\partial h}{\partial x} \int_0^Z \exp(-Z^{'}h/2)(-h)(Z - Z^{'})dZ^{'}, \tag{2.4.17}$$

so

$$\psi \sim \frac{1}{\alpha^2}\frac{\partial h}{\partial x} 2\left(\frac{2\exp(-\frac{1}{2}Zh) + Zh - 2}{h}\right). \tag{2.4.18}$$

As $Z \to \infty$, gives

$$\psi \sim \frac{2Z}{\alpha^2}\frac{\partial h}{\partial x} = -\frac{2z}{\alpha}\frac{\partial h}{\partial x}; \tag{2.4.19}$$

similarly

$$\Psi \sim r\frac{2z}{\alpha}\frac{\partial h}{\partial r}. \tag{2.4.20}$$

Evaluating the integral in (2.4.15) as $\alpha \to -\infty$ with $z = O(1)$ using the integration by parts gives

$$\psi \sim -\frac{2z}{\alpha}\frac{\partial h}{\partial x}. \tag{2.4.21}$$

The limits as $z \to 0$ and $Z \to \infty$ therefore match. The asymptotic analysis states that as $\alpha \to -\infty$, the horizontal velocity is independent of z, when z is not zero. Numerical results for a line source are shown in Figure 2.52 (the results corresponding to the streamlines in Figure 2.47). The boundary layer range $z = O(1/\alpha)$ can be seen in Figure 2.47(b), where the velocity is flowing horizontally. Above this limit plug flow is observed. Figure 2.47(b) also shows another region near the flow front, where the behaviour of the horizontal velocity component sharply increases, then falls back to zero near the flow front. This can be explained in the following analysis.

Substituting $h = \frac{1}{\alpha^{\frac{1}{2}}}H$, $z = \frac{1}{\alpha^{\frac{1}{2}}}Y$ and $z^{'} = \frac{1}{\alpha^{\frac{1}{2}}}Y^{'}$ into (2.4.15) gives

$$\psi = \frac{1}{\alpha^{\frac{5}{2}}}\frac{\partial H}{\partial x} \int_0^Y e^{(1-Y^{'}(H-Y^{'})/2)}(Y^{'} - H)(Y - Y^{'})dY^{'}, \tag{2.4.22}$$

these rescalings corresponding to the region near the flow front at which the boundary layer thickness grows to become $O(\alpha^{\frac{1}{2}})$.

Now considering the limit $\alpha \to -\infty$ for the linear viscosity model, the diffusivity given by

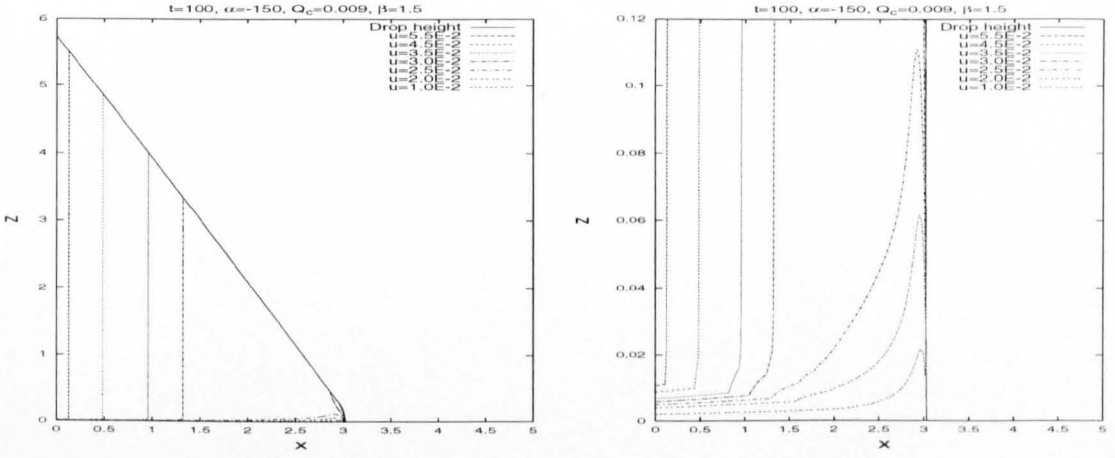

(a) Horizontal velocity profiles with $\alpha = -150$.

(b) Close up of horizontal velocity profile in 2.52(a).

FIG. 2.52. Results for the exponential viscosity model: two-dimensional spreading from a line source with $\alpha = -150$.

(2.4.5) simplifies to

$$D \sim \frac{2h}{|\alpha|} \ln\left(-\frac{2}{h^2\alpha}\right)$$

and this can be simplified further to

$$D \sim \frac{2h}{|\alpha|} \ln(1/|\alpha|).$$

Thus the free surface profiles for the linear case can now be written as

$$\frac{\partial h}{\partial t} \sim \frac{\partial}{\partial x}\left(\frac{2h}{|\alpha|} \ln(1/|\alpha|) \frac{\partial h}{\partial x}\right) \tag{2.4.23c}$$

and

$$\frac{\partial h}{\partial t} \sim \frac{1}{r}\frac{\partial}{\partial r}\left(r\frac{2h}{|\alpha|} \ln(1/|\alpha|) \frac{\partial h}{\partial r}\right). \tag{2.4.23p}$$

As shown in the analysis above for planar spreading, in the influx case we have $h \sim t^{\frac{2\beta-1}{3}}$ and $s \sim t^{\frac{\beta+1}{3}}$. This agrees with the results illustrated in Figures 2.28, where $h \propto t^{0.6}$ and $s \propto t^{0.9}$ for $\beta = 1.5$. Similarly from a point source the analysis above states that $s \sim t^{\frac{\beta-1}{2}}$ and shows good agreement with the results in Figure 2.31, where $s \propto t^{0.21}$ for $\beta = 1.4$.

2.4.4. *Bi-viscosity model*

The final model considers the step function

$$\mu = \begin{cases} 2a - 1 & \text{if } T > T_m, \\ 1 & \text{if } T < T_m, \end{cases} \tag{2.4.24}$$

where $a > 1/2$. The integral in (2.1.43) and (2.1.66) is evaluated by splitting the domain into three regions. To find the cross-sections within which the fluid attains the temperature T_m requires,

using (2.4.1),

$$T_m = \frac{1}{2}z(h-z), \tag{2.4.25}$$

so

$$z^2 - zh + 2T_m = 0 \tag{2.4.26}$$

and

$$z = \frac{1}{2}\left(h \pm (h^2 - 8T_m)^{\frac{1}{2}}\right). \tag{2.4.27}$$

Provided $h > \sqrt{8T_m}$, this gives two real roots h_+ and h_- as displayed in Figure 2.53, which shows the free surface of the drop and of the contour of temperature T_m.

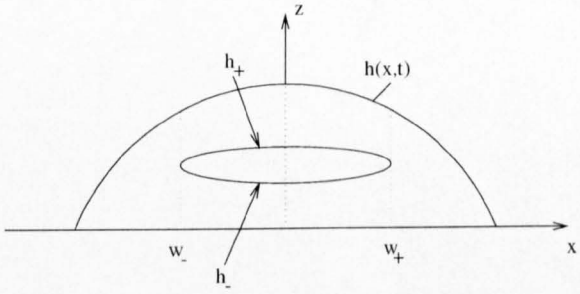

FIG. 2.53. Schematic of temperature contours for bi-viscosity model.

The viscosity in the central region, surrounded by the contours h_+ and h_-, is $2a-1$ while it is unity outside these contours. Physically this means that outer region is more viscous than the inner region provide $a > \frac{1}{2}$. Hence the diffusion integral can be split as

$$D = \int_0^{h_-} \frac{(z-h)^2}{1}dz + \int_{h_-}^{h_+} \frac{(z-h)^2}{2a-1}dz + \int_{h_+}^{h} \frac{(z-h)^2}{1}dz, \tag{2.4.28}$$

where

$$h_\pm = \frac{1}{2}\left(h \pm (h^2 - 8T_m)^{\frac{1}{2}}\right). \tag{2.4.29}$$

Evaluating (2.4.28) gives

$$D = \frac{2(h^2 - 2T_m)(1-a)(h^2 - 8T_m)^{\frac{1}{2}} + h^3(2a-1)}{3(2a-1)}, \tag{2.4.30}$$

if $h > \sqrt{8T_m}$; otherwise the diffusivity is as in the isothermal case and is given by (2.2.2). The height evolution equations (2.4.3), with diffusivity (2.4.30), applies when $h > \sqrt{8T_m}$; elsewhere the isothermal form (2.2.1c) or (2.2.1p) for axisymmetric spreading is used. The step function causes a discontinuity in the viscosity relationship and is shown in the following streamlines at $x = w_\pm$. The regions are indicated in Figure 2.53 by the dotted lines at $x = w_\pm$ and are the corresponding points on the x-axis when $h = \sqrt{8T_m}$. Note when $a = 1$, the free surface evolution equation is simply the isothermal equation.

Equation (2.4.3c) is solved numerically using the NAG routine D03PGF for planar spreading. The condition $h > \sqrt{8T_m}$ determines that the diffusivity is given by (2.4.30), otherwise the

isothermal diffusivity is used and is given by(2.2.2). The initial conditions are given by (2.2.20) and gives the results in Figures 2.54-2.56.

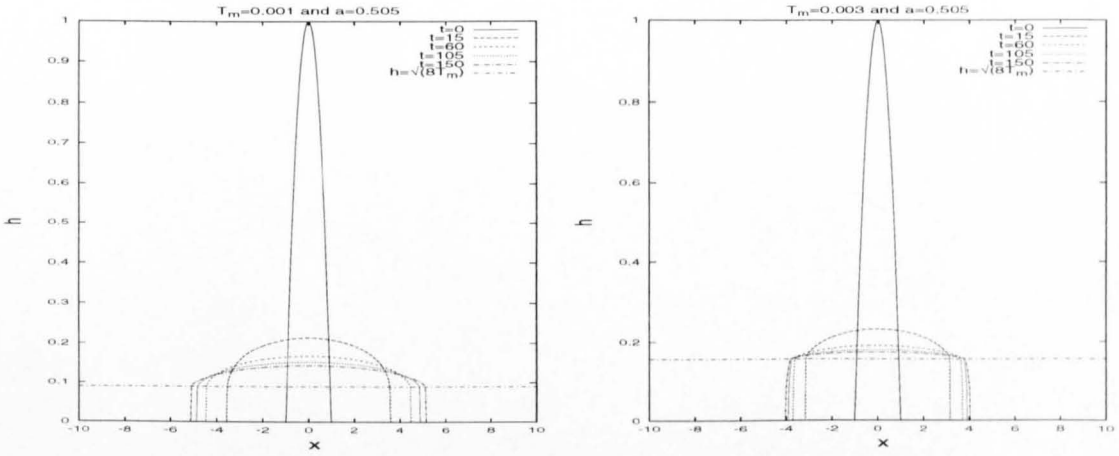

(a) Height profiles with $T_m = 0.001$.

(b) Height profiles with $T_m = 0.003$.

FIG. 2.54. Results for the bi-viscosity model: two-dimensional spreading with constant mass for $a = 0.505$.

The height profiles in Figure 2.54 show the droplet developing a very steep profile together with a plateau; increasing T_m retards the spreading process, as shown in Figure 2.54(b). Examing the streamlines, at time $t = 150$ shows the discontinuity in the viscosity relationship; see Figures 2.55(b) and 2.56(b). The line $h = \sqrt{8T_m}$, displayed in Figure 2.54, indicates the transition between regions with viscosity $2a - 1$ and unity. This is the line crossing the drop surface at the points $w_{\pm}$ indicated in Figure 2.53. The physical explanation for the discontinuity, is that the change in viscosity is very large, producing an almost solid boundary and the streamlines can be clearly seen to be restricted at this region.

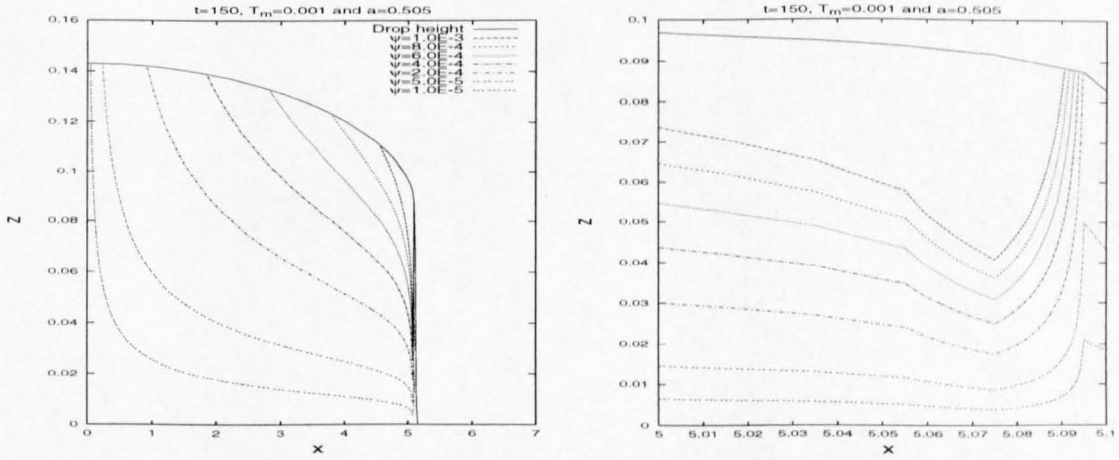

(a) Streamlines at $t = 150$ corresponding to Figure 2.54(a).

(b) Close up of streamlines in Figure 2.55(a).

FIG. 2.55. Results for the bi-viscosity model: two-dimensional spreading with constant mass.

Next we consider the bi-viscosity model for axisymmetric spreading of constant mass, governed

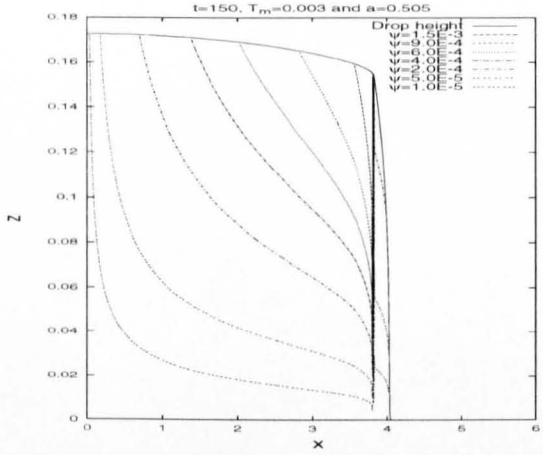

(a) Streamlines at $t = 150$ corresponding to Figure 2.54(b).

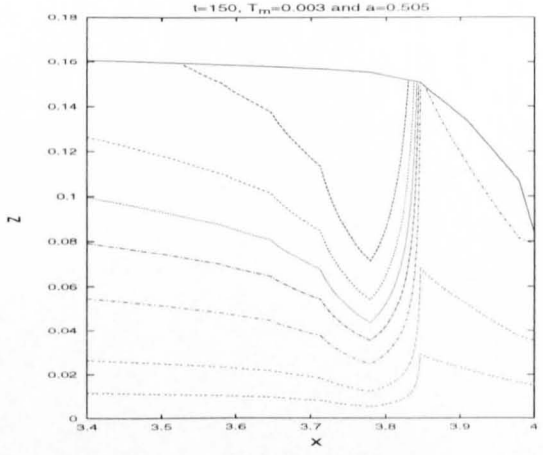

(b) Close up of streamlines in Figure 2.56(b).

FIG. 2.56. Results for the bi-viscosity model: two-dimensional spreading with constant mass.

by (2.4.3p) and the diffusivity (2.4.30) if $h > \sqrt{8T_m}$ and (2.2.2) otherwise. Using NAG routine D03PGF, subject to (2.2.26)-(2.2.27), gives the height profiles and streamlines in Figure 2.57.

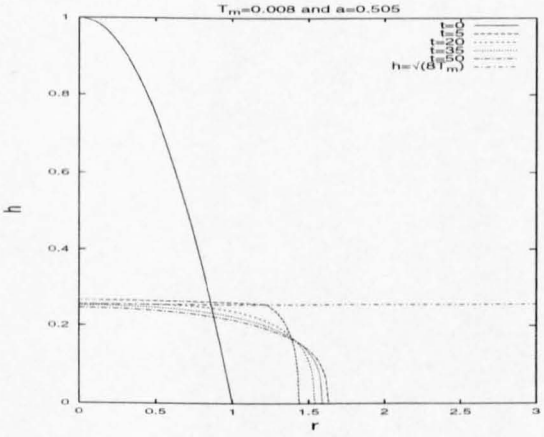

(a) Height profiles with $T_m = 0.008$.

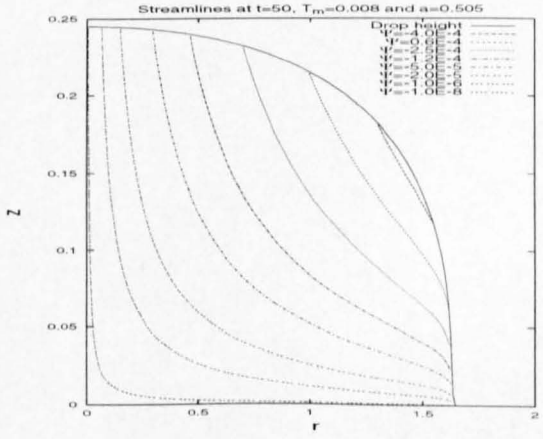

(b) Streamlines at $t = 50$.

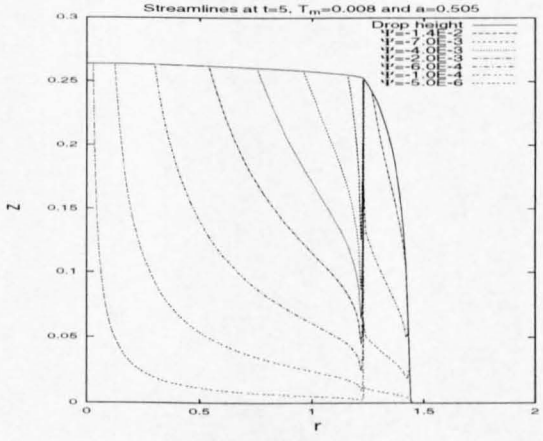

(c) Streamlines at $t = 5$.

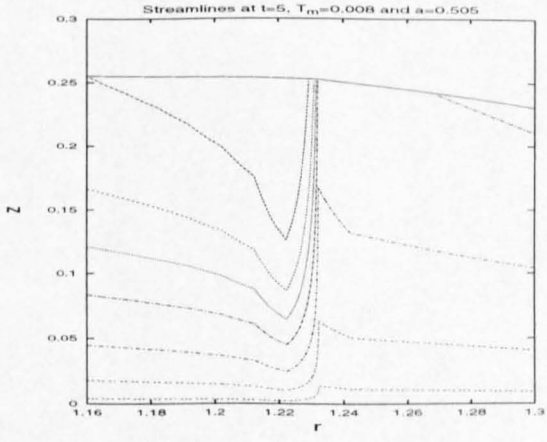

(d) Close up of streamlines in Figure 2.57(c).

FIG. 2.57. Results for the bi-viscosity model: axisymmetric spreading with constant mass.

The axisymmetric results show two different scenarios. The first occurs when $h > \sqrt{8T_m}$ at $t = 5$, when the free surface profiles are seen to develop a steep flow front followed by a plateau (similar to the equivalent planar spreading case). For $t = 5$, the discontinuity in the viscosity relationship is again exposed in the streamlines, as observed in Figure 2.57(c) and close up in Figure 2.57(d). For large time, we have $h < \sqrt{8T_m}$ everywhere and the droplet spreads isothermally. This is shown in the streamlines at $t = 50$ in Figure 2.57(b).

Finally we consider planar spreading model from a line source using the initial conditions (2.2.25). The influx boundary condition is given by (2.1.48) with the diffusivity (2.4.30) if $h > \sqrt{8T_m}$ and (2.2.2) otherwise. The results are given in Figures 2.58-2.59. The height profiles again

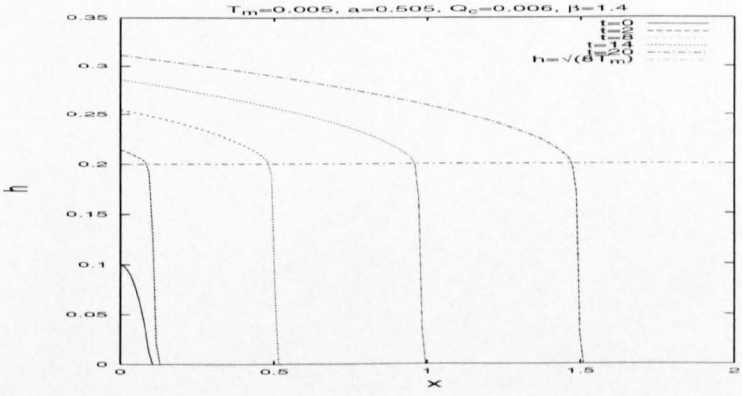

FIG. 2.58. Height profiles with line source boundary at $T_m = 0.005$, $a = 0.505$, $Q_c = 0.006$ and $\beta = 1.4$.

develop the steep flow from caused by the change in viscosity and a close up of the streamlines of Figure 2.59(a) show the behaviour in Figure 2.59(b). The axisymmetric profiles from a point source are omitted caused by problems when imposing the influx boundary condition, where numerical oscillations are observed.

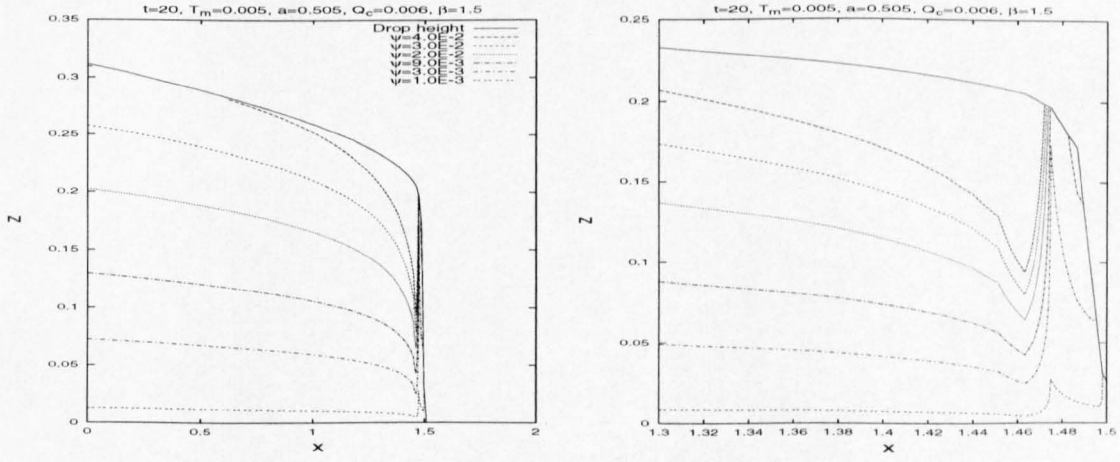

(a) Streamlines at $t = 50$ for Figure 2.58. (b) Close up of streamlines in Figure 2.59(a).

FIG. 2.59. Results for the bi-viscosity model: two-dimensional spreading from a line source.

Plotting the non-isothermal diffusivity in equation (2.4.30) against the isothermal diffusivity

(2.2.2) for $T_m = 0.001$ and $T_m = 0.04$ with $a = 0.6$ gives the results shown in Figure 2.60. The

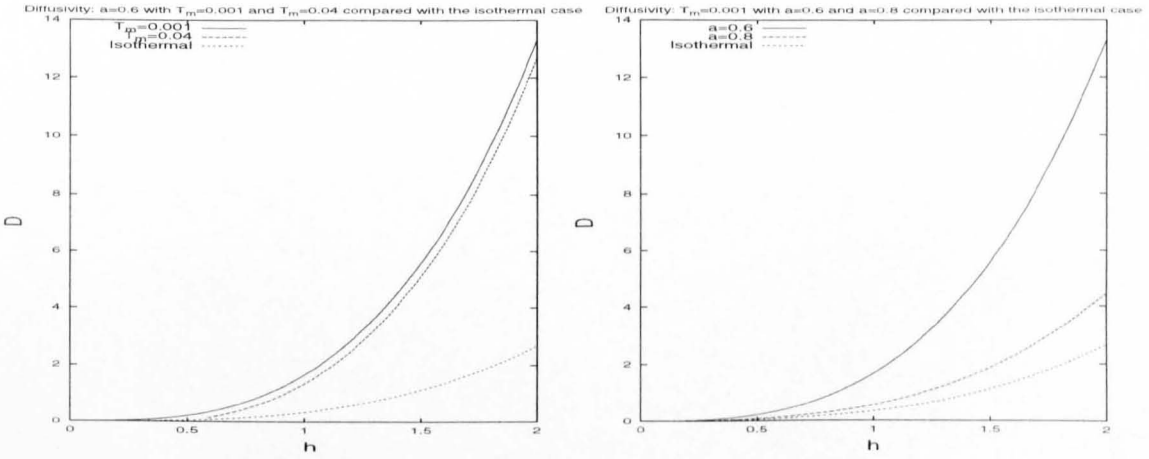

(a) Streamlines at $t = 50$ for Figure 2.58. (b) Close up of streamlines in Figure 2.59(a).

FIG. 2.60. Diffusivity for the bi-viscosity model compared with the isothermal diffusivity.

diffusivity profiles show that increasing a (where $a > \frac{1}{2}$), the behaviour tends to the isothermal case and increasing T_m, decreases the diffusivity and retards the spreading fluid. This is in agreement with the above results.

In summary the bi-viscosity model effects the flow dynamics by producing the steep flow front flow by a plateau when the condition $h > \sqrt{8T_m}$ is satisfied. Otherwise the governing free surface profiles are isothermal. Note that the influx case from the point source in an axisymmetric geometry is omitted because the condition at $r = \varepsilon$ ($h > \sqrt{8T_m}$) cannot be satisfied for all time.

2.5. Discussion

The isothermal numerical results show good agreement with the similarity solutions, giving confidence in the NAG routine D03PGF, the method of lines technique used to solve the nonlinear diffusion equation governing the free surface of the liquid drop. The NAG routine is also compared with a finite difference scheme discussed in Appendix B and shows good agreement. Conservation of mass checks are run for the constant mass and influx models and show that the results maintain the correct mass.

The steep sided drop profiles with flat surfaces developed in the simple temperature models is in agreement to experimental data by Stasiuk *et al.* (1993), as discussed in Chapter 3, and numerical results by Bercovici (1994), see Chapter 4, who used a radially varying viscosity model. As α increases or a is set close to a half, the flow field is strongly coupled to the temperature field, resulting in the steep flow front behaviour. The physical mechanism behind the steep flow front is the increase in viscosity at the front of the drop due to the decrease in temperature at the front. This restricts the movement of the liquid drop and, because of the no-slip condition on the substrate, the drop develops a steep flow front. This behaviour is similar to that observed

lava flow (Huppert *et al.* (1982)) and emphasises the importance of cooling on the dynamics of spreading melts.

CHAPTER THREE

Conduction limited model

3.1. Introduction

This chapter extends the previous work in Chapter 2 which considered the problem involving planar and axisymmetric gravity currents with temperature-dependent viscosity spreading on a horizontal smooth substrate. The temperature field is now determined by a balance between advection, diffusion and a heat source as shown below. Moreover the two-dimensional case is extended to include a line source where liquid is injected at a variable rate.

To set up the problem we first specify the initial and boundary conditions. For the fixed mass problem, the spreading drop initially has a non-dimensionalised parabolic profile of the form $z = (1 - x^2)_+$ and is positioned on a horizontal substrate $z = 0$. The liquid has an initial temperature of unity; the ambient temperature (including that along the substrate) is zero. Horizontal symmetry is assumed and the free surface is given by $z = h(x, t)$ in two-dimensional coordinates or $z = h(r, t)$ in polar coordinates (in polar coordinates the spreading drop has an initial profile of the form $z = (1-r^2)_+$ and radial symmetry is assumed). The viscosity is assumed temperature-dependent and the front of the drop at x (or r) $= s(t)$ is moving with a velocity $\dot{s}$.

The influx model is assumed to have a prescribed flux of liquid released at $x = 0$ in the two-dimensional coordinate system, as shown in Figure 3.1. Note that the axisymmetric model is not considered with a point source in this chapter due to unresolved problems when imposing the boundary condition at $r = 0$.

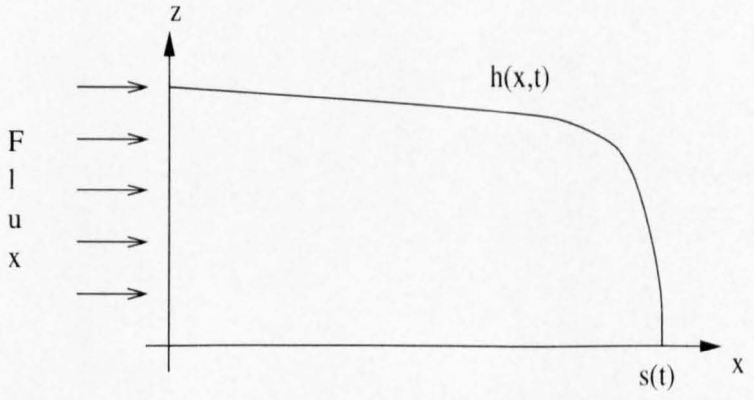

FIG. 3.1. Flux flow in two dimensions

Assuming that the volume of the liquid drop (per unit depth) increases with time as $2\beta Q_c t^{\beta-1}$, where β and Q_c are positive constants and symmetry about $x = 0$ is assumed, the global continuity equation is

$$\int_0^{s(t)} h(x,t)dx = Q_c t^{\beta}. \tag{3.1.1}$$

The influx model has a small initial mass with initial temperature of unity in order to simplify the numerics with $z = 10(0.01 - x^2)_+$.

3.1.1. *Governing equations*

From the previous chapter, the free surface profile of a fluid with temperature-dependent viscosity is given in non-dimensional form by

$$\frac{\partial h}{\partial t} = \frac{\partial}{\partial x}\left(\int_0^h \frac{(z-h)^2}{\mu} dz \frac{\partial h}{\partial x}\right), \tag{3.1.2c}$$

or

$$\frac{\partial h}{\partial t} = \frac{1}{r}\frac{\partial}{\partial r}\left(r\int_0^h \frac{(z-h)^2}{\mu} dz \frac{\partial h}{\partial r}\right). \tag{3.1.2p}$$

The letter extensions to the equation numbers indicate the two-dimensional (Cartesian) equation (c) and the axisymmetric (polar) equation (p). The respective velocity components in the x or r-direction and z-direction are

$$u = \int_0^z \frac{(z^{'} - h)}{\mu} dz^{'} \frac{\partial h}{\partial x}, \tag{3.1.3c}$$

$$u = \int_0^z \frac{(z^{'} - h)}{\mu} dz^{'} \frac{\partial h}{\partial r}, \tag{3.1.3p}$$

$$w = \frac{\partial h}{\partial x}\int_0^z \left(\frac{\partial h}{\partial x}\frac{(z-z^{'})}{\mu} + \frac{\partial \mu}{\partial x}\frac{(z^{'}-h)(z-z^{'})}{\mu^2}\right) dz^{'} - \frac{\partial^2 h}{\partial x^2}\int_0^z \frac{(z^{'}-h)(z-z^{'})}{\mu} dz^{'}, \tag{3.1.4c}$$

$$w = \left(\frac{1}{r}\frac{\partial h}{\partial r} + \frac{\partial^2 h}{\partial r^2}\right)\int_0^z \frac{(z^{'}-h)(z^{'}-z)}{\mu} dz^{'} - \frac{\partial h}{\partial r}\int_0^z \left(\frac{\partial h}{\partial r}\frac{(z^{'}-z)}{\mu} + \frac{\partial \mu}{\partial r}\frac{(z^{'}-h)(z^{'}-z)}{\mu^2}\right) dz^{'}. \tag{3.1.4p}$$

The temperature field from equation (2.1.9) is,

$$\mathrm{Pe}_r\left(\frac{\partial T}{\partial t} + u\frac{\partial T}{\partial x} + w\frac{\partial T}{\partial z}\right) = \frac{\partial^2 T}{\partial z^2} + \dot{q}, \tag{3.1.5}$$

where $\mathrm{Pe}_r = O(1)$ is the reduced Peclet number, with

$$\mathrm{Pe}_r = \epsilon^2 \mathrm{Pe}. \tag{3.1.6}$$

T is the temperature and (u, w) is the velocity field. The terms on the left-hand side of equation (3.1.5), apart from the time derivative, are the advection terms; the terms on the right-hand side represent diffusion and heat production respectively. The heat source term is neglected initially. For large Pe_r, the temperature evolution is dominated by advection. Note that the temperature equation is the same in the axisymmetric geometry, with x replaced by r.

At $x = 0$, the boundary condition for the temperature field for the constant mass case is

$$\frac{\partial T}{\partial x} = 0, \tag{3.1.7}$$

assuming horizontal symmetry. Similarly the equivalent boundary condition is applied at $r = 0$ for the axisymmetric case with constant mass. For the influx model the temperature is set to unity on $x = 0$ for all time. To formulate the influx boundary condition at $x = 0$, equation (3.1.1) is differentiated with respect to x, as in the previous chapter, to give

$$\frac{\partial h}{\partial x} + \frac{3\mu(1)\beta Q_c t^{\beta-1}}{h^3} = 0. \tag{3.1.8}$$

Note that it is assumed the temperature at the inflow boundary is always unity, implying that the viscosity is constant there.

The temperature field is coupled with the height profile by using a temperature-dependent viscosity law. The viscosity laws consider in this chapter are the exponential law, equation (3.1.9), and the bi-viscosity relationship, equation (3.1.10).

$$\mu(T) = \exp(-\alpha T), \tag{3.1.9}$$

$$\mu = \begin{cases} 2a - 1 & \text{if } T > T_m, \\ 1 & \text{if } T < T_m, \end{cases} \tag{3.1.10}$$

where α and a are positive constants; these are in non-dimensional form. The linear viscosity law applied in Chapter 2 is not used in this chapter because of the limited effects it had on the flow dynamics and also that the numerical methods are very time consuming.

The following section shows how the governing equations are solved numerically.

3.2. Numerical methods

The following sections describe the numerical procedures used to solve the governing equations for the spreading drop with temperature-dependent viscosity.

3.2.1. *Planar spreading liquid with constant mass*

The free surface evolution equation, (3.1.2c), can be written as

$$\frac{\partial h}{\partial t} = \frac{\partial}{\partial x}\left(D\frac{\partial h}{\partial x}\right), \tag{3.2.1}$$

where

$$D = \int_0^h \frac{(z-h)^2}{\mu(T)} dz.$$

The viscosity, $\mu(T)$, is coupled with the temperature field so that the viscosity field is discretised in two dimensions over the liquid in a transformed rectangular domain; see below. The temperature is solved numerically on this mesh, as shown in section 3.2.4, and the viscosity follows from the

viscosity-temperature relationship. We discretise (3.2.1), using a Crank-Nicolson implicit finite difference scheme with $h_i^n = h((i-1)\Delta x, n\Delta t)$ and

$$\frac{\partial f}{\partial x} \approx \frac{f_{i+\frac{1}{2}} - f_{i-\frac{1}{2}}}{\Delta x},$$

we obtain,

$$-r_x D_{i-\frac{1}{2}}^{n+1} h_{i-1}^{n+1} + (1 + r_x D_{i+\frac{1}{2}}^{n+1} + r_x D_{i-\frac{1}{2}}^{n+1}) h_i^{n+1} - r_x D_{i+\frac{1}{2}}^{n+1} h_{i+1}^{n+1} = d_i^n, \tag{3.2.2}$$

where

$$d_i^n = r_x D_{i-\frac{1}{2}}^n h_{i-1}^n + (1 - r_x D_{i+\frac{1}{2}}^n - r_x D_{i-\frac{1}{2}}^n) h_i^n + r_x D_{i+\frac{1}{2}}^n h_{i+1}^n,$$

$$r_x = \frac{\Delta t}{2\Delta x^2}, \quad D_{i+\frac{1}{2}} = \frac{D_{i+1} + D_i}{2} \quad \text{and} \quad D_{i-\frac{1}{2}} = \frac{D_i - D_{i-1}}{2}.$$

The Thomas algorithm (see Morton & Mayers (1994)) is used to invert the resulting tri-diagonal matrix. A time marched integral term, D_i^{n+1}, is needed, since D is dependent on h. This is calculated by first differentiating the integral with respect to time to give

$$\begin{aligned} \frac{\partial D}{\partial t} &= \int_0^h \frac{\partial}{\partial t}\left(\frac{(z-h)^2}{\mu}\right) dz, \\ &= -\int_0^h \frac{2\mu(z-h)h_t + (z-h)^2\mu_t}{\mu^2} dz, \end{aligned} \tag{3.2.3}$$

and evaluating the resulting integral by Simpson's rule. With $z = (j-1)\Delta z$ and discretising explicitly, this gives

$$D_i^{n+1} = D_i^n + \Delta t I_i^n, \tag{3.2.4}$$

with

$$I_i^n = -\int_0^{h_i^n} \frac{2\mu_{ij}^n((j-1)\Delta z - h_i^n)(h_t)_i^n + ((j-1)\Delta z - h_i^n)^2(\mu_t)_{ij}^n}{(\mu_{ij}^n)^2} dz. \tag{3.2.5}$$

We need to evaluate the temporal derivatives in the integrand. Discretising

$$h_t = \frac{\partial}{\partial x}\left(D\frac{\partial h}{\partial x}\right)$$

gives

$$\begin{aligned} (h_t)_i^n &= \frac{1}{\Delta x}\left(D_{i+\frac{1}{2}}^n \left(\frac{\partial h}{\partial x}\right)_{i+\frac{1}{2}}^n - D_{i-\frac{1}{2}}^n \left(\frac{\partial h}{\partial x}\right)_{i-\frac{1}{2}}^n\right) \\ &= \frac{1}{2\Delta x^2}\left((D_{i+1}^n + D_i^n)(h_{i+1}^n - h_i^n) - (D_i^n + D_{i-1}^n)(h_i^n - h_{i-1}^n)\right), \\ &= 2(d_i^n - h_i^n)/\Delta t; \end{aligned} \tag{3.2.6}$$

we further take

$$(\mu_t)_i^n \approx \frac{\mu_i^n - \mu_i^{n-1}}{\Delta t}.$$

In the first spatial step of the numerical scheme (at $i = 1$), symmetry of the drop is imposed via $h_0 = h_2$ and $D_0 = D_2$. The integral for D is evaluated using Simpson's rule with the viscosity evaluated at each nodal point in the z-direction from zero to h_i, the drop height at $(i-1)\Delta x$. At

$t = \Delta t$, μ_t^n is set to zero. The half drop width (front location), s, is found by locating the node where the drop height is first less than a tolerance value of 10^{-5}. Note that there is no prewetting film as used later in Chapters 4 and 5. The finite difference scheme (3.2.2) has truncation errors of $O(\Delta t^2)$ and $O(\Delta x^2)$, see Appendix C.

3.2.2. *Planar spreading liquid from a line source*

The boundary condition at $x = 0$, equation (3.1.8), for the line source model causes complications in the implicit scheme used for the constant volume problem. To deal with the problem an explicit step is used at $x = 0$ and incorporated into the Crank-Nicolson implicit method as explained below.

Discretising equation (3.2.1) at $x = 0$ with a simple explicit finite difference scheme gives

$$h_1^{n+1} = h_1^n + r_x \left[(h_2^n - h_1^n)(D_2^n + D_1^n) - (h_1^n - h_0^n)(D_1^n + D_0^n) \right], \tag{3.2.7}$$

where $r_x = \Delta t / 2\Delta x^2$ and

$$D = \int_0^h \frac{(z-h)^2}{\mu(T)} dz. \tag{3.2.8}$$

Viscosity is constant at the inflow boundary and equation (3.2.8) simplifies to

$$D = \frac{h^3}{3\mu(1)} \text{ which gives } D_1^n = \frac{(h_1^n)^3}{3\mu(1)}. \tag{3.2.9}$$

The boundary condition at $x = 0$, equation (3.1.8), in finite difference form is

$$h_0^n = h_2^n + f(h_1^n), \tag{3.2.10}$$

where

$$f(h_1^n) = \frac{6\Delta x \mu(1) \beta Q_c t^{\beta-1}}{(h_1^n)^3}.$$

Hence the explicit scheme at the flux boundary is

$$h_1^{n+1} = h_1^n + r_x \left[(h_2^n - h_1^n)(D_2^n + D_1^n) - (h_1^n - h_2^n - f(h_1)) \left(D_1^n + \frac{(h_2^n + f(h_1))^3}{3\mu(1)} \right) \right]. \tag{3.2.11}$$

The implicit method for the constant mass case in equation (3.2.2) is now adjusted to incorporate the flux boundary condition using the explicit scheme (3.2.11). This is done by simply replacing (3.2.2) at $i = 1$ by (3.2.11).

3.2.3. *Axisymmetric spreading liquid with constant mass*

In the axisymmetric case, the free surface evolution equation (2.1.66) can be written as,

$$\frac{\partial h}{\partial t} = \frac{1}{r} \frac{\partial}{\partial r} \left(rD \frac{\partial h}{\partial r} \right), \tag{3.2.12}$$

where

$$D = \int_0^h \frac{(z-h)^2}{\mu} dz.$$

Using the notation $h_i^n = h((i-1)\Delta r, n\Delta t)$ and $r_i = (i-1)\Delta r$, the Crank-Nicolson implicit finite difference scheme for (3.2.12) is

$$-r_x r_{i-\frac{1}{2}} D_{i-\frac{1}{2}}^{n+1} h_{i-1}^{n+1} + (r_i + r_x r_{i+\frac{1}{2}} D_{i+\frac{1}{2}}^{n+1} + r_x r_{i-\frac{1}{2}} D_{i-\frac{1}{2}}^{n+1}) h_i^{n+1} - r_x r_{i+\frac{1}{2}} D_{i+\frac{1}{2}}^{n+1} h_{i+1}^{n+1} = d_i^n, \quad (3.2.13)$$

where

$$d_i^n = r_x r_{i-\frac{1}{2}} D_{i-\frac{1}{2}}^n h_{i-1}^n + (r_i - r_x r_{i+\frac{1}{2}} D_{i+\frac{1}{2}}^n - r_x r_{i-\frac{1}{2}} D_{i-\frac{1}{2}}^n) h_i^n + r_x r_{i+\frac{1}{2}} D_{i+\frac{1}{2}}^n h_{i+1}^n,$$

$$r_x = \frac{\Delta t}{2\Delta r^2},\ r_{i+\frac{1}{2}} = \frac{r_{i+1} + r_i}{2},\ r_{i-\frac{1}{2}} = \frac{r_i - r_{i-1}}{2},\ D_{i+\frac{1}{2}} = \frac{D_{i+1} + D_i}{2} \text{ and } D_{i-\frac{1}{2}} = \frac{D_i - D_{i-1}}{2}.$$

The above finite difference scheme is satisfactory for $r > 0$, but problems arise at $r = 0$. The partial differential equation (3.2.12) can be rewritten at $r = 0$ using l'Hopital's rule as

$$\frac{\partial h}{\partial t} = \frac{\partial}{\partial r}\left(D\frac{\partial h}{\partial r}\right) + D\frac{\partial^2 h}{\partial r^2}; \quad (3.2.14)$$

Note that $\frac{\partial h}{\partial r} = 0$ at $r = 0$. At $i = 1$, symmetry of the drop is assumed, i.e. $h_0 = h_2$ and $D_0 = D_2$. Hence for $i = 1$ the finite difference scheme is

$$\left[1 + r_x\left(3D_1^{n+1} + D_2^{n+1}\right)\right] h_1^{n+1} - r_x\left(3D_1^{n+1} + D_2^{n+1}\right) h_2^{n+1} = d_1^n, \quad (3.2.15)$$

where

$$d_1^n = \left[1 - r_x\left(3D_1^n + D_2^n\right)\right] h_1^n + 2r_x\left(3D_1^n + D_2^n\right) h_2^n.$$

The above implicit schemes are again solved using the Thomas algorithm. The time marched integral term, D_i^{n+1}, is evaluated using equation (3.2.4) where the $(h_t)_i^n$ term in (3.2.5) is now given by

$$\begin{aligned}(h_t)_i^n &= \frac{1}{r_i \Delta r}\left(r_{i+\frac{1}{2}} D_{i+\frac{1}{2}}^n \left(\frac{\partial h}{\partial r}\right)_{i+\frac{1}{2}}^n - r_{i-\frac{1}{2}} D_{i-\frac{1}{2}}^n \left(\frac{\partial h}{\partial r}\right)_{i-\frac{1}{2}}^n\right) \\ &= \frac{1}{2r_i \Delta r^2}\left[r_{i+\frac{1}{2}}(D_{i+1}^n + D_i^n)(h_{i+1}^n - h_i^n) - r_{i-\frac{1}{2}}(D_i^n + D_{i-1}^n)(h_i^n - h_{i-1}^n)\right], \\ &= \left(\frac{d_i^n}{r} - h_i^n\right)\frac{2}{\Delta t}. \end{aligned} \quad (3.2.16)$$

Taking account of radial symmetry ($h_0 = h_2, D_0 = D_2$) and the singularity at $r = 0$ (using equation (3.2.14)), the $(h_t)_i^n$ term is modified at $i = 1$, such that

$$(h_t)_1^n = \frac{1}{\Delta r^2}\left(h_2^n - h_1^n\right)\left(D_2^n + 3D_1^n\right), \quad (3.2.17)$$

$$= \left(d_1^n - h_1^n\right)\frac{2}{\Delta t}. \quad (3.2.18)$$

3.2.4. *Transformed temperature field*

To solve for the temperature field, equation (3.1.5), numerically it is convenient if the spreading drop is mapped onto a rectangular domain, as shown in Figure 3.2. The coordinate transform is given by

$$\bar{x} = \frac{x}{s(t)}, \quad \bar{z} = \frac{z}{h(x,t)} \quad \text{and} \quad \bar{t} = t\ . \quad (3.2.19)$$

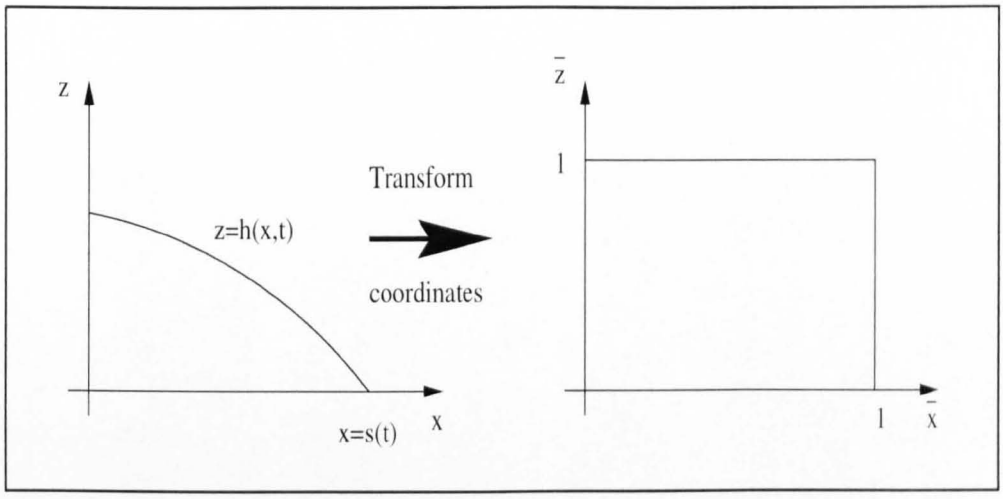

FIG. 3.2. Coordinate transformation.

Note that s and h are given from the previous time step in the numerical scheme. The chain rule gives

$$\frac{\partial}{\partial x} = \frac{1}{s}\frac{\partial}{\partial \bar{x}} - \frac{\bar{z}h_x}{h}\frac{\partial}{\partial \bar{z}} , \tag{3.2.20}$$

$$\frac{\partial}{\partial z} = \frac{1}{h}\frac{\partial}{\partial \bar{z}} , \tag{3.2.21}$$

and

$$\frac{\partial}{\partial t} = -\frac{\bar{x}\dot{s}}{s}\frac{\partial}{\partial \bar{x}} - \frac{\bar{z}h_t}{h}\frac{\partial}{\partial \bar{z}} + \frac{\partial}{\partial \bar{t}} . \tag{3.2.22}$$

The transformed temperature evolution model is now given by

$$\frac{\partial T}{\partial \bar{t}} + (u - \bar{x}s_{\bar{t}})\frac{1}{s}\frac{\partial T}{\partial \bar{x}} + \left(w - \frac{u\bar{z}}{s}\frac{\partial h}{\partial \bar{x}} - \frac{\bar{z}}{s^2}\frac{\partial h}{\partial \bar{t}} + \frac{\bar{z}\bar{x}s_{\bar{t}}}{s}\frac{\partial h}{\partial \bar{x}}\right)\frac{1}{h}\frac{\partial T}{\partial \bar{z}} = \frac{1}{h^2\mathrm{Pe}_r}\frac{\partial^2 T}{\partial \bar{z}^2} + \frac{1}{\mathrm{Pe}_r}\dot{q}, \tag{3.2.23}$$

with x replaced by r in the axisymmetric case. Note that the time-derivative term for the free surface in the planar case, as shown in equation (3.2.30) is

$$\frac{\partial h}{\partial \bar{t}} = \frac{1}{s^2}\frac{\partial}{\partial \bar{x}}\left(\int_0^1 \frac{(\bar{z}-1)^2}{\mu} d\bar{z}\frac{\partial h}{\partial \bar{x}}h^3\right) + \frac{\bar{x}\dot{s}}{s}\frac{\partial h}{\partial \bar{x}}$$

and similarly from equation (3.2.43) in axisymmetric coordinates

$$\frac{\partial h}{\partial \bar{t}} = \frac{1}{rs^2}\frac{\partial}{\partial \bar{r}}\left(r\int_0^1 \frac{(\bar{z}-1)^2}{\mu} d\bar{z}\frac{\partial h}{\partial \bar{r}}h^3\right) + \bar{r}\frac{\bar{x}\dot{s}}{s}\frac{\partial h}{\partial \bar{r}}.$$

The transformed temperature equation (3.2.23) is solved numerically using the locally one-dimensional (LoD) method as discussed in the following sections, with the velocity fields in Cartesian and polar coordinates also transformed onto the same mesh. Note that for the case when internal heating is not present the second term on the right-hand side of equation (3.2.23) is set to zero. The above transformation, called the Landau transformation, maps the point $(s, 0)$ onto a line.

The transformed boundary conditions for the temperature equation 3.2.23 are now given. The

temperature along the lines $\bar{x} = 1$, $\bar{z} = 0$ and $\bar{z} = 1$ is zero; for the consant mass case at $\bar{x} = 0$, we have

$$\frac{\partial T}{\partial \bar{z}} = 0;$$

and for the influx model we set $T = 1$ at $\bar{x} = 0$.

3.2.5. *Transformed Cartesian velocity field*

The integrals in the velocity equations (3.1.3c) and (3.1.4c) are calculated using the trapezium rule. In order to get a two-dimensional nodal map of the velocity field, the equations first have to be transformed to the square mesh, as shown in the temperature model. In order to do this, equation (2.1.36) is first transformed and solved for u, the horizontal velocity component, and then substituted into the transformed continuity equation to find w, the vertical velocity component. The transformed continuity equation is

$$\frac{\partial w}{\partial \bar{z}} = \frac{\bar{z}}{s}\frac{\partial h}{\partial \bar{x}}\frac{\partial u}{\partial \bar{z}} - \frac{h}{s}\frac{\partial u}{\partial \bar{x}}. \tag{3.2.24}$$

Transforming equation (2.1.36), we have

$$\frac{\partial u}{\partial \bar{z}} = \frac{h^2}{s}\frac{\partial h}{\partial \bar{x}}\left(\frac{\bar{z}-1}{\mu}\right). \tag{3.2.25}$$

Integrating and satisfying $u = 0$ on $\bar{z} = 0$ gives

$$u = \frac{h^2}{s}\frac{\partial h}{\partial \bar{x}}\int_0^{\bar{z}} \frac{(z^{'}-1)}{\mu} dz^{'}. \tag{3.2.26}$$

Substituting equations (3.2.25) and (3.2.26) into the transformed continuity equation (3.2.24) gives

$$\frac{\partial w}{\partial \bar{z}} = \frac{h}{s^2}\left(\left(\frac{\partial h}{\partial \bar{x}}\right)^2 h\frac{\bar{z}(\bar{z}-1)}{\mu} - \frac{\partial}{\partial \bar{x}}\left(\int_0^{\bar{z}} \frac{(z^{'}-1)}{\mu} dz^{'} h^2 \frac{\partial h}{\partial \bar{x}}\right)\right). \tag{3.2.27}$$

Integrating with respect to $\bar{z}$ subject to $w = 0$ on $\bar{z} = 0$ and interchanging the order of integration, as shown for equation (2.1.40), gives

$$w = \frac{h}{s^2}\left(\left(\frac{\partial h}{\partial \bar{x}}\right)^2 h\int_0^{\bar{z}} \frac{z^{'}(z^{'}-1)}{\mu} dz^{'} - \frac{\partial}{\partial \bar{x}}\left(\frac{\partial h}{\partial \bar{x}} h^2 \int_0^{\bar{z}} \frac{(z^{'}-1)(\bar{z}-z^{'})}{\mu} dz^{'}\right)\right). \tag{3.2.28}$$

Substituting (3.2.26) and (3.2.28) into the transformed kinematic condition,

$$\frac{\partial h}{\partial \bar{t}} + \frac{u}{s}\frac{\partial h}{\partial \bar{x}} - w - \frac{\bar{x}\dot{s}}{s}\frac{\partial h}{\partial \bar{x}} = 0, \tag{3.2.29}$$

gives the transformed free surface profile equation as

$$\frac{\partial h}{\partial \bar{t}} = \frac{1}{s^2}\frac{\partial}{\partial \bar{x}}\left(\int_0^1 \frac{(\bar{z}-1)^2}{\mu} d\bar{z} h^3 \frac{\partial h}{\partial \bar{x}}\right) + \frac{\bar{x}\dot{s}}{s}\frac{\partial h}{\partial \bar{x}}. \tag{3.2.30}$$

The nodal values of the horizontal velocity are found by discretising equation (3.2.26):

$$u_{ij} = \frac{(h_{i+1} - h_{i-1})h_i^2}{2\Delta \bar{x} s} I_{ij}^A; \tag{3.2.31}$$

where I^A is given in (3.2.35) and at $i = 1$ for the constant mass case, simplifies to

$$u_{1j} = 0. \tag{3.2.32}$$

When calculating the stream function with the influx boundary condition, the velocity components u_{1j} are required. Substituting (3.1.8) (which is transformed onto the square mesh using (3.2.19)) into (3.2.26) the horizontal velocity component at $x = 0$ is given by

$$u_{1j} = \frac{f(h_1)h_1^2}{2\Delta\bar{x}s} I^A_{1j}, \tag{3.2.33}$$

where

$$f(h_1) = \frac{6\Delta x\mu(1)\beta Q_c t^{\beta-1}}{h_1^3}.$$

On using central differences in (3.2.28), the nodal values of the vertical velocity are given by

$$w_{ij} = \frac{h_i}{s^2}\left(\left(\frac{(h_{i+1} - h_{i-1})}{2\Delta\bar{x}}\right)^2 h_i I^B_{ij} - \frac{1}{\Delta\bar{x}}\left(h_{\bar{x}_{i+\frac{1}{2}}} h^2_{i+\frac{1}{2}} I^C_{i+\frac{1}{2}j} - h_{\bar{x}_{i-\frac{1}{2}}} h^2_{i-\frac{1}{2}} I^C_{i-\frac{1}{2}j}\right)\right), \tag{3.2.34}$$

where

$$I^A = \int_0^{\bar{z}} \frac{(z^{'} - 1)}{\mu} dz^{'}, \quad I^B = \int_0^{\bar{z}} \frac{z^{'}(z^{'} - 1)}{\mu} dz^{'}, \quad I^C = \int_0^{\bar{z}} \frac{(z^{'} - 1)(\bar{z} - z^{'})}{\mu} dz^{'}. \tag{3.2.35}$$

The integrals are evaluated numerically using the trapezium rule. Taking into account the symmetry of the problem at $x = 0$ in the constant mass case, the vertical velocity component along $x = 0$ is determined by

$$w_{1j} = -\frac{2h_1}{s^2\Delta\bar{x}}\left(h_{\bar{x}_{1+\frac{1}{2}}} h^2_{1+\frac{1}{2}} I^C_{1+\frac{1}{2}j}\right). \tag{3.2.36}$$

Note that

$$h_{\bar{x}_{i+\frac{1}{2}}} = \frac{h_{i+1} - h_i}{\Delta\bar{x}} \quad h_{\bar{x}_{i-\frac{1}{2}}} = \frac{h_i - h_{i-1}}{\Delta\bar{x}}, \quad h_{i+\frac{1}{2}} = \frac{h_{i+1} + h_i}{2},$$
$$h_{i-\frac{1}{2}} = \frac{h_i + h_{i-1}}{2}, \quad I^C_{i+\frac{1}{2}j} = \frac{I^C_{i+1j} + I^C_{ij}}{2}, \quad I^C_{i-\frac{1}{2}j} = \frac{I^C_{ij} + I^C_{i-1j}}{2}.$$

3.2.6. *Transformed axisymmetric velocity*

The axisymmetric velocity equations (3.1.3p) and (3.1.4p) are similarly transformed onto a fixed square mesh. The horizontal velocity component is u, and the vertical component is w. The transformed continuity equation is

$$\frac{\partial w}{\partial\bar{z}} = \frac{h}{\bar{r}s}\left(\frac{\bar{z}}{h}\frac{\partial h}{\partial\bar{r}}\frac{\partial(\bar{r}u)}{\partial\bar{z}} - \frac{\partial(\bar{r}u)}{\partial\bar{r}}\right). \tag{3.2.37}$$

Transforming equation (2.1.64) gives

$$\frac{\partial u}{\partial\bar{z}} = \left(\frac{\bar{z} - 1}{\mu}\right)\frac{h^2}{s}\frac{\partial h}{\partial\bar{r}} \tag{3.2.38}$$

and integrating, satisfying $u = 0$ on $\bar{z} = 0$, gives

$$u = \int_0^{\bar{z}} \frac{(z^{'} - 1)}{\mu} dz^{'} \frac{h^2}{s}\frac{\partial h}{\partial\bar{r}}. \tag{3.2.39}$$

Substituting equations (3.2.38) and (3.2.39) into the transformed continuity equation (3.2.37) gives

$$\frac{\partial w}{\partial \bar{z}} = \frac{h}{s^2}\left(\left(\frac{\partial h}{\partial \bar{r}}\right)^2 h\frac{\bar{z}(\bar{z}-1)}{\mu} - \frac{1}{\bar{r}}\frac{\partial}{\partial \bar{r}}\left(\bar{r}\frac{\partial h}{\partial \bar{r}}h^2\int_0^{\bar{z}}\frac{(z^{'}-1)}{\mu}dz^{'}\right)\right). \tag{3.2.40}$$

Integrating with respect to $\bar{z}$ subject to $w = 0$ on $\bar{z} = 0$ and interchanging the order of integration gives

$$w = \frac{h}{s^2}\left(\left(\frac{\partial h}{\partial \bar{r}}\right)^2 h\int_0^{\bar{z}}\frac{z^{'}(z^{'}-1)}{\mu}dz^{'} - \frac{1}{\bar{r}}\frac{\partial}{\partial \bar{r}}\left(\bar{r}\frac{\partial h}{\partial \bar{r}}h^2\int_0^{\bar{z}}\frac{(z^{'}-1)(\bar{z}-z^{'})}{\mu}dz^{'}\right)\right). \tag{3.2.41}$$

The transformed kinematic condition is

$$\frac{\partial h}{\partial \bar{t}} + \frac{u}{s}\frac{\partial h}{\partial \bar{r}} - w - \frac{\bar{r}\dot{s}}{s}\frac{\partial h}{\partial \bar{r}} = 0. \tag{3.2.42}$$

Substituting the velocity components, (3.2.39) and (3.2.41), into (3.2.42) gives the equation for the transformed axisymmetric free surface profile as

$$\frac{\partial h}{\partial \bar{t}} = \frac{1}{rs^2}\frac{\partial}{\partial \bar{r}}\left(r\int_0^1\frac{(\bar{z}-1)^2}{\mu}d\bar{z}\frac{\partial h}{\partial \bar{r}}h^3\right) + \frac{\bar{r}\dot{s}}{s}\frac{\partial h}{\partial \bar{r}}. \tag{3.2.43}$$

Using l'Hopital's rule to calculate the vertical velocity w at $r = 0$ gives the relationship

$$w = \frac{h}{s^2}\left(\left(\frac{\partial h}{\partial \bar{r}}\right)^2 h\int_0^{\bar{z}}\frac{z^{'}(z^{'}-1)}{\mu}dz^{'} - \frac{\partial}{\partial \bar{r}}\left(\frac{\partial h}{\partial \bar{r}}h^2\int_0^{\bar{z}}\frac{(z^{'}-1)(\bar{z}-z^{'})}{\mu}dz^{'}\right)\right.$$
$$\left. -\frac{\partial^2 h}{\partial \bar{r}^2}h^2\int_0^{\bar{z}}\frac{(z^{'}-1)(\bar{z}-z^{'})}{\mu}dz^{'}\right). \tag{3.2.44}$$

The nodal values of the horizontal velocity are found by discretising equation (3.2.39):

$$u_{ij} = \frac{(h_{i+1}-h_{i-1})h_i^2}{2\Delta\bar{r}s}I_{ij}^A; \tag{3.2.45}$$

where I^A is given in (3.2.48). For the constant mass case,

$$u_{1j} = 0. \tag{3.2.46}$$

On using central differences in (3.2.41), the nodal values for the vertical components are given by

$$w_{ij} = \frac{h_i}{s^2}\left(\left(\frac{(h_{i+1}-h_{i-1})}{2\Delta\bar{r}}\right)^2 h_i I_{ij}^B -\right.$$
$$\left.\frac{1}{\bar{r}_i\Delta\bar{r}}\left(\bar{r}_{i+\frac{1}{2}}h_{\bar{r}_{i+\frac{1}{2}}}h_{i+\frac{1}{2}}^2 I_{i+\frac{1}{2}j}^C - \bar{r}_{i-\frac{1}{2}}h_{\bar{r}_{i-\frac{1}{2}}}h_{i-\frac{1}{2}}^2 I_{i-\frac{1}{2}j}^C\right)\right), \tag{3.2.47}$$

where

$$I^A = \int_0^{\bar{z}}\frac{(z^{'}-1)}{\mu}dz^{'}, \quad I^B = \int_0^{\bar{z}}\frac{z^{'}(z^{'}-1)}{\mu}dz^{'}, \quad I^C = \int_0^{\bar{z}}\frac{(z^{'}-1)(\bar{z}-z^{'})}{\mu}dz^{'}, \tag{3.2.48}$$

$$\bar{r}_{i+\frac{1}{2}} = \frac{\bar{r}_{i+1}+\bar{r}_i}{2}, \quad \bar{r}_{i-\frac{1}{2}} = \frac{\bar{r}_i+\bar{r}_{i-1}}{2}, \quad I_{i+\frac{1}{2}j}^C = \frac{I_{i+1j}^C + I_{ij}^C}{2},$$
$$I_{i-\frac{1}{2}j}^C = \frac{I_{ij}^C + I_{i-1j}^C}{2}, \quad h_{\bar{r}_{i+\frac{1}{2}}} = \frac{h_{i+1}-h_i}{\Delta\bar{r}}, \quad \text{and} \quad h_{\bar{r}_{i-\frac{1}{2}}} = \frac{h_i - h_{i-1}}{\Delta\bar{r}}.$$

Using (3.2.44) the vertical velocity component along $r = 0$ is

$$w_{1j} = -\frac{2h_1}{s^2}\left(\frac{1}{\Delta\bar{r}}\left(\left(\frac{h_2 - h_1}{\Delta\bar{r}}\right)\left(\frac{h_1 + h_2}{2}\right)^2\left(\frac{I^C_{1j} + I^C_{2j}}{2}\right)\right) + \frac{(h_2 - h_1)}{\Delta\bar{r}}h_1^2 I^C_{1j}\right), \quad (3.2.49)$$

where $h_0 = h_2$, by symmetry. The integrals are evaluated using the trapezium rule.

3.2.7. *Transformed streamlines*

The two-dimensional stream function ψ satisfies

$$u = \frac{\partial\psi}{\partial z},$$

where u is the horizontal velocity component and transforming to the square domain using (3.2.19) gives

$$u = \frac{1}{h}\frac{\partial\psi}{\partial\bar{z}} \quad (3.2.50)$$

and

$$\psi = h\int_0^{\bar{z}} u dz; \quad (3.2.51)$$

similarly it can be shown that

$$\Psi = -rh\int_0^{\bar{z}} u dz \quad (3.2.52)$$

in polar coordinates. The integrals are evaluated numerically using the trapezium rule, where u is the transformed horizontal velocity component (equation (3.2.26) in Cartesian coordinates and (3.2.39) in axisymmetric coordinates).

3.2.8. *LoD finite difference scheme for the temperature field*

The method used to solve equation (3.2.23) is the locally one dimension (LoD) operator-splitting scheme, which is a finite-difference scheme and is similar to the alternating direction implicit (ADI) method if a Crank-Nicolson scheme is used in conjunction with the splitting scheme, as explained in Mitchell & Griffiths (1980) and Allen *et al.* (1988). The method involves solving a two-dimensional problem as a sequence of two one-dimensional problems. First rewriting equation (3.2.23) as

$$\frac{\partial T}{\partial t} + a\frac{\partial T}{\partial x} + b\frac{\partial T}{\partial z} + c\frac{\partial^2 T}{\partial z^2} = \frac{1}{\mathrm{Pe}_r}\dot{q}. \quad (3.2.53)$$

The bar notation is dropped for brevity where a, b and c are defined by

$$a = \frac{(u - x\dot{s})}{s}, \quad b = \frac{1}{h}\left(w - \frac{uz}{s}\frac{\partial h}{\partial x} - \frac{z}{s^2}\frac{\partial h}{\partial t} + \frac{zx\dot{s}}{s}\frac{\partial h}{\partial x}\right), \quad c = -\frac{1}{\mathrm{Pe}_r h^2}. \quad (3.2.54)$$

Discretising (3.2.53) using the Crank-Nicolson method and with the notation $T((i-1)\Delta x, (j-1)\Delta z, n\Delta t) = T^n_{ij}$ gives

$$\frac{T^{n+1}_{ij} - T^n_{ij}}{\Delta t} + \frac{a}{2}\left(\frac{T^{n+1}_{i+1j} - T^{n+1}_{i-1j}}{2\Delta x} + \frac{T^n_{i+1j} - T^n_{i-1j}}{2\Delta x}\right) + \frac{b}{2}\left(\frac{T^{n+1}_{ij+1} - T^{n+1}_{ij-1}}{2\Delta z} + \frac{T^n_{ij+1} - T^n_{ij-1}}{2\Delta z}\right)$$

$$+\frac{c}{2}\left(\frac{T_{ij-1}^{n+1}-2T_{ij}^{n+1}+T_{ij+1}^{n+1}}{\Delta z^2}+\frac{T_{ij-1}^{n}-2T_{ij}^{n}+T_{ij+1}^{n}}{\Delta z^2}\right)=\frac{1}{\mathrm{Pe}_r}\dot{q}. \quad (3.2.55)$$

This suggests the following operator notation

$$\mathcal{F}_{xz}^{+}(T_{ij}^{n+1})=\mathcal{F}_{xz}^{-}(T_{ij}^{n})+\frac{\Delta t}{\mathrm{Pe}_r}\dot{q}, \quad (3.2.56)$$

where

$$\mathcal{F}_{xz}^{+}=\left[1+\frac{a}{2}\frac{\partial}{\partial x}+\frac{b}{2}\frac{\partial}{\partial z}+\frac{c}{2}\frac{\partial^2}{\partial z^2}\right]$$
$$\mathcal{F}_{xz}^{-}=\left[1-\frac{a}{2}\frac{\partial}{\partial x}-\frac{b}{2}\frac{\partial}{\partial z}-\frac{c}{2}\frac{\partial^2}{\partial z^2}\right]. \quad (3.2.57)$$

The spatial derivatives in the above differential marching operators are replaced by central difference operators to reproduce (3.2.55).

To derive the LoD scheme we approximate (3.2.56) by

$$\mathcal{F}_{z}^{+}(\mathcal{F}_{x}^{+}(T_{ij}^{n+1}))=\mathcal{F}_{z}^{-}(\mathcal{F}_{x}^{-}(T_{ij}^{n}))+\frac{\Delta t}{\mathrm{Pe}_r}\dot{q}, \quad (3.2.58)$$

where

$$\mathcal{F}_{x}^{+}=\left[1+\frac{a}{2}\frac{\partial}{\partial x}\right],\quad \mathcal{F}_{z}^{+}=\left[1+\frac{b}{2}\frac{\partial}{\partial z}+\frac{c}{2}\frac{\partial^2}{\partial z^2}\right],$$
$$\mathcal{F}_{x}^{-}=\left[1-\frac{a}{2}\frac{\partial}{\partial x}\right],\quad \mathcal{F}_{z}^{-}=\left[1-\frac{b}{2}\frac{\partial}{\partial z}-\frac{c}{2}\frac{\partial^2}{\partial z^2}\right]. \quad (3.2.59)$$

Now it is clear that

$$\mathcal{F}_{xz}^{+}=\mathcal{F}_{x}^{+}\mathcal{F}_{z}^{+}+O(\Delta t^2)\quad\text{and}\quad \mathcal{F}_{xz}^{-}=\mathcal{F}_{x}^{-}\mathcal{F}_{z}^{-}+O(\Delta t^2). \quad (3.2.60)$$

Rewriting (3.2.58) in terms of the bar notation introduced below gives the operator sequence as

$$\mathcal{F}_{x}^{+}(\overline{T_{ij}^{n+1}})=\mathcal{F}_{x}^{-}(T_{ij}^{n})+\frac{\Delta t}{2\mathrm{Pe}_r}\,\dot{q}$$
$$\mathcal{F}_{z}^{+}(T_{ij}^{n+1})=\mathcal{F}_{z}^{-}(\overline{T_{ij}^{n+1}})+\frac{\Delta t}{2\mathrm{Pe}_r}\,\dot{q}\,. \quad (3.2.61)$$

Note that the split only works for the heat source term if $\dot{q}$ is uniform. Thus the factored sequence of locally one-dimensional split operators, (3.2.61), provides a two-dimensional solution to the temperature evolution equation (3.1.5). The operators ($\mathcal{F}_x$ for the first sweep and $\mathcal{F}_z$ for the second sweep) are used to derive the following finite difference scheme using central differences. The order in which the operators $\mathcal{F}_x$ and $\mathcal{F}_z$ appear is irrelevant since they commute.

For the first sweep we set

$$-\frac{\Delta t a_{ij}^{n}}{4\Delta x}\overline{T_{i-1j}^{n+1}}+\overline{T_{ij}^{n+1}}+\frac{\Delta t a_{ij}^{n}}{4\Delta x}\overline{T_{i+1j}^{n+1}}=d_{ij}^{n}, \quad (3.2.62)$$

where

$$d_{ij}^{n}=\frac{\Delta t a_{ij}^{n}}{4\Delta x}T_{i-1j}^{n}+T_{ij}^{n}-\frac{\Delta t a_{ij}^{n}}{4\Delta x}T_{i+1j}^{n}+\frac{1\dot{q}}{2\mathrm{Pe}_r}\Delta t.$$

To complete the time step (Δt), the second sweep is given by

$$\left(-\frac{b_{ij}^{n}\Delta t}{4\Delta z}+\frac{c_{i}^{n}\Delta t}{2\Delta z^2}\right)T_{ij-1}^{n+1}+\left(1-\frac{c_{i}^{n}\Delta t}{\Delta z^2}\right)T_{ij}^{n+1}+\left(\frac{b_{ij}^{n}\Delta t}{4\Delta z}+\frac{c_{i}^{n}\Delta t}{2\Delta z^2}\right)T_{ij+1}^{n+1}=\overline{d_{ij}^{n+1}}, \quad (3.2.63)$$

where

$$d_{ij}^{\overline{n+1}} = \left(\frac{b_{ij}^n \Delta t}{4\Delta z} - \frac{c_i^n \Delta t}{2\Delta z^2}\right) T_{ij-1}^{\overline{n+1}} + \left(1 + \frac{c_i^n \Delta t}{\Delta z^2}\right) T_{ij}^{\overline{n+1}} + \left(-\frac{b_{ij}^n \Delta t}{4\Delta z} - \frac{c_i^n \Delta t}{2\Delta z^2}\right) T_{ij+1}^{\overline{n+1}} + \frac{\dot{q}}{2\mathrm{Pe}_r}\Delta t.$$

Note that Δt is the time step, Δx and Δz are the mesh intervals in the x and z-directions, respectively, for the transformed co-ordinate system. The finite difference scheme sweeps in the x-direction first, then sweeps along the z-direction, as depicted in Figure 3.3. The discretised coefficients a, b and c of the transformed temperature equation are

$$a_{ij}^n = \frac{u_{ij} - (i-1)\Delta x \dot{s}}{s}, \tag{3.2.64}$$

$$b_{ij}^n = \frac{1}{h_i}\left(w_{ij} - \frac{u_{ij}(j-1)\Delta z}{s}\frac{h_{i+1}^n - h_{i-1}^n}{\Delta x} - \frac{(j-1)\Delta z}{s^2}(h_t)_i^n + \frac{(j-1)\Delta z(i-1)\Delta x \dot{s}}{s}\frac{h_{i+1}^n - h_{i-1}^n}{\Delta x}\right), \tag{3.2.65}$$

and

$$c_i^n = \frac{1}{\mathrm{Pe}_r (h_i^n)^2}. \tag{3.2.66}$$

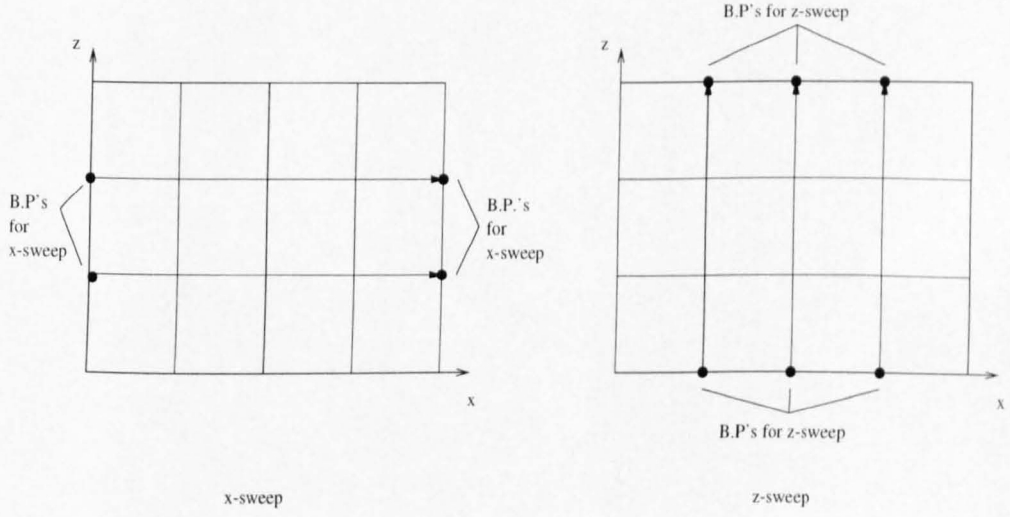

FIG. 3.3. x and z sweeps between boundary points (B.P.'s).

The temporal time derivative term for h in equation (3.2.65) needs to be evaluated and is identical to that in equation (3.2.5). Thus for the planar spreading case we have

$$(h_t)_i^n = \frac{1}{2\Delta x^2}\left((h_{i+1}^n - h_i^n)(D_{i+1}^n + D_i^n) - (h_i^n - h_{i-1}^n)(D_i^n + D_{i-1}^n)\right). \tag{3.2.67}$$

The initial step at $x = 0$ for the constant mass case is

$$\left(\frac{\partial h}{\partial t}\right)_1^n = \frac{1}{\Delta x^2}\left((h_2^n - h_1^n)(D_2^n + D_1^n)\right) \tag{3.2.68}$$

and for the influx model, using equation (3.1.8) the first step is

$$(h_t)_1^n = \frac{1}{2\Delta x^2}\left((h_2^n - h_1^n)(D_2^n + D_1^n) - (h_1^n - h_2^n - f(h_1^n))\left(D_1^n + \frac{(h_2^n + f(h_1^n))^3}{3\mu(1)}\right)\right), \quad (3.2.69)$$

where

$$f(h_1^n) = \frac{6\Delta x\mu(1)\beta Q_c t^{\beta-1}}{(h_1^n)^3}.$$

The polar relationship for the temporal derivative is

$$\left(\frac{\partial h}{\partial t}\right)_i^n = \frac{1}{2r_i\Delta r^2}\left(r_{i+\frac{1}{2}}(h_{i+1}^n - h_i^n)(D_{i+1}^n + D_i^n) - r_{i-\frac{1}{2}}(h_i^n - h_{i-1}^n)(D_i^n + D_{i-1}^n)\right) \quad (3.2.70)$$

and, taking account of radial symmetry and the singularity at $r = 0$, we have

$$\left(\frac{\partial h}{\partial t}\right)_1^n = \frac{1}{\Delta r^2}(h_2^n - h_1^n)(D_2^n + 3D_1^n). \quad (3.2.71)$$

An advantage of using the LoD scheme is that it avoids inverting a large sparse matrix (which would be the case if using the implicit method in equation (3.2.55)) by inverting a series of tridiagonal matrices instead. A disadvantage is that the LoD scheme is restricted by one-dimensional stability conditions. Unfortunately, this method alone is not capable of solving the problem. This is due to instabilities caused by the advection terms. In order to get round these instabilities, upwinding is used, as explained in the next section.

3.2.9. *Upwinding*

We implement upwinding to eliminate instabilities in the numerical scheme as discussed in Morton & Mayers (1994). The modified scheme uses a forward difference if a is negative and a backwards difference for positive a. The main drawback in the use fo upwinding, is that the numerical scheme is only first order accurate in space compared to the central differences which have truncation errors that are second order.

3.2.10. *Modified LoD difference scheme for the temperature field*

Implementing the upwinding approach in the locally one dimension schemes gives the following difference equations. The first sweep with $a > 0$ has

$$-\frac{\Delta t a_{ij}^n}{2\Delta x}T_{i-1j}^{\overline{n+1}} + \left(1 + \frac{\Delta t a_{ij}^n}{2\Delta x}\right)T_{ij}^{\overline{n+1}} = d_{ij}^n, \quad (3.2.72)$$

where

$$d_{ij}^n = \frac{\Delta t a_{ij}^n}{2\Delta x}T_{i-1j}^n + \left(1 - \frac{\Delta t a_{ij}^n}{2\Delta x}\right)T_{ij}^n + \frac{\dot{q}}{2\mathrm{Pe}_r}\Delta t$$

while for $a < 0$ has

$$\left(1 - \frac{\Delta t a_{ij}^n}{2\Delta x}\right)T_{ij}^{\overline{n+1}} + \frac{\Delta t a_{ij}^n}{2\Delta x}T_{i+1j}^{\overline{n+1}} = d_{ij}^n, \quad (3.2.73)$$

where

$$d_{ij}^n = \left(1 + \frac{\Delta t a_{ij}^n}{2\Delta x}\right)T_{ij}^n - \frac{\Delta t a_{ij}^n}{2\Delta x}T_{i+1j}^n + \frac{\dot{q}}{2\mathrm{Pe}_r}\Delta t.$$

The second sweep with $b > 0$ has

$$\left(-\frac{b_{ij}^n \Delta t}{2\Delta z} + \frac{c_i^n \Delta t}{2\Delta z^2}\right) T_{ij-1}^{n+1} + \left(1 - \frac{c_i^n \Delta t}{\Delta z^2} + \frac{b_{ij}^n \Delta t}{2\Delta z}\right) T_{ij}^{n+1} + \frac{c_i^n \Delta t}{2\Delta z^2} T_{ij+1}^{n+1} = \overline{d_{ij}^{n+1}}, \quad (3.2.74)$$

where

$$\overline{d_{ij}^{n+1}} = \left(\frac{b_{ij}^n \Delta t}{2\Delta z} - \frac{c_i^n \Delta t}{2\Delta z^2}\right) \overline{T_{ij-1}^{n+1}} + \left(1 + \frac{c_i^n \Delta t}{\Delta z^2} - \frac{b_{ij}^n \Delta t}{2\Delta z}\right) \overline{T_{ij}^{n+1}} - \frac{c_i^n \Delta t}{2\Delta z^2} \overline{T_{ij+1}^{n+1}} + \frac{\dot{q}}{2\mathrm{Pe}_r} \Delta t.$$

and for $b < 0$

$$\frac{c_i^n \Delta t}{2\Delta z^2} T_{ij-1}^{n+1} + \left(1 - \frac{b_{ij}^n \Delta t}{2\Delta z} - \frac{c_i^n \Delta t}{\Delta z^2}\right) T_{ij}^{n+1} + \left(\frac{b_{ij}^n \Delta t}{2\Delta z} + \frac{c_i^n \Delta t}{2\Delta z^2}\right) T_{ij-1}^{n+1} = \overline{d_{ij+1}^{n+1}}, \quad (3.2.75)$$

where

$$\overline{d_{ij}^{n+1}} = -\frac{c_i^n \Delta t}{2\Delta z^2} \overline{T_{ij-1}^{n+1}} + \left(1 + \frac{c_i^n \Delta t}{\Delta z^2} + \frac{b_{ij}^n \Delta t}{2\Delta z}\right) \overline{T_{ij}^{n+1}} + \left(-\frac{b_{ij}^n \Delta t}{2\Delta z} - \frac{c_i^n \Delta t}{2\Delta z^2}\right) \overline{T_{ij+1}^{n+1}} + \frac{\dot{q}}{2\mathrm{Pe}_r} \Delta t.$$

Note that a_{ij}^n, b_{ij}^n and c_{ij}^n are as defined earlier in equations (3.2.64)-(3.2.66).

3.2.11. *Mapping to the new mesh*

In the FORTRAN program, the number of mesh points is increased for the temperature and velocity fields after each time step. This is done by setting the number of mesh points along $\bar{z}$ fixed for all time, and increasing the number of the mesh points in the $\bar{x}$-direction if the liquid spreads.

Thus the temperature values have to be interpolated from the original to the new mesh. This is done by using the linear relationship

$$T = T_i + (T_{i+1} - T_n)\left(\frac{x - x_i}{\Delta x}\right). \quad (3.2.76)$$

T is the new temperature value at position x on the larger mesh, where T_{i+1} and T_i are the nearest temperature values surrounding T at positions x_{i+1} and x_i respectively from the old mesh. Note that Δx is the original mesh spacing.

3.2.12. *Development of the numerical model*

The numerical scheme used to solve the problem in this chapter was initially applied to a simple temperature problem of a sessile drop. The stationary parabolic drop was transformed to a square grid, with the one-dimensional heat equation as the temperature evolution model. The heat equation was solved analytically using separation of variables and using a Crank-Nicolson implicit finite difference numerical scheme. The results showed very good agreement.

Next the temperature evolution equation (3.1.5) was applied to the sessile drop problem (the velocity field is evaluated using the isothermal form of equations (3.1.3c) and (3.1.4c)) using two different numerical schemes. One was the locally one-dimensional (LoD) finite difference scheme explained above and the other was the alternating direction implicit (ADI) finite difference scheme, which is similar to the LoD method (see Morton & Mayers (1994). The results again showed very good agreement. The next step was to solve the full problem as discussed above.

3.2.13. *Summary of numerical methods implemented in FORTRAN code*

After setting up the initial conditions, the drop starts to cool, with the transformed velocity field on the rectangular mesh (discretised equations (3.2.31) and (3.2.34) in two dimensions or (3.2.45) and (3.2.47) in polar coordinates), front location, s, and the front location velocity, $\dot{s}$ used to solve the temperature field on the rectangular mesh using the finite difference schemes (3.2.72) to (3.2.75). Once the new temperature field has been evaluated the viscosity is calculated over the mesh and hence the updated free surface profile is obtained using the finite difference schemes (3.2.2) in two dimensions or (3.2.13) in polar coordinates. Note the first grid point in polar coordinates uses the finite difference scheme (3.2.15) to avoid the singularity at $r = 0$. The influx case in two dimensions uses the modified finite difference scheme (3.2.11) for the free surface at $x = 0$. The current temperature values are mapped onto the new mesh caused by the increased drop width and the cycle is repeated over the required time period. The above procedure is implemented into a FORTRAN 90 code and gives the results described next.

3.3. Numerical results for the exponential viscosity relationship

3.3.1. *Two-dimensional results with constant mass*

Spreading under gravity is first considered for a liquid drop with a parabolic initial profile and constant viscosity, $\alpha = 0$. The lens shaped height profiles and streamlines are shown at times $t = 1$, $t = 4$, $t = 7$ and $t = 10$ in Figure 3.4. Note that the results are obtained using 600 mesh points in the x-direction over the range [0,2], 200 mesh points in the z-direction and a time step (Δt) of 5.0×10^{-4}, unless stated otherwise.

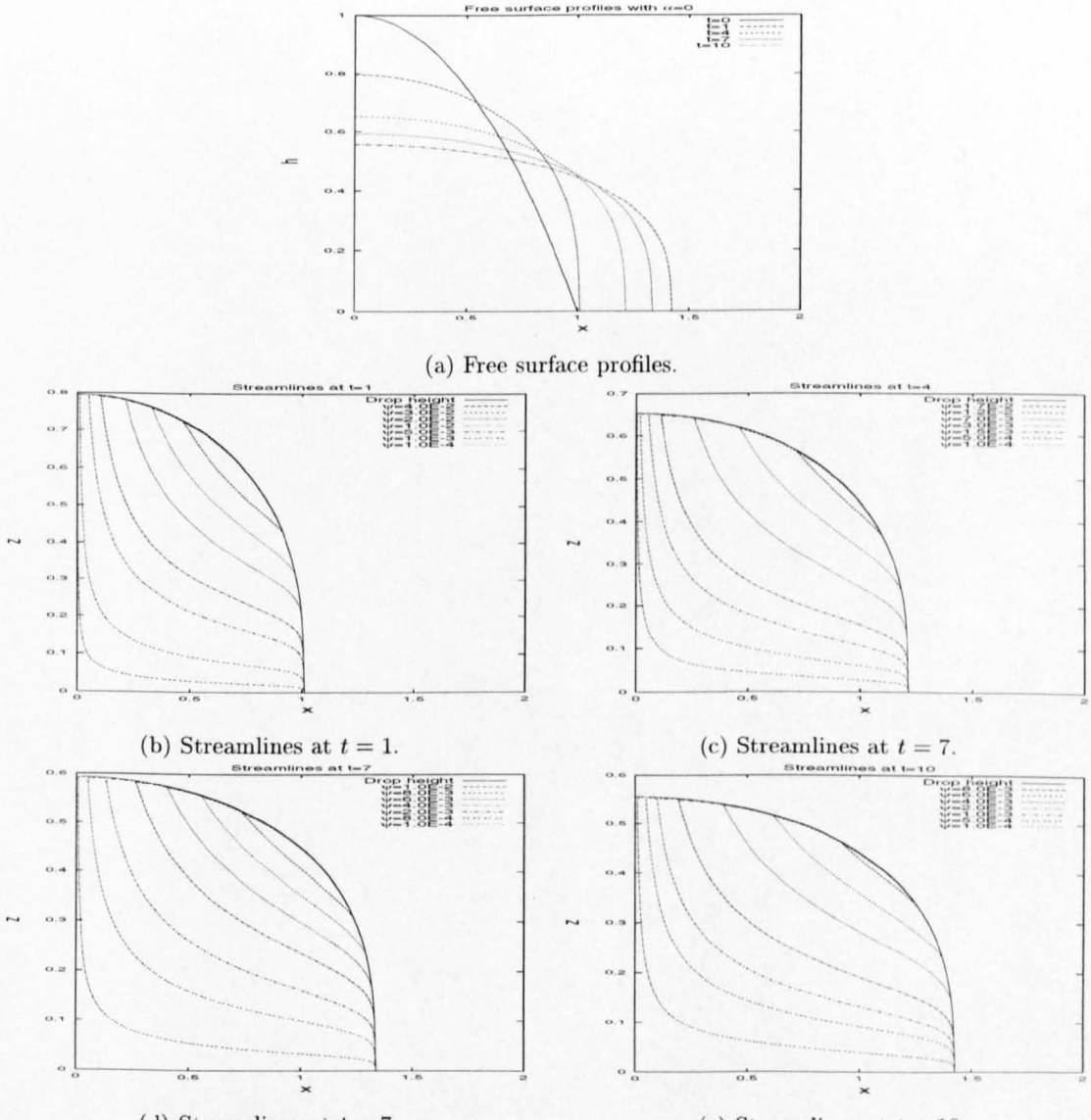

(a) Free surface profiles.

(b) Streamlines at $t = 1$.

(c) Streamlines at $t = 7$.

(d) Streamlines at $t = 7$.

(e) Streamlines at $t = 10$

FIG. 3.4. Two-dimensional results: isothermal and constant mass.

The first set of results with variable viscosity with $\alpha = 2$ and $\mathrm{Pe}_r = 10^6$ are illustrated in Figure 3.5. The temperature profiles show that there is little heat loss over the droplet for small time

and that the drop profiles develop a steep flow front. For larger time the drop profiles develop the lens shape profile as seen in the isothermal results, due to the large heat loss seen in the temperature plots. The streamlines are clearly affected by the local hot spot at the shoulder of the flow front, with the lower viscosity there inducing an upwelling motion. The reason for this is a build up of very viscous fluid near the flow front causing the fluid to flow over this cooler region and develop the steep flow front.

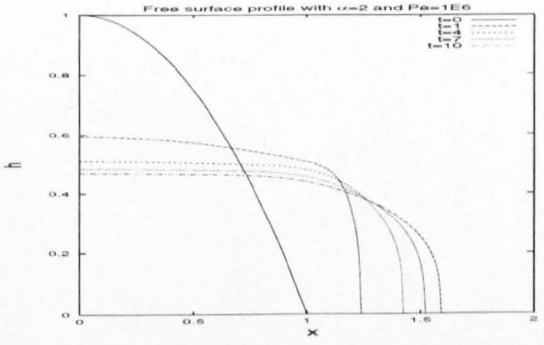

(a) Free surface profiles.

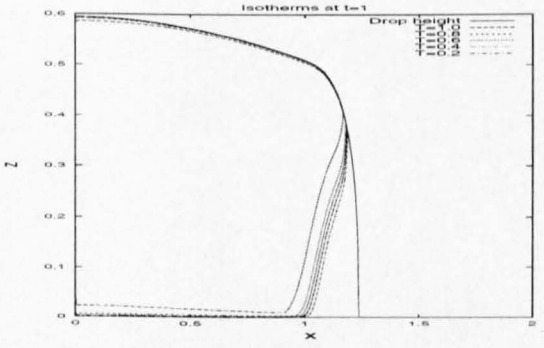

(b) Isotherms at $t = 1$.

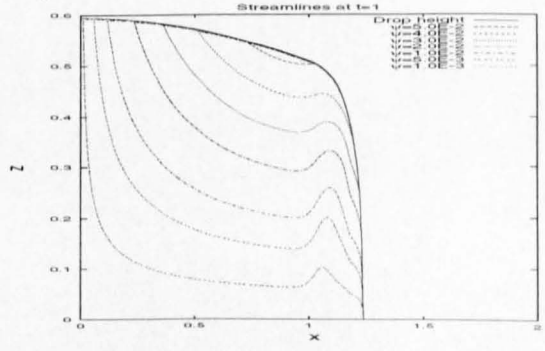

(c) Streamlines at $t = 1$.

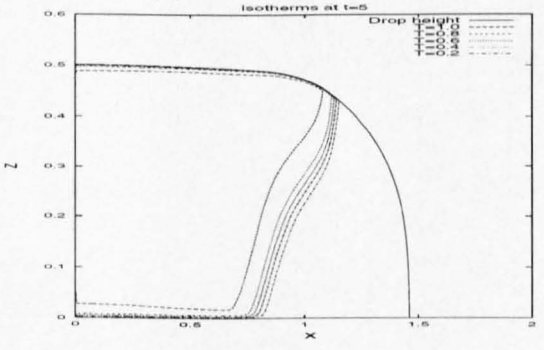

(d) Isotherms at $t = 5$.

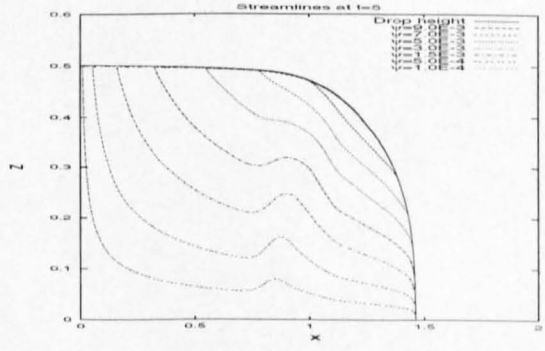

(e) Streamlines at $t = 5$

FIG. 3.5. Two-dimensional results: constant mass with $\alpha = 2$ and $\mathrm{Pe}_r = 10^6$.

Decreasing the reduced Peclet number to 10^4 gives results shown in Figure 3.6, where the coupling between the viscosity and temperature again has $\alpha = 2$. The results are similar to those with $\mathrm{Pe}_r = 10^6$ in Figure 3.5. The streamlines again show the effects of the cooler region and display an upwelling motion for the spreading liquid.

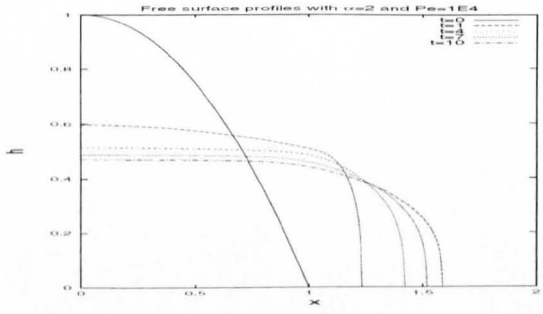

(a) Free surface profiles.

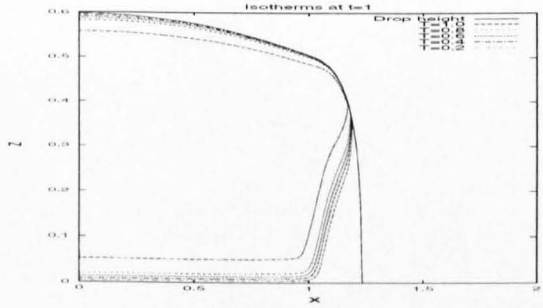

(b) Isotherms at $t = 1$.

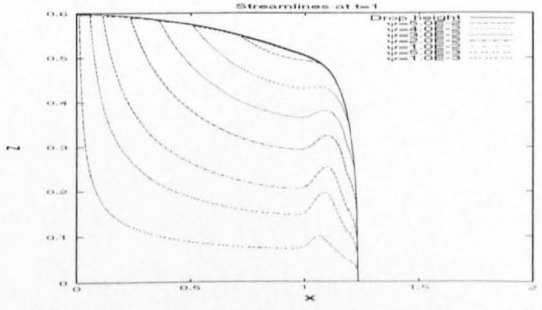

(c) Streamlines at $t = 1$.

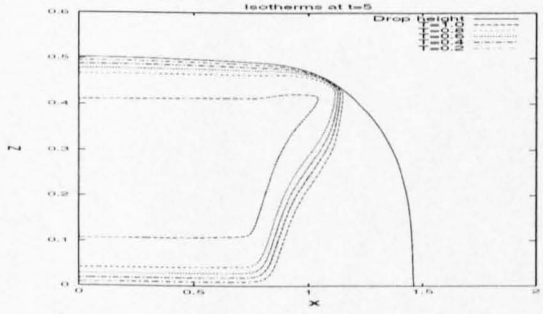

(d) Isotherms at $t = 5$.

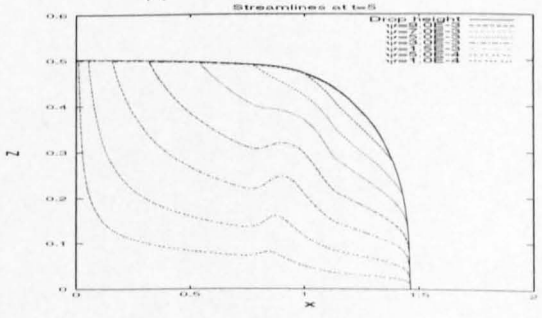

(e) Streamlines at $t = 5$

FIG. 3.6. Two-dimensional results: constant mass with $\alpha = 2$ and $\mathrm{Pe}_r = 10^4$.

The steep flow front is not as noticeable when $\mathrm{Pe}_r = 10^2$, as seen in Figures 3.7-3.8. The isotherms show that the thermal conduction is dominant (as expected for smaller Pe_r) and the respective streamlines are of a similar nature to the isothermal case for large time.

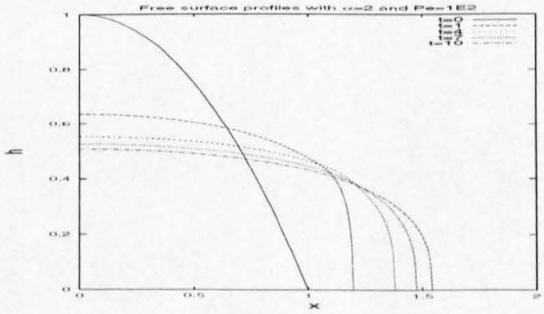

(a) Free surface profiles.

FIG. 3.7. Two-dimensional results: constant mass with $\alpha = 2$ and $\mathrm{Pe}_r = 10^2$.

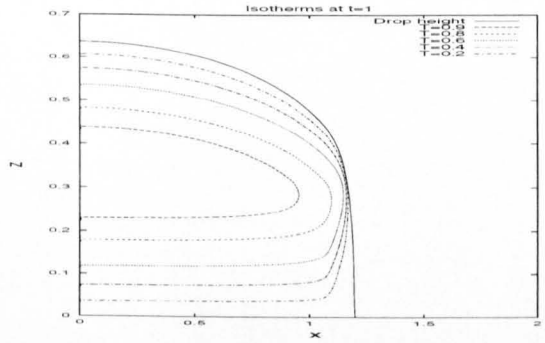

(a) Isotherms at $t = 1$.

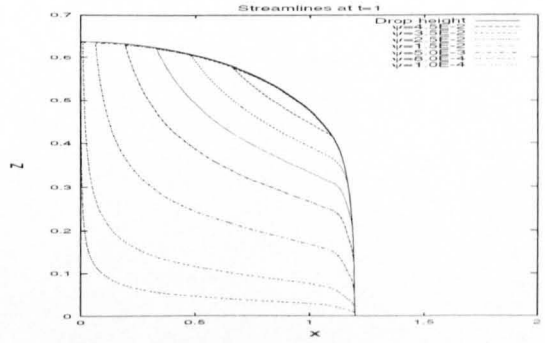

(b) Streamlines at $t = 1$.

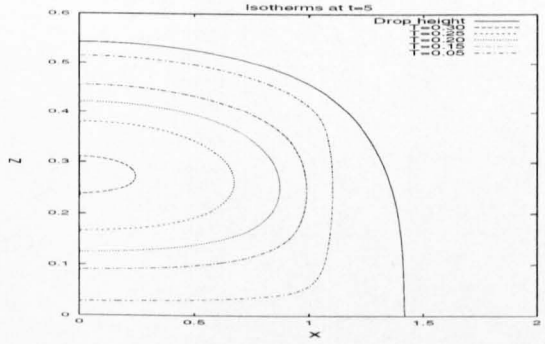

(c) Isotherms at $t = 5$.

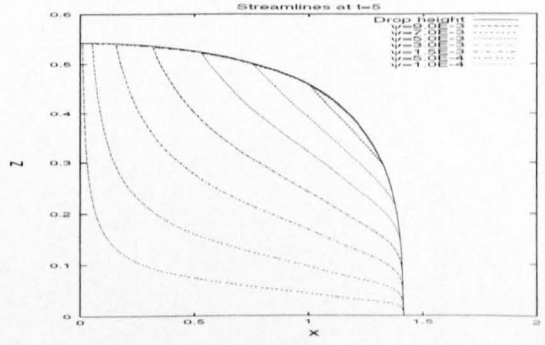

(d) Streamlines at $t = 5$

FIG. 3.8. Two-dimensional results: constant mass with $\alpha = 2$ and $\mathrm{Pe}_r = 10^2$.

The log-log plots for $\alpha = 2$ show similar spreading rates for $\mathrm{Pe}_r = 10^6$ and $\mathrm{Pe}_r = 10^4$. Decreasing Pe_r shows that the spreading rates tend to the isothermal case, as seen in Figure 3.9. This is to be expected, since for small Pe_r the droplet cools to zero quicker than for larger Pe_r.

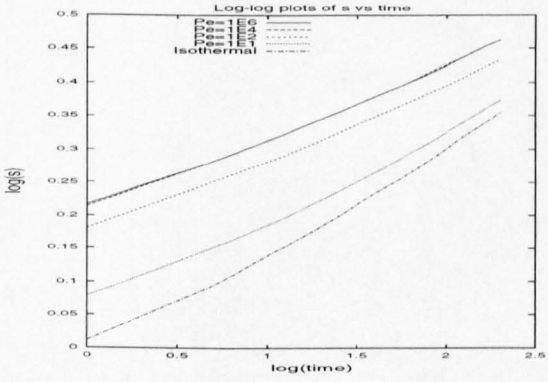

(a) Front location *vs* time.

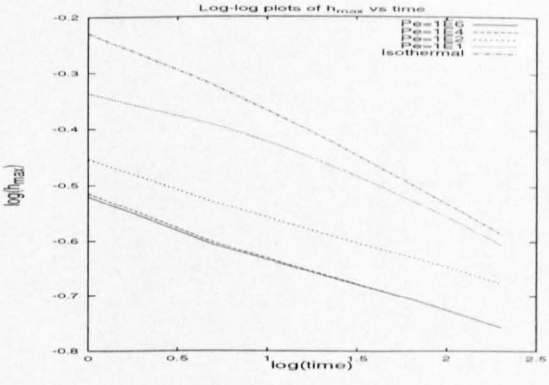

(b) h_{max} *vs* time.

FIG. 3.9. Log-log plots of front location and h_{max} *vs* time for $\alpha = 2$.

Increasing the coupling between the velocity and temperature field by setting $\alpha = 2.5$ (the maximum value attainable before the numerics fail due to oscillations developing in the free surface profiles) with $\mathrm{Pe}_r = 10^4$ gives the results in Figure 3.10. Increasing α shows a steepening of the flow front followed by a plateau, which is more prominent than that for $\alpha = 2$. The streamlines and isotherms are similar to the respective case with $\alpha = 2$.

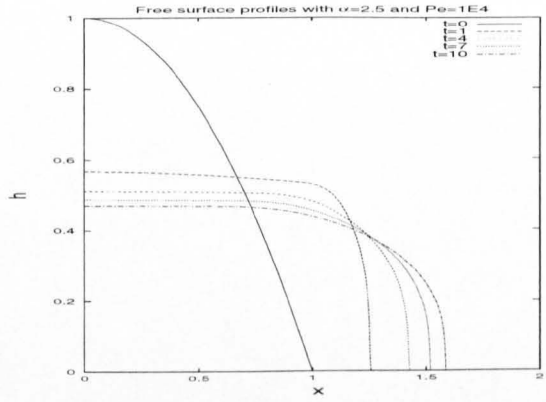

(a) Free surface profiles.

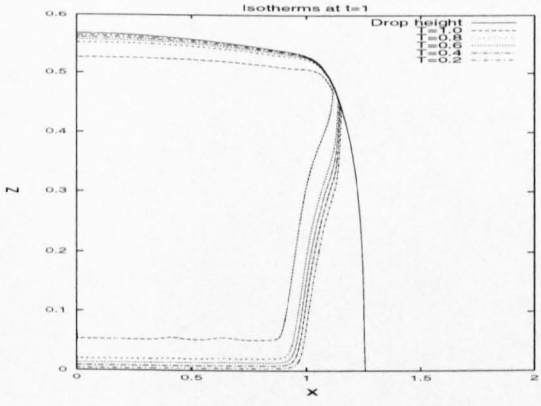

(b) Isotherms at $t = 1$.

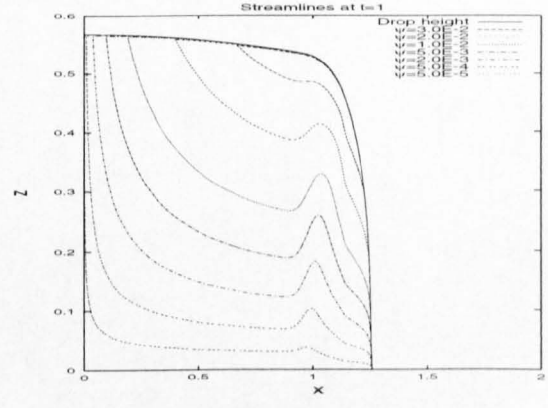

(c) Streamlines at $t = 1$.

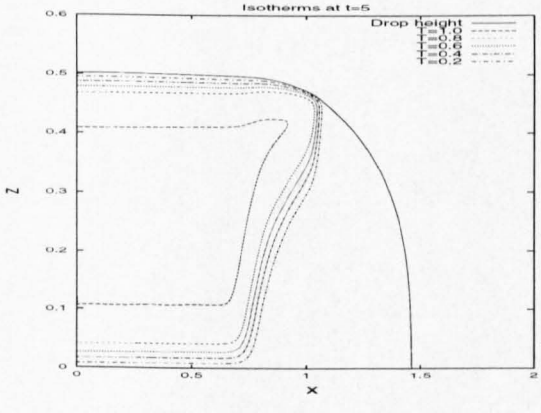

(d) Isotherms at $t = 5$.

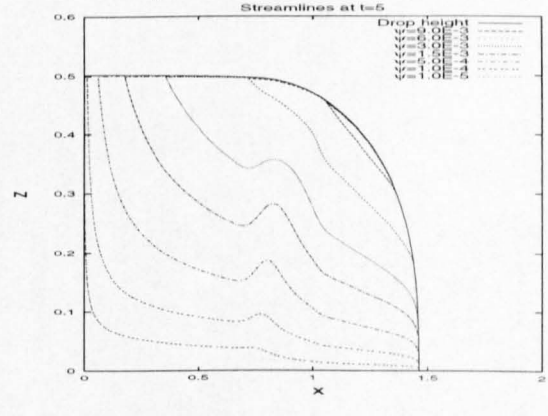

(e) Streamlines at $t = 5$

FIG. 3.10. Two-dimensional results: constant mass with $\alpha = 2.5$ and $\mathrm{Pe}_r = 10^4$.

Keeping $\alpha = 2.5$ but reducing Pe_r to $\mathrm{Pe}_r = 10^2$, Figure 3.11, leads to an initially steeper flow front than with $\alpha = 2$ and $\mathrm{Pe}_r = 10^2$ in Figure 3.7. As time increases, a smaller Pe_r leads to a greater heat loss as shown in the isotherms in Figures 3.11(b) and 3.11(d). The corresponding streamlines show that the advection terms are no longer dominant as the liquid cools and that the upwelling effect is weaker.

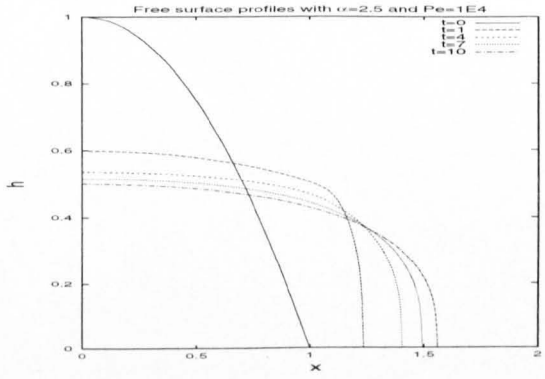

(a) Free surface profiles.

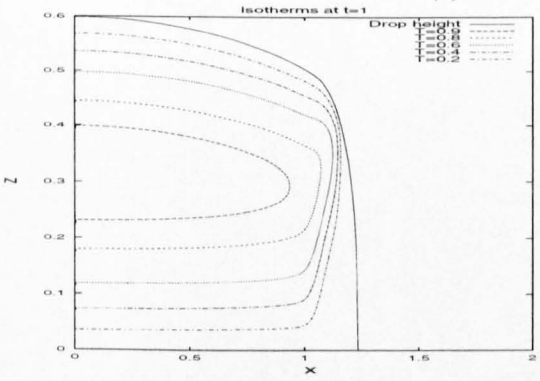

(b) Isotherms at $t = 1$.

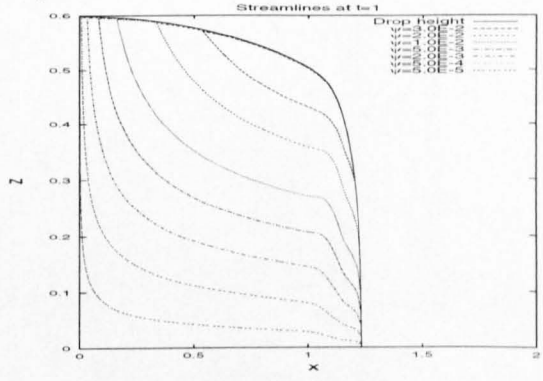

(c) Streamlines at $t = 1$.

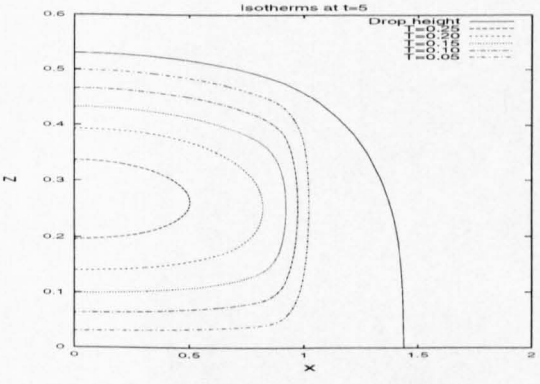

(d) Isotherms at $t = 5$.

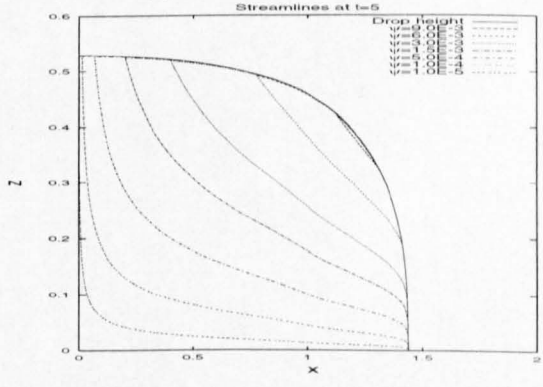

(e) Streamlines at $t = 5$

FIG. 3.11. Two-dimensional results: constant mass with $\alpha = 2.5$ and $\mathrm{Pe}_r = 10^2$.

Decreasing the reduced Peclet number to 10, Figure 3.12, leads to spreading which behaves isothermally, where the temperature rapidly tends to zero compared to the previous results with larger Peclet values. The isotherms show that the drop has cooled substantially by $t = 3$, resulting in the lens shaped free surface profiles characteristic of the isothermal case.

The log-log plots for $\alpha = 2.5$ in Figure 3.13 show similar behaviour to the plots for $\alpha = 2$, the spreading tends to be isothermal as Pe_r is decreased.

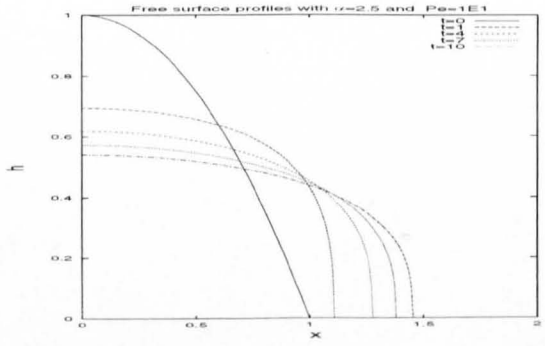

(a) Free surface profiles.

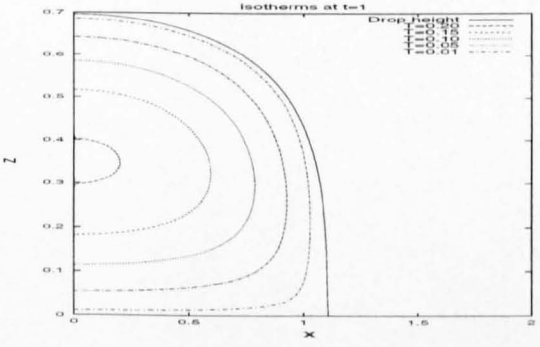

(b) Isotherms at $t = 1$.

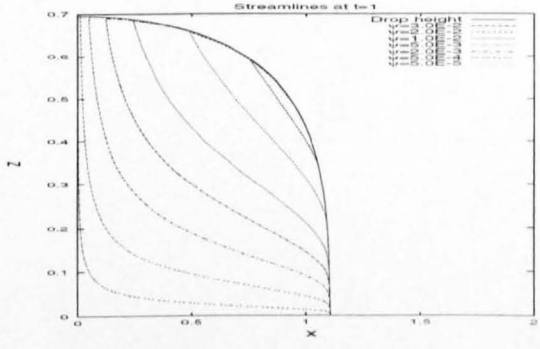

(c) Streamlines at $t = 1$.

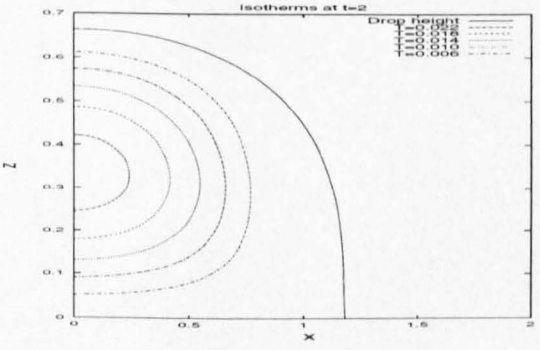

(d) Isotherms at $t = 5$.

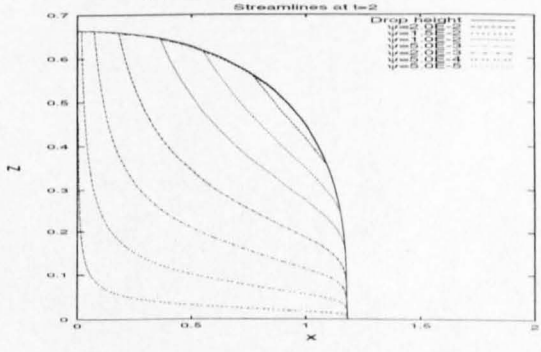

(e) Streamlines at $t = 5$

FIG. 3.12. Two-dimensional results: constant mass with $\alpha = 2.5$ and $\mathrm{Pe}_r = 10$.

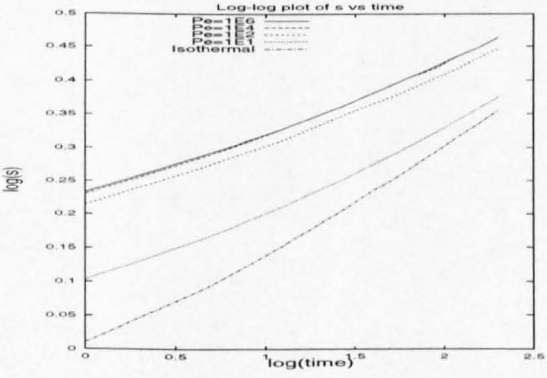

(a) Front location *vs* time.

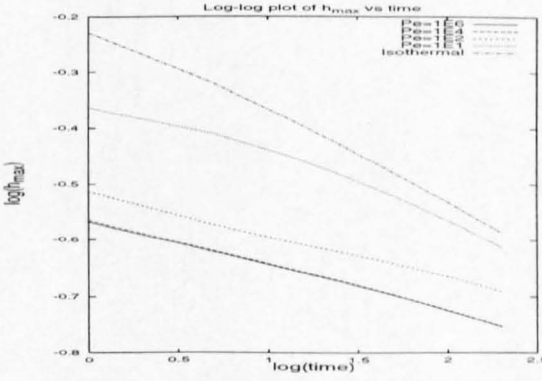

(b) h_{max} *vs* time.

FIG. 3.13. Log-log plots of front location and h_{max} *vs* time for $\alpha = 2.5$.

3.3.2. *Two-dimensional results from a line source*

The next set of results in Figure 3.14 illustrates the isothermal case of planar spreading from a line source. The variable rate of liquid injection has $Q_c = 0.009$ and $\beta = 1.5$. The streamlines at times $t = 7$ and $t = 10$ clearly show the liquid being fed from the line source, as opposed from the free surface as in the constant mass streamlines. Note that the results are obtained using 300 mesh points in the x-direction over the range [0,1], 200 mesh points in the z-direction and with a time step (Δt) of 2.0×10^{-5}.

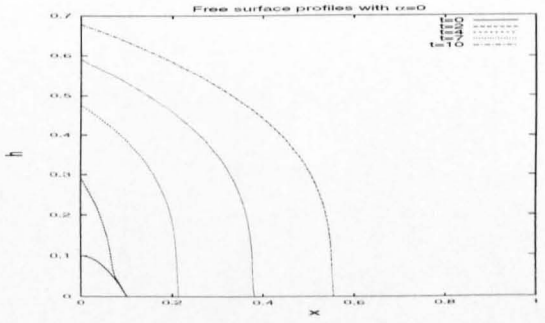

(a) Free surface profiles.

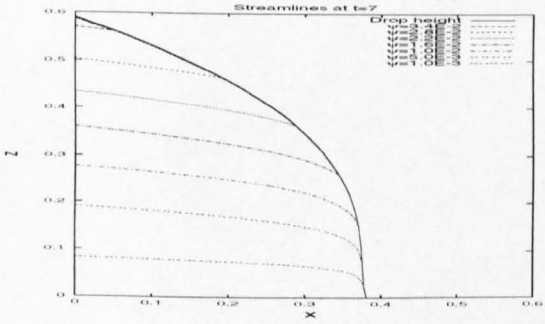

(b) Streamlines at $t = 7$.

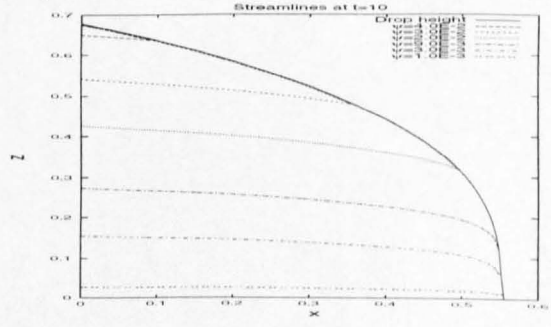

(c) Streamlines at $t = 10$.

FIG. 3.14. Two-dimensional results: isothermal with a line source.

The first set with variable viscosity has $\alpha = 2$ and $\mathrm{Pe}_r = 10^4$, shown in Figures 3.15-3.16. The free surface profiles show a steep flow front developing, the isotherms being strongly influenced by the hot liquid flowing from the line source.

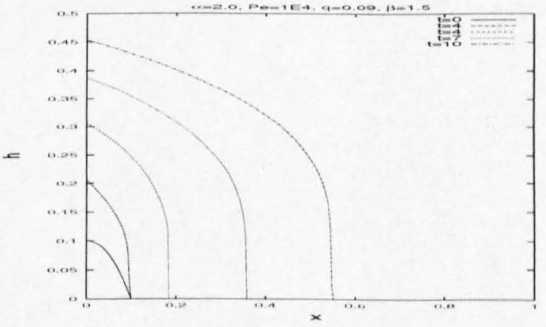

(a) Free surface profiles.

FIG. 3.15. Two-dimensional results: line source, $\alpha = 2$ and $\mathrm{Pe}_r = 10^4$.

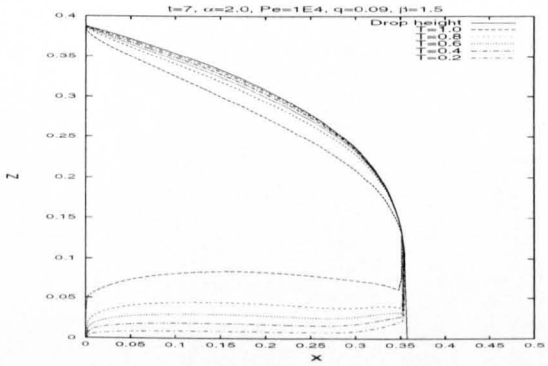

(a) Isotherms at $t = 7$.

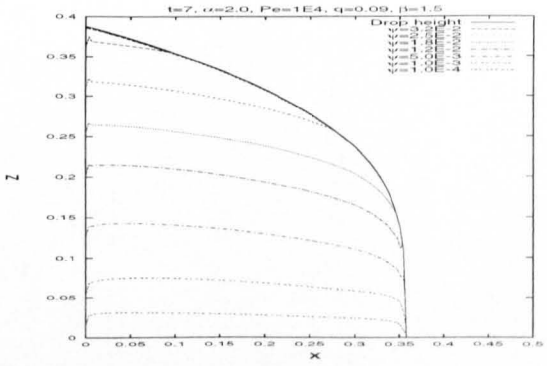

(b) Streamlines at $t = 7$.

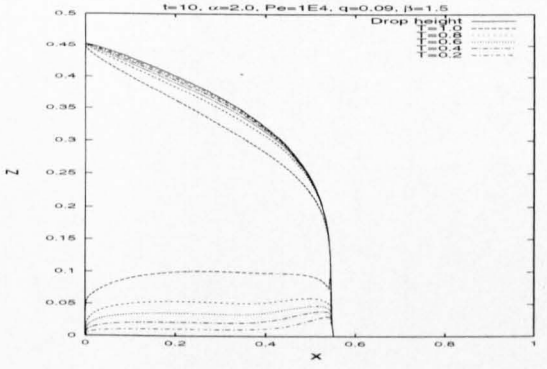

(c) Isotherms at $t = 10$.

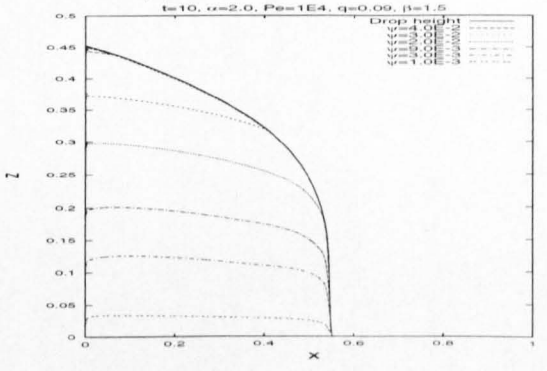

(d) Streamlines at $t = 10$

FIG. 3.16. Two-dimensional results: line source, $\alpha = 2$ and $\mathrm{Pe}_r = 10^4$.

Decreasing the Peclet number to 10^2 gives the results in Figures 3.17-3.18. The steep flow front is not as noticeable and the conduction term can be seen to affect the streamlines, the temperature loss being greater than that for a larger Peclet number.

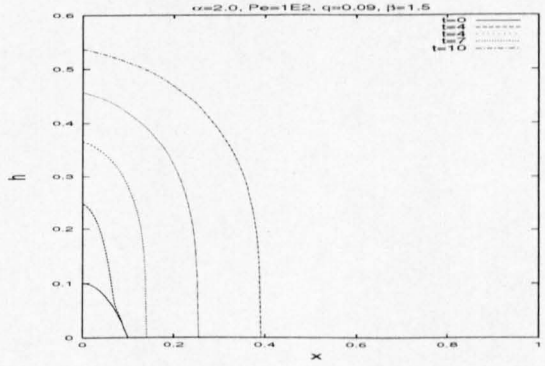

(a) Free surface profiles.

FIG. 3.17. Two-dimensional results: line source, $\alpha = 2$ and $\mathrm{Pe}_r = 10^2$.

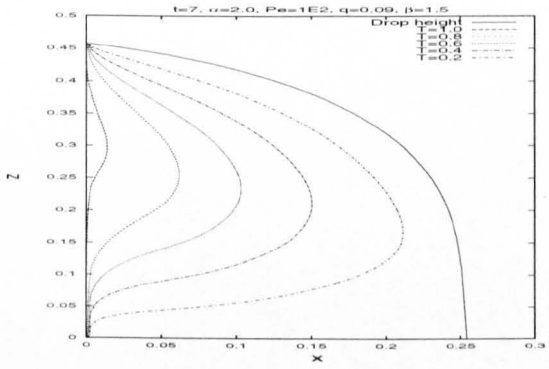

(a) Isotherms at $t = 7$.

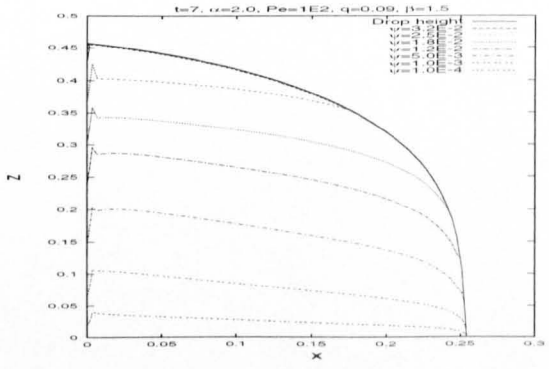

(b) Streamlines at $t = 7$.

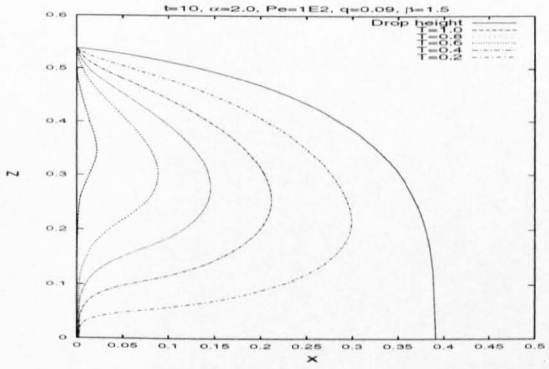

(c) Isotherms at $t = 10$.

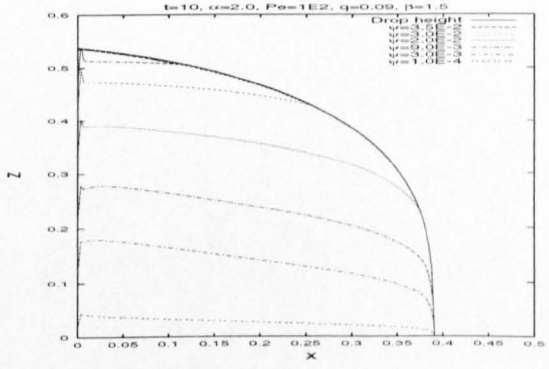

(d) Streamlines at $t = 10$

FIG. 3.18. Two-dimensional results: line source, $\alpha = 2$ and $\mathrm{Pe}_r = 10^2$.

The results with $\alpha = 2$ and $\mathrm{Pe}_r = 10$ are shown in Figure 3.19-3.20. The small value for the Peclet number leads to heat diffusing rapidly and the free surface profiles are similar to those in the isothermal case. The streamlines show the effect of the fast cooling, with an upwelling motion near the source. This is caused by the cooler liquid material being very viscous and forming a barrier causing the liquid to flow over this barrier. The numerical results show the correct behaviour, but because of the large change in viscosity, a loss of accuracy is noted. This can be improved by increasing the number of mess points, but with a subsequent increase in run time.

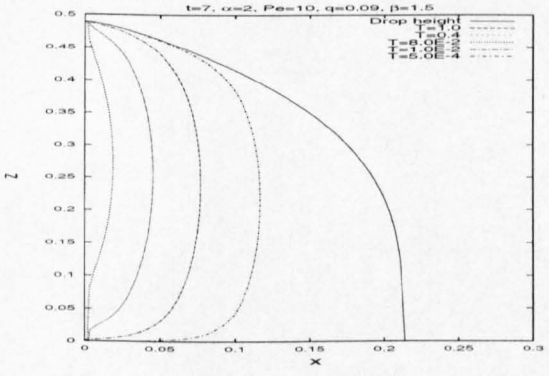

(a) Isotherms at $t = 7$.

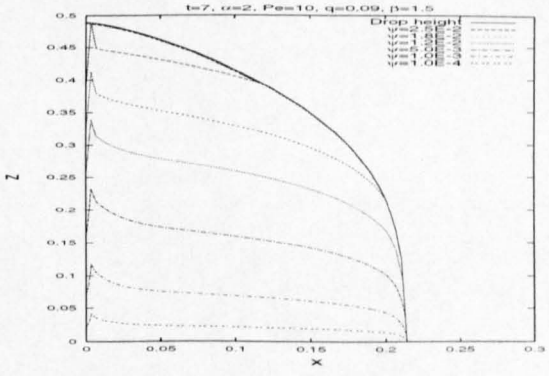

(b) Streamlines at $t = 7$.

FIG. 3.19. Two-dimensional results: line source, $\alpha = 2$ and $\mathrm{Pe}_r = 10$.

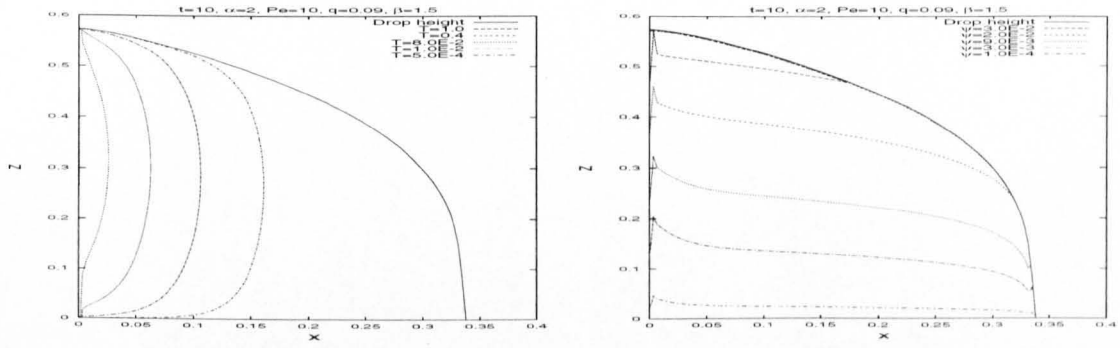

(a) Isotherms at $t = 10$. (b) Streamlines at $t = 10$

FIG. 3.20. Two-dimensional results: line source, $\alpha = 2$ and $\mathrm{Pe}_r = 10$.

The results shown in Figure 3.21 have $\alpha = 4$ and $\mathrm{Pe}_r = 10^4$. They show that, on increasing α, the steep flow front becomes more prominent (cf. the results for $\alpha = 2$ in Figure 3.15). The temperature profiles and streamlines are similar to the respective case with $\alpha = 2$.

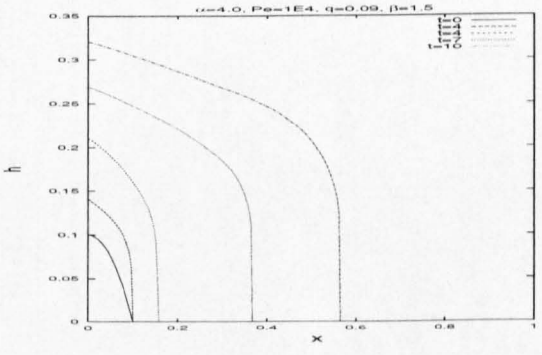

(a) Free surface profiles.

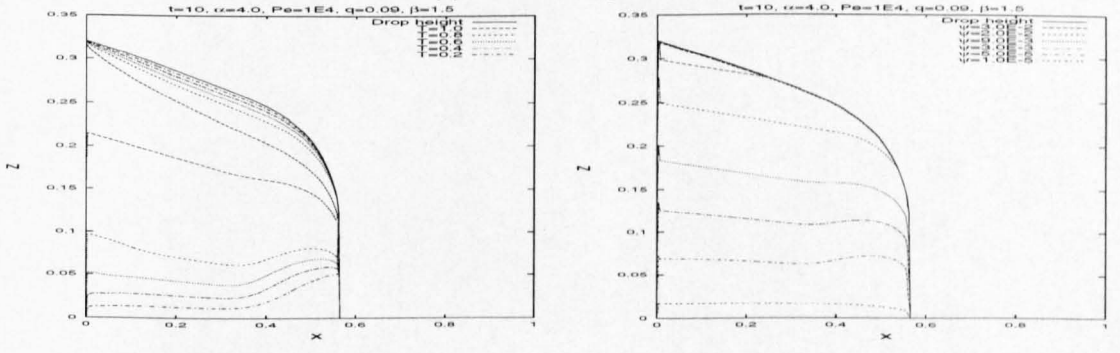

(b) Isotherms at $t = 10$. (c) Streamlines at $t = 10$.

FIG. 3.21. Two-dimensional results: line source, $\alpha = 4$ and $\mathrm{Pe}_r = 10^4$.

The results for the influx model are computationally expensive to obtain. For this reason, they were limited to a shorter time period than would be preferable. For this reason the log-log plots are not shown here. The influx results are consistent with the constant mass case: as α increases, the profiles develop a steeper flow front. The isotherms for $Pe_r = 10^2$ show good agreement qualitatively with the experimental isotherms in Stasiuk *et al.* (1993), where there is a large amount of cooling near the flow front; see Discussion for the experimental results.

3.3.3. *Axisymmetric results with constant mass*

The next set of results in Figure 3.22 are for axisymmetric spreading, starting with the case where $\alpha = 0$, i.e. isothermal spreading. The lens shaped height profiles and streamlines are shown at times $t = 1$, $t = 4$, $t = 7$ and $t = 10$. Note that the results are obtained using 600 mesh points in the r-direction over the range [0,2], 200 mesh points in the z-direction and with a time step (Δt) of 5.0×10^{-4}.

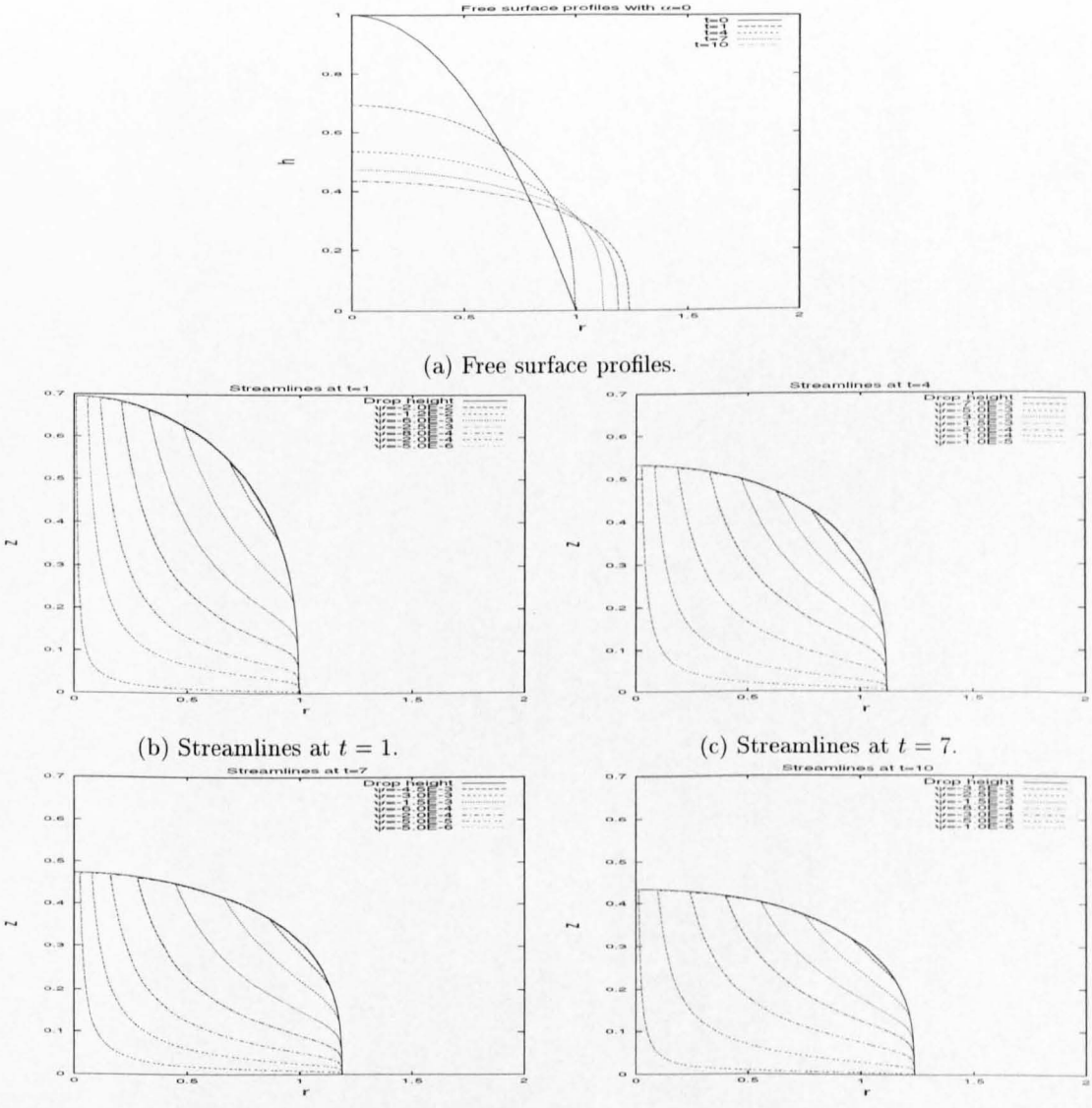

(a) Free surface profiles.

(b) Streamlines at $t = 1$.

(c) Streamlines at $t = 7$.

(d) Streamlines at $t = 7$.

(e) Streamlines at $t = 10$

FIG. 3.22. Axisymmetric results: isothermal and constant mass.

For the first set of non-isothermal results we take $\alpha = 2$ and $\mathrm{Pe}_r = 10^6$. At small times the height profiles develop a steep flow front followed by a plateau (see Figure 3.23). The isotherms at $t = 1$ and $t = 5$ show little heat loss, as expected since the conduction term is small. As the drop spreads, the isotherms show a large amount of cooling near the flow front. This can be seen

to affect the flow of the droplet, the streamlines showing an upwelling motion where the liquid is cooler, as in the two-dimensional results.

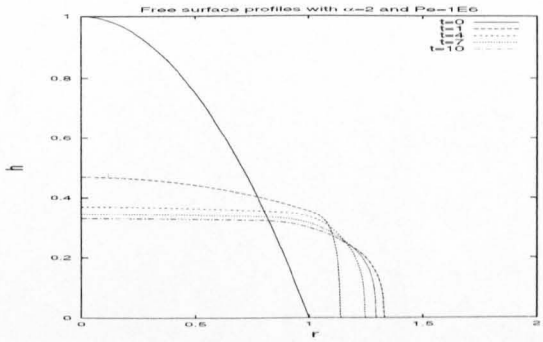

(a) Free surface profiles.

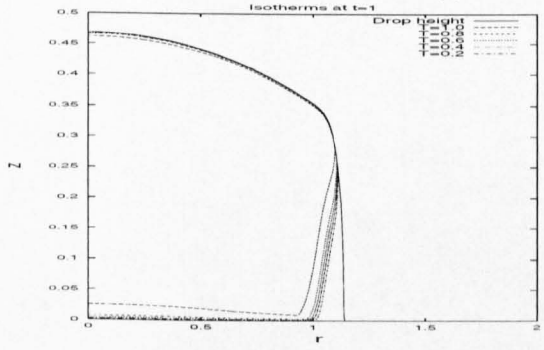

(b) Isotherms at $t = 1$.

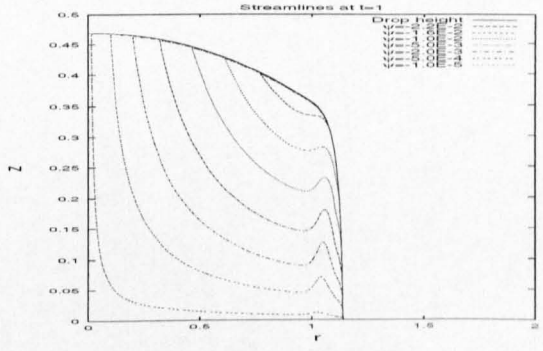

(c) Streamlines at $t = 1$.

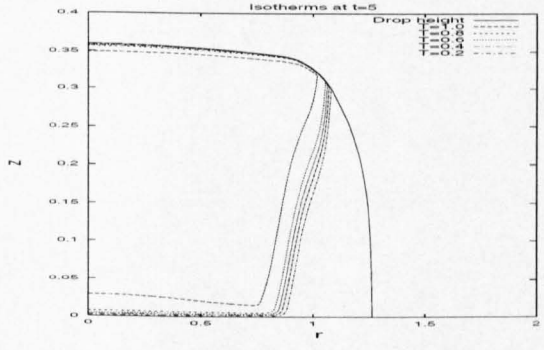

(d) Isotherms at $t = 5$.

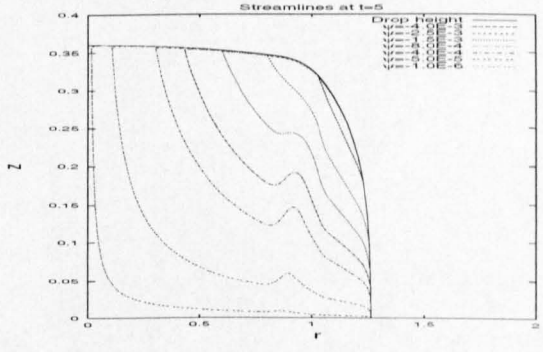

(e) Streamlines at $t = 5$

FIG. 3.23. Axisymmetric results: constant mass with $\alpha = 2$ and $\mathrm{Pe}_r = 10^6$.

Decreasing Pe_r to 10^4 gives similar results to $\mathrm{Pe}_r = 10^6$, see Figures 3.24 and 3.23, respectively. The thermal diffusion term is still small and there is little heat loss from the droplet. The streamlines again show the effect of cooling near the flow front and the free surface profiles feature a steep flow front followed by a plateau. As the drop cools, the height profiles develop a smoother flow front, as observed in the isothermal results. This is consistent with the two-dimensional results.

The results with $\mathrm{Pe}_r = 10^2$ and $\alpha = 2$ are shown in Figures 3.25-3.26. The temperature field is dominated by the diffusion term since the isotherms show a large loss of heat when compared

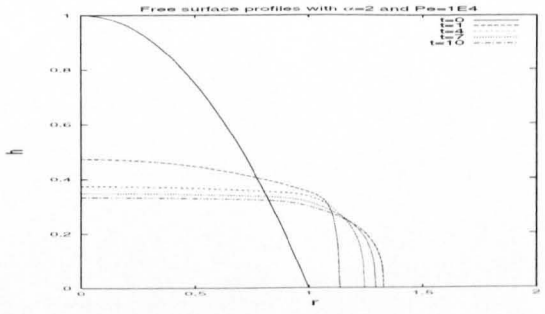

(a) Free surface profiles.

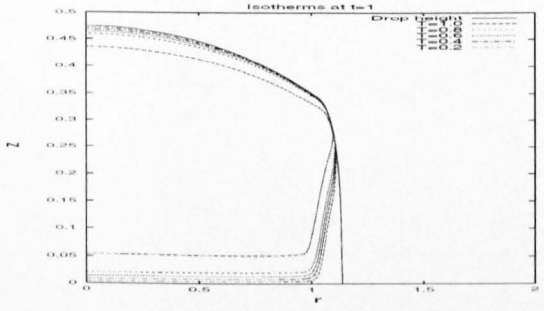

(b) Isotherms at $t = 1$.

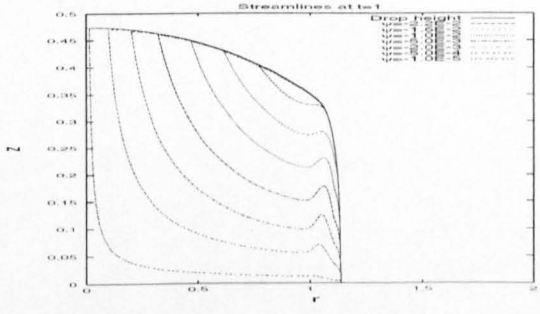

(c) Streamlines at $t = 1$.

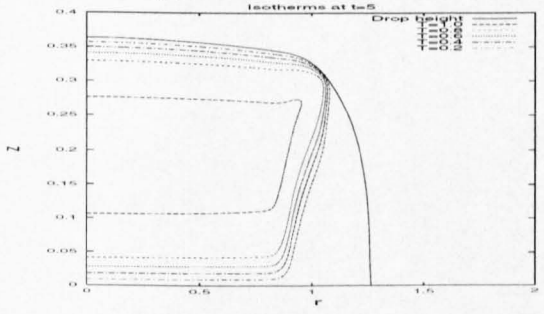

(d) Isotherms at $t = 5$.

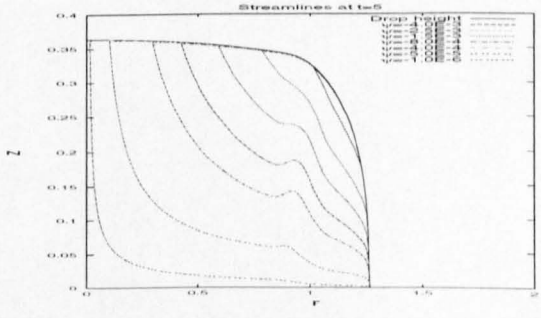

(e) Streamlines at $t = 5$

FIG. 3.24. Two-dimensional results: constant mass with $\alpha = 2$ and $\mathrm{Pe}_r = 10^4$.

to the isotherms for large Pe_r. The resulting free surface profiles develop a lens shaped profile characteristic of the isothermal case. The streamlines do not show the upwelling motion as seen in the previous results because of the conduction dominance.

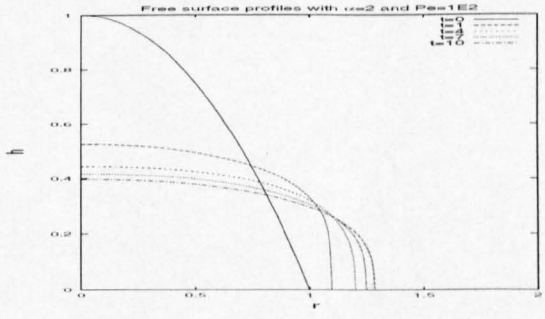

(a) Free surface profiles.

FIG. 3.25. Axisymmetric results: constant mass with $\alpha = 2$ and $\mathrm{Pe}_r = 10^2$.

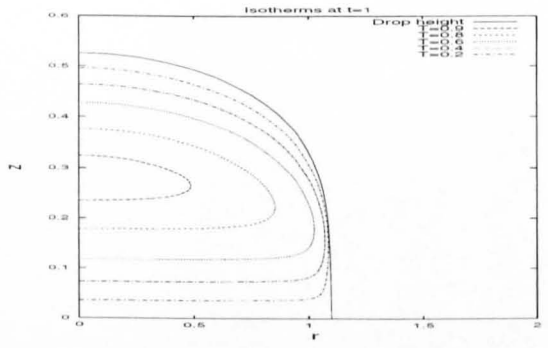

(a) Isotherms at $t = 1$.

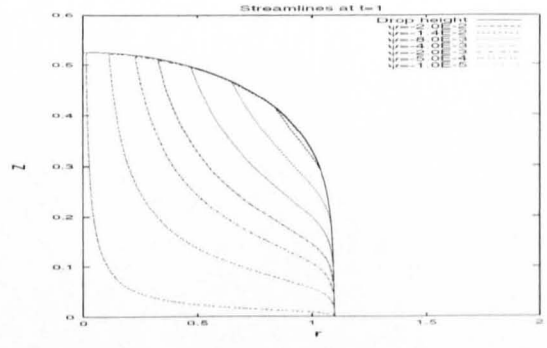

(b) Streamlines at $t = 1$.

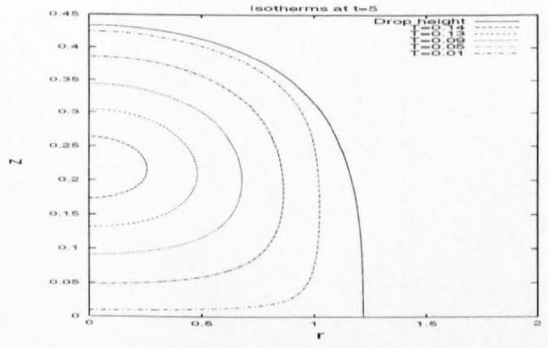

(c) Isotherms at $t = 5$.

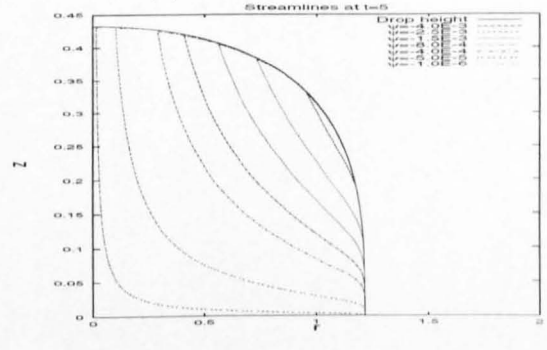

(d) Streamlines at $t = 5$

FIG. 3.26. Axisymmetric results: constant mass with $\alpha = 2$ and $\mathrm{Pe}_r = 10^2$.

As in the planar spreading results with constant mass, the log-log plots for $\alpha = 2$ show that for $\mathrm{Pe}_r = 10^6$ and $\mathrm{Pe}_r = 10^4$ they have similar spreading rates, and that for lower Pe_r the liquid tends to spread isothermally.

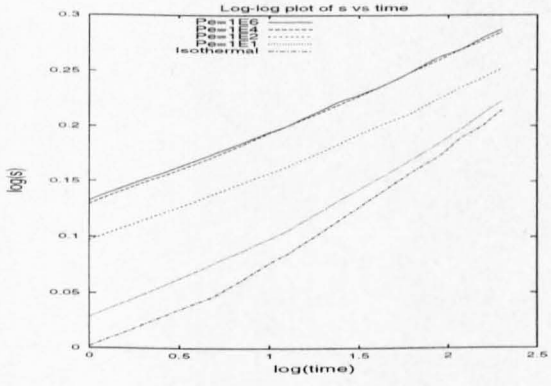

(a) Front location *vs* time.

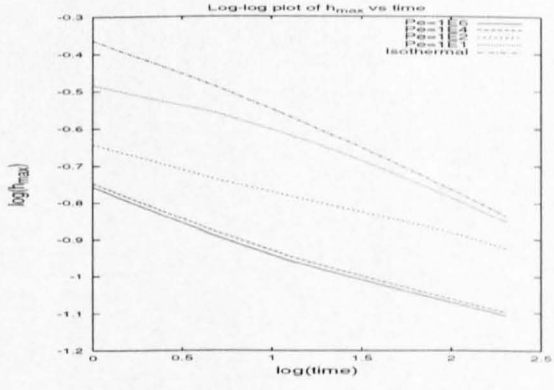

(b) h_{max} *vs* time.

FIG. 3.27. Log-log plots of front location and h_{max} *vs* time for $\alpha = 2$.

We finally consider the case when the coupling between the flow and temperature field is strengthened. For $\alpha = 2.6$ (the maximum value before numerics fail) and $\mathrm{Pe}_r = 10^4$, shown in Figure 3.28, the free surface profiles develop steeper flow fronts than for $\alpha = 2$. The isotherms and streamlines are similar to the corresponding results with $\alpha = 2$ in Figure 3.24.

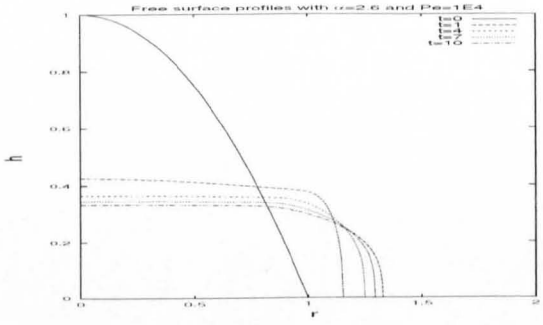

(a) Free surface profiles.

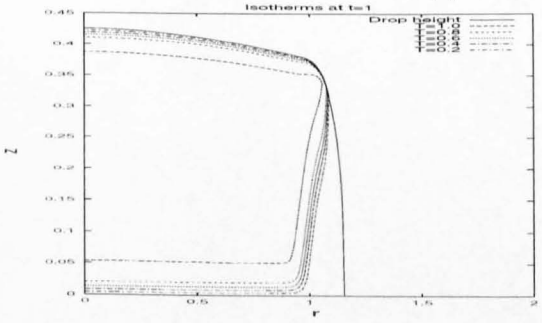

(b) Isotherms at $t = 1$.

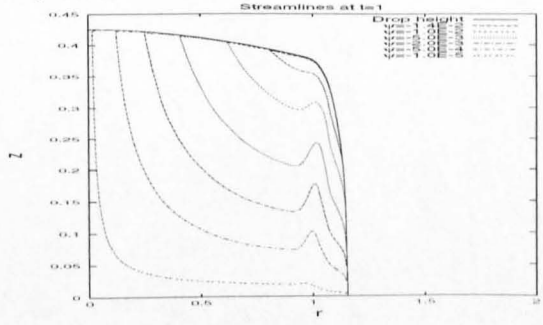

(c) Streamlines at $t = 1$.

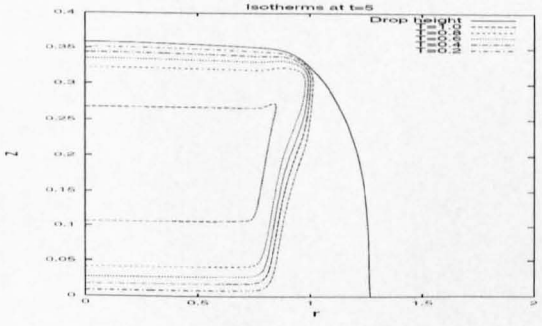

(d) Isotherms at $t = 5$.

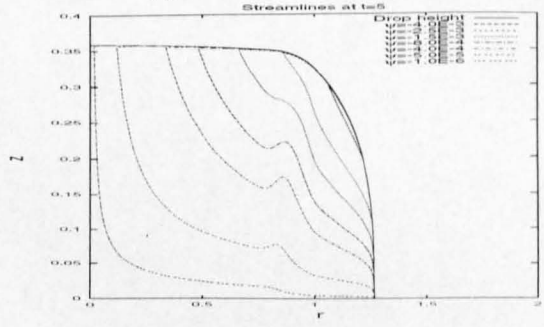

(e) Streamlines at $t = 5$

FIG. 3.28. Axisymmetric results: constant mass with $\alpha = 2.6$ and $\mathrm{Pe}_r = 10^4$.

The log-log plots for $\alpha = 2.6$ are similar to those for $\alpha = 2$ and are shown in Figure 3.29.

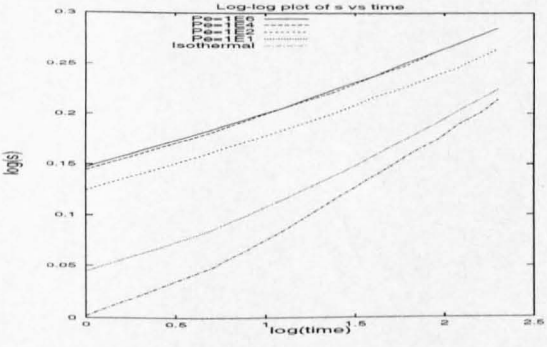

(a) Front location *vs* time.

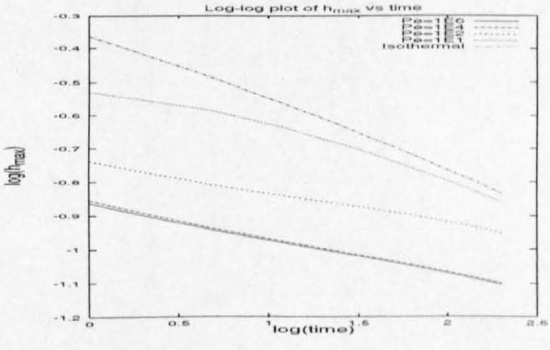

(b) h_{max} *vs* time.

FIG. 3.29. Log-log plots of front location and h_{max} *vs* time for $\alpha = 2$.

3.3.4. *Two-dimensional and axisymmetric results for constant mass and a heat source*

Introducing a constant heat source with $\dot{q} = 2500$, $\alpha = 2$ and $\mathrm{Pe}_r = 10^4$ in two dimensions leads to results shown in Figure 3.30. The isotherms show an increase in temperature, as expected. Note that the effective strength of the heat source is a combination of $\dot{q}$ and Pe_r, see (3.1.5) and hence the large value of $\dot{q}$. The isotherms are similar to the constant mass results with no heat source, but have a larger range of temperature. The free surface profiles exhibit a steep flow front followed by a plateau and, because of the heat source, the profiles do not tend to those of the isothermal case.

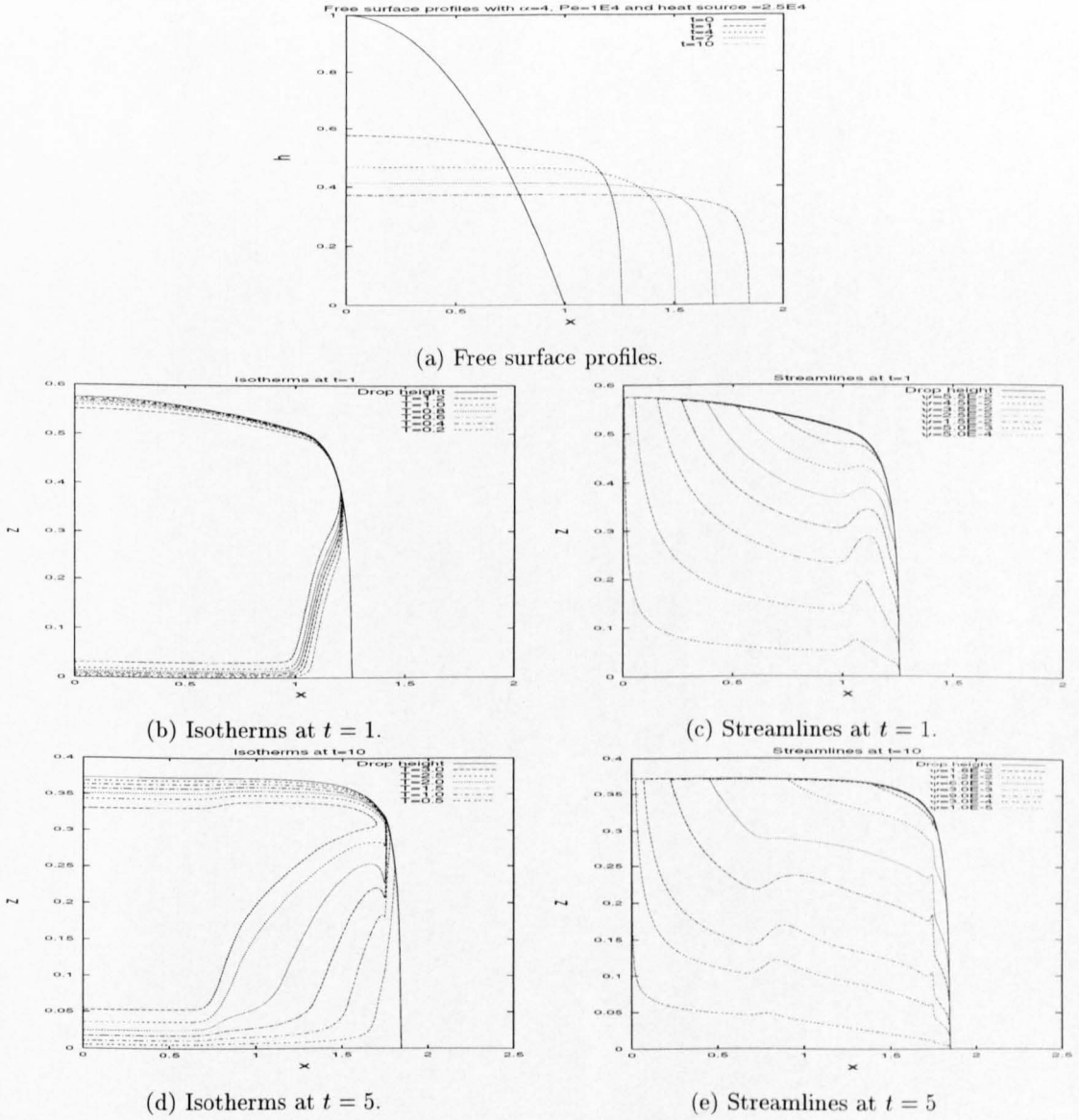

(a) Free surface profiles.

(b) Isotherms at $t = 1$.

(c) Streamlines at $t = 1$.

(d) Isotherms at $t = 5$.

(e) Streamlines at $t = 5$

FIG. 3.30. Two-dimensional results: constant mass with $\alpha = 2$, $\mathrm{Pe}_r = 10^4$ and $\dot{q} = 2500$.

Decreasing the strength of the heat source by setting $\mathrm{Pe} = 10^2$ and $\dot{q} = 25$ gives the results in Figure 3.31. Again the temperature isotherms are similar to the corresponding results with no

heat source and $\mathrm{Pe}_r = 10^2$ in Figure 3.7, albeit with a larger temperature range; the conduction term can be seen to be dominant.

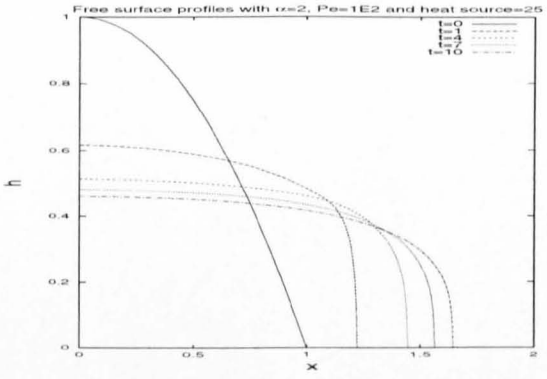

(a) Free surface profiles.

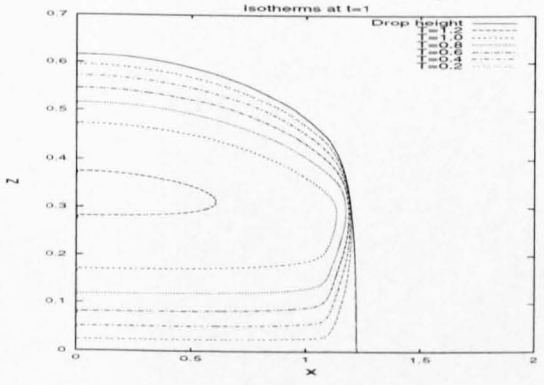

(b) Isotherms at $t = 1$.

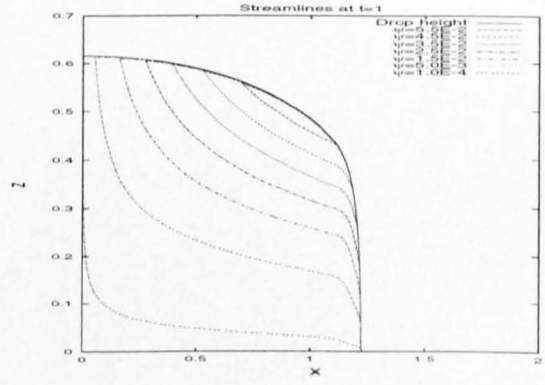

(c) Streamlines at $t = 1$.

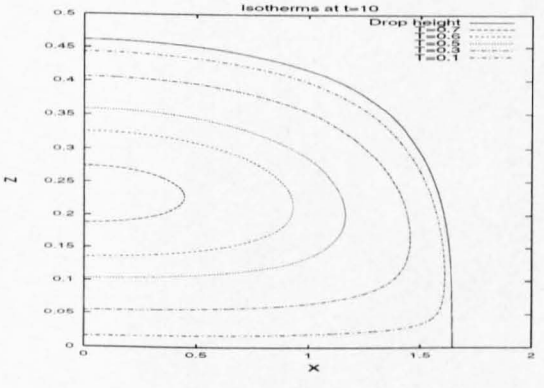

(d) Isotherms at $t = 5$.

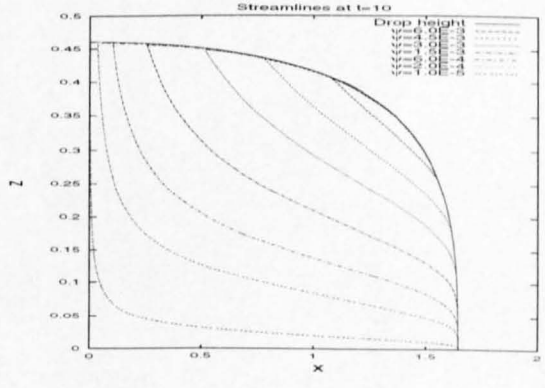

(e) Streamlines at $t = 5$

FIG. 3.31. Two-dimensional results: constant mass with $\alpha = 2$, $\mathrm{Pe}_r = 10^2$ and $\dot{q} = 25$.

Next we consider the axisymmetric case with $\mathrm{Pe}_r = 10^4$ and $\dot{q} = 2000$ in Figure 3.32. This gives similar results to the two-dimensional case in Figure 3.30, though the temperature values are lower due to the smaller value of $\dot{q}$ in the axisymmetric case.

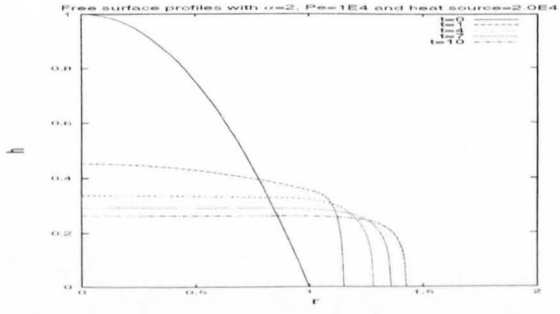

(a) Free surface profiles.

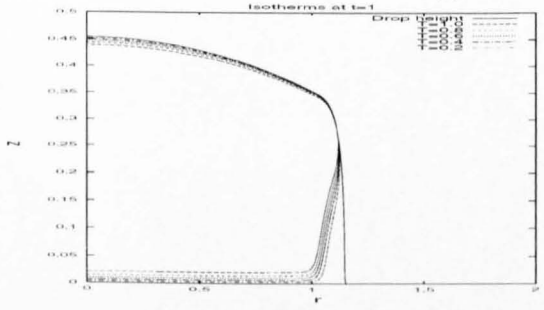

(b) Isotherms at $t = 1$.

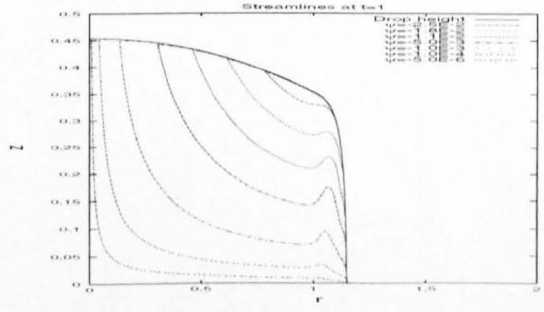

(c) Streamlines at $t = 1$.

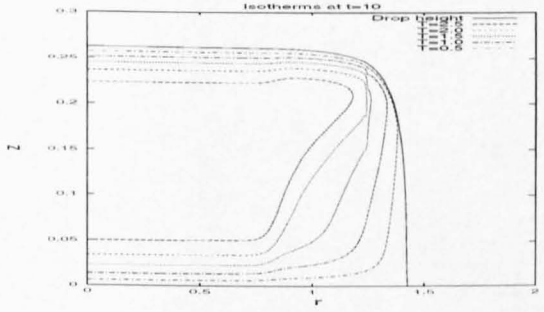

(d) Isotherms at $t = 5$.

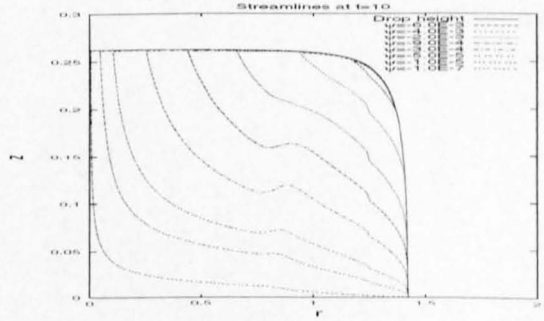

(e) Streamlines at $t = 5$

FIG. 3.32. Axisymmetric results: constant mass with $\alpha = 2$, $\mathrm{Pe}_r = 10^4$ and $\dot{q} = 2000$.

Similarly, in the axisymmetric geometry with $\mathrm{Pe}_r = 10^2$, $\dot{q} = 20$ and $\alpha = 2$ the results in Figures 3.33-3.34, show an increase in temperature when compared to the corresponding results with no heat source.

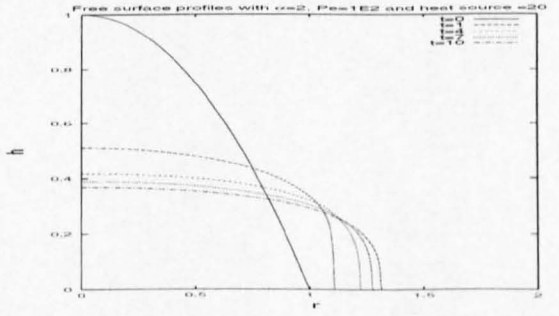

(a) Free surface profiles.

FIG. 3.33. Axisymmetric results: constant mass with $\alpha = 2$, $\mathrm{Pe}_r = 10^4$ and $\dot{q} = 20$.

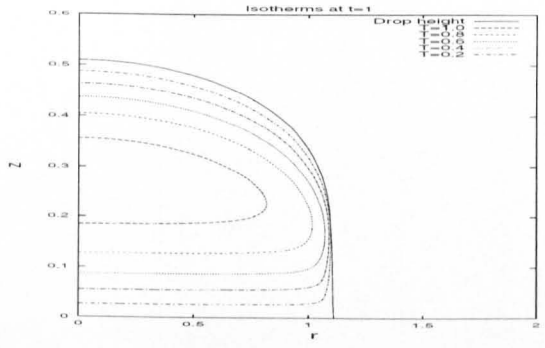

(a) Isotherms at $t = 1$.

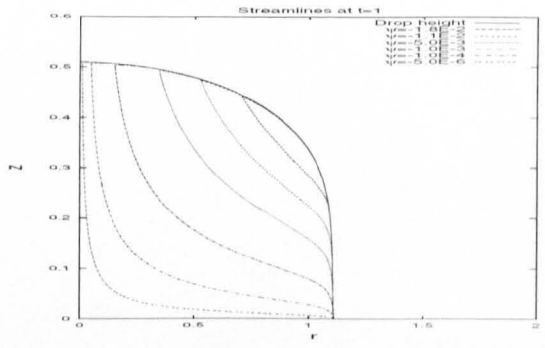

(b) Streamlines at $t = 1$.

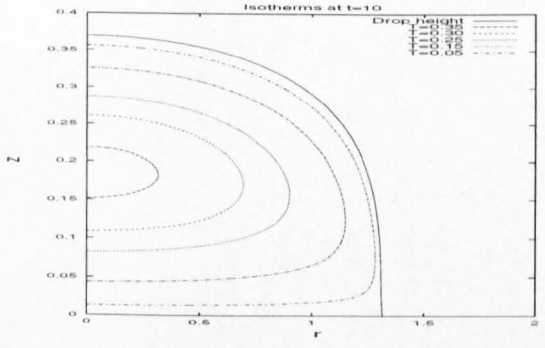

(c) Isotherms at $t = 5$.

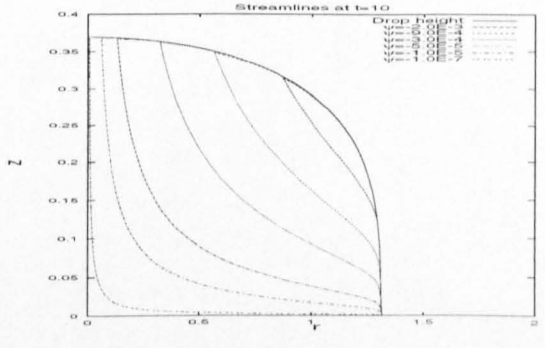

(d) Streamlines at $t = 5$

FIG. 3.34. Axisymmetric results: constant mass with $\alpha = 2$, $\mathrm{Pe}_r = 10^4$ and $\dot{q} = 20$.

3.4. Numerical results using bi-viscosity model

The following set of results consider the bi-viscosity relationship (3.1.10). First considering two-dimensional spreading with constant mass, $\mathrm{Pe}_r = 10^4$ and $a = 0.51$ (which implies a large viscosity contrast when the liquid cools) gives results shown in Figures 3.35-3.36. The discontinuity in the viscosity relationship is clearly seen to affect the streamlines, the change in viscosity occurring where $T_m = 5$. Note that the results are obtained using 600 mesh points in the horizontal direction over the range [0,2], 200 mesh points in the z-direction and with a time step (Δt) of 2.0×10^{-5}.

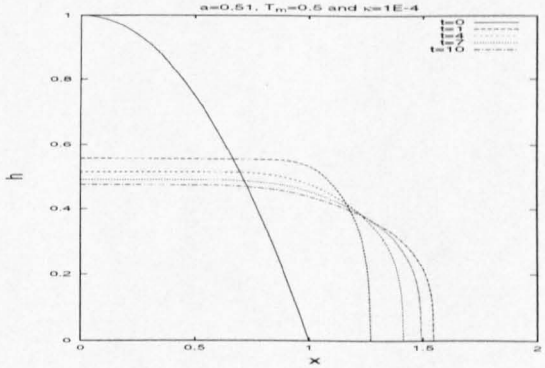

(a) Free surface profiles.

FIG. 3.35. Planar results: constant mass with $a = 0.51$, $T_m = 0.5$ $\mathrm{Pe}_r = 10^4$.

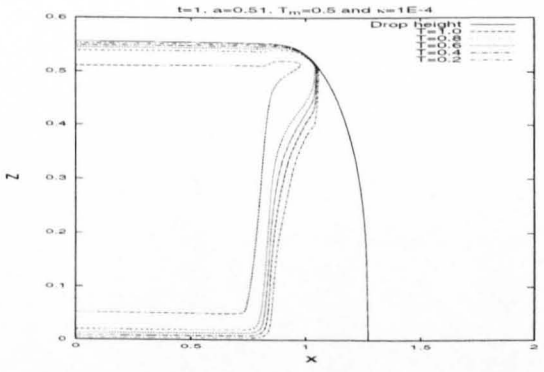

(a) Isotherms at $t = 1$.

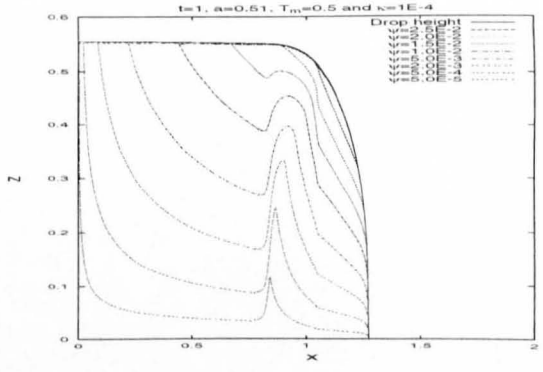

(b) Streamlines at $t = 1$.

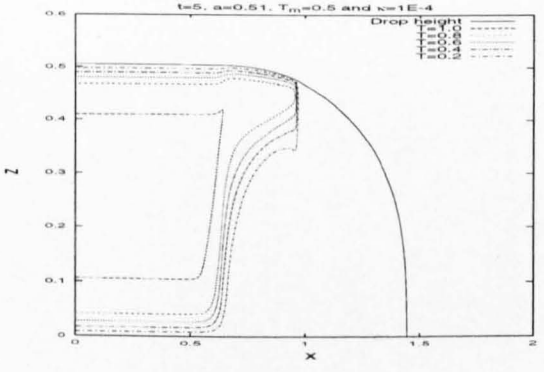

(c) Isotherms at $t = 5$.

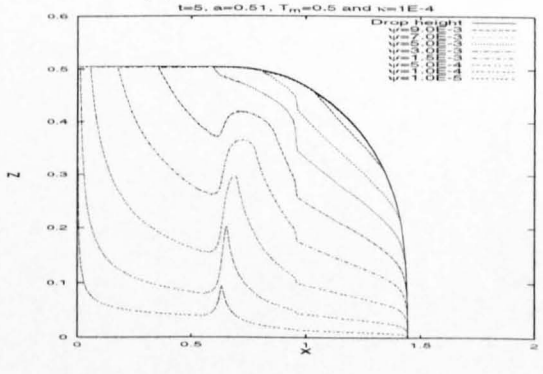

(d) Streamlines at $t = 5$

FIG. 3.36. Planar results: constant mass with $a = 0.51$, $T_m = 0.5$ $\mathrm{Pe}_r = 10^4$.

The streamlines in Figure 3.36(b) and 3.36(d) are restricted by an almost solid boundary produced by the very viscous cold region where $T < 0.5$. The restriction in the streamlines are also seen in the previous and next chapters for the bi-viscosity model.

Decreasing the viscosity contrast over the liquid by increasing a to 0.7 gives the results in Figures 3.37-3.38. The free surface profiles can be seen to spread as in the isothermal case, the temperature field having little effect on the spreading dynamics.

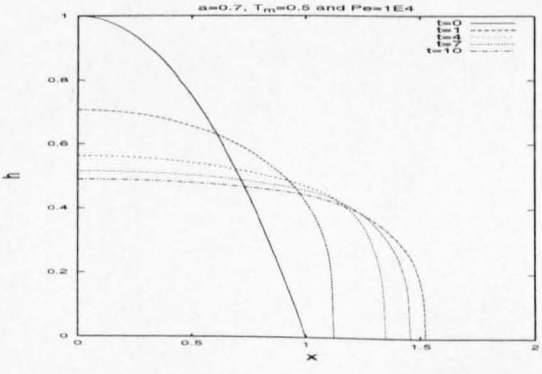

(a) Free surface profiles.

FIG. 3.37. Planar results: constant mass with $a = 0.7$, $T_m = 0.5$ $\mathrm{Pe}_r = 10^4$.

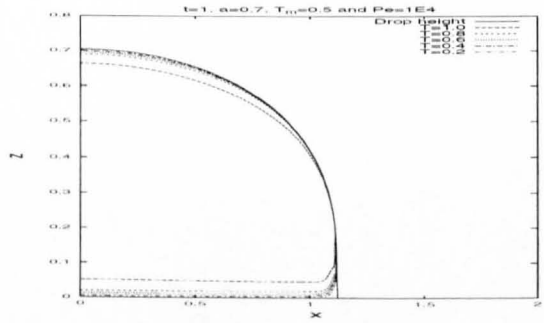

(a) Isotherms at $t = 1$.

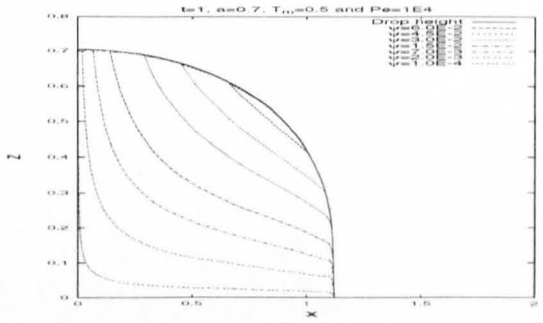

(b) Streamlines at $t = 1$.

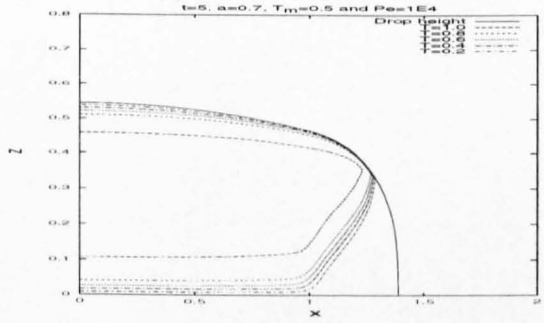

(c) Isotherms at $t = 5$.

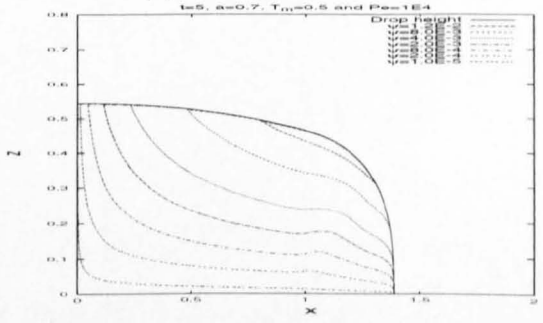

(d) Streamlines at $t = 5$

FIG. 3.38. Planar results: constant mass with $a = 0.7$, $T_m = 0.5$ $\mathrm{Pe}_r = 10^4$.

Similar results are seen in the axisymmetric geometry in Figure 3.39 with $a = 0.507$ and $\mathrm{Pe}_r = 10^6$ (for example).

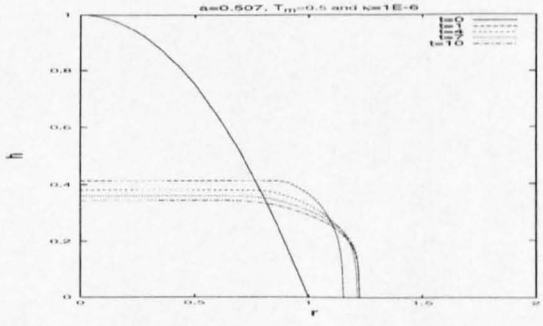

(a) Free surface profiles.

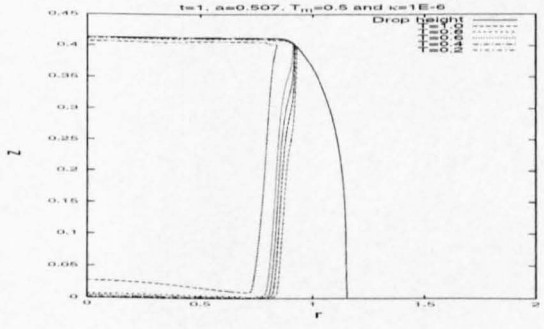

(b) Isotherms at $t = 1$.

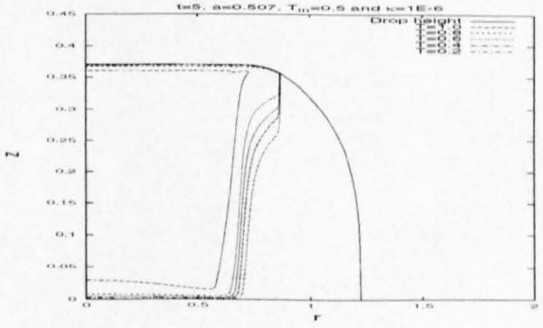

(c) Isotherms at $t = 5$.

FIG. 3.39. Axisymmetric results: constant mass with $a = 0.507$, $T_m = 0.5$, $\mathrm{Pe}_r = 10^6$.

3.5. Numerical validation

To validate the FORTRAN code which uses the above finite difference schemes, we test calculated free surface profiles against the ones calculated using the NAG routine D03PGF for the isothermal case. The first set of results in Figure 3.40 are for the planar spreading case with constant mass. The height profiles and streamlines show very good agreement.

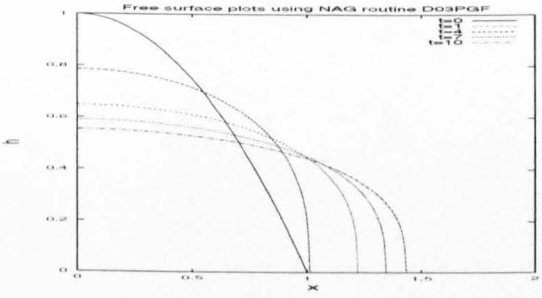

(a) Free surface profiles produced by NAG routine.

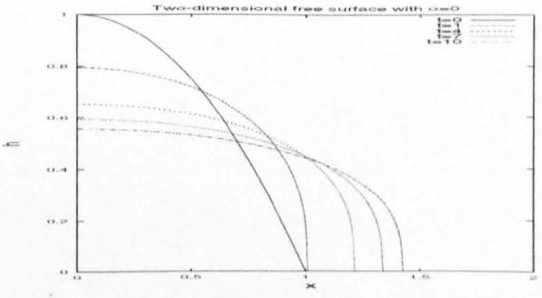

(b) Free surface profiles produced by the implicit scheme.

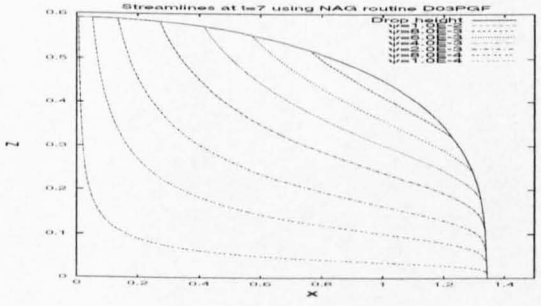

(c) Streamlines at $t = 7$ from NAG routine.

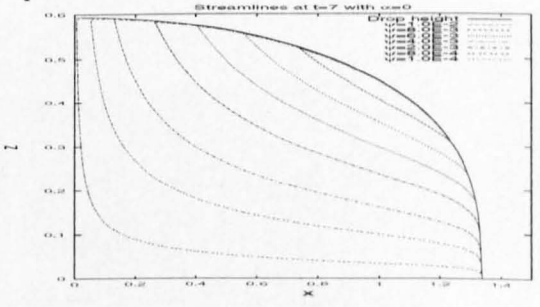

(d) Streamlines at $t = 7$ from implicit scheme..

FIG. 3.40. Two-dimensional results: NAG routine versus the implicit finite difference scheme.

The influx case for planar spreading is shown in Figures 3.41-3.42. The comparison between the two programs again shows good agreement, but is not as good as the constant mass case, because of the errors introduced by using Simpson's rule when evaluating the integral in the diffusion term at the influx boundary.

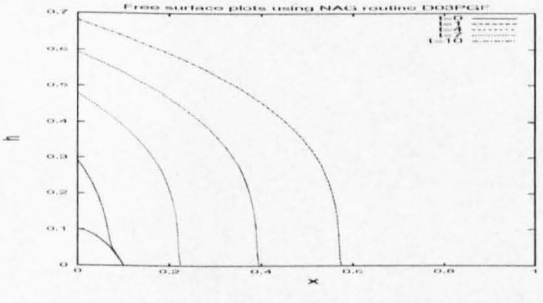

(a) Free surface profiles produced by NAG routine.

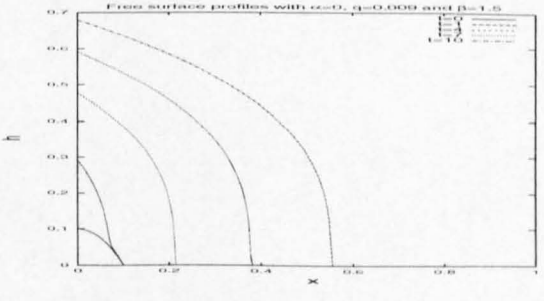

(b) Free surface profiles produced by the implicit scheme.

FIG. 3.41. Planar spreading from a line source: NAG routine versus the implicit finite difference scheme.

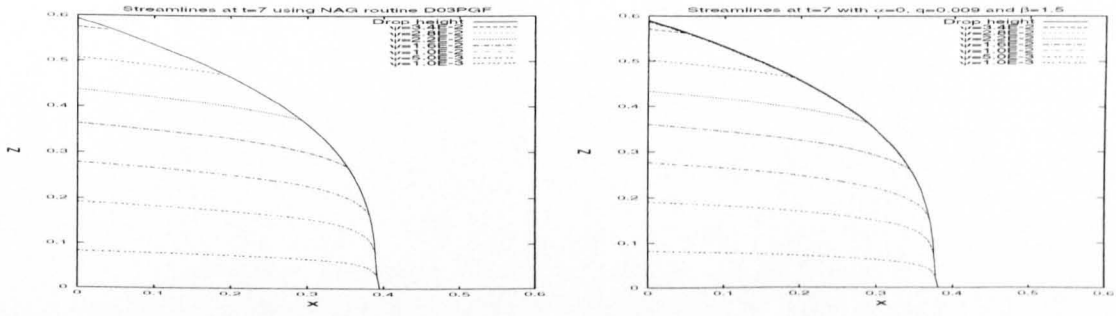

(a) Streamlines at $t = 7$ from NAG routine. (b) Streamlines at $t = 7$ from implicit scheme..

FIG. 3.42. Planar spreading from a line source: NAG routine versus the implicit finite difference scheme.

The axisymmetric profiles with constant mass show good agreement between the implicit finite difference schemes and the NAG routine D03PGF, see Figure 3.43.

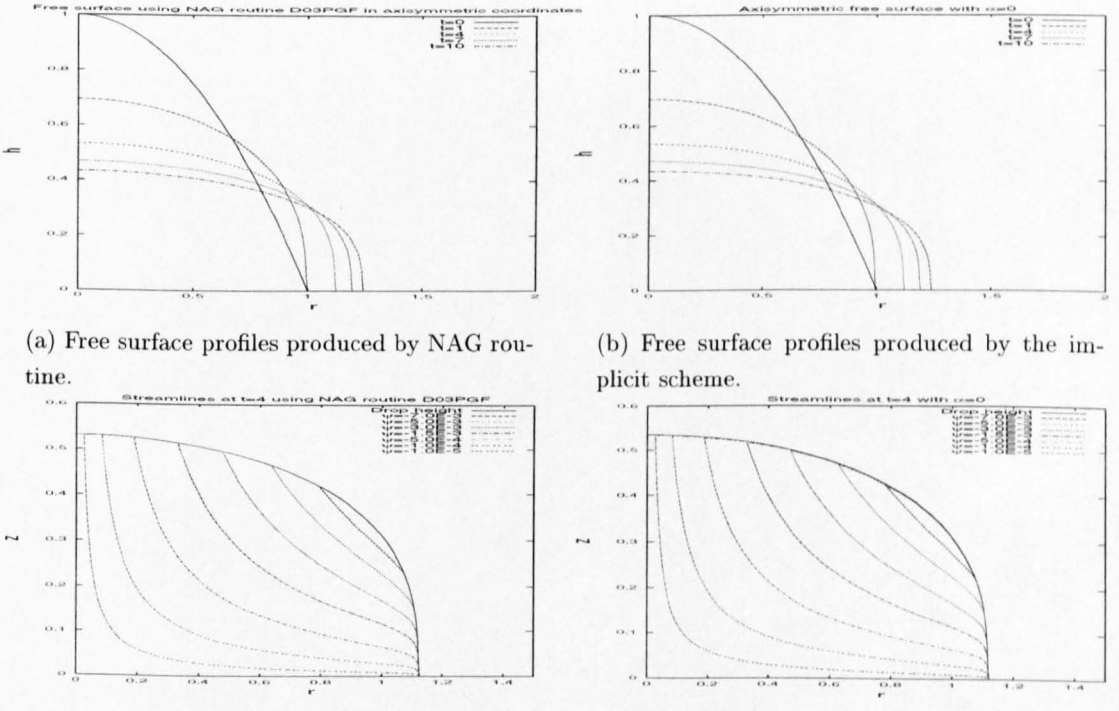

(a) Free surface profiles produced by NAG routine. (b) Free surface profiles produced by the implicit scheme.

(c) Streamlines at $t = 7$ from NAG routine. (d) Streamlines at $t = 7$ from implicit scheme..

FIG. 3.43. Axisymmetric results: NAG routine versus the implicit finite difference scheme.

Overall, the numerical results show good agreement between the NAG routine D03PGF and the above finite difference schemes for the isothermal case. The isothermal results also show good agreement with the relevant similarity solutions which gives good confidence in the finite difference schemes used to solve the problem set in this chapter.

The temperature profiles are shown to converge by mesh refinement in Figure 3.44. The following results are obtained using $\Delta t = 5 \times 10^{-4}$ with the range $[0, 2]$ in the x-direction and $[0, 1]$ in the z-direction. The isotherms in Figures 3.44(a)-(b) are shown for the constant mass case

in two-dimensions with $\mathrm{Pe}_r = 10^4$ and $\alpha = 2$. The isotherms in Figures 3.44(c)-(d) are shown for the constant mass case in two-dimensions with $\mathrm{Pe}_r = 10^2$ and $\alpha = 2$ in axisymmetric coordinates. The results in Figures 3.44(a) and 3.44(c) have 500 by 170 mesh points and in Figures 3.44(b) and 3.44(d) have 600 by 200 mesh points in the x and y-directions respectively.

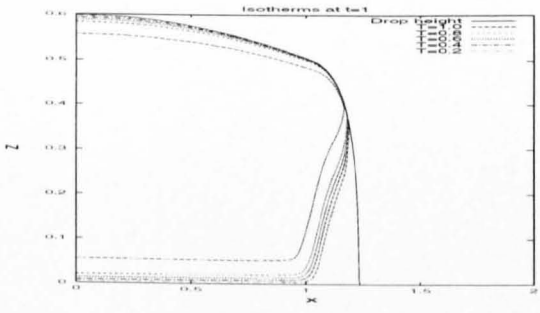

(a) Isotherms at $t = 1$ with 500 by 170 mesh points, $\mathrm{Pe}_r = 10^4$ and $\alpha = 2$.

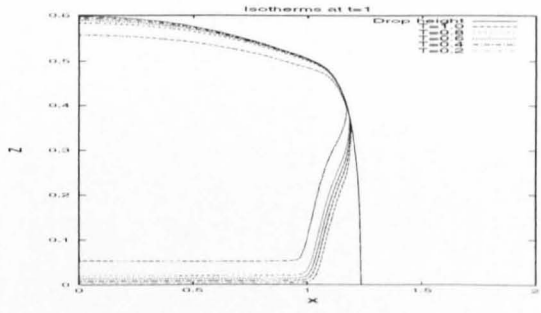

(b) Isotherms at $t = 1$ with 600 by 200 mesh points, $\mathrm{Pe}_r = 10^4$ and $\alpha = 2$.

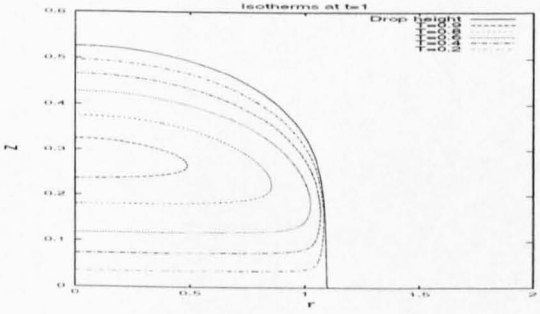

(c) Isotherms at $t = 1$ with 500 by 170 mesh points, $\mathrm{Pe}_r = 10^2$ and $\alpha = 2$.

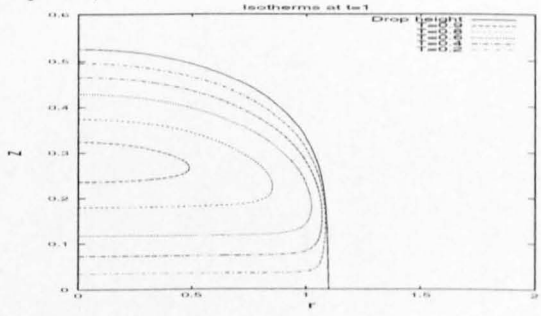

(d) Isotherms at $t = 1$ with 600 by 200 mesh points, $\mathrm{Pe}_r = 10^2$ and $\alpha = 2$.

FIG. 3.44. Mesh refinement results with 500 by 170 against 600 by 200 mesh points.

The streamlines for the influx model and the bi-viscoisty model, where there exists a large drop in temperature, show inaccuracies where the numerics cannot handle the rapid drop in viscosity as one would like. The overall behaviour is correct and the results can be slightly improved by using more mesh points, but would mean a larger run time.

3.6. Discussion

The results show that when there is little heat loss and a strong coupling between the velocity and temperature fields, the free surface profiles develop a steep flow front followed by a plateau. For later times or small Pe_r, the results tend to those of the isothermal case. The physical mechanism behind the steep front is the increase in viscosity near the flow front which retards the flow and the more mobile liquid spreads above.

The steep sided profile and plateau are also seen in experiments by Stasiuk *et al.* (1993) and in numerical results using a radially varying viscosity relationship by Bercovici (1994) (see Discussion in Chapter 4). The heat source model in Chapter 2 produced a plateau and steep

sides for very large α with the exponential viscosity law and shows qualitatively similar results for the heat source model in this chapter with $\mathrm{Pe}_r > O(10^4)$, but with a much smaller value of α than in Chapter 2.

Experimental results of Stasiuk *et al.* (1993), mentioned in the introduction, are discussed here. The development of the steep flow front followed by a plateau at times $t = 600$, 2000, and 6000 seconds is shown in Figure 3.45, as the syrup cools. The flow shape is said to satisfy

$$\frac{h}{h_0} = \left(1 - \frac{r}{r_N}\right)^{\gamma}, \tag{3.6.1}$$

where r is the radius, r_N is the radial extent of the flow at time t, h is the flow height at radius r, h_0 is the centre thickness and γ a fitting parameter. $\gamma = \frac{1}{3}$ gives the characteristic shape of the isothermal free surface as discussed by Huppert (1982b); the results show that as the syrup cools, then γ is seen to decrease and tends to a rectangular shaped profile. The isotherms illustrated in Figure 3.45(b) are seen to behave similarly to the numerical results from a line source, see Figures 3.17-3.20, with the isotherms being 'swept' back. The corresponding Peclet values for the numerical and experimental results which show the similar characteristic behaviour in the isotherms have $\mathrm{Pe}_r \leq 10^2$ (numerical) and $\mathrm{Pe} = 3.3 \times 10^2$ (experimental). Note that these Peclet numbers are not the same quantities, Pe_r being the reduced Peclet number. The experimental range for the reduced Peclet number is: $4.7 \leq \mathrm{Pe}_r \leq 10.7$ (note that ϵ changes with time for the experimental values), the results thus being consistent the numerical ones.

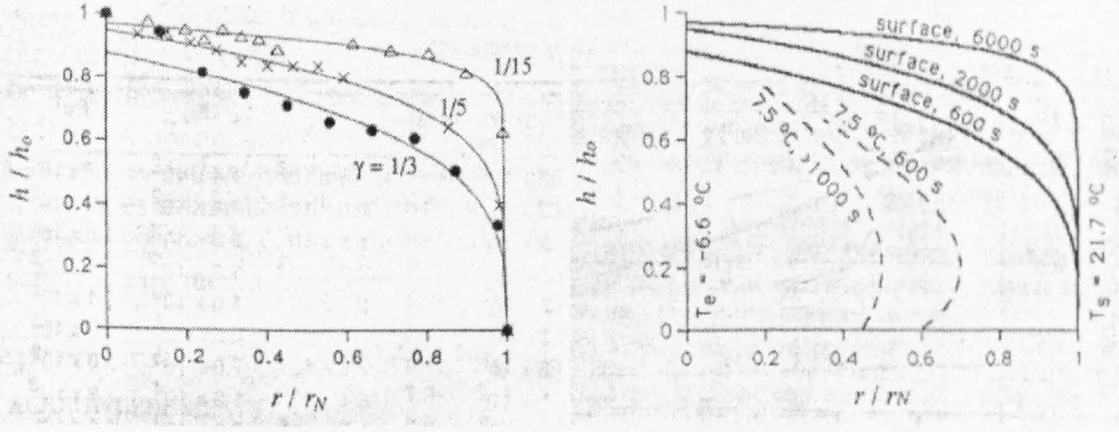

(a) Height profiles.

(b) Isotherms at times $t = 600$ and 1000 seconds.

FIG. 3.45. Experimental results with $\mathrm{Pe} = 3.3 \times 10^2$, $T_e = 21.7°$ C (eruption rate) and $T_s = -6.6°$ C (surface temperature).

CHAPTER FOUR

Temperature-dependent viscosity model with slow heat transfer through the boundaries

4.1. Introduction

In the previous two chapters the temperatures on the boundaries of the droplet have been assumed to be the same as the ambient gas and the substrate, as appropriate. In this chapter, this is not the case. The spreading of a fluid with temperature-dependent viscosity is again investigated, with the effects of Newton cooling on the drop's free surface and along the substrate now being considered. Similar boundary conditions on the free surface have been previously used in problems involving spreading fluids where the surface tension is temperature-dependent (see Ehrhard & Davis (1991), Oron *et al.* (1997) and Oron & Peles (1998); each of these took a fixed temperature value on the substrate, similar to the boundary condition in the previous chapter). A mixed boundary condition on the drop's free surface, as formulated below, and a Dirichlet boundary condition on the substrate is used by Braun *et al.* (1995) to model the spreading of a hot solder droplet.

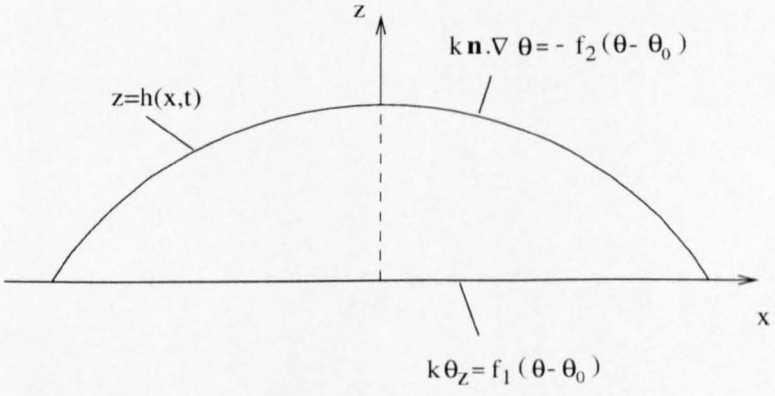

FIG. 4.1. Temperature boundary conditions

The fluid with initial temperature θ_i is again spreading on a smooth horizontal substrate; the ambient temperatures of the gas and the substrate are both taken to be θ_0, i.e. $\theta_a = \theta_s = \theta_0$ and Newton's law of cooling is considered. This states that the outward flux of heat on the boundary is proportional to the difference between the boundary temperature on the droplet's surface and the ambient temperature, as discussed in Farlow (1982). This gives

$$\text{the outward flux of heat through } z = 0 \text{ is } f_1(\theta)\,(\theta(x,0,t) - \theta_0)\,, \tag{4.1.1}$$

$$\text{the outward flux of heat through } z = h \text{ is } f_2(\theta)\,(\theta(x,h,t) - \theta_0)\,, \tag{4.1.2}$$

as indicated schematically in Figure 4.1. The variables $f_1(\theta)$ and $f_2(\theta)$ are heat-exchange coeffi-

cients and are (in general) functions of temperature; they give a measure of the heat flow across the boundaries per unit time per unit area and could include the effects of radiation, for example. In the previous chapters, the imposition of fixed boundary temperature values is equivalent to the assumption of very large heat-exchange coefficients. In the current problem the outward flux of heat on each boundary is positive, assuming that the temperature of the droplet is greater than the ambient temperature. Fourier's law states that the outward flux of heat across a boundary is proportional to the normal derivative of the temperature, so we have

$$k\frac{\partial\theta(x,0,t)}{\partial z} = f_1(\theta)\left(\theta(x,0,t)-\theta_0\right), \tag{4.1.3}$$

$$k\boldsymbol{n}.\boldsymbol{\nabla}\theta = -f_2(\theta)\left(\theta(x,h,t)-\theta_0\right) \quad \text{on } z=h(x,t), \tag{4.1.4}$$

where k is the thermal conductivity. The unit normal, $\boldsymbol{n}$, to the free surface is, from (2.1.21),

$$\boldsymbol{n} = \left(1+\left(\frac{\partial h}{\partial x}\right)^2\right)^{-\frac{1}{2}}\left(-\frac{\partial h}{\partial x},1\right), \tag{4.1.5}$$

so (4.1.4) is equivalent to

$$k\left(1+\left(\frac{\partial h}{\partial x}\right)^2\right)^{-\frac{1}{2}}\left(\frac{\partial\theta}{\partial z}-\frac{\partial h}{\partial x}\frac{\partial\theta}{\partial x}\right) = -f_2(\theta)\left(\theta(x,h,t)-\theta_0\right). \tag{4.1.6}$$

4.2. Two-dimensional formulation

The temperature equation is given by

$$\rho c\left(\frac{\partial\theta}{\partial t}+u\frac{\partial\theta}{\partial x}+w\frac{\partial\theta}{\partial z}\right) = k\left(\frac{\partial^2\theta}{\partial x^2}+\frac{\partial^2\theta}{\partial z^2}\right)+\dot{q}+2\mu e_{ij}^2, \tag{4.2.1}$$

$2\mu e_{ij}^2$ being the viscous dissipation term in which

$$e_{ij} = \frac{1}{2}\left(\frac{\partial u_i}{\partial x_j}+\frac{\partial u_j}{\partial x_i}\right). \tag{4.2.2}$$

This extra term is included to note the effects of viscous dissipation caused by shear. To derive the governing evolution equation for the temperature field in two dimensions, the corresponding temperature boundary conditions on the free surface and substrate ((4.1.3) and (4.1.6)) and the energy equation are non-dimensionalised using (2.1.5). This gives the temperature evolution equation as

$$\frac{\partial T}{\partial t}+u\frac{\partial T}{\partial x}+w\frac{\partial T}{\partial z} = \kappa\left(\epsilon^2\frac{\partial^2 T}{\partial x^2}+\frac{\partial^2 T}{\partial z^2}+\dot{q}+\mathrm{Br}\mu\left(\frac{\partial u}{\partial z}\right)^2\right), \tag{4.2.3}$$

see Appendix D, where κ^{-1} is the reduced Peclet number such that

$$\kappa = \frac{1}{\epsilon^2\mathrm{Pe}}, \qquad \epsilon = \frac{h_0}{l_0}\ \text{(aspect ratio)},$$

$\dot{q}$ is the rescaled heat source term, T is the temperature and Br is the Brinkman number defined by

$$\mathrm{Br} = \frac{U_0^2\mu_0}{k\Delta\theta}. \tag{4.2.4}$$

From (2.1.14) the Brinkman number is given by

$$\mathrm{Br} = \frac{\epsilon^2(\rho g)^2 h_0^4}{\mu_0 \Delta\theta}. \tag{4.2.5}$$

Viscous dissipation, which is usually negligible for thin films ($\epsilon^2 \ll 1$) is included here because the following asymptotic analysis includes terms of $O(\epsilon^2)$ in the energy equation, so effects of dissipation could influence the dynamics of the fluid. However, to simplify the following analysis, viscous dissipation is assumed negligible and is left for possible future work.

The non-dimensionalised boundary conditions on $z = 0$ and $z = h$ are, respectively,

$$\frac{\partial T}{\partial z} = \epsilon^2 g_1 T, \tag{4.2.6}$$

$$\frac{\partial T}{\partial z} - \epsilon^2 \frac{\partial h}{\partial x}\frac{\partial T}{\partial x} = -\epsilon^2 g_2 \left(1 + \epsilon^2 \left(\frac{\partial h}{\partial x}\right)^2\right)^{\frac{1}{2}} T, \tag{4.2.7}$$

where $\epsilon^2 g_1 = h_0 f_1(T)/k$ and $\epsilon^2 g_2 = h_0 f_2(T)/k$; $f_1(T)$ and $f_2(T)$ are assumed constant through out the following analysis. The asymptotic analysis which follows involves the canonical problem in which g_1, $g_2 = O(1)$ with $\kappa = O(\epsilon^{-2})$. We write $\gamma = \kappa\epsilon^2$. Note that $\gamma^{-1} = \mathrm{Pe} = O(1)$, so that this model is conduction dominated. Moreover we write $\dot{q} = \epsilon^2 \dot{Q}$ where $\dot{Q} = O(1)$.

Let

$$T \sim T_0(x, z, t) + \epsilon^2 T_1(x, z, t) \tag{4.2.8}$$

and substituting into (4.2.3) gives the leading order terms as

$$\frac{\partial^2 T_0}{\partial z^2} = 0. \tag{4.2.9}$$

Integrating gives

$$T_0 = A(x, t) + B(x, t)z \tag{4.2.10}$$

and the leading terms from the boundary condition at $z = 0$ imply that $\frac{\partial T_0}{\partial z} = 0$, hence $B(x, t)$ is equal to zero and T_0 is a function of x and t only. Thus the expansion (4.2.8) can be simplified to

$$T \sim T_0(x, t) + \epsilon^2 T_1(x, z, t). \tag{4.2.11}$$

Substituting the simplified perturbation expansion, (4.2.11), in (4.2.3) gives

$$\frac{\partial T_0}{\partial t} + u\frac{\partial T_0}{\partial x} = \gamma\left(\frac{\partial^2 T_1}{\partial z^2} + \frac{\partial^2 T_0}{\partial x^2} + \dot{Q}\right). \tag{4.2.12}$$

Similarly substituting the perturbation expansion into the boundary condition on the free surface gives

$$\frac{\partial T_1}{\partial z} = -g_2 T_0 + \frac{\partial h}{\partial x}\frac{\partial T_0}{\partial x}; \tag{4.2.13}$$

on $z = 0$ we have

$$\frac{\partial T_1}{\partial z} = g_1 T_0. \tag{4.2.14}$$

For brevity we shall suppress subscripts on u and h. Rearranging the temperature equation (4.2.12) such that

$$\frac{\partial^2 T_1}{\partial z^2} = \frac{1}{\gamma}\frac{\partial T_0}{\partial t} + \frac{1}{\gamma}u\frac{\partial T_0}{\partial x} - \frac{\partial^2 T_0}{\partial x^2} - \dot{Q} \tag{4.2.15}$$

and integrating with respect to z using (4.2.14) gives

$$\frac{\partial T_1}{\partial z} = \frac{1}{\gamma}\frac{\partial T_0}{\partial t}z + \frac{1}{\gamma}\int_0^z u dz' \frac{\partial T_0}{\partial x} - \frac{\partial^2 T_0}{\partial x^2}z - \dot{Q}z + g_1 T_0. \tag{4.2.16}$$

The horizontal velocity, from (2.1.37), simplifies to

$$\int_0^z u dz' = \frac{1}{\mu}\frac{\partial h}{\partial x}\int_0^z \left(\frac{(z')^2}{2} - z' h\right) dz', \tag{4.2.17}$$

$$= \frac{1}{\mu}\frac{\partial h}{\partial x}\left(\frac{z^3}{6} - \frac{z^2}{2}h\right). \tag{4.2.18}$$

Using the boundary condition (4.2.13) on $z = h$ then gives

$$\frac{\partial T_1}{\partial z} = \frac{h}{\gamma}\frac{\partial T_0}{\partial t} - \frac{h^3}{3\gamma\mu}\frac{\partial h}{\partial x}\frac{\partial T_0}{\partial x} - h\frac{\partial^2 T_0}{\partial x^2} - \dot{Q}h + g_1 T_0, \tag{4.2.19}$$

$$= -g_2 T_0 + \frac{\partial h}{\partial x}\frac{\partial T_0}{\partial x}. \tag{4.2.20}$$

Dropping the subscripts, the leading order temperature field is thus given by

$$\frac{\partial T}{\partial t} = \frac{(h^3 + 3\mu\gamma)}{3\mu h}\frac{\partial h}{\partial x}\frac{\partial T}{\partial x} + \gamma\frac{\partial^2 T}{\partial x^2} - \frac{\gamma}{h}(g_1 + g_2)T + \gamma\dot{Q}. \tag{4.2.21}$$

Since the temperature field is dependent on x and t only, the governing equations for the free surface, (2.1.43), simplifies to

$$\frac{\partial h}{\partial t} = \frac{1}{3}\frac{\partial}{\partial x}\left(\frac{h^3}{\mu(T)}\frac{\partial h}{\partial x}\right) \tag{4.2.22}$$

and the 'diffusivity' is given by

$$D(h) = \frac{h^3}{3\mu(T)}. \tag{4.2.23}$$

Using (4.2.22), equation (4.2.21) can be rewritten in the physically more transparent energy balance form

$$\frac{\partial(hT)}{\partial t} = \gamma\frac{\partial}{\partial x}\left(h\frac{\partial T}{\partial x}\right) + \frac{1}{3}\frac{\partial}{\partial x}\left(\frac{h^3 T}{\mu(T)}\frac{\partial h}{\partial x}\right) - \gamma(g_1 + g_2)T + h\gamma\dot{Q}. \tag{4.2.24}$$

The left-hand represents the rate of change of the total energy, the first term on the right-hand side temperature diffusion (which is dependent on the height profile in a cross section), the next term advection, where the mean horizontal velocity in the z-direction being

$$\bar{u} = -\frac{h^3}{3\mu}\frac{\partial h}{\partial x}, \tag{4.2.25}$$

the next term the heat loss across the boundaries and the last term the energy produced by the heat source.

The governing energy equation, (4.2.21) in two dimensions and (4.3.16) below in axisymmetric coordinates, is a special case of the three-dimensional case derived in Chapter 5. Similarly the

free surface equations (4.2.22) and (4.3.17) are special cases of the three-dimensional case derived in Chapter 5.

4.3. Axisymmetric formulation

The derivation of the governing temperature equation in axisymmetric coordinates follows in a similar fashion. The same boundary conditions on the substrate and free surface (x becomes r) apply; the major difference is the non-dimensionalised temperature evolution equation, from (2.1.56),

$$\frac{\partial T}{\partial t} + u\frac{\partial T}{\partial x} + w\frac{\partial T}{\partial z} = \kappa\left(\frac{\partial^2 T}{\partial z^2} + \frac{\epsilon^2}{r}\frac{\partial}{\partial r}\left(r\frac{\partial T}{\partial r}\right) + \dot{q}\right), \tag{4.3.1}$$

where κ^{-1} is the reduced Peclet number such that

$$\kappa = \frac{1}{\epsilon^2 \mathrm{Pe}}, \quad \epsilon = \frac{h_0}{l_0} \text{ (aspect ratio)},$$

$\dot{q}$ is the heat source and T is temperature. The non-dimensionalised boundary conditions on $z = 0$ and $z = h$ are, respectively,

$$\frac{\partial T}{\partial z} = \epsilon^2 g_1 T, \tag{4.3.2}$$

$$\frac{\partial T}{\partial z} - \epsilon^2 \frac{\partial h}{\partial r}\frac{\partial T}{\partial r} = -\epsilon^2 g_2 \left(1 + \epsilon^2\left(\frac{\partial h}{\partial r}\right)^2\right)^{\frac{1}{2}} T, \tag{4.3.3}$$

where $\epsilon^2 g_1 = h_0 f_1/k$ and $\epsilon^2 g_2 = h_0 f_2/k$. The asymptotic analysis which follows is as the two-dimensional case where g_1, $g_2 = O(1)$ and $\kappa = O(\epsilon^{-2})$. We again write $\gamma = \kappa\epsilon^2$ and $\dot{q} = \epsilon^2 \dot{Q}$ with $\dot{Q} = O(1)$.

Let

$$T \sim T_0(r, z, t) + \epsilon^2 T_1(r, z, t) \tag{4.3.4}$$

and substituting into (4.3.1) gives a similar leading order problem to that in the two-dimensional case,

$$\frac{\partial^2 T_0}{\partial z^2} = 0, \tag{4.3.5}$$

and the expansion (4.3.4) simplifies to

$$T \sim T_0(r, t) + \epsilon^2 T_1(r, z, t). \tag{4.3.6}$$

Substituting the simplified perturbation expansion, (4.3.6), in (4.3.1) gives

$$\frac{\partial T_0}{\partial t} + u\frac{\partial T_0}{\partial r} = \gamma\left(\frac{\partial^2 T_1}{\partial z^2} + \frac{1}{r}\frac{\partial}{\partial r}\left(r\frac{\partial T_0}{\partial r}\right) + \dot{Q}\right). \tag{4.3.7}$$

Similarly substituting into the boundary condition on the free surface gives

$$\frac{\partial T_1}{\partial z} = -g_2 T_0 + \frac{\partial h}{\partial r}\frac{\partial T_0}{\partial r}; \tag{4.3.8}$$

on $z = 0$ we have

$$\frac{\partial T_1}{\partial z} = g_1 T_0. \tag{4.3.9}$$

For brevity the subscripts on u and h are suppressed. Rearranging the temperature equation (4.3.7) such that

$$\frac{\partial^2 T_1}{\partial z^2} = \frac{1}{\gamma}\frac{\partial T_0}{\partial t} + \frac{1}{\gamma}u\frac{\partial T_0}{\partial r} - \frac{1}{r}\frac{\partial}{\partial r}\left(r\frac{\partial T_0}{\partial r}\right) - \dot{Q} \tag{4.3.10}$$

and integrating with respect to z using (4.3.9) gives

$$\frac{\partial T_1}{\partial z} = \frac{1}{\gamma}\frac{\partial T_0}{\partial t}z + \frac{1}{\gamma}\int_0^z u dz' \frac{\partial T_0}{\partial r} - \frac{1}{r}\frac{\partial}{\partial r}\left(r\frac{\partial T_0}{\partial r}\right)z - \dot{Q}z + g_1 T_0 \tag{4.3.11}$$

The horizontal velocity, from (2.1.63), simplifies to

$$\int_0^z u dz' = \frac{1}{\mu}\frac{\partial h}{\partial r}\int_0^z \left(\frac{(z')^2}{2} - z'h\right) dz', \tag{4.3.12}$$

$$= \frac{1}{\mu}\frac{\partial h}{\partial r}\left(\frac{z^3}{6} - \frac{z^2}{2}h\right). \tag{4.3.13}$$

Using the boundary condition (4.3.8) on $z = h$ then gives

$$\frac{\partial T_1}{\partial z} = \frac{h}{\gamma}\frac{\partial T_0}{\partial t} - \frac{h^3}{3\gamma\mu}\frac{\partial h}{\partial r}\frac{\partial T_0}{\partial r} - h\frac{1}{r}\frac{\partial}{\partial r}\left(r\frac{\partial T_0}{\partial r}\right) - \dot{Q}h + g_1 T_0, \tag{4.3.14}$$

$$= -g_2 T_0 + \frac{\partial h}{\partial r}\frac{\partial T_0}{\partial r}. \tag{4.3.15}$$

The leading order temperature equation, where the subscripts are dropped, is given by

$$\frac{\partial T}{\partial t} = \frac{(h^3 + 3\mu\gamma)}{3\mu h}\frac{\partial h}{\partial r}\frac{\partial T}{\partial r} + \frac{\gamma}{r}\frac{\partial T}{\partial r} + \gamma\frac{\partial^2 T}{\partial r^2} - \frac{\gamma}{h}(g_1 + g_2)T + \gamma\dot{Q}. \tag{4.3.16}$$

The temperature field is dependent on r and t only, so the governing equation, (2.1.66), for the height profile in axisymmetric coordinates simplifies to

$$\frac{\partial h}{\partial t} = \frac{1}{r}\frac{\partial}{\partial r}\left(rD\frac{\partial h}{\partial r}\right), \tag{4.3.17}$$

where the diffusivity is given by (4.2.23). Equations (4.3.16)-(4.3.17) imply (cf.(4.2.24))

$$\frac{\partial (hT)}{\partial t} = \frac{\gamma}{r}\frac{\partial}{\partial r}\left(rh\frac{\partial T}{\partial r}\right) + \frac{1}{3r}\frac{\partial}{\partial r}\left(\frac{rh^3 T}{\mu(T)}\frac{\partial h}{\partial r}\right) - \gamma(g_1 + g_2)T + h\gamma\dot{Q}. \tag{4.3.18}$$

4.4. Numerical methods

The governing equations for the temperature field, (4.2.21) in Cartesian coordinates and (4.3.16) in polar coordinates, and for the free surface profile, (4.2.22) and (4.3.17), are now solved numerically, the equations being coupled through the viscosity relationship

$$\mu = e^{-\alpha T}, \tag{4.4.1}$$

where α is a positive constant. Further results are also obtained using a step function for the viscosity relationship, as explained in section 4.6.

The initial condition for the height profile, at $t = 0$, is $h = (1 - x^2)_+ + 10^{-6}$, where a prewetting

film of thickness 10^{-6} has been included to avoid the difficulty of tracking a sharp flow front (note that in the axisymmetric case x becomes r). The initial temperature of the drop and the prewetting film is set to unity and horizontal symmetry is assumed at $x = 0$ (or radial symmetry at $r = 0$). This gives Neumann boundary conditions for the height profiles and temperature at $x = 0$ and $r = 0$. For the influx case a small initial mass is used to simplify the FORTRAN code with the prewetting film and has the form at $t = 0$, $h = 10(0.01 - x^2)_+ + 10^{-6}$ and the temperature at $x = 0$ is set to unity across the domain, with the influx temperature also always being unity. To close the temperature and free surface model, the boundary conditions imposed at the end of the numerical domain are

$$\text{at } x = L \quad \frac{\partial T}{\partial x} = \frac{\partial h}{\partial x} = 0, \tag{4.4.2}$$

where in practice we take L as the spatial range depicted in the numerical results below. The first of these corresponds to conservation of heat, whereby,

$$\text{as} \quad x \to \infty \quad h\frac{\partial T}{\partial x} \to 0. \tag{4.4.3}$$

The influx model is assumed to have a variable flux of fluid released at a rate $2\beta q_c t^{\beta-1}$ in the planar case, corresponding to a line source at $x = 0$. Assuming horizontal symmetry, the global continuity equation is

$$\int_0^{s(t)} h(x,t)dx = q_c t^{\beta}. \tag{4.4.4}$$

Differentiating (4.4.4) with respect to t and using the free surface equation (4.2.22), as derived in (2.1.48), gives the boundary condition at $x = 0$ as

$$\frac{\partial h}{\partial x} = -\frac{3\mu\beta q_c t^{\beta-1}}{h^3}, \tag{4.4.5}$$

where the viscosity, μ, is constant since the temperature is unity at $x = 0$.

The temperature field coupled to the free surface profile by the viscosity, μ, is calculated numerically using the finite difference scheme given in Section 4.4.1. The viscosity is evaluated at each nodal point in the x-direction over the fluid using the calculated temperature field and then the free surface profile is updated using the algorithm given in Section 4.4.3.

The finite difference schemes are nearly identical to the schemes used in Chapter 3 for the height profiles in two-dimensional coordinates (equation (3.2.2)), for the influx model in two-dimensional coordinates (equation (3.2.11)) and for axisymmetric coordinates (equation (3.2.13)). The major difference is the D term defined in (4.4.15) below. The modifications to the finite difference scheme are given for the two-dimensional case only, since the new time marching scheme for D is the same for both the line source and the axisymmetric algorithms given in Chapter 3.

4.4.1. *Temperature field in two-dimensional coordinates*

The temperature evolution equation, (4.2.21), can be written in the form

$$\frac{\partial T}{\partial t} + a\frac{\partial T}{\partial x} + b\frac{\partial^2 T}{\partial x^2} + cT = \gamma\dot{Q}, \tag{4.4.6}$$

where

$$a = -\frac{(h^3 + 3\mu\gamma)}{3\mu h}\frac{\partial h}{\partial x}, \quad b = -\gamma \quad \text{and} \quad c = \frac{\gamma}{h}(g_1 + g_2).$$

A suitable time marching scheme is the implicit Crank-Nicolson method, where $T((i-1)\Delta x, n\Delta t) = T_i^n$. Discretising equation (4.4.6) using upwinding (a always being greater than zero in view of symmetry about $x = 0$), gives

$$\left(-\frac{a_i^n \Delta t}{2\Delta x} + \frac{b\Delta t}{2\Delta x^2}\right) T_{i-1}^{n+1} + \left(1 + \frac{a_i^n \Delta t}{2\Delta x} - \frac{b\Delta t}{\Delta x^2} + \frac{c_i^n \Delta t}{2}\right) T_i^{n+1} + \frac{b\Delta t}{2\Delta x^2} T_{i+1}^{n+1} = d_i^n, \quad (4.4.7)$$

where

$$d_i^n = \left(\frac{a_i^n \Delta t}{2\Delta x} - \frac{b\Delta t}{2\Delta x^2}\right) T_{i-1}^n + \left(1 - \frac{a_i^n \Delta t}{2\Delta x} + \frac{b\Delta t}{\Delta x^2} - \frac{c_i^n \Delta t}{2}\right) T_i^n - \frac{b\Delta t}{2\Delta x^2} T_{i+1}^n + \gamma \dot{Q} \Delta t,$$

$$a_i^n = -\frac{((h_i^n)^3 + 3\mu_i^n \gamma)}{3\mu_i^n h_i^n} \frac{h_{i+1}^n - h_{i-1}^n}{2\Delta x} \quad \text{and} \quad c_i^n = \frac{\gamma}{h_i^n}(g_1 + g_2).$$

The boundary condition at $i = 1$ for constant mass is as stated earlier, (4.4.2), so that $T_0 = T_2$ and gives

$$\left(1 + \frac{a_1^n \Delta t}{2\Delta x} - \frac{b\Delta t}{\Delta x^2} + \frac{c_1^n \Delta t}{2}\right) T_1^{n+1} + \left(-\frac{a_1^n \Delta t}{2\Delta x} + \frac{b\Delta t}{\Delta x^2}\right) T_2^{n+1} = d_1^n, \quad (4.4.8)$$

where

$$d_1^n = \left(1 - \frac{a_1^n \Delta t}{2\Delta x} + \frac{b\Delta t}{\Delta x^2} - \frac{c_1^n \Delta t}{2}\right) T_1^n + \left(\frac{a_1^n \Delta t}{2\Delta x} - \frac{b\Delta t}{\Delta x^2}\right) T_2^n + \gamma \dot{Q} \Delta t,$$

$$a_1^n = 0 \quad \text{and} \quad c_1^n = \frac{\gamma}{h_1^n}(g_1 + g_2).$$

For the injection boundary condition, the initial temperature at $x = 0$ is unity which changes the finite difference scheme to

$$T_1^{n+1} = d_1^n, \quad (4.4.9)$$

where d_1^n is set to unity.

4.4.2. *Temperature field in polar coordinates*

The temperature evolution equation, (4.3.16), can be written as

$$\frac{\partial T}{\partial t} + a\frac{\partial T}{\partial r} + b\frac{\partial^2 T}{\partial r^2} + cT = \gamma \dot{Q}, \quad (4.4.10)$$

where

$$a = -\frac{(h^3 + 3\mu\gamma)}{3\mu h}\frac{\partial h}{\partial r} - \frac{\gamma}{r}, \quad b = -\gamma \quad \text{and} \quad c = \frac{\gamma}{h}(g_1 + g_2).$$

Using the implicit Crank-Nicolson method, where $T((i-1)\Delta r, n\Delta t) = T_i^n$, and discretising equation (4.4.6) using upwinding gives

$$\left(-\frac{a_i^n \Delta t}{2\Delta r} + \frac{b\Delta t}{2\Delta r^2}\right) T_{i-1}^{n+1} + \left(1 + \frac{a_i^n \Delta t}{2\Delta r} - \frac{b\Delta t}{\Delta r^2} + \frac{c_i^n \Delta t}{2}\right) T_i^{n+1} + \frac{b\Delta t}{2\Delta r^2} T_{i+1}^{n+1} = d_i^n, \quad (4.4.11)$$

where

$$d_i^n = \left(\frac{a_i^n \Delta t}{2\Delta r} - \frac{b\Delta t}{2\Delta r^2}\right) T_{i-1}^n + \left(1 - \frac{a_i^n \Delta t}{2\Delta r} + \frac{b\Delta t}{\Delta r^2} - \frac{c_i^n \Delta t}{2}\right) T_i^n - \frac{b\Delta t}{2\Delta r^2} T_{i+1}^n + \gamma \dot{Q} \Delta t,$$

$$a_i^n = -\frac{((h_i^n)^3 + 3\mu_i^n \gamma)}{3\mu_i^n h_i^n} \frac{h_{i+1} - h_{i-1}}{2\Delta r} - \frac{\gamma}{(i-1)\Delta r} \quad \text{and} \quad c_i^n = \frac{\gamma}{h_i^n}(g_1 + g_2).$$

The boundary condition at $i = 1$ for the constant mass case from (4.4.2) gives $T_0 = T_2$, and using l'Hopital's rule with

$$a = -\frac{(h^3 + 3\mu\gamma)}{3\mu h} \frac{\partial h}{\partial r}, \quad b = -2\gamma \quad \text{and} \quad c = \frac{\gamma}{h}(g_1 + g_2),$$

gives

$$\left(1 + \frac{a_1^n \Delta t}{2\Delta r} - \frac{b\Delta t}{\Delta r^2} + \frac{c_1^n \Delta t}{2}\right) T_1^{n+1} + \left(-\frac{a_1^n \Delta t}{2\Delta r} + \frac{b\Delta t}{\Delta r^2}\right) T_2^{n+1} = d_1^n, \tag{4.4.12}$$

where

$$d_1^n = \left(1 - \frac{a_1^n \Delta t}{2\Delta r} + \frac{b\Delta t}{\Delta r^2} - \frac{c_1^n \Delta t}{2}\right) T_1^n + \left(\frac{a_1^n \Delta t}{2\Delta r} - \frac{b\Delta t}{\Delta r^2}\right) T_2^n + \gamma \dot{Q} \Delta t,$$

$$a_1^n = 0 \quad \text{and} \quad c_1^n = \frac{\gamma}{h_1^n}(g_1 + g_2).$$

The numerical schemes (4.4.7) and (4.4.11) have truncation errors $O(\Delta t)$ in time and $O(\Delta x)$ in space. The principal part of the truncation error is

$$\left(c\Delta t \frac{\partial T}{\partial t} + a\frac{\Delta x}{2}\frac{\partial^2 T}{\partial x^2} + a\frac{\Delta t}{2}\frac{\partial^2 T}{\partial x \partial t} + \frac{\Delta t}{2}\frac{\partial^2 T}{\partial t^2}\right)\Bigg|_i^n. \tag{4.4.13}$$

4.4.3. *Two-dimensional numerical scheme for the free surface with constant mass*

The drop height evolution equation (4.2.22) in Cartesian coordinates can be written as

$$\frac{\partial h}{\partial t} = \frac{\partial}{\partial x}\left(D\frac{\partial h}{\partial x}\right), \tag{4.4.14}$$

where

$$D = \frac{h^3}{3\mu(x,t)}. \tag{4.4.15}$$

Discretising (4.4.14) (using the notation $h_i^n = h((i-1)\Delta x, n\Delta t)$) by the Crank-Nicolson implicit finite difference scheme gives,

$$-r_x D_{i-\frac{1}{2}}^{n+1} h_{i-1}^{n+1} + (1 + r_x D_{i+\frac{1}{2}}^{n+1} + r_x D_{i-\frac{1}{2}}^{n+1}) h_i^{n+1} - r_x D_{i+\frac{1}{2}}^{n+1} h_{i+1}^{n+1} = d_i^n, \tag{4.4.16}$$

where

$$d_i^n = r_x D_{i-\frac{1}{2}}^n h_{i-1}^n + (1 - r_x D_{i+\frac{1}{2}}^n - r_x D_{i-\frac{1}{2}}^n) h_i^n + r_x D_{i+\frac{1}{2}}^n h_{i+1}^n,$$

$$r_x = \frac{\Delta t}{2\Delta x^2}, \quad D_{i+\frac{1}{2}} = \frac{D_{i+1} + D_i}{2} \quad \text{and} \quad D_{i-\frac{1}{2}} = \frac{D_i - D_{i-1}}{2}.$$

The above implicit scheme is solved using the Thomas algorithm to invert the tri-diagonal matrix, as explained in Morton & Mayers (1994). The time marched term, D_i^{n+1}, is found by

differentiating D with respect to time.

$$\frac{\partial D}{\partial t} = \frac{3\mu h^2 h_t - h^3 \mu_t}{3\mu^2} \tag{4.4.17}$$

Discretising explicitly gives

$$D_i^{n+1} = D_i^n + \Delta t \frac{3\mu_i^n (h^2)_i^n (h_t)_i^n - (h^3)_i^n (\mu_t)_i^n}{3(\mu^2)_i^n}, \tag{4.4.18}$$

where $(h_t)_i^n$ is discretised using (4.4.14) to give

$$(h_t)_i^n = \frac{1}{2\Delta x^2}\left[(h_{i+1}^n - h_i^n)(D_{i+1}^n + D_i^n) - (h_i^n - h_{i-1}^n)(D_i^n + D_{i-1}^n)\right], \tag{4.4.19}$$

$$= 2(d_i^n - h_i^n)/\Delta t. \tag{4.4.20}$$

The quantity d_i^n is defined in (4.4.16) and $(\mu_t)_i^n$ is found by using the backwards time marching scheme

$$(\mu_t)_i^n \approx \frac{\mu_i^n - \mu_i^{n-1}}{\Delta t}.$$

For the first spatial step in the numerical scheme, at $i = 1$, symmetry of the drop is used, implying $h_0 = h_2$ and $D_0 = D_2$. The half drop width, s, is found by calculating the number of nodes where the drop height is larger than a small tolerance value (10^{-5}). The temperature profiles are truncated at this point when plotting the temperature profiles seen in the numerical results.

4.4.4. *Streamlines*

To help interpret the behaviour of the spreading viscous fluid, a stream function is used, as discussed in Chapter 2. In the Cartesian two-dimensional case, ψ is calculated from the horizontal velocity, u, as derived in equation (2.1.37) which here simplifies to

$$u = \frac{z}{\mu(T)}\left(\frac{z}{2} - h(x,t)\right)\frac{\partial h(x,t)}{\partial x}. \tag{4.4.21}$$

Hence equation (2.1.29), the relationship between the horizontal velocity and stream function, gives

$$\psi = \frac{z^2}{2\mu(T)}\left(\frac{z}{3} - h(x,t)\right)\frac{\partial h(x,t)}{\partial x}. \tag{4.4.22}$$

Similarly, in the axisymmetric geometry the Stokes stream function is given from equation (2.1.62) by

$$\Psi = -r\frac{z^2}{2\mu(T)}\left(\frac{z}{3} - h(r,t)\right)\frac{\partial h(r,t)}{\partial r}. \tag{4.4.23}$$

Note that the horizontal velocity component is identical in two-dimensional and axisymmetric coordinates (though x becomes r) and in all the following results the vertical space is set with 200 mesh points.

4.5. Numerical results using the exponential viscosity relationship

4.5.1. *Two-dimensional results with constant mass*

The first set of results (in Figure 4.2) show the constant viscosity case, $\alpha = 0$, for a fixed mass of fluid spreading on the horizontal substrate over the time range $0 \leq t \leq 30$ with $\Delta t = 10^{-4}$. The case $\alpha = 0$ is equivalent to the fluid being at zero temperature. The numerical results show good agreement (to four decimal places) between the NAG routine D03PGF, and the finite difference scheme described in Appendix B, over the range $0 \leq x \leq 3$ (with for 600 mesh points in both schemes) and establishes high confidence in the numerical method described above. The height profiles can be seen to have the expected lens shape profiles.

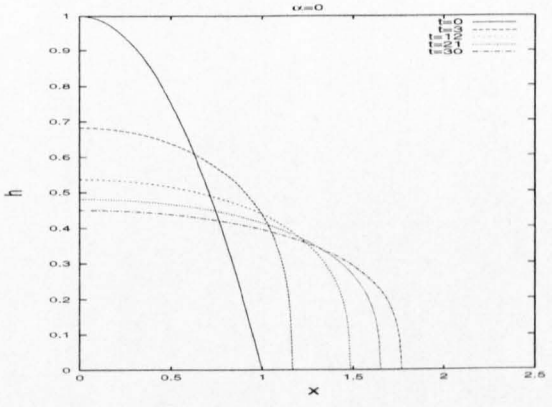

(a) Free surface profiles.

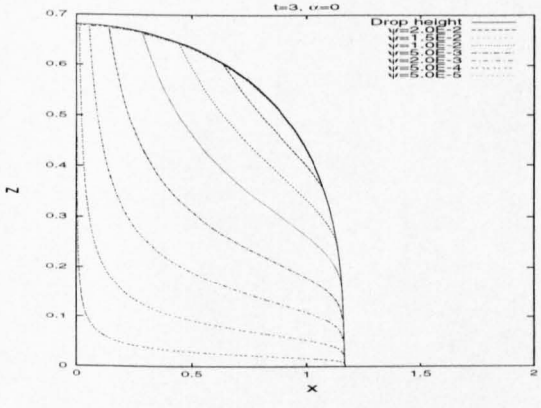

(b) Streamlines at $t = 3$.

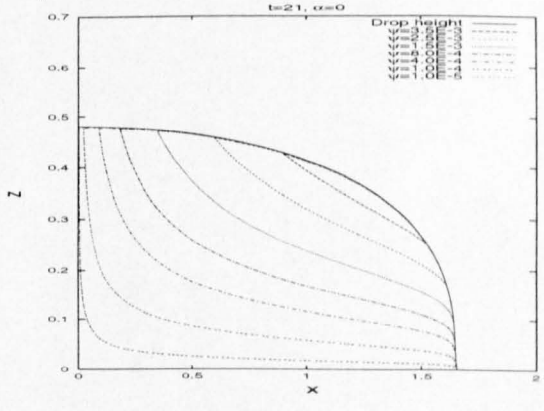

(c) Streamlines at $t = 21$.

FIG. 4.2. Two-dimensional results: isothermal and constant mass.

The first set of variable viscosity results with $\mathrm{Pe} = 10^8$ and $\alpha = 2$ are shown in Figure 4.3 for the same time range, mesh spacing and time step as the isothermal results (the same time step and mesh spacing are used in the following results, unless stated otherwise). The large value of the Peclet number implies that there is little heat loss, with the majority of the fluid being near the initial temperature of unity, as seen in Figure 4.3(b). The corresponding profiles are seen to spread isothermally, although a small amount of heat loss is seen near the flow front. The streamlines in Figures 4.3(c)-4.3(d) show little effect from the temperature field.

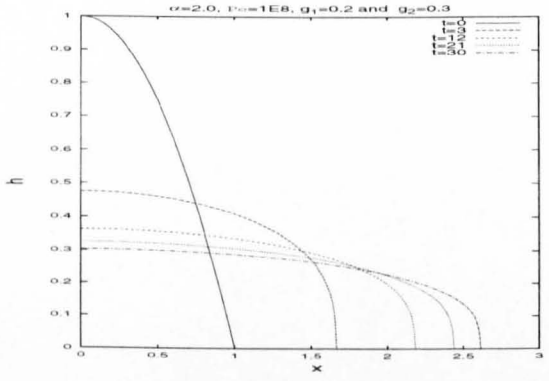

(a) Free surface profiles.

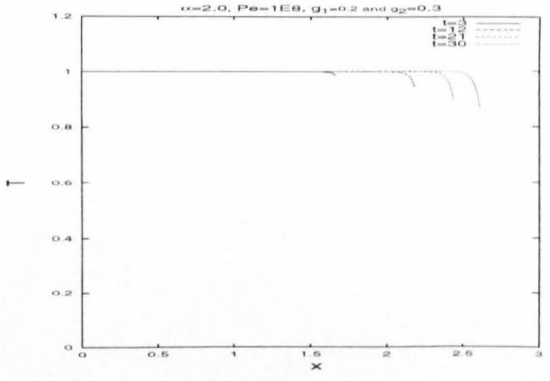

(b) Temperature profiles.

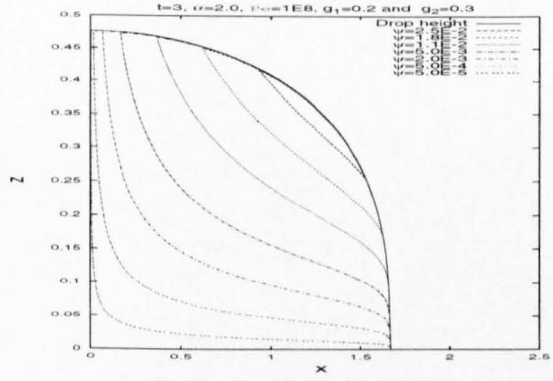

(c) Streamlines at $t = 3$.

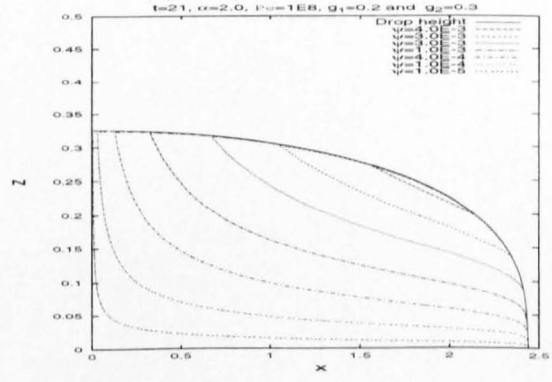

(d) Streamlines at $t = 21$.

FIG. 4.3. Two-dimensional results with constant mass, $\alpha = 2$ and $\mathrm{Pe} = 10^8$.

Decreasing the Peclet number to $\mathrm{Pe} = 10^7$ with $\alpha = 2$ gives the results in Figure 4.4. The results show that the liquid has retarded to a greater extent over the same time range for the results in Figure 4.3 with $\mathrm{Pe} = 10^8$. This is due to the greater heat loss near the flow front seen in Figure 4.4(b) causing an increase in viscosity there.

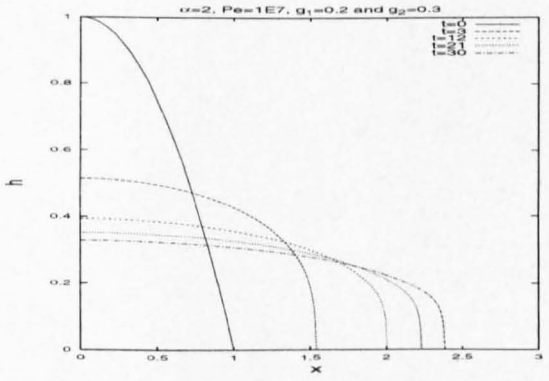

(a) Free surface profiles.

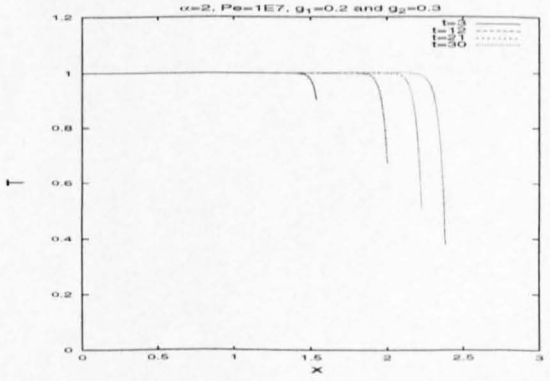

(b) Temperature profiles.

FIG. 4.4. Two-dimensional results with constant mass, $\alpha = 2$ and $\mathrm{Pe} = 10^7$.

The next set of results with variable viscosity are illustrated in Figure 4.5. The height profiles are seen to develop steep flow fronts with $\alpha = 2$ and $\mathrm{Pe} = 10^6$. Large Peclet number implies that the thermal diffusivity in the model is small and that there is still little heat loss, as seen in the

temperature profiles. Near the flow front, there is more heat loss due to the fluid being thinner in this region. The streamlines show no noticeable effects of the temperature field. The steep profiles are most noticeable in the Peclet number range $10^5 < \mathrm{Pe} < 10^7$, caused by the heat loss near the contact line.

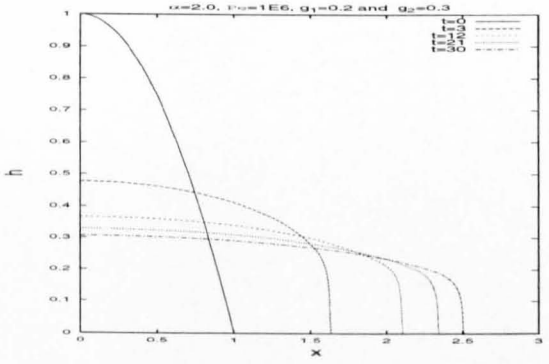

(a) Free surface profiles.

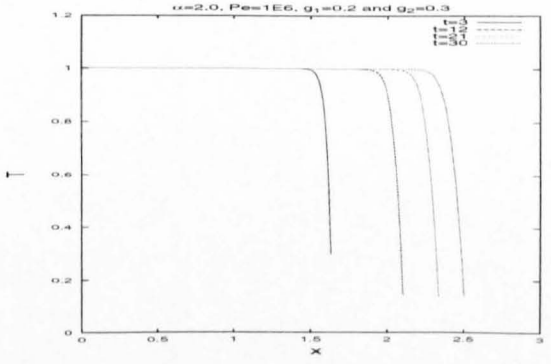

(b) Temperature profiles.

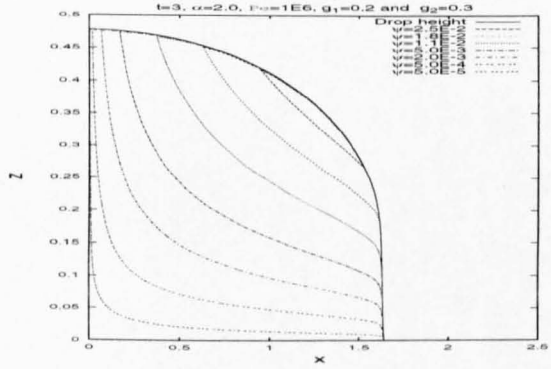

(c) Streamlines at $t = 3$.

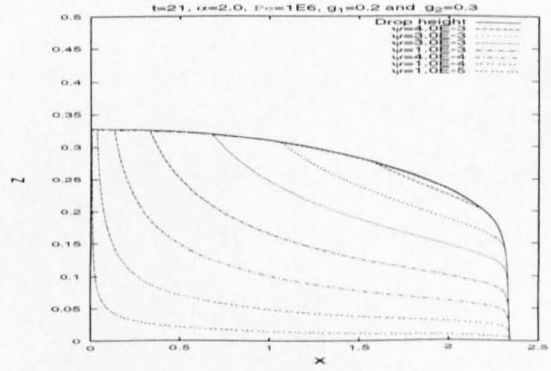

(d) Streamlines at $t = 21$.

FIG. 4.5. Two-dimensional results with constant mass, $\alpha = 2$ and $\mathrm{Pe} = 10^6$.

Setting $\mathrm{Pe} = 10^5$ and $\alpha = 2$ gives the results in Figure 4.6. The heat loss is not as significant as in Figure 4.5 with $\mathrm{Pe} = 10^6$; implying that the temperature evolution equation (4.2.21) is not a monotonic decreasing relationship as Pe decreases.

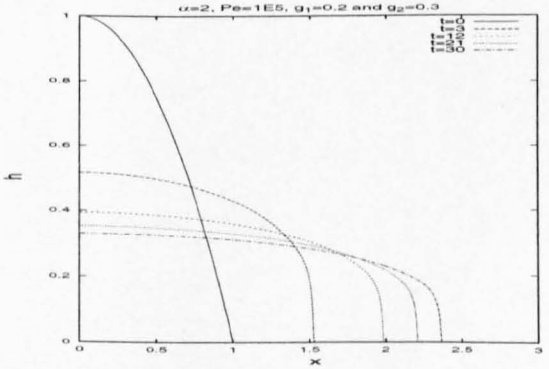

(a) Free surface profiles.

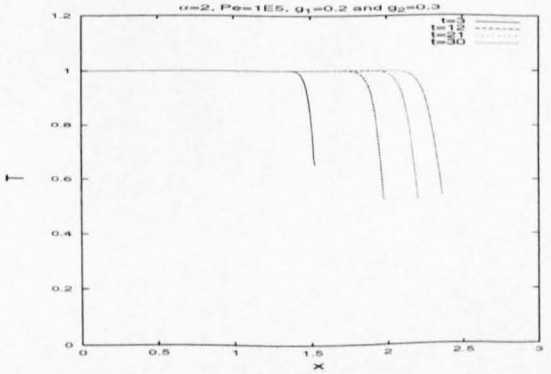

(b) Temperature profiles.

FIG. 4.6. Two-dimensional results with constant mass, $\alpha = 2$ and $\mathrm{Pe} = 10^5$.

Decreasing the Peclet number to 10^4 but keeping $\alpha = 2$, shown in Figure 4.7, results in the steep flow front not being as noticeable and gives results that are similar to the isothermal case (and to the earlier results with $\mathrm{Pe} = 10^8$). The temperature evolution equation is clearly not a monotonic decreasing relationship, the temperature profiles are again dominated by the advection terms.

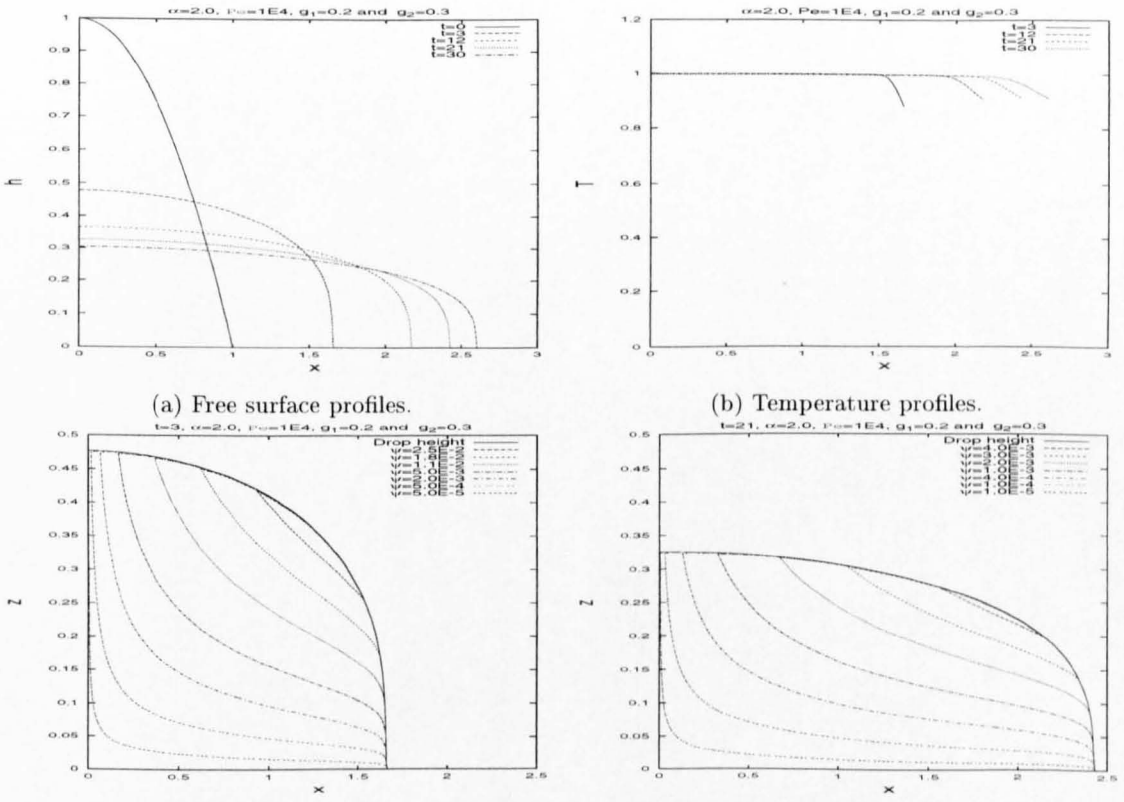

(a) Free surface profiles.

(b) Temperature profiles.

(c) Streamlines at $t = 3$.

(d) Streamlines at $t = 21$.

FIG. 4.7. Two-dimensional results with constant mass, $\alpha = 2$ and $\mathrm{Pe} = 10^4$.

For $\alpha = 2$ with $\mathrm{Pe} = 10^2$, Figure 4.8 shows that the height profiles develop a lens shape profile, similar to the isothermal case. The temperature profiles show that the diffusion terms are becoming more significant as $\mathrm{Pe} \to 0$, the heat loss over the drop is now being more noticeable (and more uniform) than in the previous sets of results. As the temperature decreases, the viscosity increases which can be seen to retard the spreading.

The next set of results, shown in Figure 4.9, are with $\mathrm{Pe} = 1$ and $\alpha = 2$. The free surface profiles in Figure 4.9(a) show little effect from the temperature field and are similar to the isothermal results in Figure 4.2 ($\mu = 1$). The reason for this can be seen by inspecting the temperature profiles in Figure 4.9(b). The diffusion term is clearly dominant, resulting in a fast rate of heat loss, leading to the temperature cooling to zero. The temperature profile shown in Figure 4.9(b) is at $t = 3$ and for later time the profiles are zero.

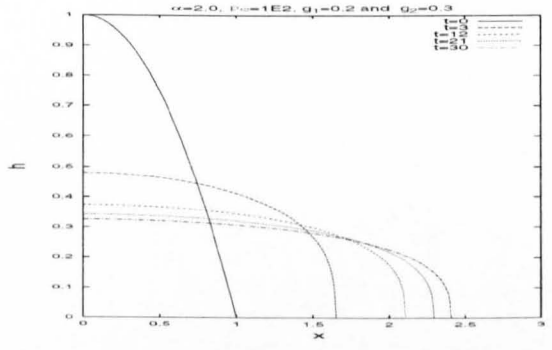

(a) Free surface profiles.

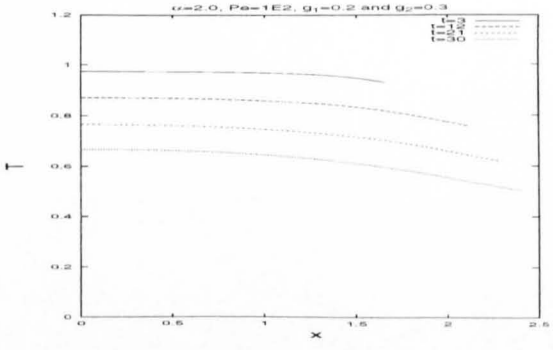

(b) Temperature profiles.

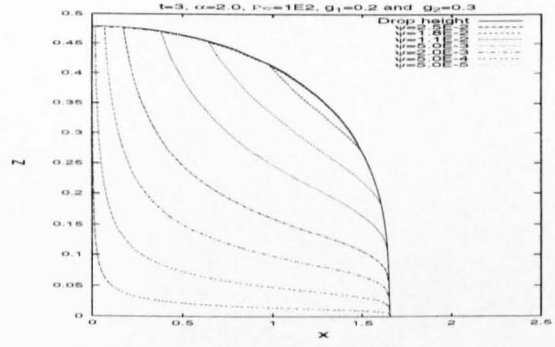

(c) Streamlines at $t = 3$.

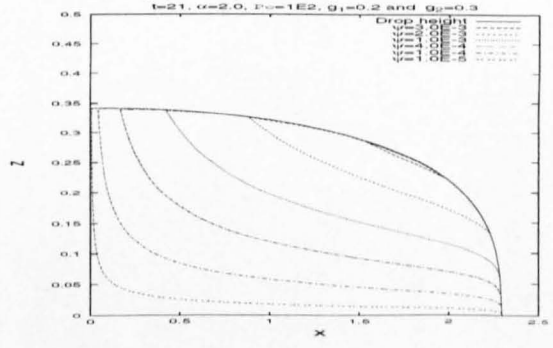

(d) Streamlines at $t = 21$.

FIG. 4.8. Two-dimensional results with constant mass, $\alpha = 2$ and $\mathrm{Pe} = 10^2$.

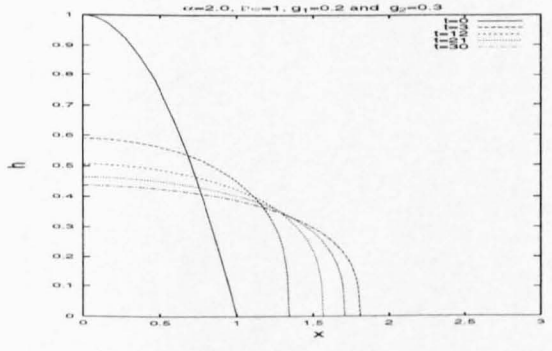

(a) Free surface profiles.

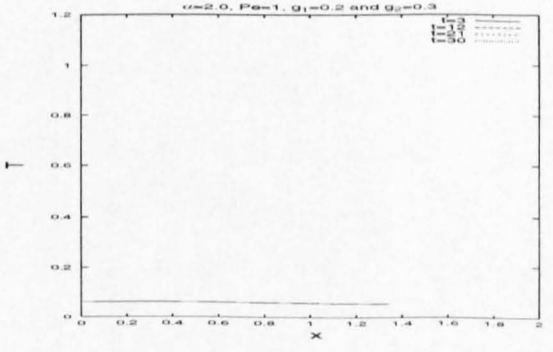

(b) Temperature profiles.

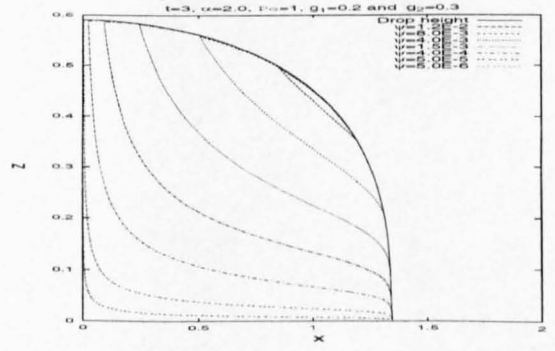

(c) Streamlines at $t = 3$.

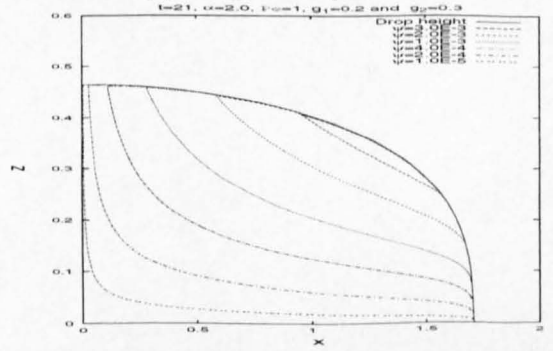

(d) Streamlines at $t = 21$.

FIG. 4.9. Two-dimensional results with constant mass, $\alpha = 2$ and $\mathrm{Pe} = 1$.

The log-log plots in Figure 4.10 show the rate at which the drop height falls at $x = 0$ and the rate at which the front location, s, spreads for the range of Peclet numbers $1 \leq \mathrm{Pe} \leq 10^8$, compared to the isothermal rate ($\mu = 1$). The front location, s, is found numerically using a small tolerance value (10^{-4}), such that s corresponds to where $h(x,t)$ becomes less than 10^{-4}. The rate at which the fluid is spreading is seen to be initially at an isothermal rate (majority of temperature still at unity), as can be seen by comparing the result for $\mathrm{Pe} = 10^8$ and for the isothermal case, which are parallel. As the Peclet number is decreased, the rate at which the fluid spreads, Figures 4.10(a) and 4.10(b), tends to the isothermal case ($\mu = 1$). This is expected, because the initial temperature of unity has cooled to zero. For $\mathrm{Pe} = 10^8$, $s \approx t^{0.2}$ and $h \approx t^{-0.2}$ which agrees with the isothermal spreading rates and the similarity solutions, see equation (2.2.10).

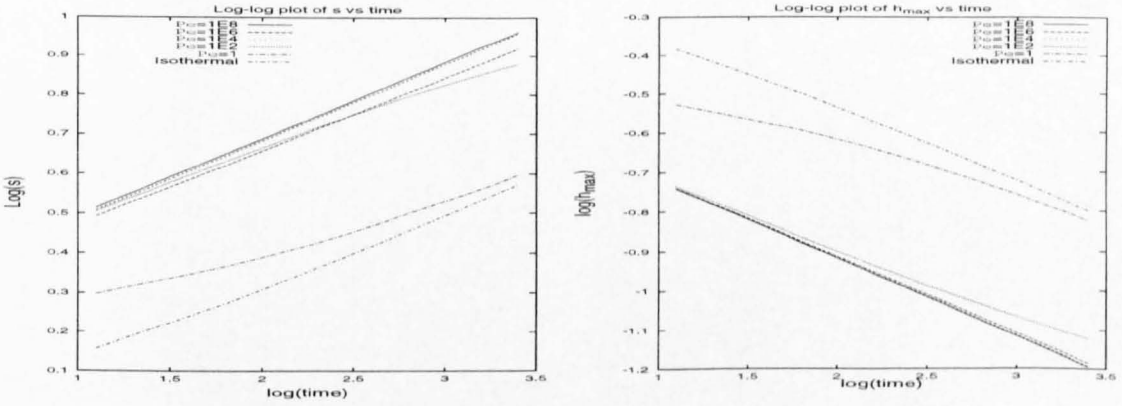

(a) Front location *vs* time. (b) h_{max} *vs* time.

FIG. 4.10. Log-log plots of front location and h_{max} *vs* time for $\alpha = 2$.

We now consider in more detail the interesting cases where the free surface develops a steep flow front. Increasing the coupling between the flow and temperature fields, by increasing α in the exponential viscosity relationship, is now considered.

Increasing α to 7.1 in Figure 4.11 , the maximum value before numerics fail, gives rise to oscillations in the height profiles with $\Delta t = 2 \times 10^{-5}$, note that the time step is decreased from the previous set of results to allow for the increase in viscosity, and $\mathrm{Pe} = 10^5$, over the range $0 \leq x \leq 4$ with 600 mesh points, leads to results with steep flow fronts followed by a developing plateau. The temperature profiles and streamlines are similar to the results with $\alpha = 2$. The time range is $0 \leq t \leq 2.0$, because increasing α increases the diffusivity and, to account for the increase in the spreading rate, the time range is reduced.

The range of Peclet values over which the liquid develops a steep front is larger than for $\alpha = 2$, for which a steep flow front is seen roughly over the range $10^4 \leq \mathrm{Pe} \leq 10^7$. Decreasing the Peclet number to $\mathrm{Pe} = 10$ gives the results in Figures 4.12. As in the case for $\alpha = 2$ with small Peclet number ($\mathrm{Pe} \leq O(10)$ say), the viscosity is rapidly increasing, because of the temperature loss, causing the spreading to retard; see Figure 4.12(a).

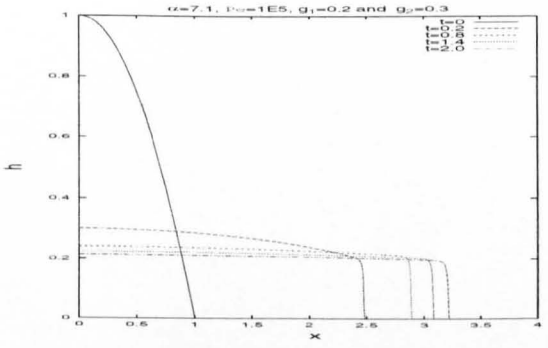

(a) Free surface profiles.

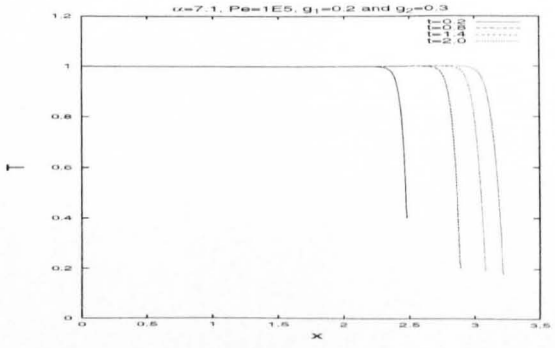

(b) Temperature profiles.

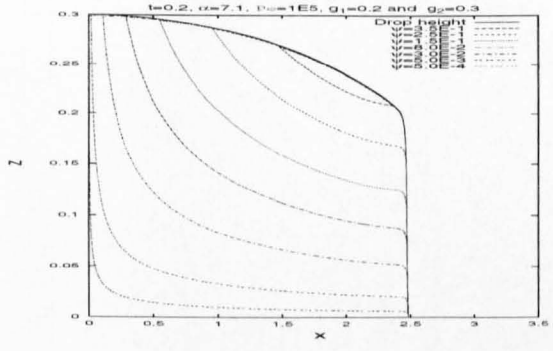

(c) Streamlines at $t = 0.2$.

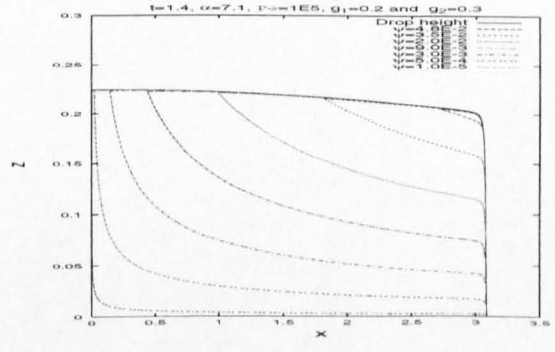

(d) Streamlines at $t = 1.4$.

FIG. 4.11. Two-dimensional results with $\alpha = 7.1$ and $\mathrm{Pe} = 10^5$.

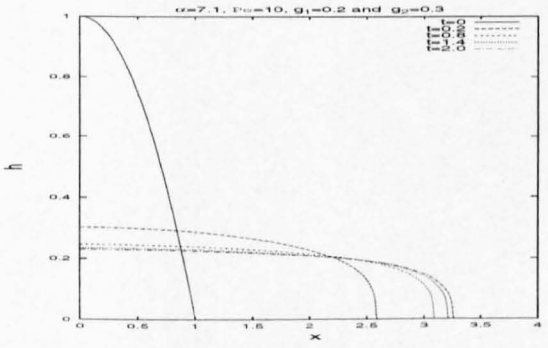

(a) Free surface profiles.

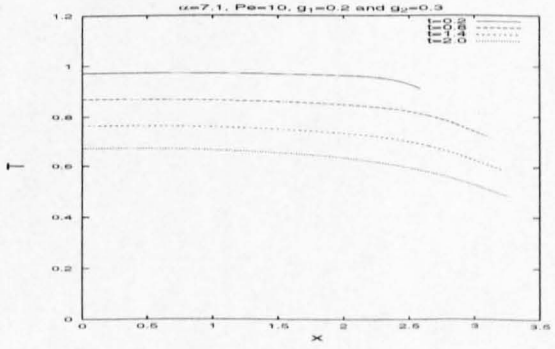

(b) Temperature profiles.

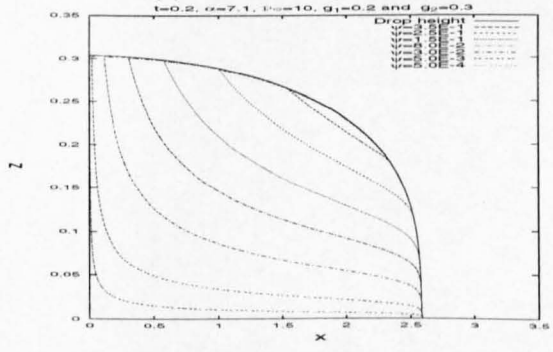

(c) Streamlines at $t = 0.2$.

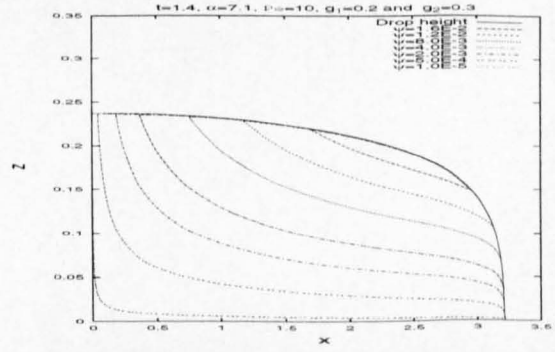

(d) Streamlines at $t = 1.4$.

FIG. 4.12. Two-dimensional results with $\alpha = 7.1$ and $\mathrm{Pe} = 10$.

The corresponding log-log plots with $\alpha = 4$ (Figure 4.13(a)) show that as Pe decreases the

spreading tends to the isothermal case ($\mu = 1$). Again the spreading rates for Pe $= 10^8$ show good agreement with the similarity solutions for the isothermal case.

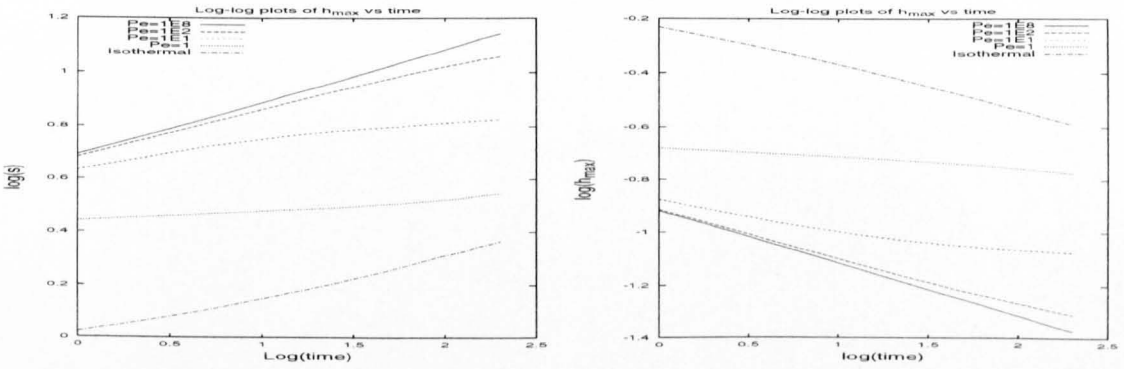

(a) Front location *vs* time. (b) h_{max} *vs* time.

FIG. 4.13. Log-log plots of front location and h_{max} *vs* time for $\alpha = 4$.

The diffusivity, D, is given by equation (4.2.23) for the non-isothermal problem and for the isothermal case, $\mu(T) = 1$, simplifies to (2.2.2). The diffusivity can be seen in Figure 4.14 to be clearly affected by the viscosity variation when Pe $= 10^5$; the viscosity sharply increases near the contact lines, due to the heat loss occurring there (see Figure 4.14(b)) and causes the diffusion profiles to develop a steep front when compared with the isothermal diffusion profiles (see Figure 4.14(a)).

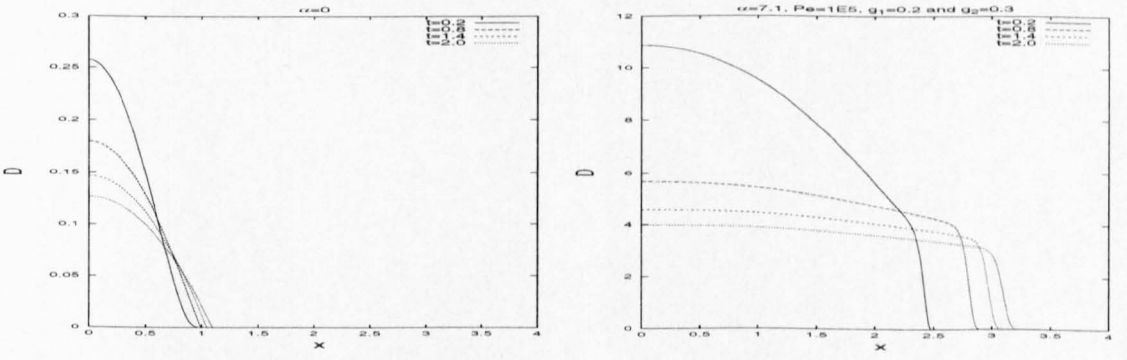

(a) Isothermal diffusivity. (b) Diffusivity for $\alpha = 7.1$ and Pe $= 10^5$.

FIG. 4.14. Comparison between the isothermal and non-isothermal diffusivities.

The results in Figure 4.15 show the effects of increasing g_1 and g_2 and show that the temperature profiles quickly lose heat for large enough heat-exchange coefficients, as expected. Note that $g_1 = 0$ and $g_2 = 200$ appear (in 4.2.21) only in the combination $g_1 + g_2$. The first set of results in Figures 4.15(a)-4.15(b) show that setting $g_1 = g_2 = 0$ (so there is no heat loss) the fluid spreads isothermally ($\mu(T = 1)$). Increasing g_1 and g_2 to 10^3 in Figures 4.15(c)-4.15(d), shows that the heat loss is significant, especially near the flow front where the fluid is thinner, and the free surface profiles are seen to develop a steep flow front. In Figures 4.15(e)-4.15(f), with $g_1 = g_2 = 10^5$,

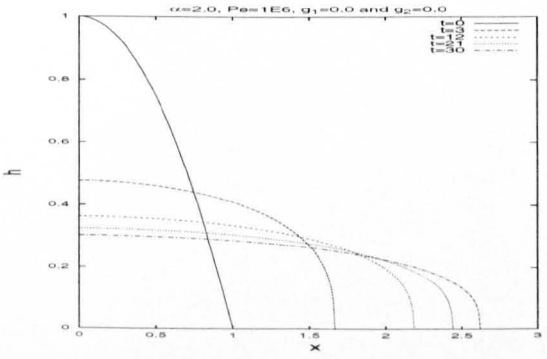

(a) Free surface profiles with $g_1 = g_2 = 0$.

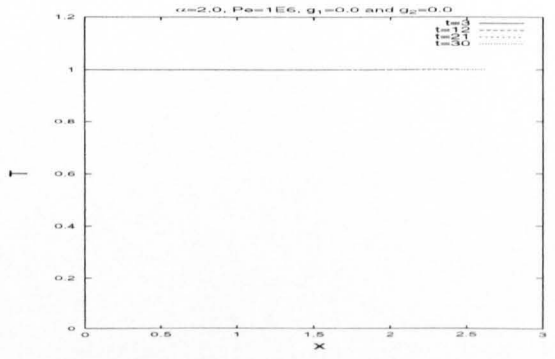

(b) Temperature profiles with $g_1 = g_2 = 0$.

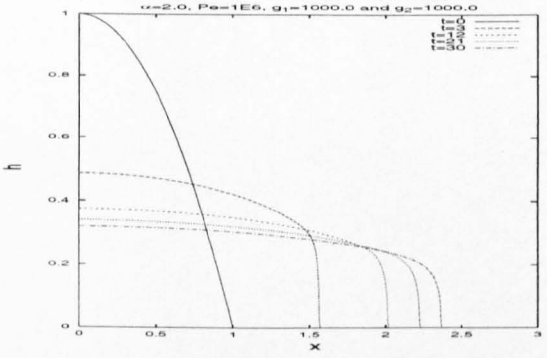

(c) Free surface profile with $g_1 = g_2 = 10^3$.

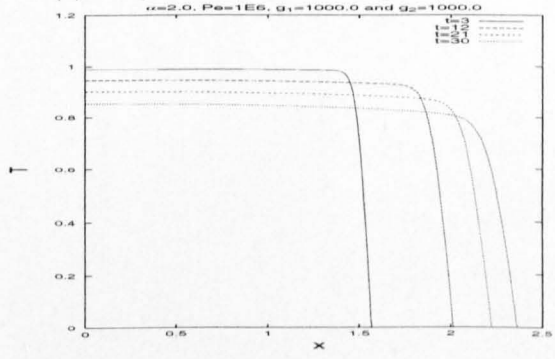

(d) Temperature profiles with $g_1 = g_2 = 10^3$.

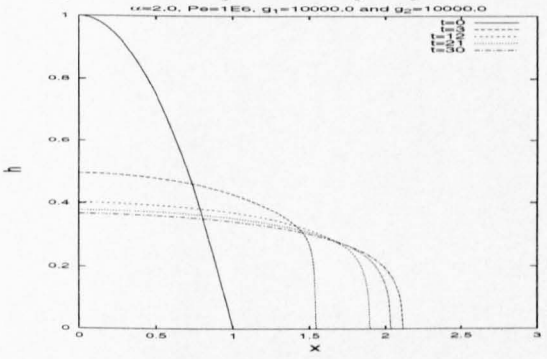

(e) Free surface profiles with $g_1 = g_2 = 10^5$.

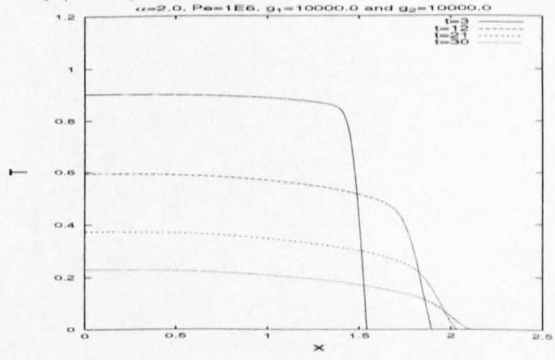

(f) Temperature profile with $g_1 = g_2 = 10^5$.

FIG. 4.15. Two-dimensional results with $g_1 = g_2$ from 0 to 10^5, with $\alpha = 2$ and $\mathrm{Pe} = 10^5$.

the heat can be seen to be quickly diffusing, with the resulting free surface profiles clearly being retarded by the increase in viscosity.

The next set of results in Figure 4.16 include the heat source term in equation (4.2.21). The effects of the internal heat generation are illustrated in Figure 4.16(b) for $\mathrm{Pe} = 10^4$ and $\dot{Q} = 200$. The temperature profile is almost constant across the fluid, apart from near the flow front where the fluid is thinnest. The corresponding free surface profiles in Figure 4.16(a) are characteristic of the isothermal case, as expected because of the near constant temperature across the fluid. The heat source is strong enough to keep the temperature growing with time. Similar results are shown in Figures 4.16(c)-4.16(d) for $\mathrm{Pe} = 10^2$ and $\dot{Q} = 10$, where there is a large amount of internal heat being generated. Decreasing the Peclet number further, such that $\mathrm{Pe} = 1$ and $\dot{Q} = 6$

(cf. Figures 4.16(e)-4.16(f)), shows that the diffusion term is more dominant than in the previous set of results, and the heat loss is seen for larger time to be greater than the heat generated by the heat source. Note that a large value of $\dot{Q}$ is used with a large Peclet number and is decreased as the Peclet number decreases. This is because the effective strength of the heat source source is a combination of the Peclet number and $\dot{Q}$, see equation (4.2.21).

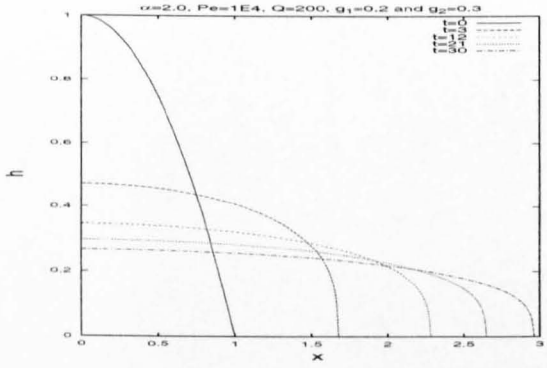

(a) Free surface profiles with Pe $= 10^4$ and $\dot{Q} =$ 200.

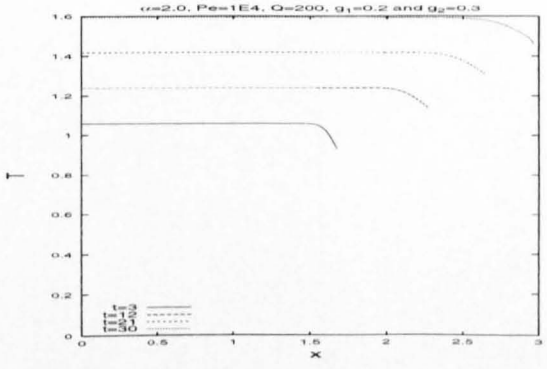

(b) Temperature profiles with Pe $= 10^4$ and $\dot{Q} = 200$.

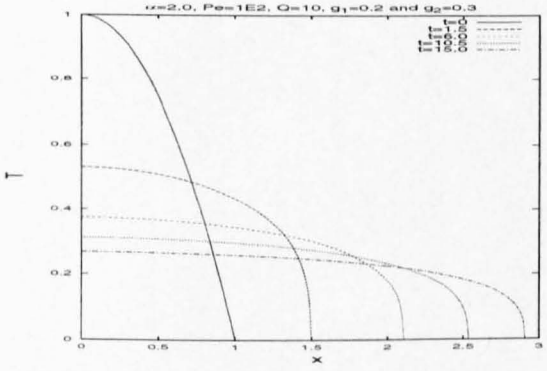

(c) Free surface profile with Pe $= 10^2$ and $\dot{Q} =$ 10.

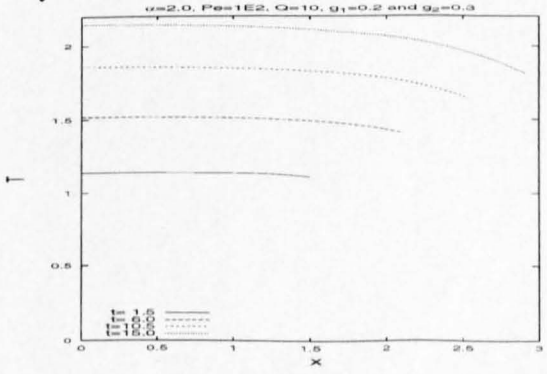

(d) Temperature profiles with Pe $= 10^2$ and $\dot{Q} = 10$.

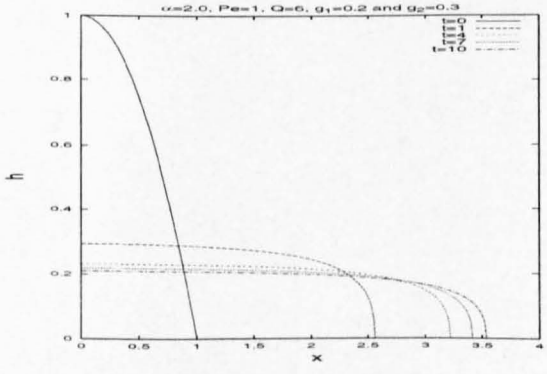

(e) Free surface profiles with Pe $= 1$ and $\dot{Q} = 6$.

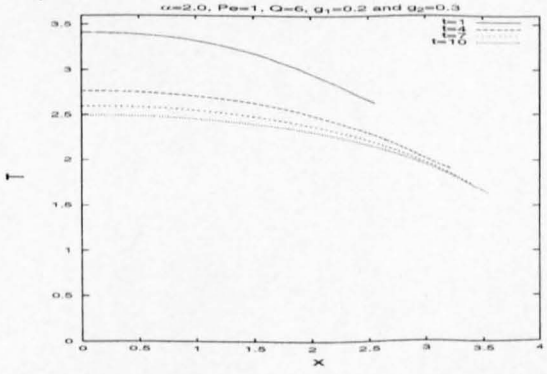

(f) Temperature profile with Pe $= 1$ and $\dot{Q} = 6$.

FIG. 4.16. Two-dimensional results with a heat source, $\alpha = 2$ and Pe $= 10^4$ to Pe $= 1$.

4.5.2. *Two-dimensional results with influx from a line source*

The following sets of results for planar spreading show the effect of an influx of fluid from a line source, with $q_c = 0.009$ and $\beta = 1.5$. Again, the first set of results in Figure 4.17 show the constant viscosity case, $\alpha = 0$. The numerical results in Figure 4.17 show good agreement (to three decimal places) with the NAG routine D03PGF, over the same range $0 \leq x \leq 2$ for 600 mesh points with $\Delta t = 10^{-5}$ and $0 \leq t \leq 20$ and establishes confidence in the numerical technique described above. The height profiles can be seen to have a lens shape profile, shown with the streamlines at times $t = 8$ and $t = 20$, and can be seen to be fed from the line source.

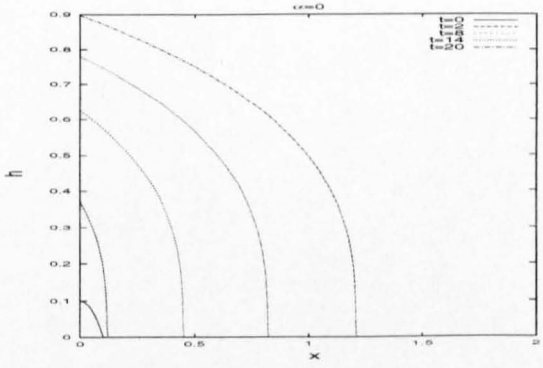

(a) Free surface profiles.

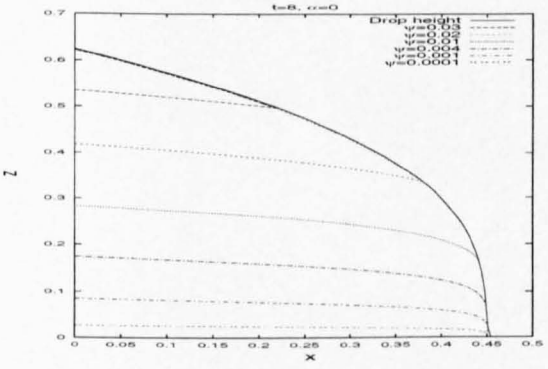

(b) Streamlines at $t = 8$.

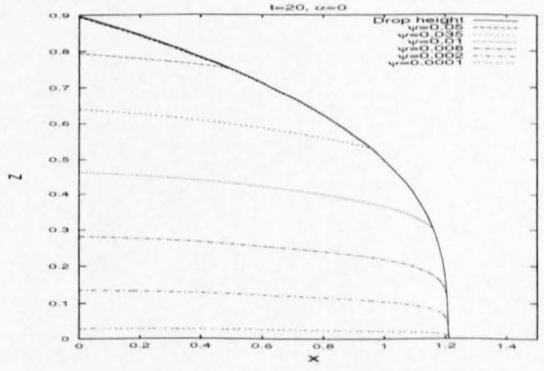

(c) Streamlines at $t = 20$.

FIG. 4.17. Two-dimensional results: isothermal with a line source.

Including the temperature field gives the first set of variable viscosity results in Figure 4.18, where the same mesh spacings, time step and time range are used. As in the corresponding constant mass case with $\mathrm{Pe} = 10^8$, the temperature profiles show little heat loss and the fluid behaves isothermally ($\mu(T = 1)$).

The results in Figure 4.19 show the height profiles developing a steep flow front for $\alpha = 2$ and $\mathrm{Pe} = 10^6$. The variable viscosity model can be seen to redistribute the mass, the flow front being retarded compared to the previous set of results. The temperature profiles and streamlines show similar results to the constant mass case, most of the fluid still being at temperature unity, apart from near the flow front where the fluid is thinnest.

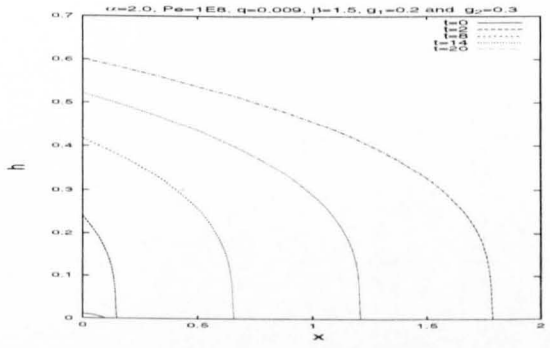

(a) Free surface profiles.

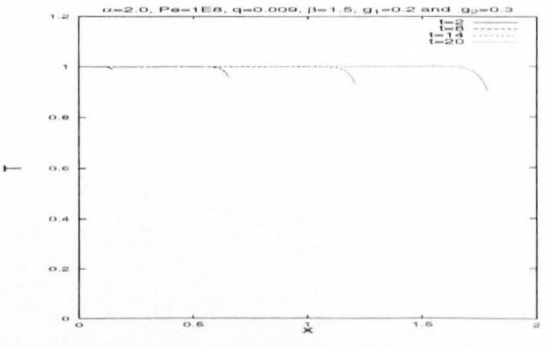

(b) Temperature profiles.

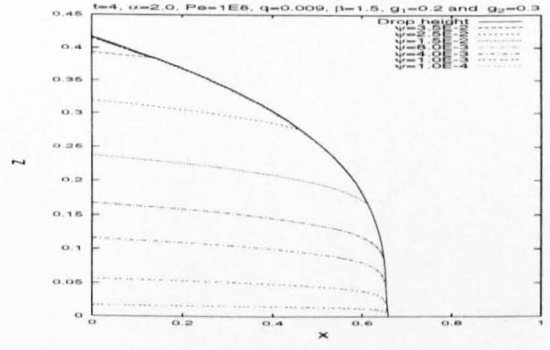

(c) Streamlines at $t = 8$.

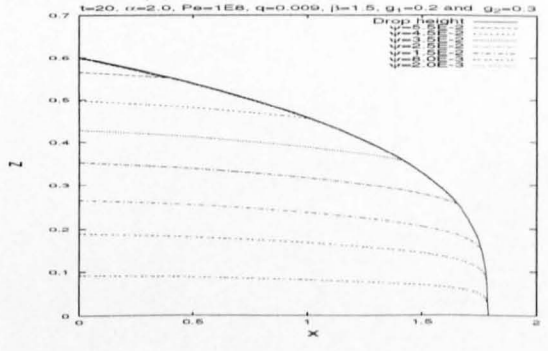

(d) Streamlines at $t = 20$.

FIG. 4.18. Two-dimensional results for a line source with $\alpha = 2$ and $\mathrm{Pe} = 10^8$.

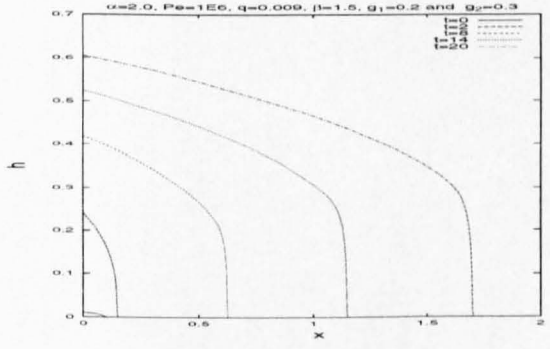

(a) Free surface profiles.

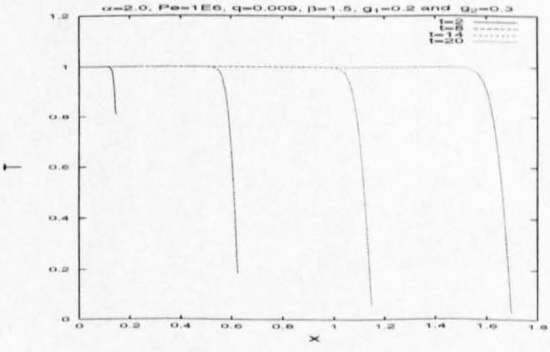

(b) Temperature profiles.

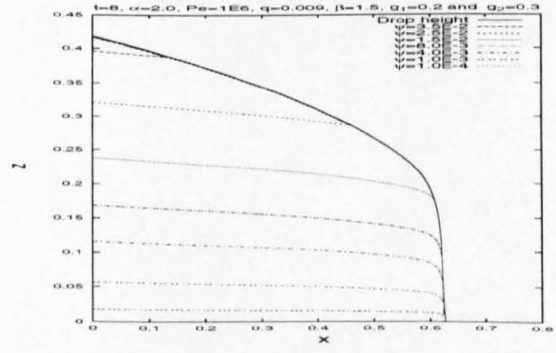

(c) Streamlines at $t = 8$.

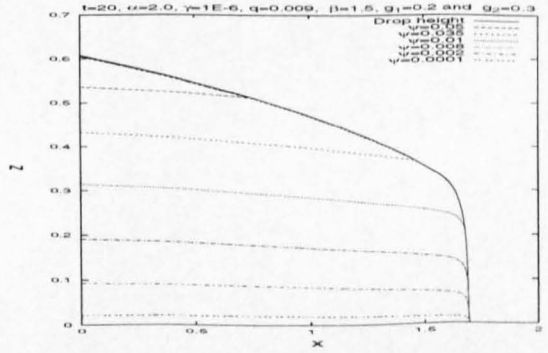

(d) Streamlines at $t = 20$.

FIG. 4.19. Two-dimensional results for a line source with $\alpha = 2$ and $\mathrm{Pe} = 10^6$.

Decreasing Pe to 10^4 with $\alpha = 2$, the free surface profiles in Figure 4.20 are almost identical to the set of results in Figure 4.18 where $\mathrm{Pe} = 10^8$. The temperature profiles show that the advection terms are again dominant. This is consistent with the results for constant mass and implies that the temperature field does not decrease monotonically with Pe. Again the streamlines for the variable viscosity model are of a similar nature to the constant viscosity ones.

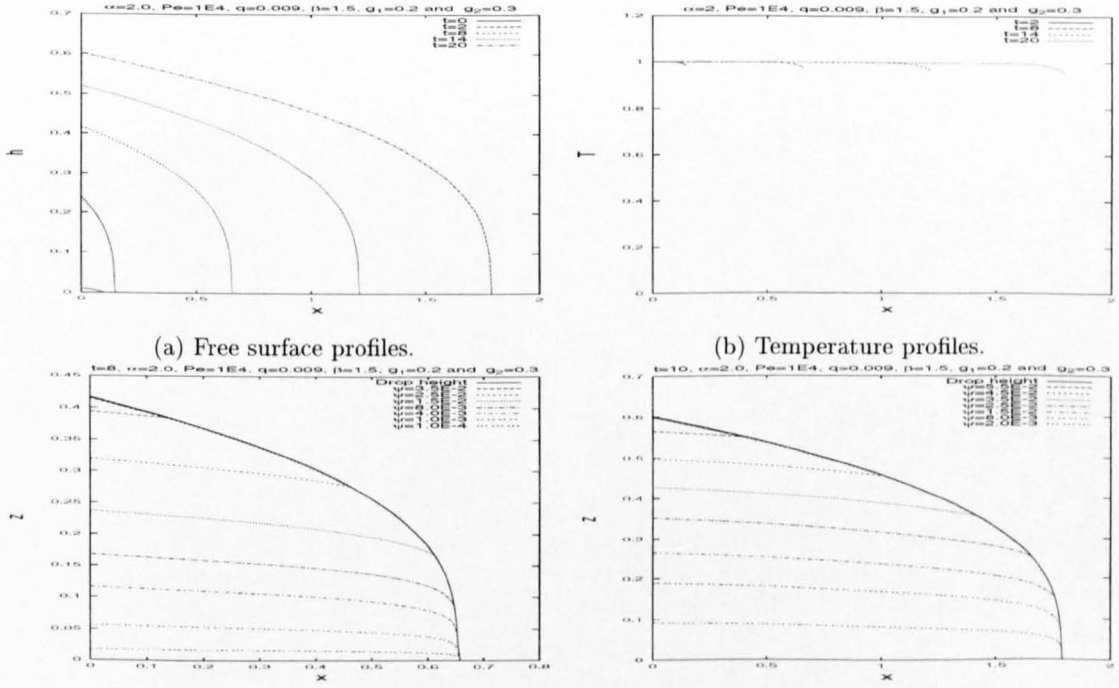

(a) Free surface profiles.

(b) Temperature profiles.

(c) Streamlines at $t = 8$.

(d) Streamlines at $t = 20$.

FIG. 4.20. Two-dimensional results for a line source with $\alpha = 2$ and $\mathrm{Pe} = 10^4$.

Decreasing the Peclet number further ($\mathrm{Pe} = 10^2$) and keeping $\alpha = 2$, the height profiles are again seen to be developing a lens shape profile (Figures 4.21-4.22). The temperature profiles show that the diffusion terms are becoming more dominant as $\mathrm{Pe} \to 0$, the heat loss over the drop being more noticeable than in the previous set of results. The constant hot source of fluid can be seen to keep the temperature at unity at $x = 0$.

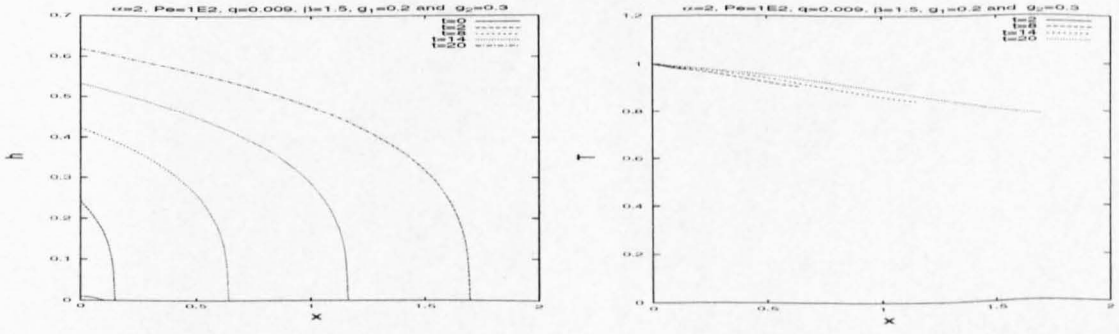

(a) Free surface profiles.

(b) Temperature profiles.

FIG. 4.21. Two-dimensional results for a line source with $\alpha = 2$ and $\mathrm{Pe} = 10^2$.

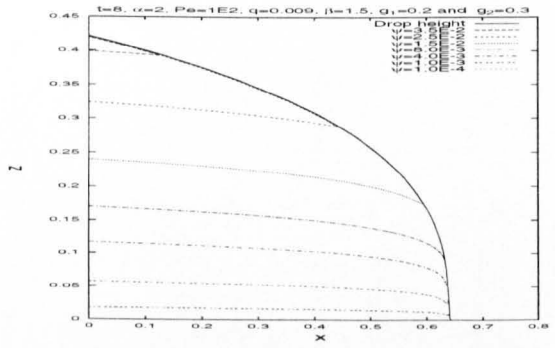

(a) Streamlines at $t = 8$.

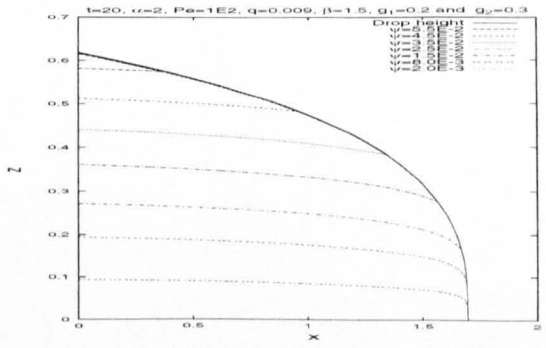

(b) Streamlines at $t = 20$.

FIG. 4.22. Two-dimensional results for a line source with $\alpha = 2$ and $\mathrm{Pe} = 10^2$.

Figure 4.23 gives the results for $\mathrm{Pe} = 10$ and $\alpha = 2$. The free surface profiles are again lens shaped, as in the isothermal results. The temperature profiles show the heat being lost quickly, as compared with the simulations above. This is consistent with the constant mass case, but because of the fixed temperature value at $x = 0$, the temperature profiles never tend to zero and will always have an effect on the height profiles.

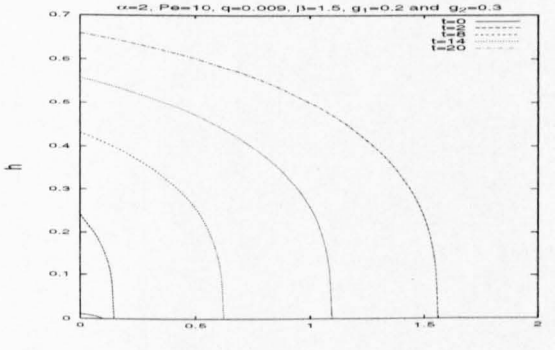

(a) Free surface profiles.

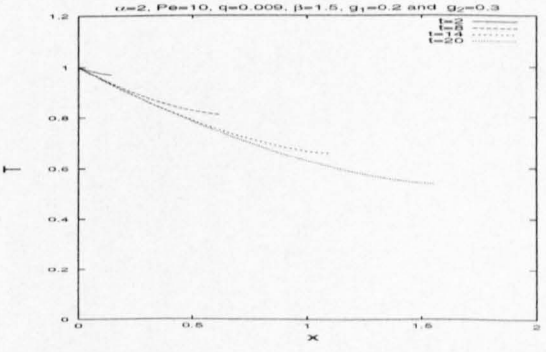

(b) Temperature profiles.

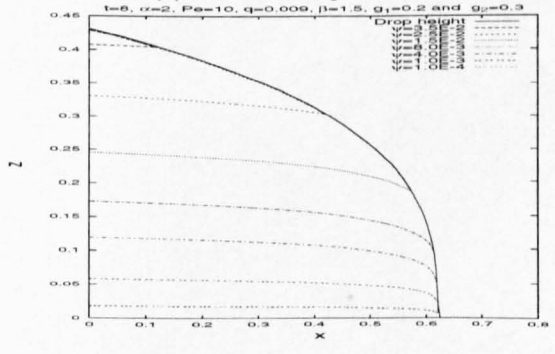

(c) Streamlines at $t = 8$.

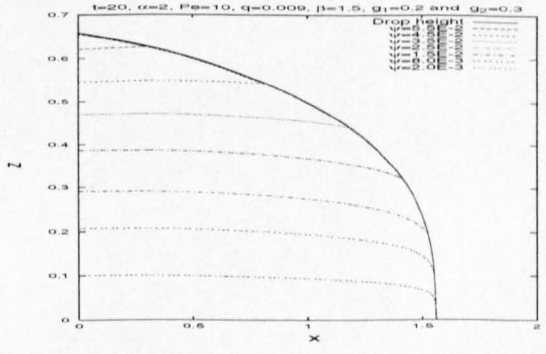

(d) Streamlines at $t = 20$.

FIG. 4.23. Two-dimensional results for a line source with $\alpha = 2$ and $\mathrm{Pe} = 10$.

The log-log plots for the influx model show that as the Peclet number decreases the spreading reaches a maximum rate and does not tend to the isothermal model ($\mu = 1$) for large time, in contrast to the constant mass case. This is caused by the influx model having a fixed temperature from the line source and an equilibrium is reached between the heat source at the inflow boundary

and the cooling rate, see Figure 4.24(a). Similar behaviour is observed for the rate the drop height varies at $x = 0$ in Figure 4.24(b). The spreading rate for the fluid with $\mathrm{Pe} = 10^8$ has the behaviour $s \approx t^{1.1}$ and $h \approx t^{0.4}$. This agrees with the isothermal rate in the log-log plot and the similarity solutions for the isothermal case where $s \sim t^{\frac{3\beta+1}{5}}$ and $h \sim t^{\frac{2\beta-1}{5}}$, noting that $\beta = 1.5$.

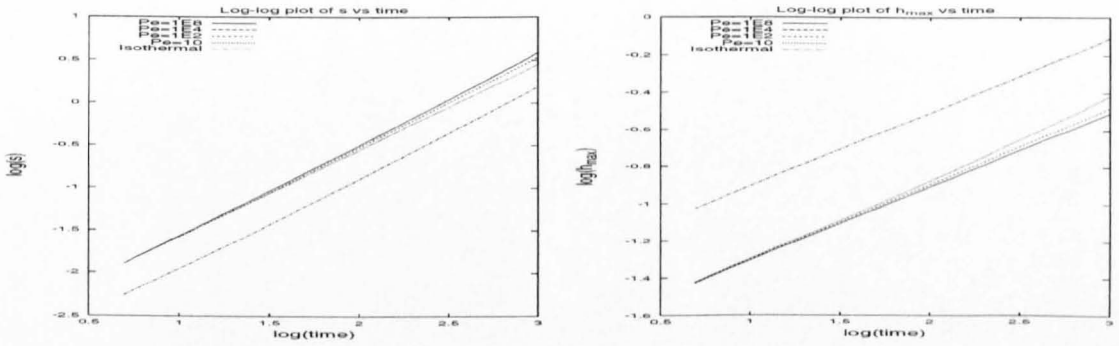

(a) Front location *vs* time. (b) h_{max} *vs* time.

FIG. 4.24. Log-log plots of front location and h_{max} *vs* time for $\alpha = 2$.

Again looking at the case of large α, illustrated in Figure 4.25, where α is increased to 7.1 (the maximum value before the numerics fail, giving rise to oscillations in the height profiles) with $\Delta t = 10^{-5}$ and 600 mesh points over the ranges $0 \leq t \leq 10$ and $0 \leq x \leq 3$ with $\mathrm{Pe} = 10^5$, shows the free surface profiles developing a steep flow front followed by a plateau. The temperature

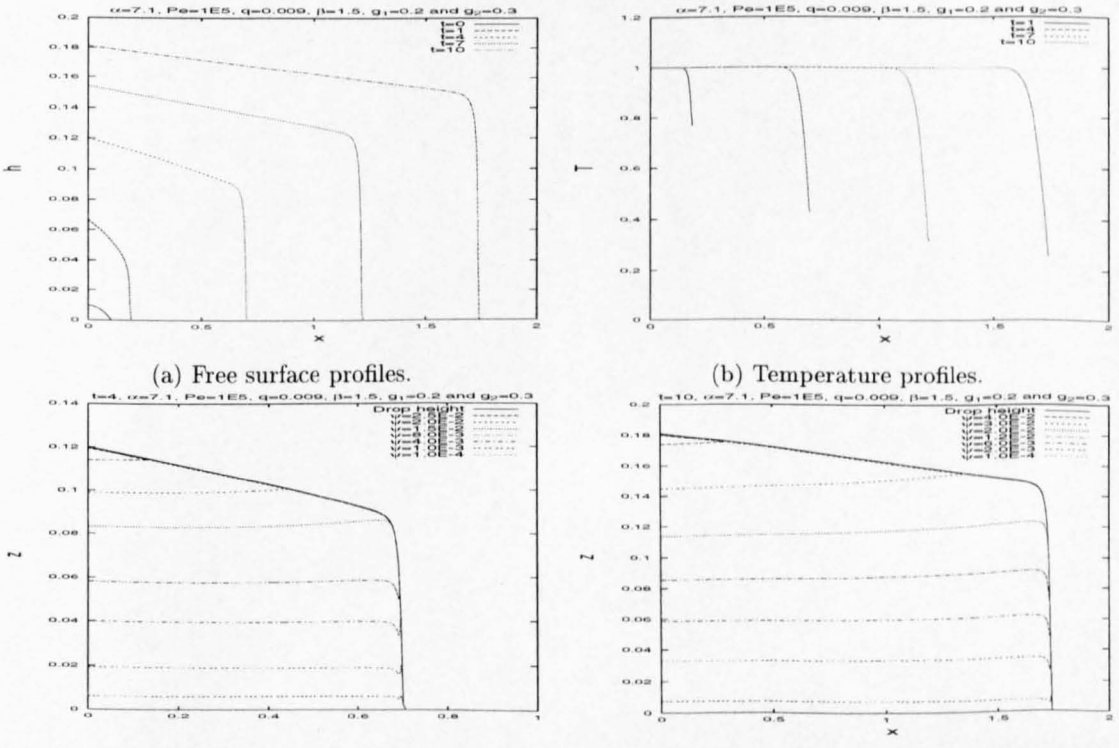

(a) Free surface profiles. (b) Temperature profiles.

(c) Streamlines at $t = 8$. (d) Streamlines at $t = 20$.

FIG. 4.25. Two-dimensional results with $\alpha = 7.1$ and $\mathrm{Pe} = 10^5$.

profiles and streamlines are similar to results with $\alpha = 2$ and $\mathrm{Pe} = 10^6$, there being a large amount of cooling where the free surface is thinnest.

The log-log plots with $\alpha = 4.0$ in Figures 4.26(a) and 4.26(b) show similar results to Figure 4.24 ($\alpha = 2$), where the results for $\mathrm{Pe} = 10^8$ is shown to spread isothermally. Again, as Pe decreases, the spreading does not behave isothermally, but tends to a maximum rate due to the heat source on the influx boundary.

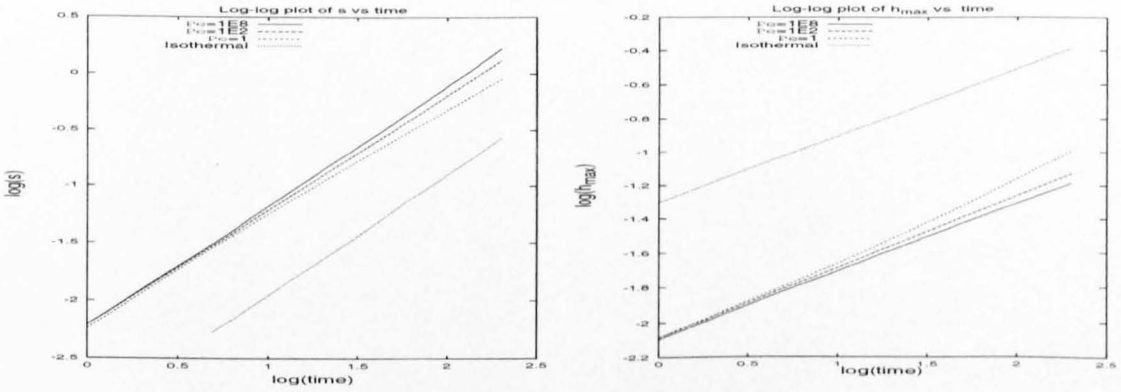

(a) Front location *vs* time. (b) h_{max} *vs* time.

FIG. 4.26. Log-log plots of front location and h_{max} *vs* time for $\alpha = 4$.

4.5.3. *Axisymmetric results with constant mass*

The next set of results in Figures 4.27-4.28 are for the axisymmetric case with constant mass. The free surface profiles and streamlines show the constant viscosity case, $\alpha = 0$, and again show good agreement (to four decimal places) with the NAG routine D03PGF over the range $0 \leq r \leq 2$ for 600 mesh points and time step $\Delta t = 10^{-4}$ in the range $0 \leq t \leq 30$ establishing confidence in the numerical schemes derived above. The height profiles have a lens shape, shown with the streamlines at times $t = 3$ and $t = 21$.

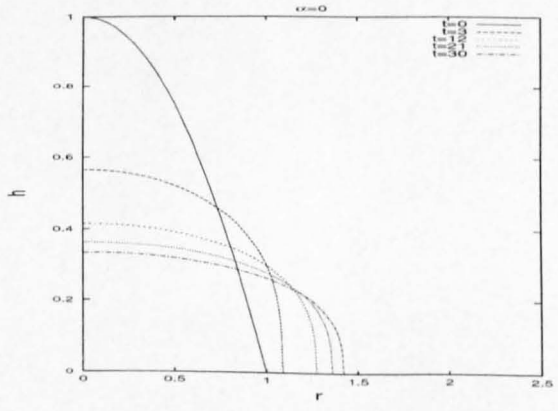

(a) Free surface profiles.

FIG. 4.27. Axisymmetric results: isothermal and constant mass.

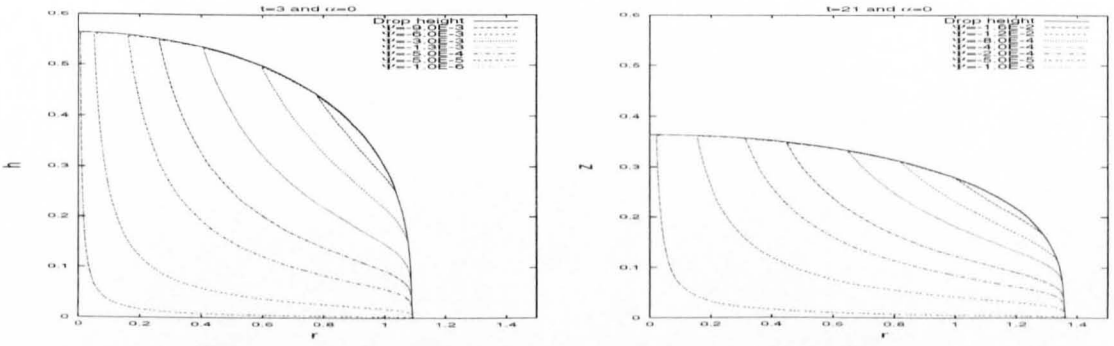

(a) Streamlines at $t = 3$. (b) Streamlines at $t = 21$.

FIG. 4.28. Axisymmetric results: isothermal and constant mass.

Introducing the temperature field gives the first set of non-isothermal results in the axisymmetric geometry shown in Figure 4.29 with $\mathrm{Pe} = 10^8$ and $\alpha = 2$. The same time range with the same time step and mesh points and spacings are used as in the isothermal case in Figure 4.27. The height profiles show the characteristic lens shape associated with the isothermal case due to the small amount of heat loss in the fluid. Again the streamlines are of a similar nature to the constant viscosity streamlines and the temperature is approximately unity, apart from near the flow front.

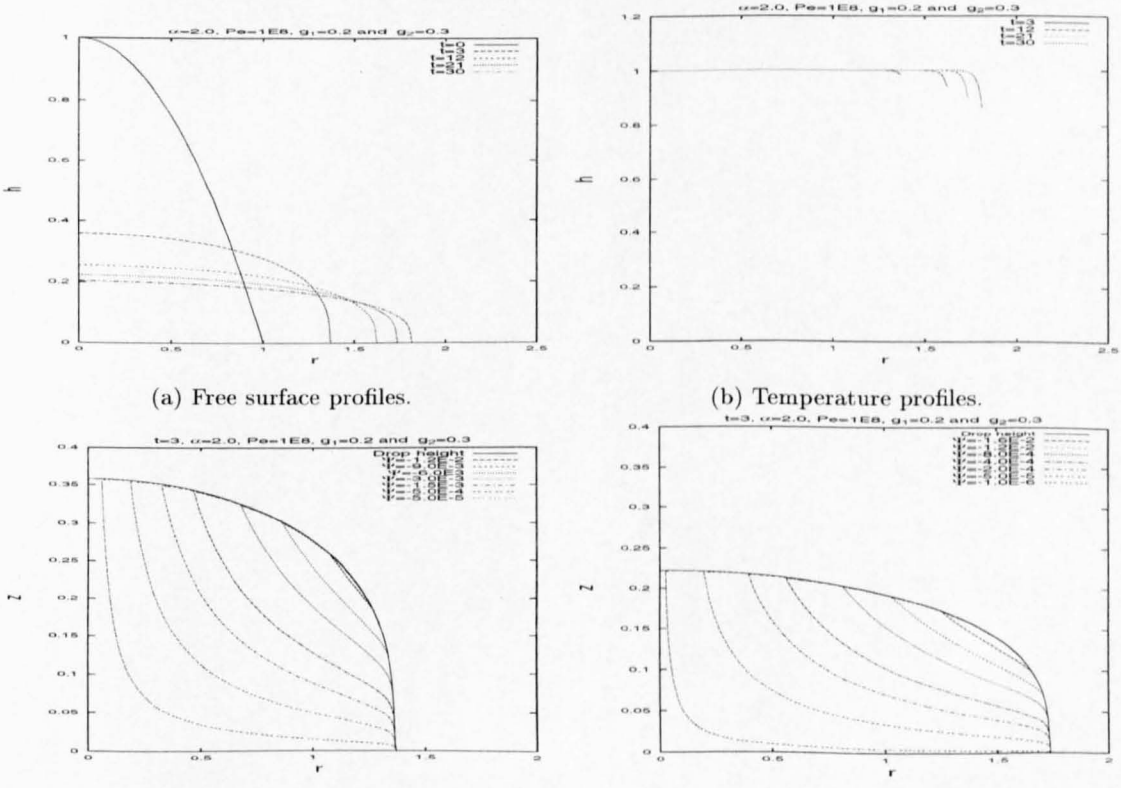

(a) Free surface profiles. (b) Temperature profiles.

(c) Streamlines at $t = 3$. (d) Streamlines at $t = 21$.

FIG. 4.29. Axisymmetric results with $\alpha = 2$ and $\mathrm{Pe} = 10^8$.

Setting $\mathrm{Pe} = 10^7$ with $\alpha = 2$ gives the results in Figure 4.30. As in the equivalent two-

dimensional results the liquid has retarded caused by the increase in heat loss near the front front.

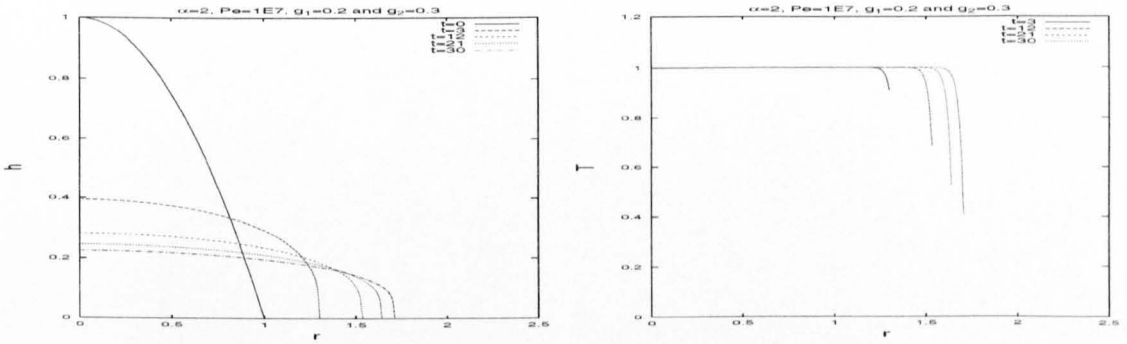

(a) Free surface profiles. (b) Temperature profiles.

FIG. 4.30. Axisymmetric results with $\alpha = 2$ and $\mathrm{Pe} = 10^7$.

The next set of results show that decreasing the Peclet number to 10^6, but keeping $\alpha = 2$, leads to a steep flow front, caused by the increase in viscosity at the flow front, the temperature profiles showing a large amount of cooling near the flow front. In the range $10^5 < \mathrm{Pe} < 10^7$, the free surface is clearly affected by the temperature field (developing the steep flow front), as in the two-dimensional case.

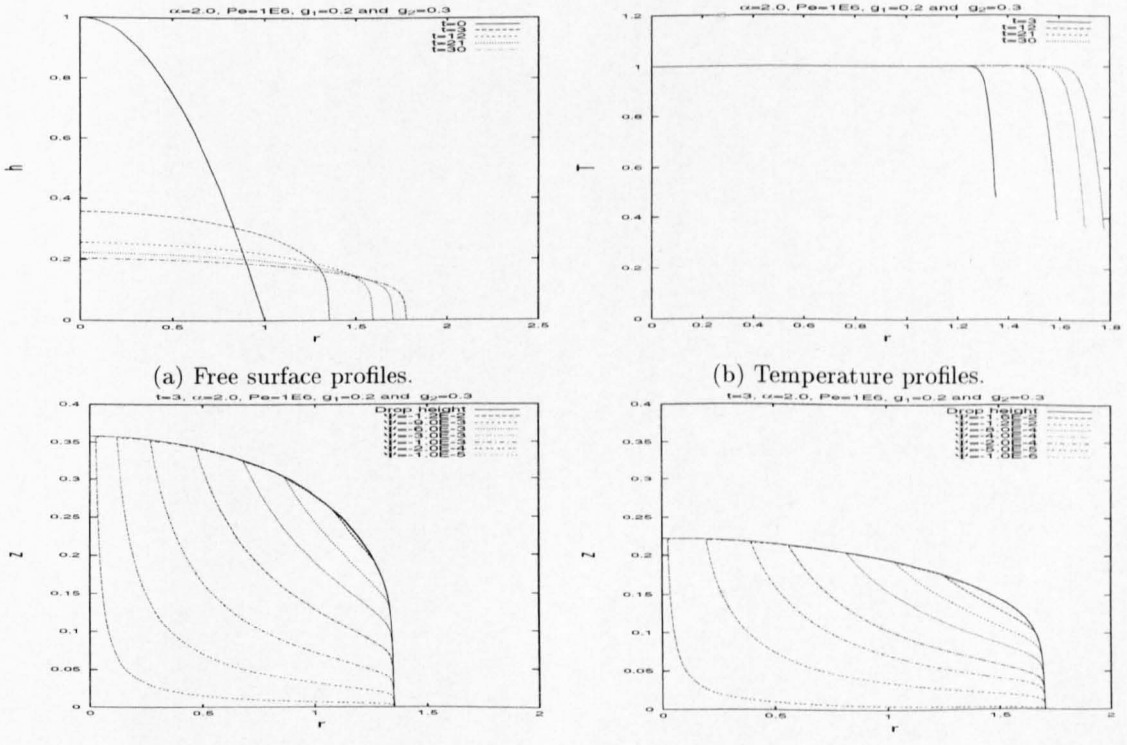

(a) Free surface profiles. (b) Temperature profiles.

(c) Streamlines at $t = 1$. (d) Streamlines at $t = 7$.

FIG. 4.31. Axisymmetric results with $\alpha = 2$ and $\mathrm{Pe} = 10^6$.

The results for $\alpha = 2$ and $\mathrm{Pe} = 10^5$ are shown in Figure 4.32. As seen in the two-dimensional results, the temperature is clearly not a monotonic decreasing function of Pe.

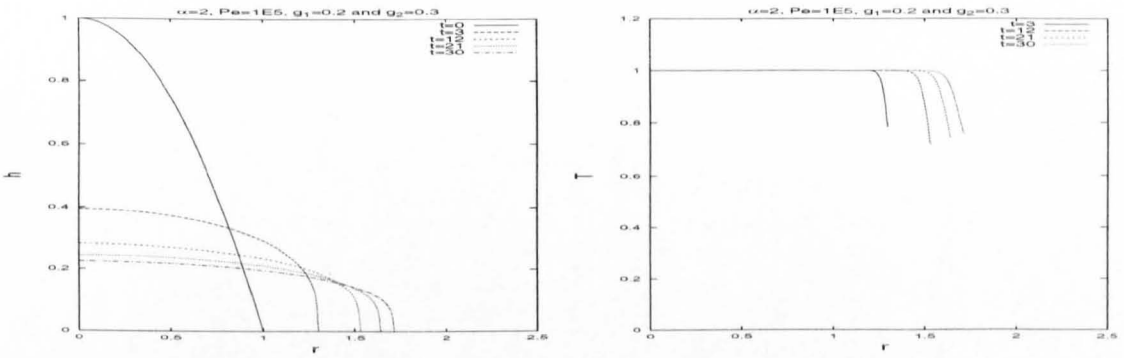

(a) Free surface profiles. (b) Temperature profiles.

FIG. 4.32. Axisymmetric results with $\alpha = 2$ and $\mathrm{Pe} = 10^5$.

Decreasing Pe to 10^4 and then 10^2, keeping $\alpha = 2$, gives the results in Figures 4.33 and 4.34, respectively. Figure 4.33 shows little heat loss in the temperature profiles and results in a similar profile to that shown in Figure 4.29. Figure 4.34 shows temperature profiles with a larger heat loss and results in the typical lens shaped free surface profiles. As the temperature decreases, the viscosity increases, which can be seen to retard the rate at which the fluid spreads.

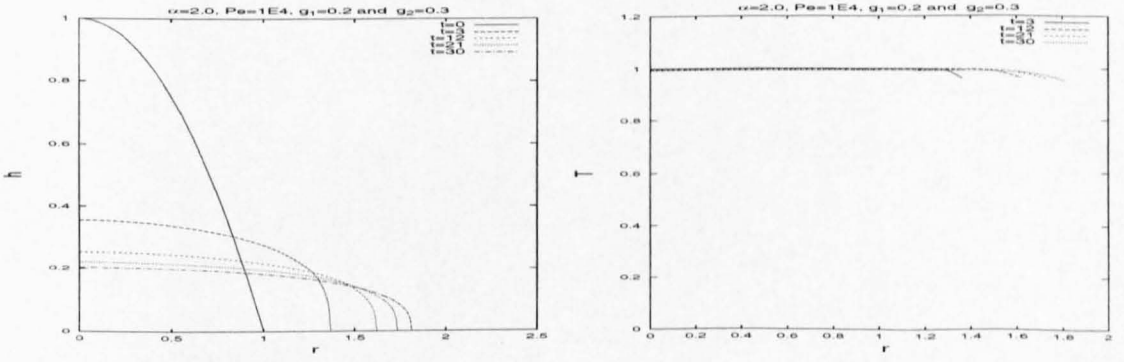

(a) Free surface profiles. (b) Temperature profiles.

FIG. 4.33. Axisymmetric results with $\alpha = 2$ and $\mathrm{Pe} = 10^4$.

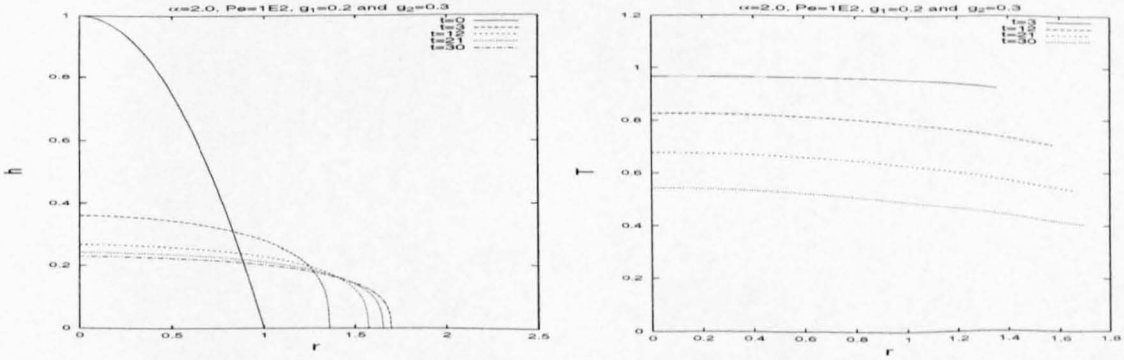

(a) Free surface profiles. (b) Temperature profiles.

FIG. 4.34. Axisymmetric results with $\alpha = 2$ and $\mathrm{Pe} = 10^2$.

Decreasing Pe further, to Pe = 1, leads to the smooth lens profile becoming prominent, as shown in Figure 4.35. The temperature profiles show the heat being lost quickly, resulting in isothermal spreading ($\mu = 1$).

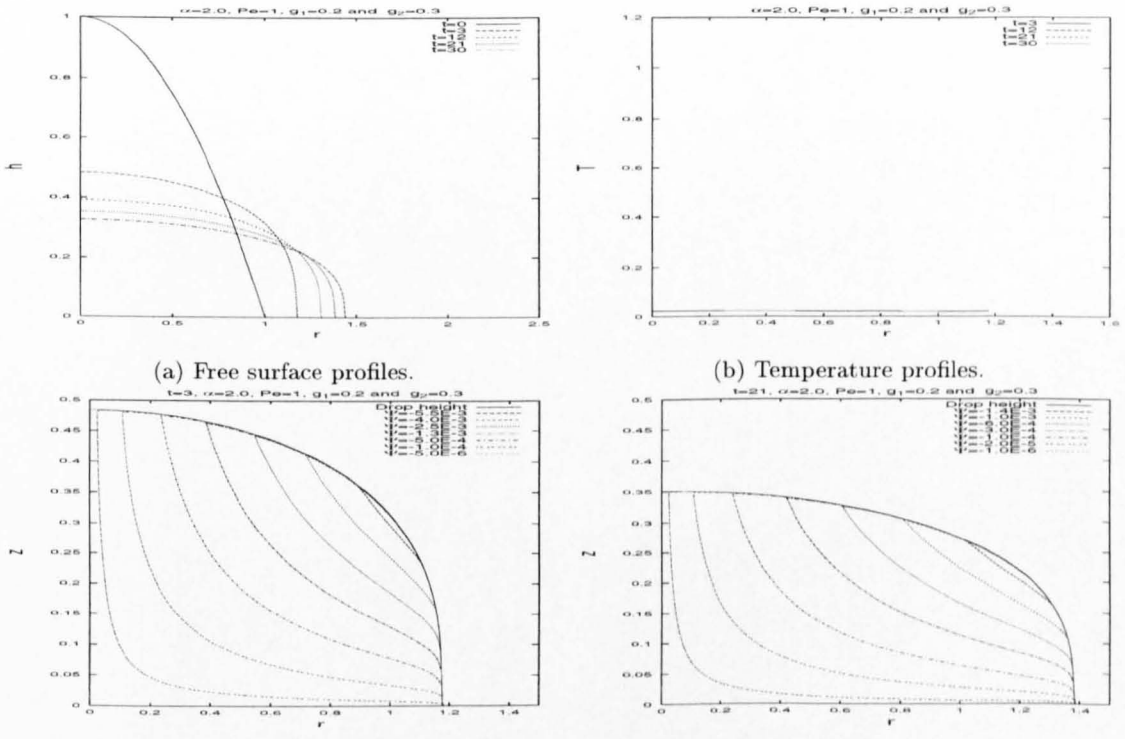

(a) Free surface profiles.

(b) Temperature profiles.

(c) Streamlines at $t = 3$.

(d) Streamlines at $t = 21$.

FIG. 4.35. Axisymmetric results with $\alpha = 2$ and Pe = 1.

The log-log plots in Figure 4.36 show that the spreading rates are initially isothermal, due to the small initial heat loss, and then as the Peclet number decreases the spreading again behaves isothermally as the fluid cools to zero. Similarly, the drop height at $r = 0$ is seen to fall isothermally for small Pe. The isothermal profile is shown to spread at $s \approx t^{0.124}$ and $h \approx t^{0.24}$ and shows good agreement to the similarity solutions in (2.2.13). Similarly the numerical results for Pe = 10^8 spread at the isothermal rate and agrees with the planar spreading case.

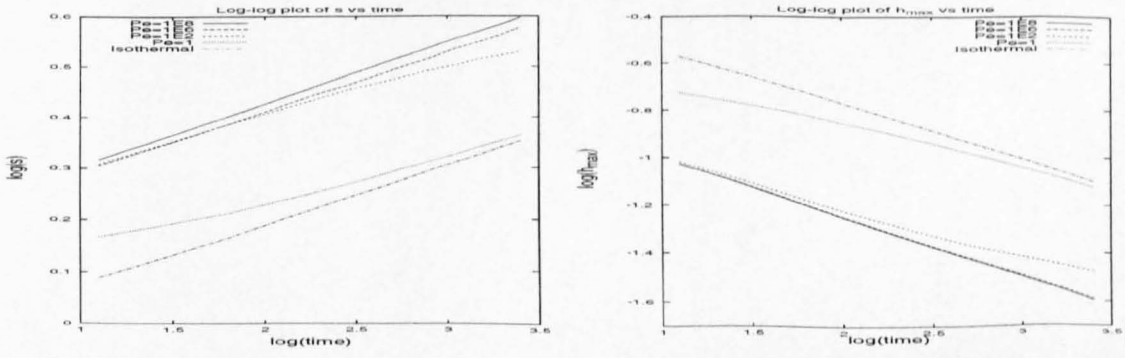

(a) Front location *vs* time.

(b) h_{max} *vs* time.

FIG. 4.36. Log-log plots of front location and h_{max} *vs* time for $\alpha = 2$.

The most interesting profiles again correspond to large α. Increasing α to 7.7 (which is the largest value of α before the numerics fail by producing oscillations) with $\Delta t = 2 \times 10^{-5}$ over the spatial and time ranges $0 \leq x \leq 3.5$, $0 \leq t \leq 10$ with 600 mesh points and with $\mathrm{Pe} = 10^5$ gives a steep flow front followed by a plateau, see Figure 4.37.

The log-log plots with $\alpha = 4.0$ show that as Pe decreases the spreading behaves more isothermally; see Figure 4.38(a). This is also seen for the drop height at $r = 0$ with small Pe, shown in Figure 4.38(b). The isothermal spreading rates and the results for $\mathrm{Pe} = 10^8$ show good agreement with the similarity solutions, see (2.2.13).

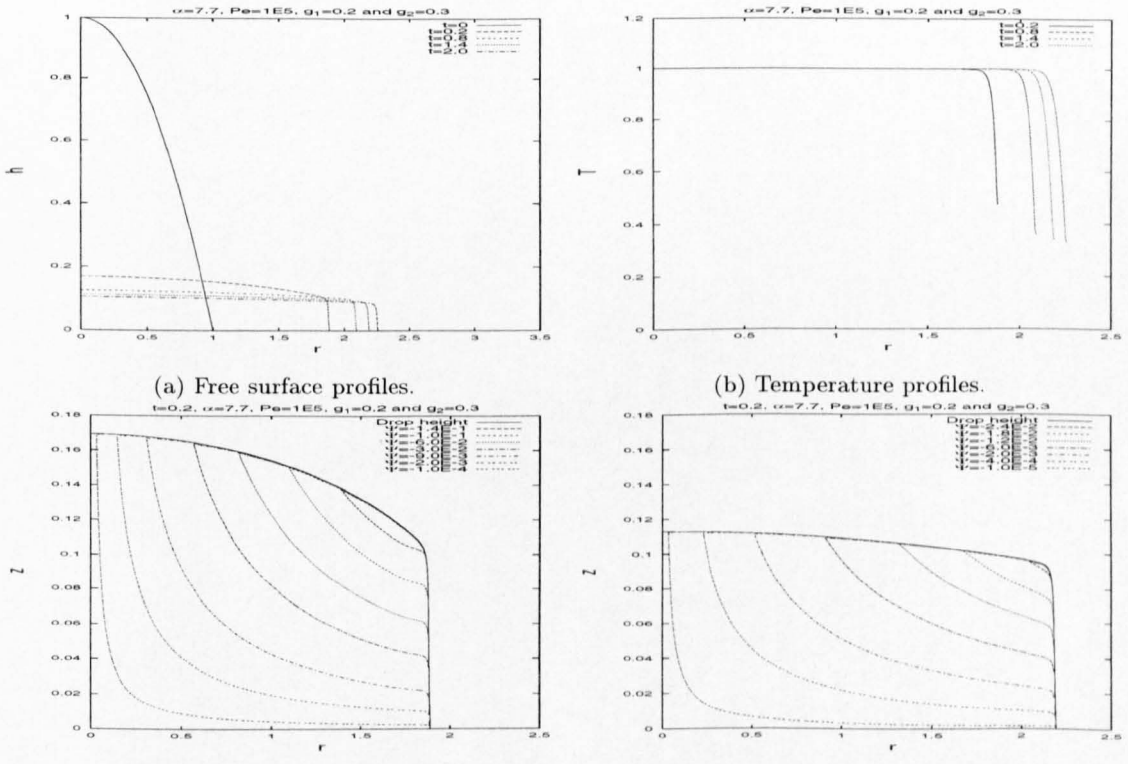

(a) Free surface profiles.

(b) Temperature profiles.

(c) Streamlines at $t = 0.2$.

(d) Streamlines at $t = 1.4$.

FIG. 4.37. Axisymmetric results with $\alpha = 7.7$ and $\mathrm{Pe} = 10^5$.

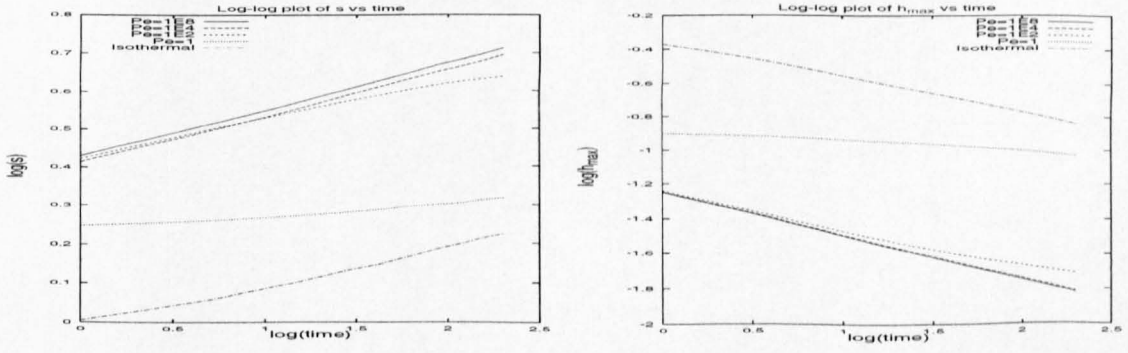

(a) Front location *vs* time.

(b) h_{max} *vs* time.

FIG. 4.38. Log-log plots of front location and h_{max} *vs* time for $\alpha = 4.0$.

The inclusion of the heat source term is now shown in Figure 4.39 with $\alpha = 4$. The temperature profiles can be seen in Figure 4.39(b) to be increasing with time for $\mathrm{Pe} = 10^4$ and $\dot{Q} = 200$. Decreasing the Peclet number to $\mathrm{Pe} = 10^2$ and with a heat source term of strength $\dot{Q} = 10$ in Figures 4.39(c)-4.39(d), again shows the growth in temperature. Note that the effective strength of the heat source term is dependent of the combination of the Peclet number and $\dot{Q}$, see equation (4.3.16). The results with $\mathrm{Pe} = 1$ in Figures 4.39(e)-4.39(f) show an initial large increase in temperature, but T eventually decreases with time due to the heat loss being greater than the gain from the source. The spreading of the corresponding free surface profiles is seen to be retarded as the temperature falls.

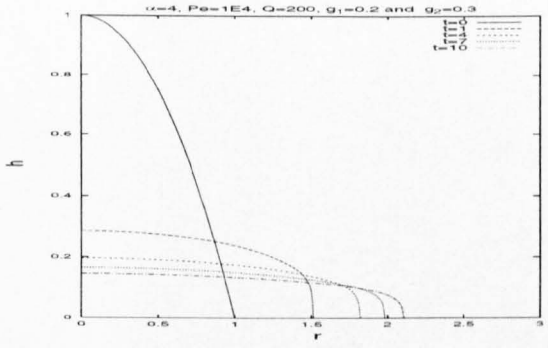

(a) Free surface profiles with $\mathrm{Pe} = 10^4$ and $\dot{Q} = 200$.

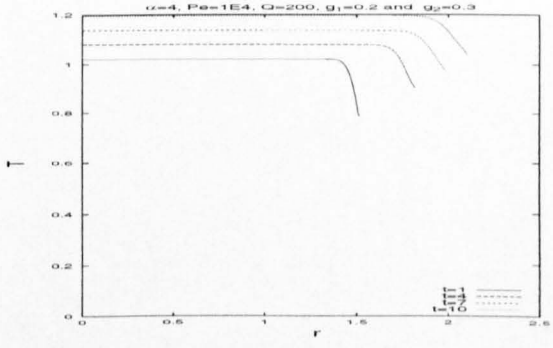

(b) Temperature profiles with $\mathrm{Pe} = 10^4$ and $\dot{Q} = 200$.

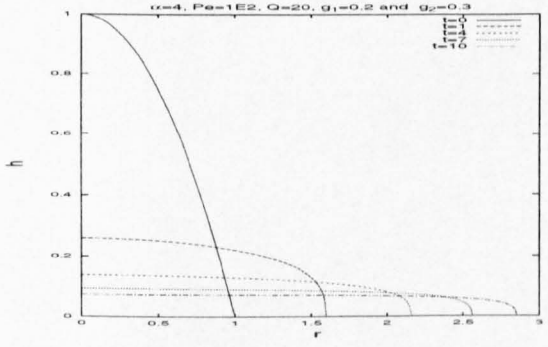

(c) Free surface profile with $\mathrm{Pe} = 10^2$ and $\dot{Q} = 20$.

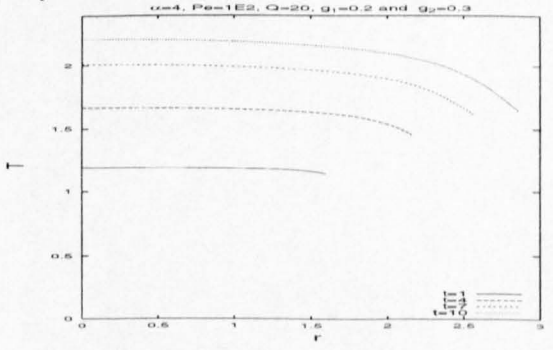

(d) Temperature profiles with $\mathrm{Pe} = 10^2$ and $\dot{Q} = 20$.

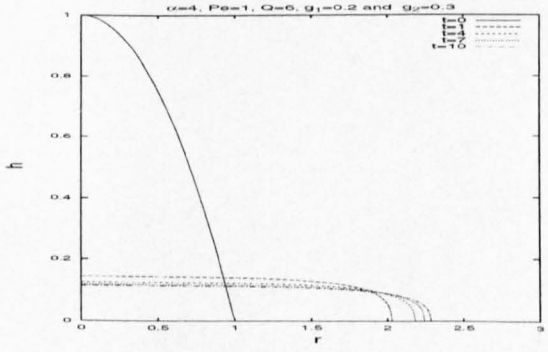

(e) Free surface profiles with $\mathrm{Pe} = 1$ and $\dot{Q} = 6$.

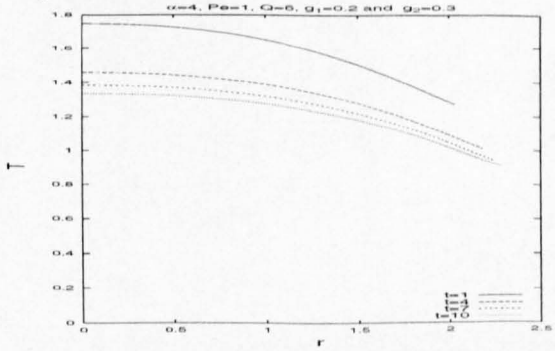

(f) Temperature profile with $\mathrm{Pe} = 1$ and $\dot{Q} = 6$.

FIG. 4.39. Axisymmetric results with a heat source, $\alpha = 4$, $g_1 = 0.2$, $g_2 = 0.3$ from $\mathrm{Pe} = 10^4$ to $\mathrm{Pe} = 1$.

4.6. Numerical results using the bi-viscosity model

To model in a simple way crusting around a spreading drop, the step function

$$\mu = \begin{cases} 2a - 1 & \text{if } T > T_m, \\ 1 & \text{if } T < T_m, \end{cases} \tag{4.6.1}$$

is used. Setting $a = 0.505$ gives a large viscosity ratio between the region with temperature less than $T_m = 0.5$ and the region with T greater than T_m (the initial temperature of the droplet is unity). Note that both regions are treated as being in liquid states, but the region near the boundary has a very large viscosity compared to the inner region. The following numerical results are in the range $0 \leq x \leq 3$ (x becomes r for axisymmetric spreading) with 600 mesh points in the x-direction and a time step of $\Delta t = 10^{-5}$. Setting $\mathrm{Pe} = 10^5$ gives a free surface profile with a steep flow front caused by the sharp increase in viscosity near the front, as shown in Figure 4.40(a). The temperature profiles are shown in Figure 4.40(b) and are similar to the previous profiles with $\mathrm{Pe} = 10^5$, as might be expected.

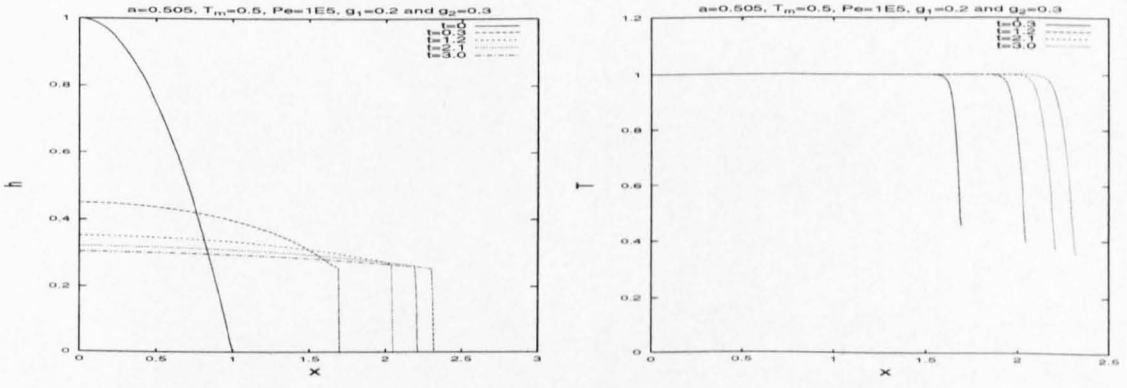

(a) Free surface profiles. (b) Temperature profiles.

FIG. 4.40. Free surface and temperature profiles using bi-viscosity model with $a = 0.505$ and $\mathrm{Pe} = 10^5$.

The streamlines show more interesting behaviour and are shown in Figure 4.41 at time $t = 3$. The

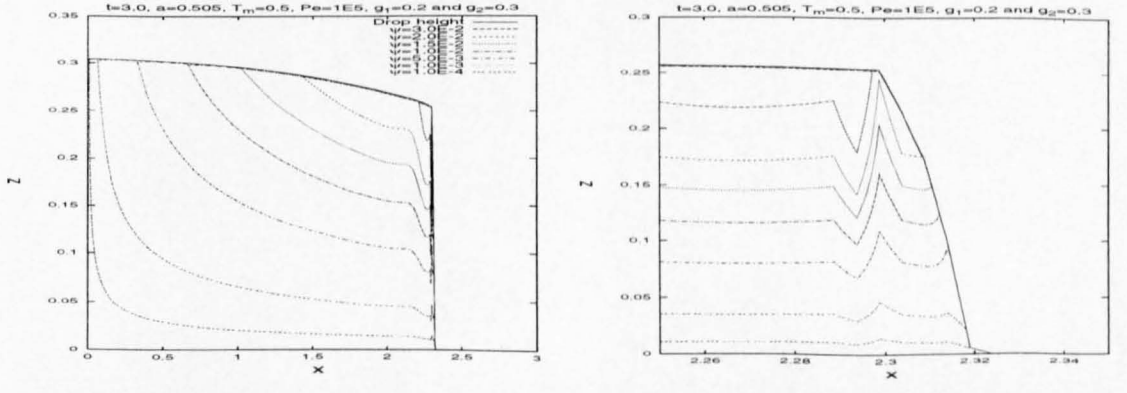

(a) Streamlines at $t = 4$. (b) Close up of streamlines in Figure 4.41(a).

FIG. 4.41. Streamlines at $t = 3.0$ using bi-viscosity model with $a = 0.505$ and $\mathrm{Pe} = 10^5$.

close up in Figure 4.41(b) shows the discontinuity in the viscosity relationship clearly affecting

the streamlines. This is in agreement with the previous chapters, where the flow is restricted as if approaching an almost solid boundary.

The results with Pe = 10^8, Figure 4.42, show almost isothermal behaviour, since $\mu = 2a - 1$ holds everywhere.

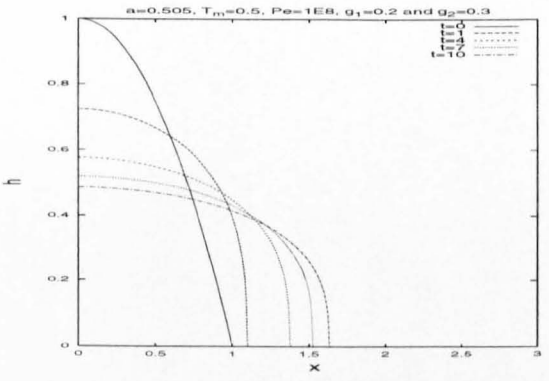

(a) Free surface profiles.

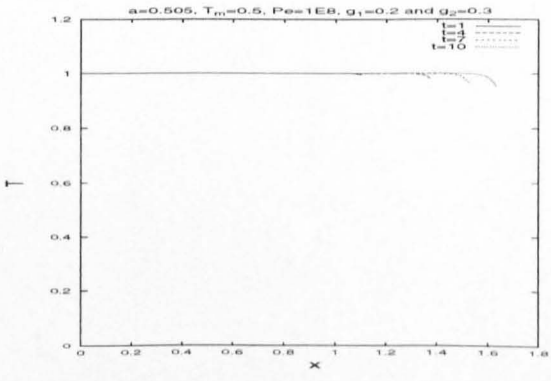

(b) Temperature profiles.

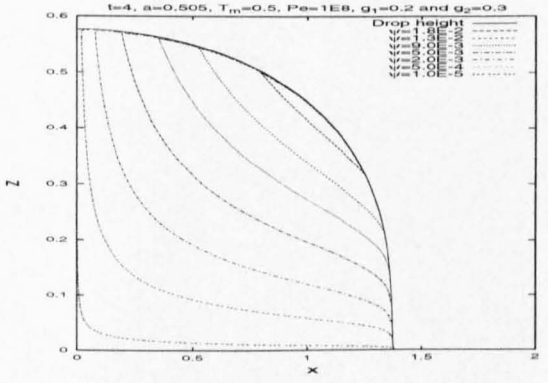

(c) Streamlines at $t = 4$.

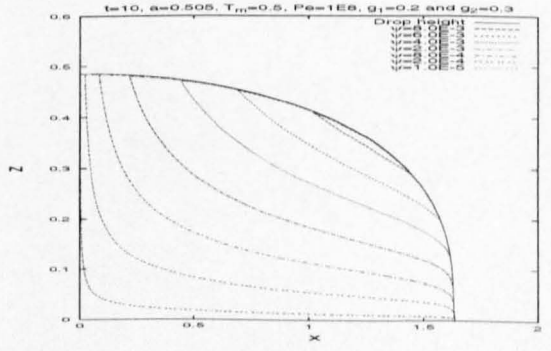

(d) Streamlines at $t = 10$.

FIG. 4.42. Results using the bi-viscosity model with $a = 0.505$ and Pe = 10^8.

The results in Figure 4.43 also show isothermal behaviour, but for different reasons, the temperature profiles being almost uniform (see Figure 4.43(b)). Once the temperature decreases below T_m ($T_m = 0.5$) the spreading is seen to be retarded compared to Figure 4.42(a).

Increasing a to 0.75, which implies a smaller viscosity contrast, gives height profiles similar to the isothermal model, as shown in Figure 4.44(a).

The axisymmetric free surface profiles are very similar to the two-dimensional ones. Setting Pe = 10^5 and $T_m = 0.5$ gives those in Figure 4.45(a). The streamlines show more interesting behaviour; see Figure 4.46. The close up in Figure 4.46(b) again exposes the discontinuity in the viscosity relationship.

Decreasing to Pe = 10, with $a = 0.505$, gives the results in Figure 4.47. The free surface can be seen to produce a rounder flow front which is caused by the temperature diffusing more rapidly as shown in Figure 4.47(b). The spreading can be seen to be retarded compared to the results

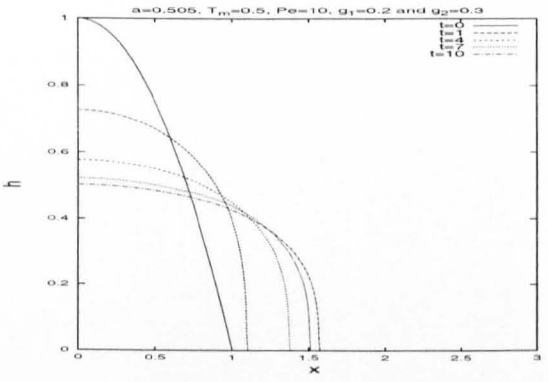

(a) Free surface profiles.

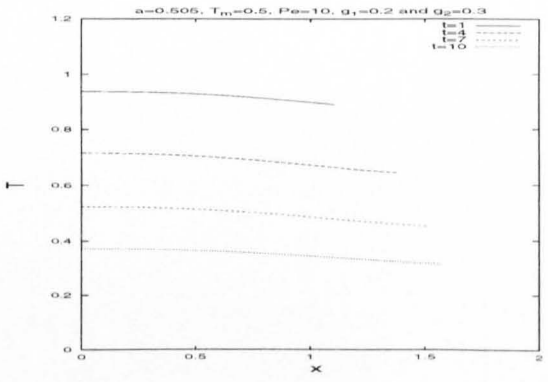

(b) Temperature profiles.

FIG. 4.43. Free surface and temperature profiles using bi-viscosity model with $a = 0.505$ and $\mathrm{Pe} = 10$.

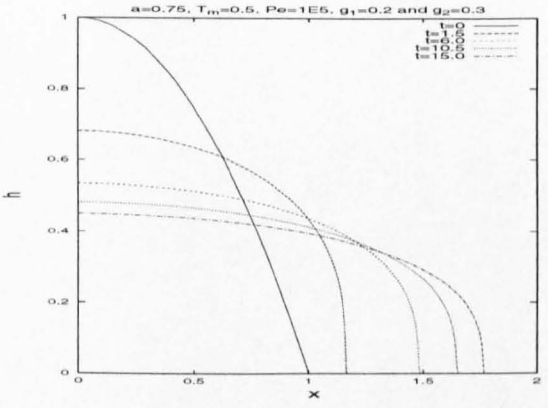

(a) Free surface profiles.

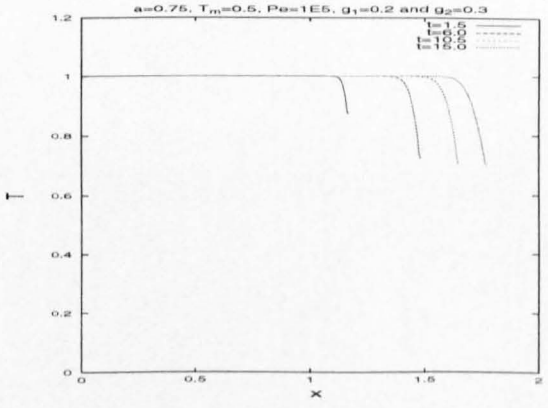

(b) Temperature profiles.

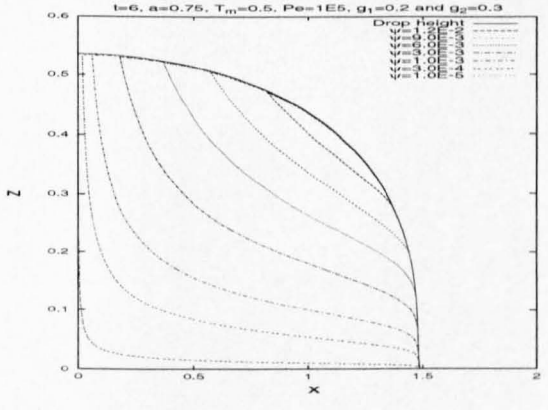

(c) Streamlines at $t = 6.0$.

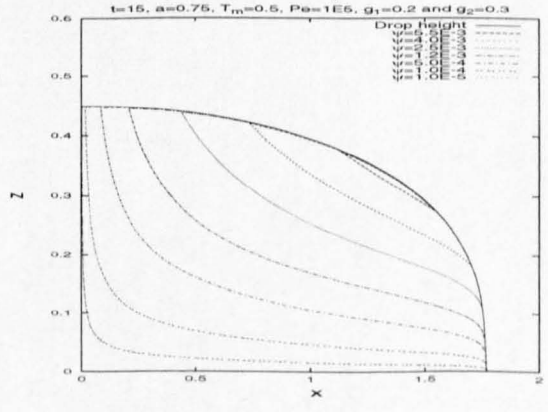

(d) Streamlines at $t = 15.0$.

FIG. 4.44. Results for the bi-viscosity model with $\mathrm{Pe} = 10^5$, $a = 0.75$ and $T_m = 0.5$.

with $\mathrm{Pe} = 10^5$ in Figure 4.45. This is due to the sharp increase in viscosity caused by the rapid temperature loss.

The inclusion of a line source for the bi-viscosity model gives similar free surface profiles as in the constant mass simulations in Figure 4.48(a). The influx boundary condition leads to the height of the droplet increasing and the temperature profiles for $\mathrm{Pe} = 10^5$ show little heat loss.

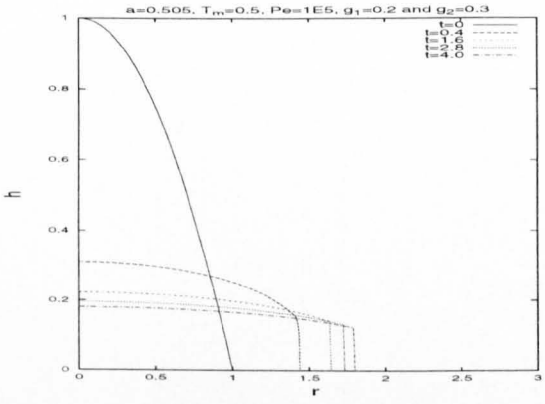

(a) Free surface profiles.

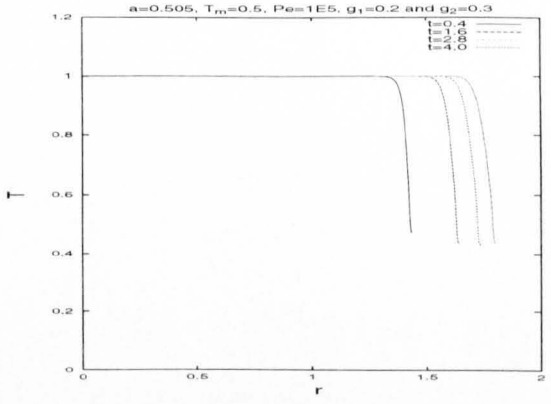

(b) Temperature profiles.

FIG. 4.45. Free surface and temperature profiles using bi-viscosity model with $a = 0.505$ and $\mathrm{Pe} = 10^5$.

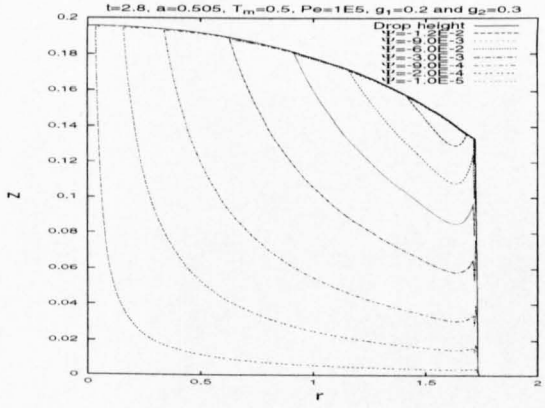

(a) Streamlines at $t = 2.8$.

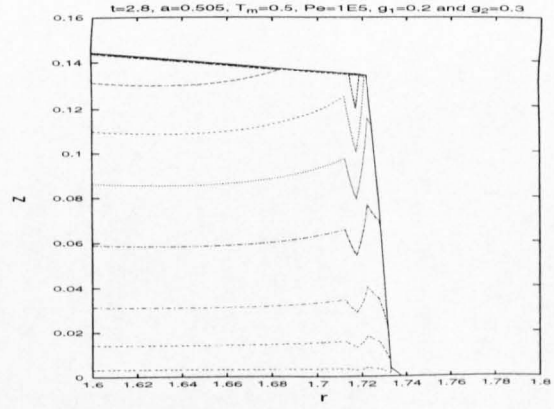

(b) Close up of streamlines in Figure 4.41(a).

FIG. 4.46. Streamlines at $t = 2.8$ using bi-viscosity model with $a = 0.505$ and $\mathrm{Pe} = 10^5$.

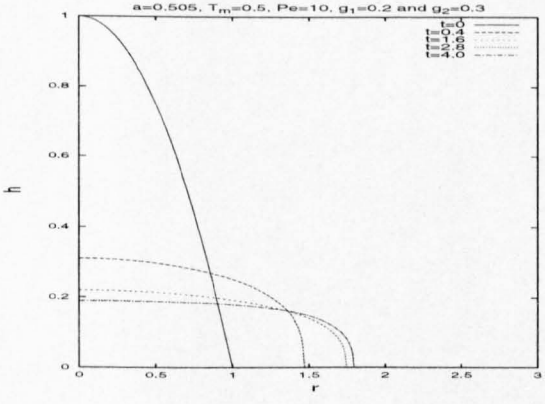

(a) Free surface profiles.

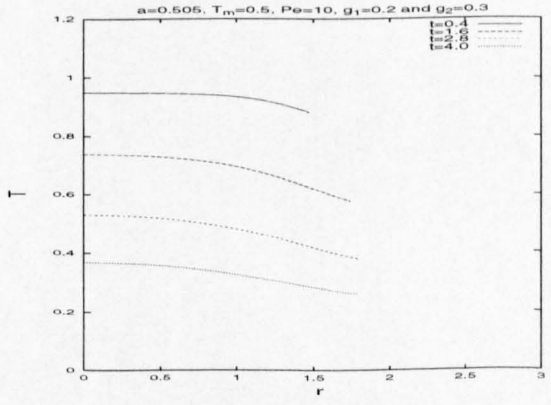

(b) Temperature profiles.

FIG. 4.47. Free surface profiles using bi-viscosity model with $a = 0.505$ and $\mathrm{Pe} = 10$.

The discontinuity in the viscosity relationship is shown to effect the streamlines again in Figure 4.49 which is caused by the sudden increase in viscosity in the cooler region of the fluid.

The final set of results with $\mathrm{Pe} = 10^2$ and $a = 0.505$ in Figure 4.50 show the initial profiles spreading isothermally (due to the temperature profiles initially being greater than 0.5 every

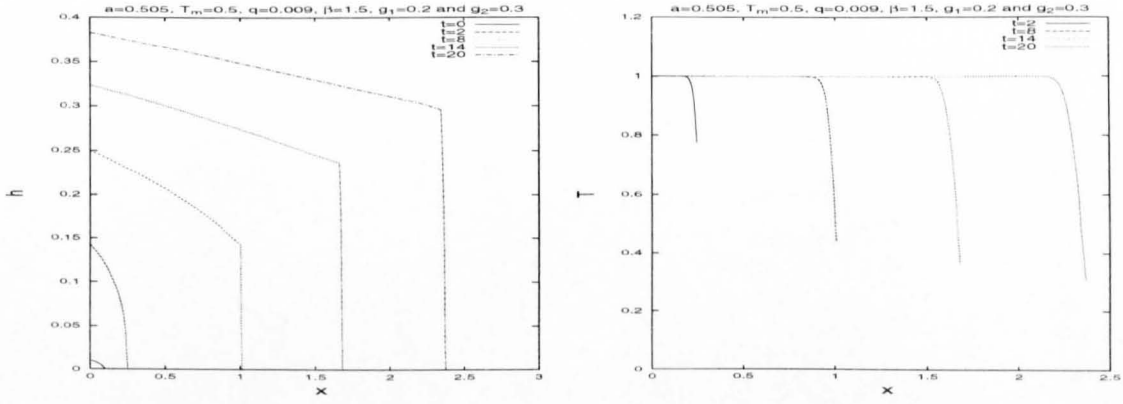

(a) Free surface profiles. (b) Temperature profiles.

FIG. 4.48. Free surface and temperature profiles with a line source at $a = 0.505$ and $\mathrm{Pe} = 10^5$.

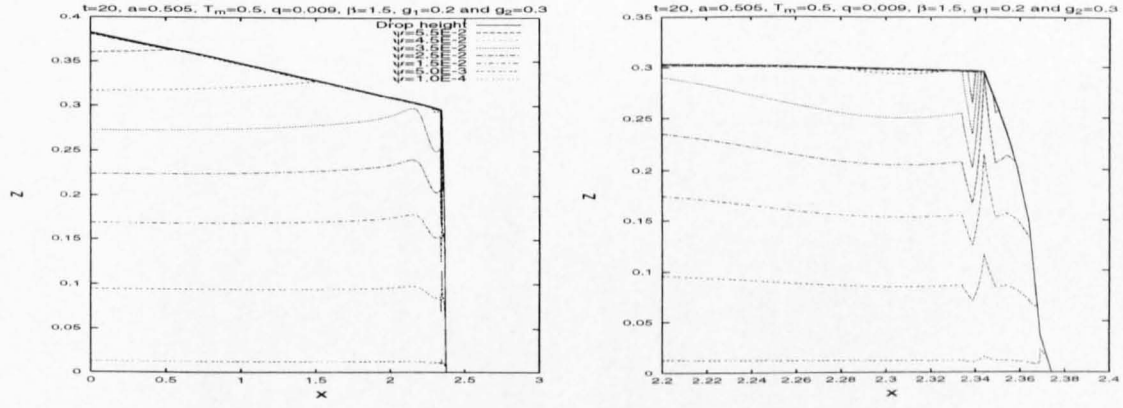

(a) Streamlines at $t = 20$. (b) Close up of streamlines in Figure 4.49(a).

FIG. 4.49. Streamlines at $t = 20$ using bi-viscosity model with $a = 0.505$ and $\mathrm{Pe} = 10^5$.

where). For larger time, as the temperature decreases, the free surface profiles are observed to develop a steep flow front as the droplet cools near the front.

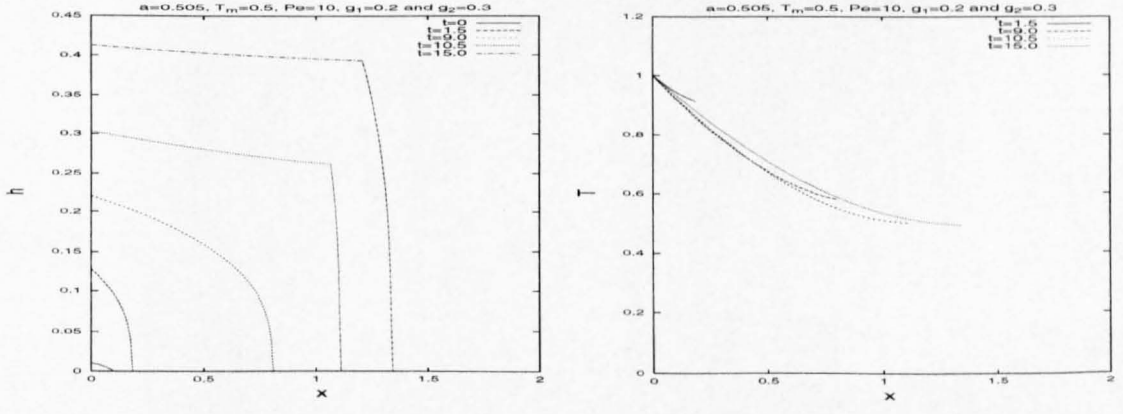

(a) Free surface profiles. (b) Temperature profiles.

FIG. 4.50. Free surface and temperature profiles with a line source at $a = 0.505$ and $\mathrm{Pe} = 10^2$.

4.7. Discussion

The numerical results for the constant viscosity case show good agreement between the FORTRAN 90 code developed using the finite difference schemes discussed above and the NAG routine D03PGF. This NAG routine showed good agreement with the similarity solutions described in Chapter 2. The numerical results have also been checked to be mesh-independent. The FORTRAN code is developed from the numerical algorithms described is Section 4.4, where the NAG routine can only be used for the isothermal case. Checks on the numerical simulations involved showed that the solutions conserved mass or, for the influx case, that the mass increased at the correct rate.

The fluid flow is again shown to develop a steep front and plateau when the coupling between the temperature and velocity field is sufficiently strong (i.e. for large α in the exponential viscosity relationship). The steep front only develops when the temperature field has cooled near the front and the majority of the fluid is still near its initial temperature, or is increasing due to a heat source. This causes an increase in viscosity in the flow front region and due to the condition of no-slip, the mass is redistributed to form the steep front, consistent with experimental data given by Stasiuk *et al.* (1993) for example. The steep flow front is also in agreement to the numerical model results in Bercovici (1994) as discussed below. The governing energy equation leads for large Peclet number ($\mathrm{Pe} = 10^8$, say) to isothermal flow with viscosity $\mu(T = 1)$. Decreasing the Peclet number (to $\mathrm{Pe} = 10^6$, say), the heat loss along the boundaries dominates and causes the steep flow morphology. The advection terms dominate again when $\mathrm{Pe} = 10^4$ and the free surface profiles take an isothermal form (with viscosity $\mu(1)$). Decreasing the Peclet number further leads to the heat loss dominating and the free surface to spread isothermally (with viscosity $\mu(0)$). The overall results are also in agreement with the results in the previous Chapter with the conduction limited temperature model. The only difference being that for large Peclet values the results are not initially isothermal ($\mu(T = 1)$).

The steep front is observed in the bi-viscosity model when the viscosity has a large contrast, consistent with earlier models in this thesis.

The viscosity relationship in the model discussed by Bercovici (1994) has an inverse dependence on the dimensionless temperature, θ, to capture the large variation in viscosity, μ, when the fluid is coldest; thus he takes

$$\mu(\theta) = \frac{\mu_h \mu_c}{\mu_h + (\mu_c - \mu_h)\theta}, \tag{4.7.1}$$

where μ_h and μ_c are the viscosities of the hottest and coldest liquid. Radial symmetry about $r = 0$ is assumed and the vertical velocity component is averaged out to give the governing equations for the free surface and temperature transport as:

$$\frac{\partial H}{\partial t} = \frac{1}{r}\frac{\partial}{\partial r}\left(r(1 + v\Theta)H^3 \frac{\partial H}{\partial r}\right), \tag{4.7.2}$$

$$\frac{\partial \Theta}{\partial t} = (1 + v\Theta)H^2 \frac{\partial H}{\partial r}\frac{\partial \Theta}{\partial r} - \frac{\Theta}{H^2}, \tag{4.7.3}$$

where $\upsilon = \mu^{'}/\mu_h$ is the viscosity contrast, $\mu^{'} = 9(\mu_c - \mu_h)/10$, H is the free surface and Θ is the averaged temperature with the ansatz

$$\theta = 6\Theta(r,t)\frac{z}{H}\left(1 - \frac{z}{H}\right). \tag{4.7.4}$$

The governing equation for the temperature transport in equation (4.7.3) can be seen to be a simplification of the temperature model used in this chapter in equation (4.3.16); where γ is set to zero and conduction is assumed negligible. The initial conditions adapted are:

$$H(r,0) = \begin{cases} (1 - r^2/r_N^2)^{1/3} & \text{for} \quad r \leq r_N, \\ 0 & \text{for} \quad r > r_N, \end{cases} \tag{4.7.5}$$

$$\Theta(r,0) = \exp(-(r/r_N)^{20}). \tag{4.7.6}$$

The Θ profile is thus almost isothermal, but with a smooth transition to the set zero ambient temperature at $r = r_N$.

Numerical results obtained by Bercovici (1994) with constant mass are illustrated in Figure 4.51. The first profile shows the initial conditions, where the initial temperature is shown on the right edge of the frame. The second frame shows the isothermal case, which agrees with Huppert (1982b); the bottom frame has $\upsilon = 10^3$ and shows the free surface developing a steep flow front followed by a plateau and showing similar behaviour to the results in this chapter. The results are equivalent to those with large Pe values (since $\gamma = 0$ in the Bercovici model); the results with $\mathrm{Pe} = 10^7$ in this chapter show the steep flow front and plateau developing.

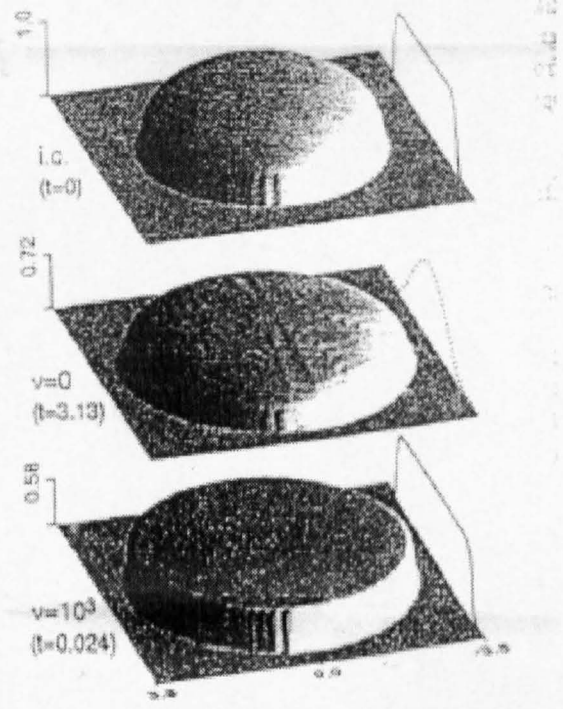

FIG. 4.51. Bercovici numerical results

Further results in Bercovici (1994) show the effects of a line source, which is seen to give a similar steep flow front profile.

In summary, the various parameters investigated in this chapter, show that if the fluid cools near the flow front and that the remaining body of fluid is still at its initial temperature or is increasing due to a heat source then the resulting free surface profiles will develop a steep front followed by a plateau.

CHAPTER FIVE

Three-dimensional temperature-dependent viscosity model with slow heat transfer through the boundaries

5.1. Introduction

This chapter concerns the spreading of gravity currents in three dimensions. The model from Chapter 4 is extended to include an extra spatial dimension on the substrate, considering the spreading of a liquid under gravity, g, on a flat horizontal smooth substrate, as shown in Figure 5.1.

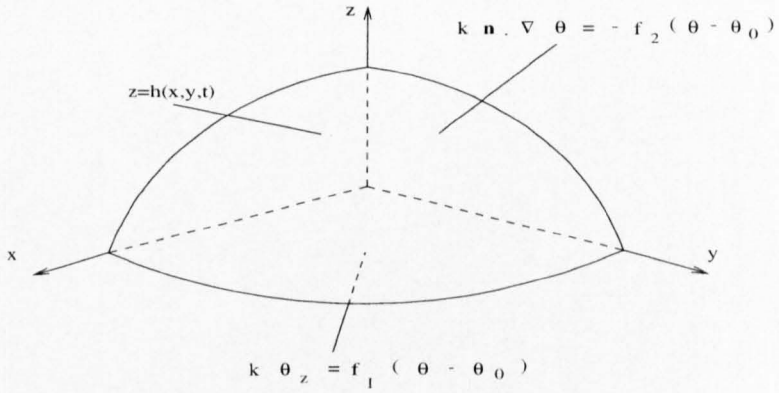

FIG. 5.1. Cartesian coordinates of spreading droplet

The substrate is the (x, y) plane and the free surface is given by $z = h(x, y, t)$. The horizontal velocity components are u and v, in the x and y-directions, respectively, and the vertical velocity, w, is in the z-direction. The liquid has an initial temperature θ_i and the ambient temperature of the gas and the substrate is taken to be θ_0. As in Chapter 4, the boundary temperature of the liquid is not necessarily the same as the ambient temperature and in order to formulate the boundary conditions for the temperature field, Newton's law of cooling is considered with Fourier's law. Using the analysis from Chapter 4, the boundary condition on the substrate is

$$k\frac{\partial\theta(x,y,0,t)}{\partial z} = f_1(\theta)\,(\theta(x,y,0,t) - \theta_0) \tag{5.1.1}$$

and on the free surface we have

$$k\boldsymbol{n}.\boldsymbol{\nabla}\theta = -f_2(\theta)\,(\theta(x,y,h,t) - \theta_0)\,, \tag{5.1.2}$$

where the normal, $\boldsymbol{n}$, to the free surface is given by equation (5.2.18), derived in the following section, to give

$$k\left(1+\left(\frac{\partial h}{\partial x}\right)^2+\left(\frac{\partial h}{\partial y}\right)^2\right)^{-\frac{1}{2}}\left(\frac{\partial\theta}{\partial z}-\frac{\partial h}{\partial x}\frac{\partial\theta}{\partial x}-\frac{\partial h}{\partial y}\frac{\partial\theta}{\partial y}\right) = -f_2(\theta)\,(\theta(x,y,h,t)-\theta_0)\,. \tag{5.1.3}$$

The variables $f_1(\theta)$ and $f_2(\theta)$ are the heat-exchange coefficients (which are functions of the temperature θ) giving a measure of the heat transfer across the boundaries per unit temperature per unit time per unit area, and k is the thermal conductivity.

5.2. Governing equations and derivation in three-dimensions

To formulate the governing equations for the free surface of the liquid and the temperature evolution equation, the primitive equations are first non-dimensionalised. The Cartesian three-dimensional Navier-Stokes equations for a Newtonian liquid of constant density, ρ, and variable viscosity, μ, are given by

$$\rho\left(\frac{\partial u}{\partial t}+u\frac{\partial u}{\partial x}+v\frac{\partial u}{\partial y}+w\frac{\partial u}{\partial z}\right)=-\frac{\partial p}{\partial x}+\frac{\partial}{\partial x}\left(\mu\frac{\partial u}{\partial x}\right)+\frac{\partial}{\partial y}\left(\mu\frac{\partial u}{\partial y}\right)+\frac{\partial}{\partial z}\left(\mu\frac{\partial u}{\partial z}\right)$$
$$+\frac{d\mu}{d\theta}\left(\frac{\partial\theta}{\partial x}\frac{\partial u}{\partial x}+\frac{\partial\theta}{\partial y}\frac{\partial v}{\partial x}+\frac{\partial\theta}{\partial z}\frac{\partial w}{\partial x}\right), \tag{5.2.1}$$

$$\rho\left(\frac{\partial v}{\partial t}+u\frac{\partial v}{\partial x}+v\frac{\partial v}{\partial y}+w\frac{\partial v}{\partial z}\right)=-\frac{\partial p}{\partial y}+\frac{\partial}{\partial x}\left(\mu\frac{\partial v}{\partial x}\right)+\frac{\partial}{\partial y}\left(\mu\frac{\partial v}{\partial y}\right)+\frac{\partial}{\partial z}\left(\mu\frac{\partial v}{\partial z}\right)$$
$$+\frac{d\mu}{d\theta}\left(\frac{\partial\theta}{\partial x}\frac{\partial u}{\partial y}+\frac{\partial\theta}{\partial y}\frac{\partial v}{\partial y}+\frac{\partial\theta}{\partial z}\frac{\partial w}{\partial y}\right), \tag{5.2.2}$$

$$\rho\left(\frac{\partial w}{\partial t}+u\frac{\partial w}{\partial x}+v\frac{\partial w}{\partial y}+w\frac{\partial w}{\partial z}\right)=-\frac{\partial p}{\partial z}+\frac{\partial}{\partial x}\left(\mu\frac{\partial w}{\partial x}\right)+\frac{\partial}{\partial y}\left(\mu\frac{\partial w}{\partial y}\right)+\frac{\partial}{\partial z}\left(\mu\frac{\partial w}{\partial z}\right)$$
$$+\frac{d\mu}{d\theta}\left(\frac{\partial\theta}{\partial x}\frac{\partial u}{\partial z}+\frac{\partial\theta}{\partial y}\frac{\partial v}{\partial z}+\frac{\partial\theta}{\partial z}\frac{\partial w}{\partial z}\right)-\rho g, \tag{5.2.3}$$

where p denotes pressure, and the continuity equation is

$$\frac{\partial u}{\partial x}+\frac{\partial v}{\partial y}+\frac{\partial w}{\partial z}=0. \tag{5.2.4}$$

The energy equation governing the temperature evolution is

$$\rho c\left(\frac{\partial\theta}{\partial t}+u\frac{\partial\theta}{\partial x}+v\frac{\partial\theta}{\partial y}+w\frac{\partial\theta}{\partial z}\right)=k\left(\frac{\partial^2\theta}{\partial x^2}+\frac{\partial^2\theta}{\partial y^2}+\frac{\partial^2\theta}{\partial z^2}\right)+\dot{q}, \tag{5.2.5}$$

where c is the specific heat of the liquid and $\dot{q}$ is the strength of a heat source. We define the aspect ratio as $\epsilon=h_0/l_0$, where l_0 is a typical length scale in the horizontal direction and h_0 is the scale in the z-direction. Similarly, U_0 is a typical horizontal velocity in the x and y-direction and μ_0 is a typical viscosity scale. The equations are non-dimensionalised by introducing

$$\begin{gathered}x=l_0x^*,\quad y=l_0y^*,\quad z=h_0z^*,\quad u=U_0u^*,\quad v=U_0v^*,\quad w=\epsilon U_0w^*,\\ \mu=\mu_0\mu^*,\quad T=\frac{\theta-\theta_1}{\Delta\theta},\quad \dot{q}=\frac{k\Delta\theta}{h_0^2}\dot{q}^*,\quad t=\frac{l_0}{U_0}t^*,\quad\text{and}\quad p=\frac{U_0\mu_0l_0}{h_0^2}p^*.\end{gathered} \tag{5.2.6}$$

The temperature is measured relative to θ_1 in units $\Delta\theta$ where, $\Delta\theta=\theta_i-\theta_0$ and $\theta_1=\theta_0$.

Dropping the star notation for clarity, the Navier-Stokes equations and energy equation transform to

$$\epsilon^2R\left(\frac{\partial u}{\partial t}+u\frac{\partial u}{\partial x}+v\frac{\partial u}{\partial y}+w\frac{\partial u}{\partial z}\right)=-\frac{\partial p}{\partial x}+\epsilon^2\frac{\partial}{\partial x}\left(\mu\frac{\partial u}{\partial x}\right)+\epsilon^2\frac{\partial}{\partial y}\left(\mu\frac{\partial u}{\partial y}\right)$$
$$+\frac{\partial}{\partial z}\left(\mu\frac{\partial u}{\partial z}\right)+\epsilon^2\frac{d\mu}{dT}\left(\frac{\partial T}{\partial x}\frac{\partial u}{\partial x}+\frac{\partial T}{\partial y}\frac{\partial v}{\partial x}+\frac{\partial T}{\partial z}\frac{\partial w}{\partial x}\right), \tag{5.2.7}$$

$$\epsilon^2 R\left(\frac{\partial v}{\partial t}+u\frac{\partial v}{\partial x}+v\frac{\partial v}{\partial y}+w\frac{\partial v}{\partial z}\right)=-\frac{\partial p}{\partial y}+\epsilon^2\frac{\partial}{\partial x}\left(\mu\frac{\partial v}{\partial x}\right)+\epsilon^2\frac{\partial}{\partial y}\left(\mu\frac{\partial v}{\partial y}\right)$$
$$+\frac{\partial}{\partial z}\left(\mu\frac{\partial v}{\partial z}\right)+\epsilon^2\frac{d\mu}{dT}\left(\frac{\partial T}{\partial x}\frac{\partial u}{\partial y}+\frac{\partial T}{\partial y}\frac{\partial v}{\partial y}+\frac{\partial T}{\partial z}\frac{\partial w}{\partial y}\right), \quad (5.2.8)$$

$$\epsilon^4 R\left(\frac{\partial w}{\partial t}+u\frac{\partial w}{\partial x}+v\frac{\partial w}{\partial y}+w\frac{\partial w}{\partial z}\right)=-\frac{\partial p}{\partial z}+\epsilon^4\frac{\partial}{\partial x}\left(\mu\frac{\partial w}{\partial x}\right)+\epsilon^4\frac{\partial}{\partial y}\left(\mu\frac{\partial w}{\partial y}\right)$$
$$+\epsilon^2\frac{\partial}{\partial z}\left(\mu\frac{\partial w}{\partial z}\right)+\epsilon^2\frac{d\mu}{dT}\left(\frac{\partial T}{\partial x}\frac{\partial u}{\partial z}+\frac{\partial T}{\partial y}\frac{\partial v}{\partial z}+\frac{\partial T}{\partial z}\frac{\partial w}{\partial z}\right)-\frac{\rho\epsilon^3 g l_0^2}{\mu_0 U_0}, \quad (5.2.9)$$

$$\frac{\partial u}{\partial x}+\frac{\partial v}{\partial y}+\frac{\partial w}{\partial z}=0, \quad (5.2.10)$$

$$\epsilon^2\mathrm{Pe}\left(\frac{\partial T}{\partial t}+u\frac{\partial T}{\partial x}+v\frac{\partial T}{\partial y}+w\frac{\partial T}{\partial z}\right)=\epsilon^2\frac{\partial^2 T}{\partial x^2}+\epsilon^2\frac{\partial^2 T}{\partial y^2}+\frac{\partial^2 T}{\partial z^2}+\dot{q}, \quad (5.2.11)$$

where the Reynolds number, Prandtl number and Peclet number are defined respectively as

$$R=\frac{\rho U_0 l_0}{\mu_0}, \quad \mathrm{Pr}=\frac{c\mu_0}{k} \quad \text{and} \quad \mathrm{Pe}=R\mathrm{Pr}=\frac{\rho c U_0 l_0}{k}.$$

On assuming $\epsilon^2 \ll 1$ (small aspect ratio) and $\epsilon^2 R \ll 1$ (small reduced Reynolds number) the Navier-Stokes equations are reduced to the following lubrication equations

$$-\frac{\partial p}{\partial x}+\frac{\partial}{\partial z}\left(\mu\frac{\partial u}{\partial z}\right)=0, \quad (5.2.12)$$

$$-\frac{\partial p}{\partial y}+\frac{\partial}{\partial z}\left(\mu\frac{\partial v}{\partial z}\right)=0, \quad (5.2.13)$$

$$\frac{\partial p}{\partial z}=-1. \quad (5.2.14)$$

The boundary conditions on the substrate and free surface are now considered. Along the impermeable, no-slip substrate, the velocities u, v and w are zero. On the free surface the kinematic condition states that liquid particles on the surface remain on the surface. Thus the material derivative of $F(x,y,z,t)=z-h(x,y,t)$ is equal to zero, i.e.

$$\frac{\partial F}{\partial t}+(\mathbf{u}.\nabla)F=0,$$

or

$$\frac{\partial h}{\partial t}+u\frac{\partial h}{\partial x}+v\frac{\partial h}{\partial y}-w=0. \quad (5.2.15)$$

The components of stress σ on the free surface are given by

$$\sigma_i=T_{ij}n_j, \quad (5.2.16)$$

where T_{ij} is the stress tensor and the free surface has unit normal $\mathbf{n}$. T_{ij} is given by

$$T_{ij}=-p\delta_{ij}+\mu\left(\frac{\partial u_i}{\partial x_j}+\frac{\partial u_j}{\partial x_i}\right), \quad (5.2.17)$$

where δ_{ij} is the Kronecker delta. The unit normal to the free surface is

$$\boldsymbol{n}=\frac{1}{|\boldsymbol{\nabla}F(x,y,z,t)|}\boldsymbol{\nabla}F(x,y,z,t),$$
$$=\left(1+\left(\frac{\partial h}{\partial x}\right)^2+\left(\frac{\partial h}{\partial y}\right)^2\right)^{-\frac{1}{2}}\left(-\frac{\partial h}{\partial x},-\frac{\partial h}{\partial y},1\right), \quad (5.2.18)$$

where $F(x, y, z, t)$ is as defined above. Rescaling the normal derivative using (5.2.6), with $\epsilon^2 \ll 1$ leading to

$$\left(1 + \epsilon^2 \left(\frac{\partial h^*}{\partial x^*}\right)^2 + \epsilon^2 \left(\frac{\partial h^*}{\partial y^*}\right)^2\right)^{-\frac{1}{2}} \sim 1, \tag{5.2.19}$$

gives

$$\boldsymbol{n} \sim (-\epsilon \frac{\partial h^*}{\partial x^*}, -\epsilon \frac{\partial h^*}{\partial y^*}, 1). \tag{5.2.20}$$

The component of normal stress in the x-direction at the surface is

$$\sigma_1 = \frac{U_0\mu_0}{h_0}\frac{\partial h^*}{\partial x^*}p^* - \frac{2\mu_0 U_0 h_0}{l_0^2}\mu^*\frac{\partial u^*}{\partial x^*}\frac{\partial h^*}{\partial x^*} - \frac{\mu_0 U_0 h_0}{l_0^2}\mu^*\left(\frac{\partial u^*}{\partial y^*} + \frac{\partial v^*}{\partial x^*}\right)\frac{\partial h^*}{\partial y^*} + \mu_0\mu^*\left(\frac{U_0}{h_0}\frac{\partial u^*}{\partial z^*} + \frac{h_0 U_0}{l_0^2}\frac{\partial w^*}{\partial x^*}\right), \tag{5.2.21}$$

that in the y-direction is

$$\sigma_2 = -\frac{\mu_0 U_0 h_0}{l_0^2}\mu^*\left(\frac{\partial v^*}{\partial x^*} + \frac{\partial u^*}{\partial y^*}\right)\frac{\partial h^*}{\partial x^*} + \frac{U_0\mu_0}{h_0}\frac{\partial h^*}{\partial y^*}p^* - \frac{2\mu_0 U_0 h_0}{l_0^2}\mu^*\frac{\partial v^*}{\partial y^*}\frac{\partial h^*}{\partial y^*} + \mu_0\mu^*\left(\frac{U_0}{h_0}\frac{\partial v^*}{\partial z^*} + \frac{h_0 U_0}{l_0^2}\frac{\partial w^*}{\partial y^*}\right), \tag{5.2.22}$$

and that in the z-direction is

$$\sigma_3 = -\frac{\mu_0 h_0}{l_0}\mu^*\frac{\partial h^*}{\partial x^*}\left(\frac{h_0 U_0}{l_0^2}\frac{\partial w^*}{\partial x^*} + \frac{U_0}{h_0}\frac{\partial u^*}{\partial z^*}\right) - \frac{\mu_0 h_0}{l_0}\mu^*\frac{\partial h^*}{\partial y^*}\left(\frac{h_0 U_0}{l_0^2}\frac{\partial w^*}{\partial y^*} + \frac{U_0}{h_0}\frac{\partial v^*}{\partial z^*}\right) - \frac{U_0\mu_0 l_0}{h_0^2}p^* + \frac{2\mu_0 h_0 U_0}{l_0^2}\mu^*\frac{\partial w^*}{\partial z^*}. \tag{5.2.23}$$

Writing

$$\sigma_1^* = \frac{U_0\mu_0}{h_0}\sigma_1, \quad \sigma_2^* = \frac{U_0\mu_0}{h_0}\sigma_2 \quad \text{and} \quad \sigma_3^* = \frac{U_0\mu_0 l_0}{h_0^2}\sigma_3,$$

where the star notation is again dropped, the leading order terms in (5.2.21), (5.2.22) and (5.2.23) are

$$\sigma_1 = \frac{\partial h}{\partial x}p + \mu\frac{\partial u}{\partial z}, \tag{5.2.24}$$

$$\sigma_2 = \frac{\partial h}{\partial y}p + \mu\frac{\partial v}{\partial z}, \tag{5.2.25}$$

$$\sigma_3 = -p. \tag{5.2.26}$$

Assuming that stress is continuous on the interface and that $\mu_{gas} \ll \mu_{liquid}$ (and neglecting surface tension) requires $\sigma_1 = \sigma_2 = \sigma_3 = 0$, giving

$$\text{at } z = h \quad p = 0, \quad \mu\frac{\partial u}{\partial z} = 0 \quad \text{and} \quad \mu\frac{\partial v}{\partial z} = 0. \tag{5.2.27}$$

We now derive the governing free surface and temperature equations.

5.2.1. *Three-dimensional free surface equation derivation*

The lubrication equations with $\mu = \mu(T)$ and $T = T(x, y, z, t)$, and the boundary conditions are summarised below.

$$-\frac{\partial p}{\partial x} + \frac{\partial}{\partial z}\left(\mu \frac{\partial u}{\partial z}\right) = 0, \tag{5.2.28}$$

$$-\frac{\partial p}{\partial y} + \frac{\partial}{\partial z}\left(\mu \frac{\partial v}{\partial z}\right) = 0, \tag{5.2.29}$$

$$\frac{\partial p}{\partial z} = -1, \tag{5.2.30}$$

$$\frac{\partial u}{\partial x} + \frac{\partial v}{\partial y} + \frac{\partial w}{\partial z} = 0, \tag{5.2.31}$$

subject to

$$\text{on } z = 0 \quad u = 0, \quad v = 0 \quad \text{and} \quad w = 0, \tag{5.2.32}$$

$$\text{on } z = h \quad p = 0, \quad \mu \frac{\partial u}{\partial z} = 0, \quad \mu \frac{\partial v}{\partial z} = 0, \quad \text{and} \quad \frac{\partial h}{\partial t} + u\frac{\partial h}{\partial x} + v\frac{\partial h}{\partial y} - w = 0. \tag{5.2.33}$$

From equations (5.2.30) and (5.2.33) we have

$$p = h(x, y, t) - z, \tag{5.2.34}$$

and on substituting this in (5.2.28) we obtain

$$\frac{\partial}{\partial z}\left(\mu \frac{\partial u}{\partial z}\right) = \frac{\partial h}{\partial x}.$$

Integrating with respect to z and using (5.2.33) gives

$$\frac{\partial u}{\partial z} = \frac{1}{\mu}\frac{\partial h}{\partial x}(z - h). \tag{5.2.35}$$

Integrating again and satisfying the no-slip conditions gives

$$u = \frac{\partial h}{\partial x}\int_0^z \frac{(z' - h)}{\mu} dz'. \tag{5.2.36}$$

Similarly substituting the pressure equation (5.2.34) in (5.2.29) gives,

$$v = \frac{\partial h}{\partial y}\int_0^z \frac{(z' - h)}{\mu} dz'. \tag{5.2.37}$$

From the equation of continuity (5.2.31),

$$\frac{\partial w}{\partial z} = -\left(\frac{\partial^2 h}{\partial x^2} + \frac{\partial^2 h}{\partial y^2}\right)\int_0^z \frac{(z' - h)}{\mu} dz' + \frac{\partial h}{\partial x}\int_0^z \left(\frac{1}{\mu}\frac{\partial h}{\partial x} + \frac{\partial \mu}{\partial x}\frac{(z' - h)}{\mu^2}\right) dz' + \frac{\partial h}{\partial y}\int_0^z \left(\frac{1}{\mu}\frac{\partial h}{\partial y} + \frac{\partial \mu}{\partial y}\frac{(z' - h)}{\mu^2}\right) dz',$$

which subject to $w = 0$ on $z = 0$ gives

$$w = -\left(\frac{\partial^2 h}{\partial x^2} + \frac{\partial^2 h}{\partial y^2}\right)\int_0^z \int_0^{z''} \frac{(z' - h)}{\mu} dz' dz'' + \frac{\partial h}{\partial x}\int_0^z \int_0^{z''} \left(\frac{1}{\mu}\frac{\partial h}{\partial x} + \frac{\partial \mu}{\partial x}\frac{(z' - h)}{\mu^2}\right) dz' dz'' + \frac{\partial h}{\partial y}\int_0^z \int_0^{z''} \left(\frac{1}{\mu}\frac{\partial h}{\partial y} + \frac{\partial \mu}{\partial y}\frac{(z' - h)}{\mu^2}\right) dz' dz''. \tag{5.2.38}$$

Equation (5.2.38) can be simplified by changing the order of the integration: the integral has the form

$$\int_0^z \int_0^{z''} f(x,y,z,t)dz'dz'', \tag{5.2.39}$$

which on interchanging the order becomes

$$\int_0^z \int_{z'}^{z''} f(x,y,z,t)dz''dz' = \int_0^z f(x,y,z,t)(z-z')dz'. \tag{5.2.40}$$

Hence equation (5.2.38) implies

$$w = \frac{\partial}{\partial x}\left(\int_0^z \frac{(h-z')(z-z')}{\mu}dz'\frac{\partial h}{\partial x}\right) + \frac{\partial}{\partial y}\left(\int_0^z \frac{(h-z')(z-z')}{\mu}dz'\frac{\partial h}{\partial y}\right). \tag{5.2.41}$$

Finally, using the kinematic condition at $z = h$ and the velocity equations (5.2.36), (5.2.37) and (5.2.41) gives

$$\frac{\partial h}{\partial t} - \left(\frac{\partial^2 h}{\partial x^2} + \frac{\partial^2 h}{\partial y^2}\right)\int_0^h \frac{(z-h)^2}{\mu}dz + \frac{\partial h}{\partial x}\int_0^h \left(\frac{2(z-h)}{\mu}\frac{\partial h}{\partial x} + \frac{\partial \mu}{\partial x}\frac{(z-h)^2}{\mu^2}\right)dz$$
$$+\frac{\partial h}{\partial y}\int_0^h \left(\frac{2(z-h)}{\mu}\frac{\partial h}{\partial y} + \frac{\partial \mu}{\partial y}\frac{(z-h)^2}{\mu^2}\right)dz = 0. \tag{5.2.42}$$

The above equation simplifies to

$$\frac{\partial h}{\partial t} = \frac{\partial}{\partial x}\left(\int_0^h \frac{(z-h)^2}{\mu}dz\frac{\partial h}{\partial x}\right) + \frac{\partial}{\partial y}\left(\int_0^h \frac{(z-h)^2}{\mu}dz\frac{\partial h}{\partial y}\right). \tag{5.2.43}$$

Equation (5.2.43) governs the evolution of a drop of liquid with temperature-dependent viscosity in Cartesian coordinates. Writing it in vector from gives

$$\frac{\partial h}{\partial t} = \nabla_{(x,y)}\cdot\left(D\nabla_{(x,y)}h\right), \tag{5.2.44}$$

where the 'diffusivity' is given by

$$D = \int_0^h \frac{(z-h)^2}{\mu}dz. \tag{5.2.45}$$

5.2.2. *Three-dimensional temperature evolution equation derivation*

To derive the governing evolution equation for the temperature field in three dimensions, the corresponding temperature boundary conditions on the free surface and substrate ((5.1.1) and (5.1.3)) are non-dimensionalised using (5.2.6). The non-dimensionalised temperature evolution equation, from (5.2.11), can be written as

$$\frac{\partial T}{\partial t} + u\frac{\partial T}{\partial x} + v\frac{\partial T}{\partial y} + w\frac{\partial T}{\partial z} = \kappa\left(\frac{\partial^2 T}{\partial z^2} + \epsilon^2\frac{\partial^2 T}{\partial x^2} + \epsilon^2\frac{\partial^2 T}{\partial y^2} + \dot{q}\right), \tag{5.2.46}$$

where κ^{-1} is the reduced Peclet number such that

$$\kappa = \frac{1}{\epsilon^2 \mathrm{Pe}}, \quad \text{and} \quad \epsilon = \frac{h_0}{l_0} \text{ (aspect ratio)}.$$

The non-dimensionalised boundary conditions on $z = 0$ and $z = h(x,y,t)$ are, respectively,

$$\frac{\partial T}{\partial z} = \epsilon^2 g_1 T, \tag{5.2.47}$$

$$\frac{\partial T}{\partial z} - \epsilon^2 \frac{\partial h}{\partial x}\frac{\partial T}{\partial x} - \epsilon^2 \frac{\partial h}{\partial y}\frac{\partial T}{\partial y} = -\epsilon^2 g_2 \left(1 + \epsilon^2 \left(\frac{\partial h}{\partial x}\right)^2 + \epsilon^2 \left(\frac{\partial h}{\partial y}\right)^2\right)^{\frac{1}{2}} T, \tag{5.2.48}$$

where $\epsilon^2 g_1 = h_0 f_1(T)/k$ and $\epsilon^2 g_2 = h_0 f_2(T)/k$; $f_1(T)$ and $f_2(T)$ are assumed constant throughout the following analysis. The asymptotic analysis which follows involves the canonical problem in which g_1, $g_2 = O(1)$ with $\kappa = O(\epsilon^{-2})$. We write $\gamma = \kappa\epsilon^2$ (so γ is the inverse Peclet number) and $\dot{q} = \epsilon^2 \dot{Q}$ with $\dot{Q} = O(1)$.

We let

$$T \sim T_0(x, y, z, t) + \epsilon^2 T_1(x, y, z, t) \tag{5.2.49}$$

and, substituting into (5.2.46), obtain the leading order terms as

$$\frac{\partial^2 T_0}{\partial z^2} = 0. \tag{5.2.50}$$

Integrating gives

$$T_0 = A(x, y, t) + B(x, y, t)z \tag{5.2.51}$$

and the leading terms from the boundary condition at $z = 0$ imply that $\frac{\partial T_0}{\partial z} = 0$, so $B(x, y, t)$ is equal to zero to give T_0 as a function of x, y and t only. Thus the perturbation (5.2.49) can be simplified to

$$T \sim T_0(x, y, t) + \epsilon^2 T_1(x, y, z, t). \tag{5.2.52}$$

Substituting the simplified perturbation expansion, (5.2.52), in (5.2.46) gives

$$\frac{\partial T_0}{\partial t} + u\frac{\partial T_0}{\partial x} + v\frac{\partial T_0}{\partial y} = \gamma\left(\frac{\partial^2 T_1}{\partial z^2} + \frac{\partial^2 T_0}{\partial x^2} + \frac{\partial^2 T_0}{\partial y^2} + \dot{Q}\right). \tag{5.2.53}$$

Similarly substituting into the boundary condition on the free surface gives

$$\text{on } z = h \quad \frac{\partial T_1}{\partial z} = -g_2 T_0 + \frac{\partial h}{\partial x}\frac{\partial T_0}{\partial x} + \frac{\partial h}{\partial y}\frac{\partial T_0}{\partial y}, \tag{5.2.54}$$

while

$$\text{on } z = 0 \quad \frac{\partial T_1}{\partial z} = g_1 T_0. \tag{5.2.55}$$

We suppress subscripts on u, v and h and henceforth assume that the quantities are leading order approximations. Rearranging (5.2.53) gives

$$\frac{\partial^2 T_1}{\partial z^2} = \frac{1}{\gamma}\frac{\partial T_0}{\partial t} + \frac{1}{\gamma}u\frac{\partial T_0}{\partial x} + \frac{1}{\gamma}v\frac{\partial T_0}{\partial y} - \frac{\partial^2 T_0}{\partial x^2} - \frac{\partial^2 T_0}{\partial y^2} - \dot{Q} \tag{5.2.56}$$

and integrating with respect to z using (5.2.55) implies

$$\frac{\partial T_1}{\partial z} = \frac{1}{\gamma}\frac{\partial T_0}{\partial t}z + \frac{1}{\gamma}\int_0^z u dz' \frac{\partial T_0}{\partial x} + \frac{1}{\gamma}\int_0^z v dz' \frac{\partial T_0}{\partial y} - \frac{\partial^2 T_0}{\partial x^2}z - \frac{\partial^2 T_0}{\partial y^2}z - \dot{Q}z + g_1 T_0 \tag{5.2.57}$$

The horizontal velocity in the x-direction, from (5.2.36), simplifies to

$$\int_0^z u dz' = \frac{1}{\mu}\frac{\partial h}{\partial x}\int_0^z \left(\frac{(z')^2}{2} - z'h\right) dz', \tag{5.2.58}$$

$$= \frac{1}{\mu}\frac{\partial h}{\partial x}\left(\frac{z^3}{6} - \frac{z^2}{2}h\right), \tag{5.2.59}$$

with a similar result for v (using (5.2.37)). Using the boundary condition (5.2.54) on $z = h$ then gives

$$\frac{\partial T_1}{\partial z} = \frac{h}{\gamma}\frac{\partial T_0}{\partial t} - \frac{h^3}{3\gamma\mu}\frac{\partial h}{\partial x}\frac{\partial T_0}{\partial x} - \frac{h^3}{3\gamma\mu}\frac{\partial h}{\partial y}\frac{\partial T_0}{\partial y} - h\frac{\partial^2 T_0}{\partial x^2} - h\frac{\partial^2 T_0}{\partial y^2} - \dot{Q}h + g_1 T_0, \tag{5.2.60}$$

$$= -g_2 T_0 + \frac{\partial h}{\partial x}\frac{\partial T_0}{\partial x} + \frac{\partial h}{\partial y}\frac{\partial T_0}{\partial y}. \tag{5.2.61}$$

Dropping the subscripts, the leading order temperature field is thus given by

$$\frac{\partial T}{\partial t} = \frac{(h^3 + 3\mu\gamma)}{3\mu h}\frac{\partial h}{\partial x}\frac{\partial T}{\partial x} + \frac{(h^3 + 3\mu\gamma)}{3\mu h}\frac{\partial h}{\partial y}\frac{\partial T}{\partial y} + \gamma\frac{\partial^2 T}{\partial x^2} + \gamma\frac{\partial^2 T}{\partial y^2} - \frac{\gamma}{h}(g_1 + g_2)T + \gamma\dot{Q} \tag{5.2.62}$$

or, in vector notation,

$$\frac{\partial T}{\partial t} = \frac{(h^3 + 3\mu\gamma)}{3\mu h}\nabla_{(x,y)}\cdot(h\nabla_{(x,y)}T) + \gamma\nabla^2_{(x,y)}T - \frac{\gamma}{h}(g_1 + g_2)T + \gamma\dot{Q}. \tag{5.2.63}$$

Since the temperature field is dependent on x, y and t only, the governing equations for the free surface, (5.2.44), simplifies to

$$\frac{\partial h}{\partial t} = \frac{1}{3}\frac{\partial}{\partial x}\left(\frac{h^3}{\mu(T)}\frac{\partial h}{\partial x}\right) + \frac{1}{3}\frac{\partial}{\partial y}\left(\frac{h^3}{\mu(T)}\frac{\partial h}{\partial y}\right) \tag{5.2.64}$$

or in vector form

$$\frac{\partial h}{\partial t} = \nabla_{(x,y)}\cdot\left(D\nabla_{(x,y)}h\right), \tag{5.2.65}$$

where the 'diffusivity' is given by

$$D = \frac{h^3}{3\mu(T)}. \tag{5.2.66}$$

Using (5.2.64), equation (5.2.62) can be rewritten in the physically more transparent energy balance form

$$\frac{\partial(hT)}{\partial t} = \gamma\frac{\partial}{\partial x}\left(h\frac{\partial T}{\partial x}\right) + \gamma\frac{\partial}{\partial y}\left(h\frac{\partial T}{\partial y}\right) + \frac{1}{3}\frac{\partial}{\partial x}\left(\frac{h^3 T}{\mu(T)}\frac{\partial h}{\partial x}\right) + \frac{1}{3}\frac{\partial}{\partial y}\left(\frac{h^3 T}{\mu(T)}\frac{\partial h}{\partial y}\right) - \gamma(g_1 + g_2)T + h\gamma\dot{Q} \tag{5.2.67}$$

or, again in vector notation,

$$\frac{\partial(hT)}{\partial t} = \gamma\nabla_{(x,y)}\cdot\left(h\nabla_{(x,y)}T\right) + \frac{1}{3}\nabla_{(x,y)}\cdot\left(\frac{h^3 T}{\mu(T)}\nabla_{(x,y)}h\right) - \gamma(g_1 + g_2)T + h\gamma\dot{Q}. \tag{5.2.68}$$

5.3. Numerical methods

The method used to solve the governing equations for the free surface and temperature field is the LoD finite difference method, discussed in Chapter 3. The initial condition at $t = 0$ for the temperature of the liquid is $T = 1$ over the entire numerical domain. The initial condition for the free surface has a prewetting film as in the previous chapter. Four different initial conditions are considered for the free surface, namely

$$h(x,y,t) = (1 - x^2)_+ + 10^{-6}, \qquad h(x,y,t) = (1 - x^2 + \varepsilon\cos(\lambda y))_+ + 10^{-6},$$

$$h = (1 - x^2 - y^2)_+ + 10^{-6}, \qquad h = \left(1 - x^2 - y^2 + \varepsilon\cos\left(\lambda\arctan\left(\frac{y}{x}\right)\right)\right)_+ + 10^{-6}$$

where λ and ε are parameters which control the initial perturbations and are discussed in more detail in the following sections. The flow front of the liquid is set numerically as twice the prewetting film.

Around the finite numerical domain (which is specified in Section 5.4) the following boundary conditions are applied

$$\text{at } x = 0 \text{ and } x = L_1 \quad \frac{\partial h}{\partial x} = \frac{\partial T}{\partial x} = 0, \tag{5.3.1}$$

$$\text{at } y = 0 \text{ and } y = L_2 \quad \frac{\partial h}{\partial y} = \frac{\partial T}{\partial y} = 0, \tag{5.3.2}$$

where L_1 and L_2 are depicted in the numerical results shown below. Such conditions correspond to symmetry of the geometry or the thermal ones can be viewed as approximately conservation of heat, i.e.

$$\text{as} \quad x \to \infty \quad h\frac{\partial T}{\partial x} \to 0 \quad \text{and} \quad y \to \infty \quad h\frac{\partial T}{\partial y} \to 0. \tag{5.3.3}$$

The governing free surface equation is coupled to the temperature equation using the viscosity relationship

$$\mu = e^{-\alpha T}, \tag{5.3.4}$$

where $\alpha \geq 0$ is a dimensionless constant and $T \geq 0$ is the dimensionless temperature.

5.3.1. *Operator-split algorithm for the three-dimensional free surface profile*

We first discretise the governing equation for the free surface, (5.2.65), using the Crank-Nicolson method with the notation $h_{ij}^n = h((i-1)\Delta x, (j-1)\Delta y, n\Delta t)$ to give

$$\begin{aligned}\frac{h_{ij}^{n+1} - h_{ij}^n}{\Delta t} = {} & \frac{1}{2\Delta x}\left(D_{i+\frac{1}{2}j}^{n+1} h_{x_{i+\frac{1}{2}j}}^{n+1} - D_{i-\frac{1}{2}j}^{n+1} h_{x_{i-\frac{1}{2}j}}^{n+1}\right) + \frac{1}{2\Delta x}\left(D_{i+\frac{1}{2}j}^{n} h_{x_{i+\frac{1}{2}j}}^{n} - D_{i-\frac{1}{2}j}^{n} h_{x_{i-\frac{1}{2}j}}^{n}\right) \\ & + \frac{1}{2\Delta y}\left(D_{ij+\frac{1}{2}}^{n+1} h_{y_{ij+\frac{1}{2}}}^{n+1} - D_{ij-\frac{1}{2}}^{n+1} h_{y_{ij-\frac{1}{2}}}^{n+1}\right) + \frac{1}{2\Delta y}\left(D_{ij+\frac{1}{2}}^{n} h_{y_{ij+\frac{1}{2}}}^{n} - D_{ij-\frac{1}{2}}^{n} h_{y_{ij-\frac{1}{2}}}^{n}\right),\end{aligned} \tag{5.3.5}$$

where

$$h_{x_{i+\frac{1}{2}j}} = \frac{h_{i+1j} - h_{ij}}{\Delta x}, \quad h_{y_{ij-\frac{1}{2}}} = \frac{h_{ij} - h_{ij-1}}{\Delta y}, \quad D_{i+\frac{1}{2}j} = \frac{D_{i+1j} + D_{ij}}{2} \quad \text{and} \quad D_{i-\frac{1}{2}j} = \frac{D_{ij} - D_{i-1j}}{2}.$$

This suggests the operator notation

$$\mathcal{L}_{xy}^{-}(h_{ij}^{n+1}) = \mathcal{L}_{xy}^{+}(h_{ij}^{n}), \tag{5.3.6}$$

where

$$\mathcal{L}_{xy}^{-} = \left[1 - \frac{\Delta t}{2}\frac{\partial}{\partial x}\left(D\frac{\partial}{\partial x}\right) - \frac{\Delta t}{2}\frac{\partial}{\partial y}\left(D\frac{\partial}{\partial y}\right)\right], \tag{5.3.7}$$

$$\mathcal{L}_{xy}^{+} = \left[1 + \frac{\Delta t}{2}\frac{\partial}{\partial x}\left(D\frac{\partial}{\partial x}\right) + \frac{\Delta t}{2}\frac{\partial}{\partial y}\left(D\frac{\partial}{\partial y}\right)\right]. \tag{5.3.8}$$

The spatial derivatives in the above differential marching operators are replaced by central finite difference operators to reproduce (5.3.5).

To derive the LoD scheme we approximate (5.3.6) by

$$\mathcal{L}_y^-(\mathcal{L}_x^-(h_{ij}^{n+1})) = \mathcal{L}_y^+(\mathcal{L}_x^+(h_{ij}^n)), \tag{5.3.9}$$

where

$$\begin{aligned} \mathcal{L}_x^- &= \left[1 - \frac{\Delta t}{2}\frac{\partial}{\partial x}\left(D\frac{\partial}{\partial x}\right)\right], \quad \mathcal{L}_y^- = \left[1 - \frac{\Delta t}{2}\frac{\partial}{\partial y}\left(D\frac{\partial}{\partial y}\right)\right], \\ \mathcal{L}_x^+ &= \left[1 + \frac{\Delta t}{2}\frac{\partial}{\partial x}\left(D\frac{\partial}{\partial x}\right)\right], \quad \mathcal{L}_x^+ = \left[1 + \frac{\Delta t}{2}\frac{\partial}{\partial y}\left(D\frac{\partial}{\partial y}\right)\right]. \end{aligned} \tag{5.3.10}$$

Now it is clear that

$$\mathcal{L}_{xy}^- = \mathcal{L}_x^-\mathcal{L}_y^- + O(\Delta t^2) \quad \text{and} \quad \mathcal{L}_{xy}^+ = \mathcal{L}_x^+\mathcal{L}_y^+ + O(\Delta t^2). \tag{5.3.11}$$

Rewriting (5.3.9) in terms of the bar notation used below gives

$$\mathcal{L}_x^-(h_{ij}^{\overline{n+1}}) = \mathcal{L}_x^+(h_{ij}^n)), \tag{5.3.12}$$

$$\mathcal{L}_y^-(h_{ij}^{n+1}) = \mathcal{L}_y^+(h_{ij}^{\overline{n+1}})). \tag{5.3.13}$$

The factored sequence of locally one-dimensional split operators is shown to provide a suitable two-dimensional solution to the free surface profile equation (5.2.43). Note that $\mathcal{L}_x$ is applied for the first sweep and $\mathcal{L}_y$ for the second sweep.

The bar notation is now introduced for the intermediate results of the first operator, where a Crank-Nicolson implicit finite difference scheme is applied over each sweep by applying suitable finite difference operators for the differential operators, (5.3.10), where i and $j = 1, ..., N$ (N being the number of mesh points in the x and y-directions). The first sweep is given by

$$-r_x D_{i-\frac{1}{2}j}^{\overline{n+1}} h_{i-1j}^{\overline{n+1}} + (1 + r_x D_{i+\frac{1}{2}j}^{\overline{n+1}} + r_x D_{i-\frac{1}{2}j}^{\overline{n+1}}) h_{ij}^{\overline{n+1}} - r_x D_{i+\frac{1}{2}j}^{\overline{n+1}} h_{i+1j}^{\overline{n+1}} = d_i^n, \tag{5.3.14}$$

where

$$d_{ij}^n = r_x D_{i-\frac{1}{2}j}^n h_{i-1j}^n + (1 - r_x D_{i+\frac{1}{2}j}^n - r_x D_{i-\frac{1}{2}j}^n) h_{ij}^n + r_x D_{i+\frac{1}{2}j}^n h_{i+1j}^n,$$

$$r_x = \frac{\Delta t}{2\Delta x^2}, \quad D_{i+\frac{1}{2}j} = \frac{D_{i+1j} + D_{ij}}{2} \quad \text{and} \quad D_{i-\frac{1}{2}j} = \frac{D_{ij} - D_{i-1j}}{2}.$$

The time marched term, $D_{ij}^{\overline{n+1}}$, is found by differentiating D with respect to time, giving

$$\frac{\partial D}{\partial t} = \frac{3\mu h^2 h_t - h^3 \mu_t}{3\mu^2}. \tag{5.3.15}$$

Discretising explicitly implies

$$D_{ij}^{\overline{n+1}} = D_{ij}^n + \Delta t \frac{3\mu_{ij}^n (h^2)_{ij}^n (h_t)_{ij}^n - (h^3)_{ij}^n (\mu_t)_{ij}^n}{3(\mu^2)_{ij}^n}, \tag{5.3.16}$$

where $(h_t)_{ij}^n$ is found by discretising $\mathcal{L}_x^-(h_{ij}^n)$ using $(h_t)_{ij}^n = (h_{ij}^n - \mathcal{L}_x^-(h_{ij}^n))/\Delta t$ to give

$$(h_t)_{ij}^n = \frac{1}{2\Delta x^2}\left[(h_{i+1j}^n - h_i^n)(D_{i+1j}^n + D_{ij}^n) - (h_{ij}^n - h_{i-1j}^n)(D_i^n + D_{i-1j}^n)\right]. \tag{5.3.17}$$

To complete the time step, the final sweep is given by

$$-r_y D_{ij-\frac{1}{2}}^{n+1} h_{ij-1}^{n+1} + (1 + r_y D_{ij+\frac{1}{2}}^{n+1} + r_y D_{ij-\frac{1}{2}}^{n+1}) h_{ij}^{n+1} - r_y D_{ij+\frac{1}{2}}^{n+1} h_{ij+1}^{n+1} = d_{ij}^{\overline{n+1}}, \tag{5.3.18}$$

where

$$d_{ij}^{\overline{n+1}} = r_y D_{ij-\frac{1}{2}}^{\overline{n+1}} h_{ij-1}^{\overline{n+1}} + (1 - r_x D_{ij+\frac{1}{2}}^{\overline{n+1}} - r_x D_{ij-\frac{1}{2}}^{\overline{n+1}}) h_{ij}^{\overline{n+1}} + r_x D_{ij+\frac{1}{2}}^{\overline{n+1}} h_{ij+1}^{\overline{n+1}}.$$

Similarly the term D^{n+1} is found by differentiating D with respect to t and discretising to give

$$D_{ij}^{n+1} = D_i^{\overline{n+1}} + \Delta t \frac{3\mu_{ij}^n (h^2)_{ij}^{\overline{n+1}} (h_t)_{ij}^{\overline{n+1}} - (h^3)_{ij}^{\overline{n+1}} (\mu_t)_{ij}^{\overline{n+1}}}{3(\mu^2)_{ij}^{\overline{n+1}}}, \tag{5.3.19}$$

where $(h_t)_i^{\overline{n+1}}$ is found by discretising $\mathcal{L}_y^-(h_i^{\overline{n+1}})$ such that $(h_t)_i^{\overline{n+1}} = (h_i^{\overline{n+1}} - \mathcal{L}_y^-(h_i^{\overline{n+1}}))/\Delta t$ giving

$$(h_t)_{ij}^{\overline{n+1}} = \frac{1}{2\Delta y^2}\left[(h_{ij+1}^{\overline{n+1}} - h_{ij}^{\overline{n+1}})(D_{ij+1}^{\overline{n+1}} + D_{ij}^{\overline{n+1}}) - (h_{ij}^{\overline{n+1}} - h_{ij-1}^{\overline{n+1}})(D_{ij}^{\overline{n+1}} + D_{ij-1}^{\overline{n+1}})\right]. \tag{5.3.20}$$

We note that

$$r_y = \frac{\Delta t}{2\Delta y^2}, \quad D_{ij+\frac{1}{2}} = \frac{D_{ij+1} + D_{ij}}{2} \quad D_{ij-\frac{1}{2}} = \frac{D_{ij} - D_{ij-1}}{2},$$

and that $(\mu_t)_i^n = (\mu_t)_i^{\overline{n+1}}$, so that the rate of change of viscosity with time is assumed to be the same over the x and y sweeps, and is evaluated using the backward time marching scheme

$$(\mu_t)_{ij}^n \approx \frac{\mu_{ij}^n - \mu_{ij}^{n-1}}{\Delta t}.$$

The above implicit schemes are solved using the Thomas algorithm (see Morton & Mayers (1994)). The boundary conditions (5.3.1) and (5.3.2) gives

$$\begin{aligned}
&\text{at } i = 1 \quad h_{0j} = h_{2j} \quad \text{and} \quad D_{0j} = D_{2j}, \qquad \text{at } i = N \quad h_{N+1j} = h_{N-1j} \quad \text{and} \quad D_{N+1j} = D_{N-1j},\\
&\text{at } j = 1 \quad h_{i0} = h_{i2} \quad \text{and} \quad D_{i0} = D_{i2}, \qquad \text{at } j = N \quad h_{iN+1} = h_{iN-1} \quad \text{and} \quad D_{iN+1} = D_{iN-1}.
\end{aligned}$$

5.3.2. *Operator split algorithm for the temperature equation*

We again start with the two-dimensional operator for the temperature equation, where the discretising (5.2.67) using the Crank-Nicolson method and the notation $T((i-1)\Delta x, (j-1)\Delta y, n\Delta t) = T_{ij}^n$ gives

$$\begin{aligned}
\frac{T_{ij}^{n+1} - T_{ij}^n}{\Delta t} = {} & \frac{(a_x)_{ij}^n}{2}\left(\frac{T_{ij}^{n+1} - T_{i-1j}^{n+1}}{\Delta x} + \frac{T_{ij}^n - T_{i-1j}^n}{\Delta x}\right) + \frac{(a_y)_{ij}^n}{2}\left(\frac{T_{ij}^{n+1} - T_{ij-1}^{n+1}}{\Delta y} + \frac{T_{ij}^n - T_{ij-1}^n}{\Delta y}\right)\\
& + \frac{b}{2}\left(\frac{T_{i-1j}^{n+1} - T_{ij}^{n+1} + T_{i+1j}^{n+1}}{\Delta x^2} + \frac{T_{i-1j}^n - T_{ij}^n + T_{i+1j}^n}{\Delta x^2}\right) + \frac{b}{2}\left(\frac{T_{ij-1}^{n+1} - T_{ij}^{n+1} + T_{ij+1}^{n+1}}{\Delta y^2}\right.\\
& \left. + \frac{T_{ij-1}^n - T_{ij}^n + T_{ij+1}^n}{\Delta y^2}\right) + c_{ij}^n\left(\frac{T_{ij}^{n+1} + T_{ij}^n}{2}\right) + \gamma\dot{Q},
\end{aligned} \tag{5.3.21}$$

where a_x, a_y and c are defined in (5.3.33)-(5.3.34). The scheme assumes that the spreading is in the positive (x, y) quadrant such that a backwards difference scheme is applied for the advection terms. This suggests the following operator notation

$$\mathcal{L}_{xy}^{*-}(T_{ij}^{n+1}) = \mathcal{L}_{xy}^{*-}(T_{ij}^n) + \Delta t\gamma\dot{Q}, \tag{5.3.22}$$

where

$$\mathcal{L}_{xy}^{*-} = \left[1 - \frac{\Delta t a_x}{2}\frac{\partial}{\partial x} - \frac{\Delta t a_y}{2}\frac{\partial}{\partial y} - \frac{\Delta t b}{2}\frac{\partial^2}{\partial x^2} - \frac{\Delta t b}{2}\frac{\partial^2}{\partial y^2} - \frac{\Delta t c}{2}\right], \tag{5.3.23}$$

$$\mathcal{L}_{xy}^{*+} = \left[1 + \frac{\Delta t a_x}{2}\frac{\partial}{\partial x} + \frac{\Delta t a_y}{2}\frac{\partial}{\partial y} + \frac{\Delta t b}{2}\frac{\partial^2}{\partial x^2} + \frac{\Delta t b}{2}\frac{\partial^2}{\partial y^2} + \frac{\Delta t c}{2}\right]. \tag{5.3.24}$$

As in the previous case for the free surface, to reproduce the finite difference scheme (5.3.21), the above differential marching operators are replaced by finite difference operators.

To derive the LoD scheme we approximate (5.3.22) by

$$\mathcal{L}_y^{*-}(\mathcal{L}_x^{*-}(T_{ij}^{n+1})) = \mathcal{L}_y^{*-}(\mathcal{L}_x^{*-}(T_{ij}^{n})) + \Delta t \gamma \dot{Q}, \tag{5.3.25}$$

where

$$\mathcal{L}_x^{*-} = \left[1 - \frac{\Delta t a_x}{2}\frac{\partial}{\partial x} - \frac{\Delta t b}{2}\frac{\partial^2}{\partial x^2} - \frac{\Delta t c}{4}\right], \quad \mathcal{L}_y^{*-} = \left[1 - \frac{\Delta t a_y}{2}\frac{\partial}{\partial y} - \frac{\Delta t b}{2}\frac{\partial^2}{\partial y^2} - \frac{\Delta t c}{4}\right], \tag{5.3.26}$$

$$\mathcal{L}_x^{*+} = \left[1 + \frac{\Delta t a_x}{2}\frac{\partial}{\partial x} + \frac{\Delta t b}{2}\frac{\partial^2}{\partial x^2} + \frac{\Delta t c}{4}\right], \quad \mathcal{L}_y^{*+} = \left[1 + \frac{\Delta t a_y}{2}\frac{\partial}{\partial y} + \frac{\Delta t b}{2}\frac{\partial^2}{\partial y^2} + \frac{\Delta t c}{4}\right]. \tag{5.3.27}$$

Note that

$$\mathcal{L}_{xy}^{*-} = \mathcal{L}_x^{*-}\mathcal{L}_y^{*-} + O(\Delta t^2), \quad \mathcal{L}_{xy}^{*+} = \mathcal{L}_x^{*+}\mathcal{L}_y^{*+} + O(\Delta t^2). \tag{5.3.28}$$

Rewriting (5.3.25) in terms of the bar notation gives

$$\mathcal{L}_x^{*-}(\overline{T_{ij}^{n+1}}) = \mathcal{L}_x^{*+}(T_{ij}^{n})) + \frac{\Delta t \gamma \dot{Q}}{2} \tag{5.3.29}$$

$$\mathcal{L}_y^{*-}(T_{ij}^{n+1}) = \mathcal{L}_y^{*+}(\overline{T_{ij}^{n+1}})) + \frac{\Delta t \gamma \dot{Q}}{2} \tag{5.3.30}$$

The operators in (5.3.25) are discretised and, applying upwinding to the advective terms, where a_x and a_y (defined below) can be assumed to be greater than zero by considering the positive quadrant of the (x, y) plane only and with no influx of liquid. The bar notation is used to indicate the intermediate results of the first operator and the finite difference schemes are expressed as

$$\left(\frac{a_x \Delta t}{2\Delta x} - \frac{b\Delta t}{2\Delta x^2}\right)\overline{T_{i-1j}^{n+1}} + \left(1 - \frac{a_x \Delta t}{2\Delta x} + \frac{b\Delta t}{\Delta x^2} - \frac{c\Delta t}{4}\right)\overline{T_{ij}^{n+1}} - \frac{b\Delta t}{2\Delta x^2}\overline{T_{i+1j}^{n+1}} = d_{ij}^{n}, \tag{5.3.31}$$

where

$$d_{ij}^{n} = \left(-\frac{a_x \Delta t}{2\Delta x} + \frac{b\Delta t}{2\Delta x^2}\right)T_{i-1j}^{n} + \left(1 + \frac{a_x \Delta t}{2\Delta x} - \frac{b\Delta t}{\Delta x^2} + \frac{c\Delta t}{4}\right)T_{ij}^{n} + \frac{b\Delta t}{2\Delta x^2}T_{i+1j}^{n} + \frac{1}{2}\gamma \dot{Q}\Delta t.$$

Note that the heat source term is split over each sweep. To complete the time step we take

$$\left(\frac{a_y \Delta t}{2\Delta y} - \frac{b\Delta t}{2\Delta y^2}\right)T_{ij-1}^{n+1} + \left(1 - \frac{a_y \Delta t}{2\Delta y} + \frac{b\Delta t}{\Delta y^2} - \frac{c\Delta t}{4}\right)T_{ij}^{n+1} - \frac{b\Delta t}{2\Delta y^2}T_{ij+1}^{n+1} = \overline{d_{ij}^{n+1}}, \tag{5.3.32}$$

where

$$\overline{d_{ij}^{n+1}} = \left(-\frac{a_y \Delta t}{2\Delta y} + \frac{b\Delta t}{2\Delta y^2}\right)\overline{T_{ij-1}^{n+1}} + \left(1 + \frac{a_y \Delta t}{2\Delta y} - \frac{b\Delta t}{\Delta y^2} + \frac{c\Delta t}{4}\right)\overline{T_{ij}^{n+1}} + \frac{b\Delta t}{2\Delta x^2}\overline{T_{ij+1}^{n+1}} + \frac{1}{2}\gamma \dot{Q}\Delta t.$$

Noting that

$$a_x = \frac{(h^3 + 3\mu\gamma)}{3\mu h}\frac{\partial h}{\partial x}, \quad a_y = \frac{(h^3 + 3\mu\gamma)}{3\mu h}\frac{\partial h}{\partial y}, \quad b = \gamma \quad \text{and} \quad c = -\frac{\gamma}{h}(g_1 + g_2), \tag{5.3.33}$$

and discretising, gives

$$(a_x)_{ij}^n = \frac{((h_{ij}^n)^3 + 3\mu_{ij}^n\gamma)}{3\mu_{ij}^n h_{ij}^n}\frac{(h_{i+1j}^n - h_{i-1j}^n)}{2\Delta x}, \quad (a_y)_{ij}^n = \frac{((h_{ij}^n)^3 + 3\mu_{ij}^n\gamma)}{3\mu_{ij}^n h_{ij}^n}\frac{(h_{ij+1}^n - h_{ij-1}^n)}{2\Delta y},$$
$$c_{ij}^n = -\frac{\gamma}{h_{ij}^n}(g_1 + g_2). \tag{5.3.34}$$

The boundary condition at $i = 1$ from (5.3.1) gives $T_{0j} = T_{2j}$ and the first step of the finite difference scheme for the x-sweep is

$$\left(1 - \frac{a_x\Delta t}{2\Delta x} + \frac{b\Delta t}{\Delta x^2} - \frac{c\Delta t}{4}\right)T_{1j}^{\overline{n+1}} + \left(\frac{a_x\Delta t}{2\Delta x} - \frac{b\Delta t}{\Delta x^2}\right)T_{2j}^{\overline{n+1}} = d_{1j}^n, \tag{5.3.35}$$

where

$$d_{1j}^n = \left(1 + \frac{a_x\Delta t}{2\Delta x} - \frac{b\Delta t}{\Delta x^2} + \frac{c\Delta t}{4}\right)T_{1j}^n + \left(-\frac{a_x\Delta t}{2\Delta x} + \frac{b\Delta t}{\Delta x^2}\right)T_{2j}^n + \frac{1}{2}\gamma\dot{Q}\Delta t;$$

at $i = N$, equation (5.3.1) gives $T_{N+1j} = T_{N-1j}$ and the last step for the x-sweep is

$$\left(\frac{a_x\Delta t}{2\Delta x} - \frac{b\Delta t}{\Delta x^2}\right)T_{N-1j}^{\overline{n+1}} + \left(1 - \frac{a_x\Delta t}{2\Delta x} + \frac{b\Delta t}{\Delta x^2} - \frac{c\Delta t}{4}\right)T_{Nj}^{\overline{n+1}} = d_{Nj}^n, \tag{5.3.36}$$

where

$$d_{Nj}^n = \left(-\frac{a_x\Delta t}{2\Delta x} + \frac{b\Delta t}{\Delta x^2}\right)T_{N-1j}^n + \left(1 + \frac{a_x\Delta t}{2\Delta x} + \frac{b\Delta t}{\Delta x^2} + \frac{c\Delta t}{4}\right)T_{Nj}^n + \frac{1}{2}\gamma\dot{Q}\Delta t.$$

Similarly for the y-sweep, the boundary condition at $j = 1$ from (5.3.2) gives $T_{i0} = T_{i2}$ and hence the first step of the finite difference scheme for the y-sweep as

$$\left(1 - \frac{a_y\Delta t}{2\Delta y} + \frac{b\Delta t}{\Delta y^2} - \frac{c\Delta t}{4}\right)T_{i1}^{n+1} + \left(\frac{a_y\Delta t}{2\Delta y} - \frac{b\Delta t}{\Delta y^2}\right)T_{i2}^{n+1} = d_{i1}^{\overline{n+1}}, \tag{5.3.37}$$

where

$$d_{i1}^{\overline{n+1}} = \left(1 + \frac{a_y\Delta t}{2\Delta y} - \frac{b\Delta t}{\Delta y^2} + \frac{c\Delta t}{4}\right)T_{i1}^{\overline{n+1}} + \left(-\frac{a_y\Delta t}{2\Delta y} + \frac{b\Delta t}{\Delta y^2}\right)T_{i2}^{\overline{n+1}} + \frac{1}{2}\gamma\dot{Q}\Delta t;$$

at $j = N$, since (5.3.2) gives $T_{iN+1} = T_{iN-1}$, so we have that

$$\left(\frac{a_y\Delta t}{2\Delta y} - \frac{b\Delta t}{\Delta y^2}\right)T_{iN-1}^{n+1} + \left(1 - \frac{a_y\Delta t}{2\Delta y} + \frac{b\Delta t}{\Delta y^2} - \frac{c\Delta t}{4}\right)T_{iN}^{n+1} = d_{iN}^{\overline{n+1}}, \tag{5.3.38}$$

where

$$d_{iN}^{\overline{n+1}} = \left(-\frac{a_y\Delta t}{2\Delta y} + \frac{b\Delta t}{\Delta y^2}\right)T_{iN-1}^{\overline{n+1}} + \left(1 + \frac{a_y\Delta t}{2\Delta y} - \frac{b\Delta t}{\Delta y^2} + \frac{c\Delta t}{4}\right)T_{iN}^{\overline{n+1}} + \frac{1}{2}\gamma\dot{Q}\Delta t.$$

5.3.3. *Summary*

The numerical methods encoded in the FORTRAN code is briefly summarised here. The initial height profile and temperature are set up. Over the time step Δt the liquid is first allowed to cool, which is solved using (5.3.31)-(5.3.38), and then the new viscosity is evaluated which is used to calculated the free surface profile ((5.3.14)-(5.3.20)). This process is repeated over the required time period.

5.4. Results

5.4.1. *Planar spreading*

The results in this section are for the two-dimensional spreading case which is then extended to include non-planar perturbations. The first set of results has the initial condition at $t = 0$ for the height profile as

$$h(x, y, t) = (1 - x^2)_+ + 10^{-6}. \tag{5.4.1}$$

The initial temperature of the liquid is unity and the liquid is assumed to spread in the positive (x, y) plane. The numerical domain is $[0, 3]$ in both the x and y-directions and the boundary conditions (5.3.1)-(5.3.2) are applied at the boundary of the numerical domain.

First we consider the isothermal case, $\alpha = 0$, Figure 5.2. The results are shown with $\Delta t = 10^{-3}$ and with 120 by 120 mesh points, these values being used for the subsequent set of results unless stated otherwise. The free surface profiles show good agreement with the equivalent isothermal results in the previous chapter, see Figures 5.2(d) and 4.2. The contour plot in Figure 5.2(c) shows the planar spreading of the liquid.

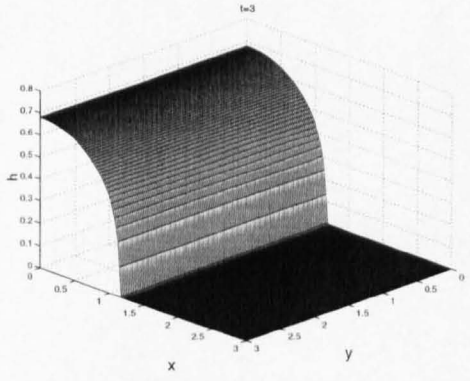

(a) Free surface profile at $t = 3$.

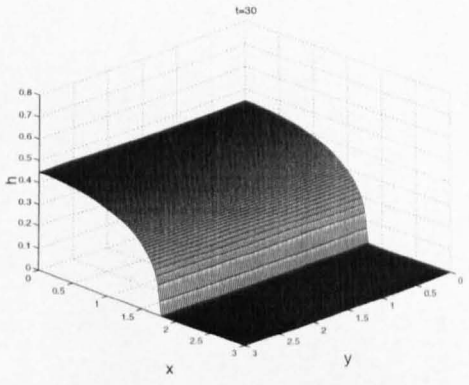

(b) Free surface profile at $t = 30$.

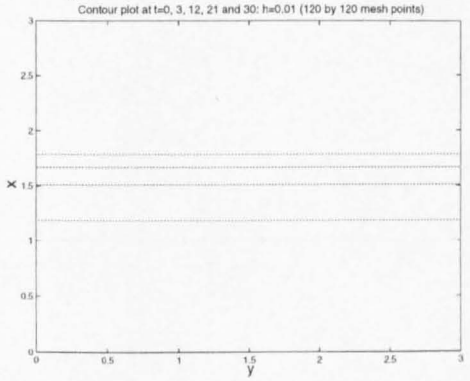

(c) Contour plot of $h = 0.01$

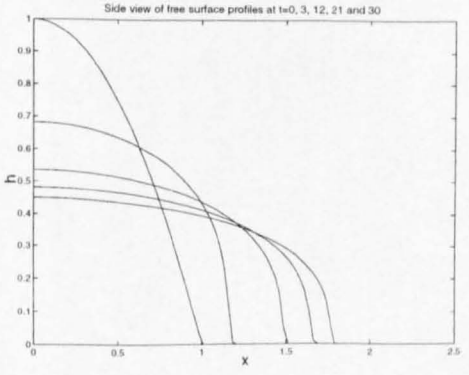

(d) Free surface profile along the x-axis at times $t = 0, 3, 12, 21$ and 30.

FIG. 5.2. Isothermal spreading with 120 by 120 mesh points.

Non-isothermal results for $\alpha = 2$ and $\mathrm{Pe} = 10^6$ are shown in Figure 5.3. The results again show good visual agreement to the equivalent planar case in Chapter 4, see Figure 4.5, giving confidence in the numerical scheme. The results can be seen to develop a steep flow front, as in the respective results in Chapter 4. Note that the temperature profiles are shown over the entire domain here, where they are truncated at the flow front as in Chapter 4. Good agreement is seen between the temperature profiles here and in the corresponding results in Chapter 4.

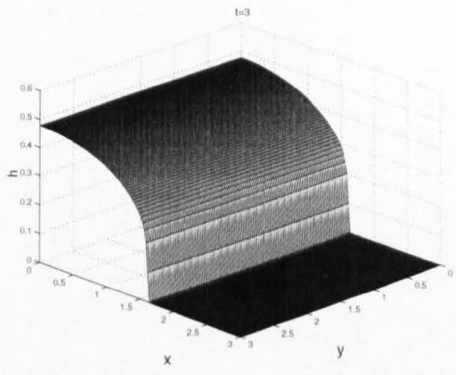

(a) Free surface profile at $t = 3$.

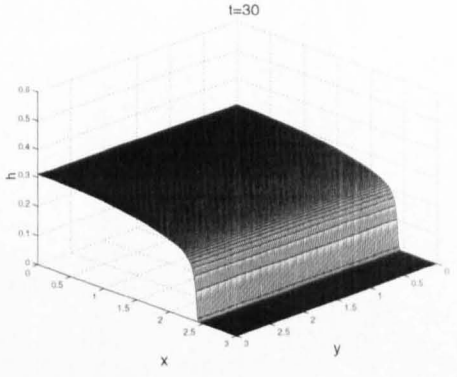

(b) Free surface profile at $t = 30$.

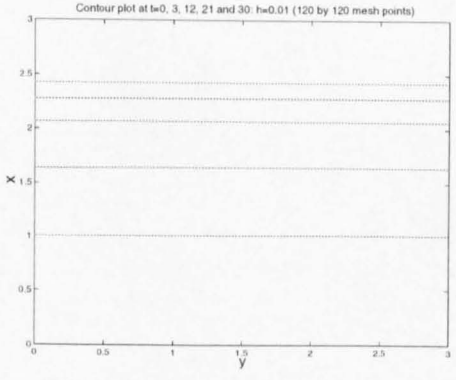

(c) Contour plot of $h = 0.01$.

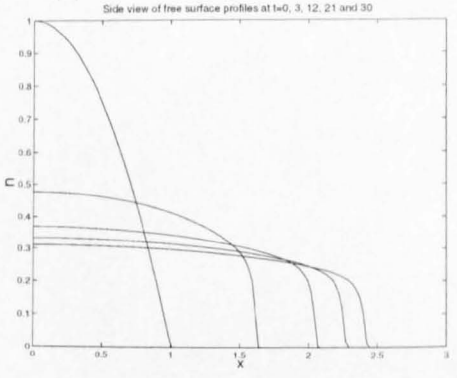

(d) Free surface profile along the x-axis at times $t = 0, 3, 12, 21$ and 30.

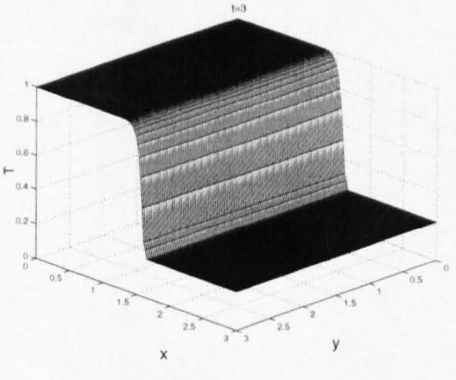

(e) Temperature profile at $t = 3$.

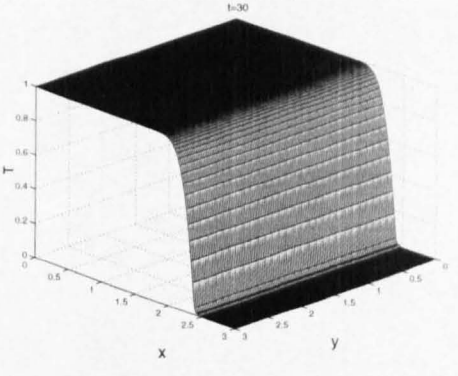

(f) Temperature profile at $t = 30$.

FIG. 5.3. Nonisothermal spreading: $\alpha = 2$, $\mathrm{Pe} = 10^6$ with 120 by 120 mesh points and $g_1 + g_2 = 0.5$.

Results for $\alpha = 2$ and $\mathrm{Pe} = 10^4$, Figure 5.4, show agreement with the planar spreading results shown in Figure 4.7 in Chapter 4.

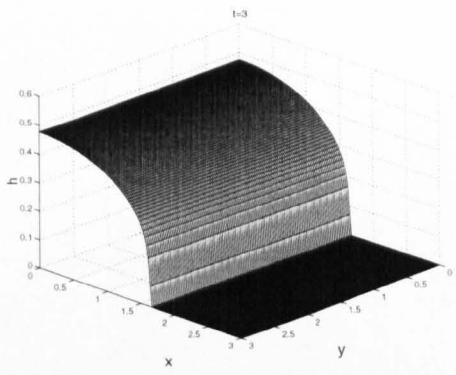

(a) Free surface profile at $t = 3$.

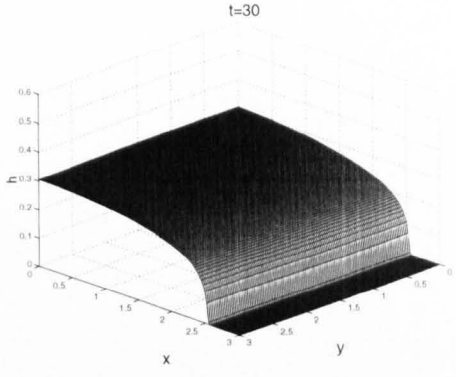

(b) Free surface profile at $t = 30$.

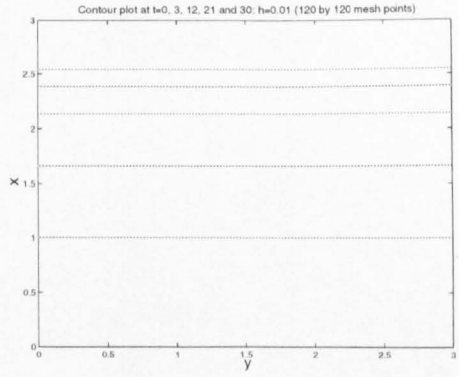

(c) Contour plot of $h = 0.01$

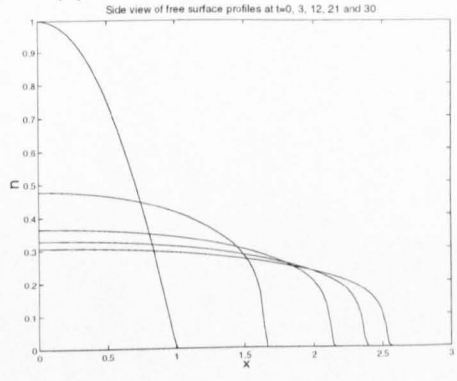

(d) Free surface profile along the x-axis at times $t = 0, 3, 12, 21$ and 30.

FIG. 5.4. Nonisothermal spreading: $\alpha = 2$, $\mathrm{Pe} = 10^4$ with 120 by 120 mesh points and $g_1 + g_2 = 0.5$.

The next set of results show the evolution of non-planar perturbations, the initial conditions for the free surface at $t = 0$ being given by

$$h(x, y, t) = (1 - x^2 + \varepsilon \cos(\lambda y))_+ + 10^{-6}; \tag{5.4.2}$$

see Figure 5.5. Note that in the following results we take $\varepsilon = 0.09$ and $\lambda = 20$, where ε is the amplitude and λ the wavelength of the initial perturbations.

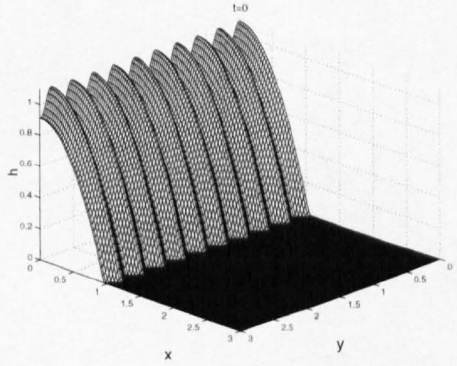

(a)

FIG. 5.5. Initial conditions, $\varepsilon = 0.09$ and $\lambda = 20$.

The first set of results in Figure 5.6 show that the perturbations rapidly disappear in the isothermal case.

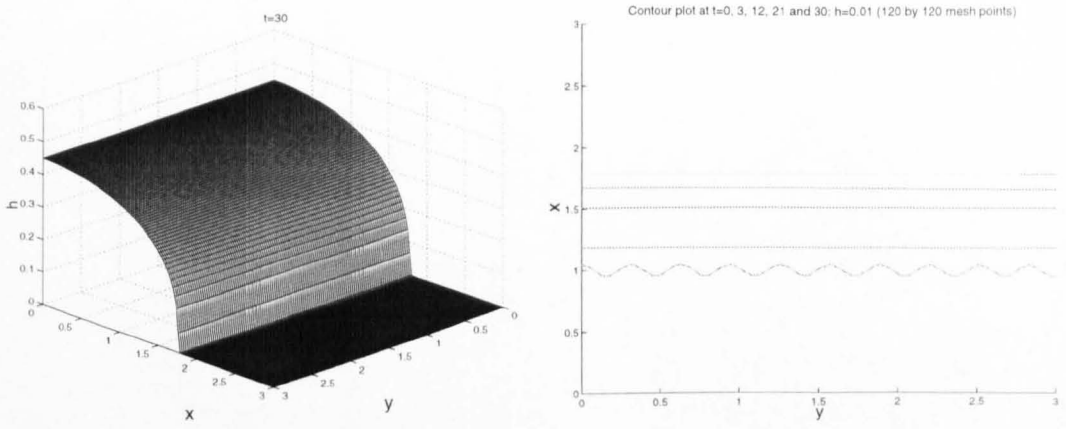

(a) (b)

FIG. 5.6. Isothermal spreading, $\varepsilon = 0.09$ and $\lambda = 20$ with 120 by 120 mesh points. a) Free surface profile at $t = 30$. b) Contour plot of $h = 0.01$ at $t = 0, 3, 12, 21$ and 30.

The set of nonisothermal results in Figures 5.7-5.8 with $\alpha = 8$ and $\mathrm{Pe} = 10^3$ show the perturbations growing as the liquid spreads. Initially the fingering is damped, but as time increases the instabilities are clearly seen to modulate, as shown in the contour plot in Figure 5.7(b). In the following results, $\Delta t = 5 \times 10^{-6}$ over the time scale $[0, 0.04]$ with 120 by 120 mesh points in the square spatial domain $[0, 3] \times [0, 3]$. The small time scale is used because large α increases the diffusivity, which implies a rapid spreading rate.

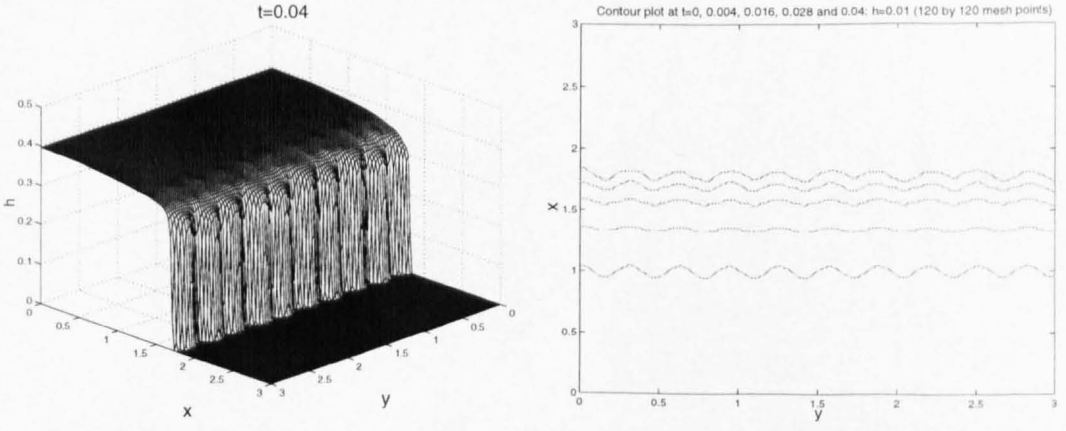

(a) (b)

FIG. 5.7. Nonisothermal spreading: three dimensions with $\mathrm{Pe} = 10^3$, $\alpha = 8.0$ and $g_1 + g_2 = 0.5$. a) Free surface profile at $t = 0.04$. b) Contour plots of $h = 0.01$ at $t = 0, 0.004, 0.012, 0.028$ and 0.04.

The temperature profiles in Figures 5.8(a) and 5.8(b), at times $t = 0.004$ and $t = 0.04$, respectively, illustrate how the temperature is affected by the perturbations on the free surface. The flow front can be distinguished from the temperature profiles by the sharp change seen across the profile and reveals the pre-wetted region.

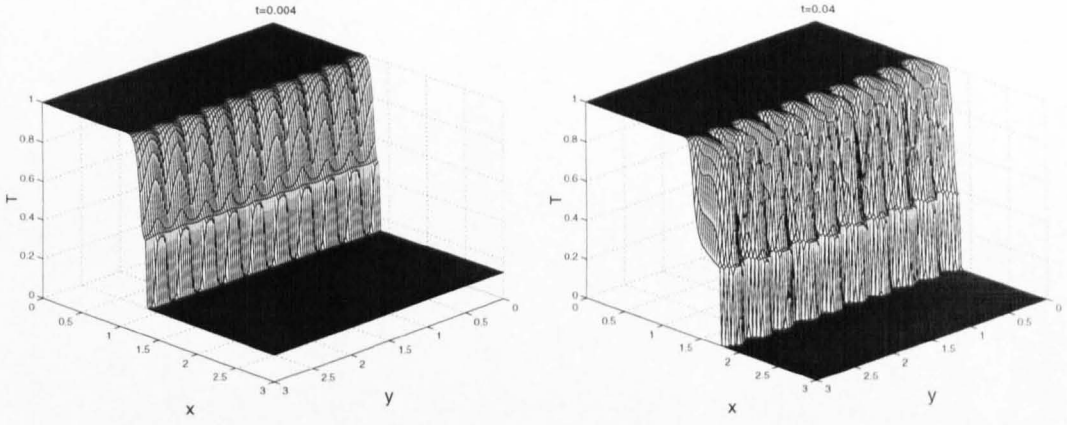

(a) (b)

FIG. 5.8. Nonisothermal spreading: three dimensions with $\mathrm{Pe} = 10^3$, $\alpha = 8.0$ and $g_1 + g_2 = 0.5$. a) Temperature profile at $t = 0.004$. b) Temperature profile at $t = 0.04$

For longer time, $t \leq 0.3$, Figure 5.9 for $\mathrm{Pe} = 10^3$ and $\alpha = 8.0$ shows that the perturbations become damped, see Figure 5.7. This is consistent with the heat loss being significant enough that the behaviour becomes isothermal again.

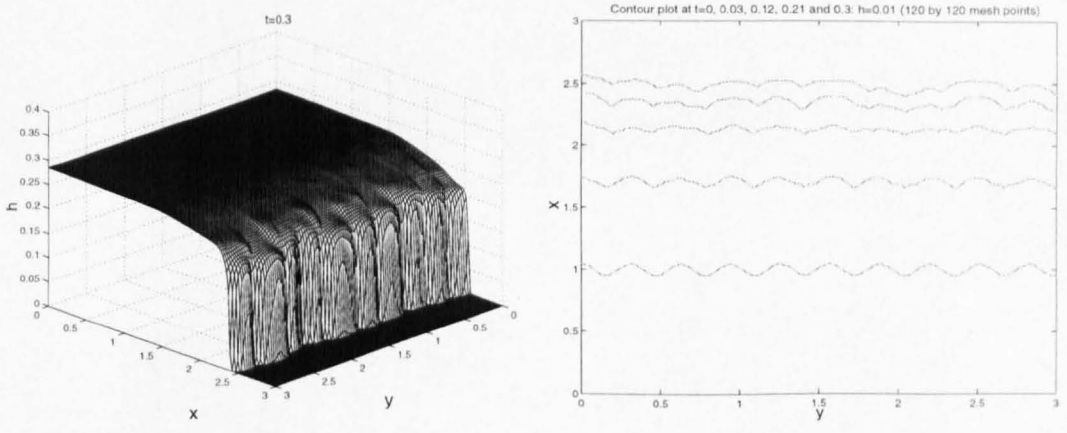

(a) (b)

FIG. 5.9. Nonisothermal spreading: three dimensions with $\mathrm{Pe} = 10^3$, $\alpha = 8.0$ and $g_1 + g_2 = 0.5$. a) Free surface profile at $t = 0.3$ b) Contour plots of $h = 0.01$ at $t = 0, 0.03, 0.12, 0.21$ and 0.3.

The contour plots in Figure 5.10 show that with $\mathrm{Pe} = 10^5$ and $\mathrm{Pe} = 10^8$ and $\alpha = 8$, the perturbations attenuate, the results being consistent with the corresponding results in the axisymmetric geometry shown in the following section.

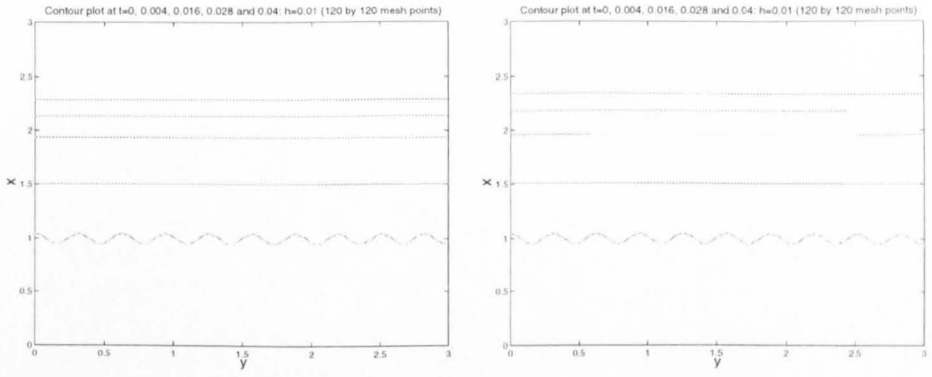

(a) (b)

FIG. 5.10. Nonisothermal spreading: three dimensions with $\alpha = 8.0$ and $g_1 + g_2 = 0.5$. a) Contour plots of $h = 0.01$, $\mathrm{Pe} = 10^5$ at $t = 0, 0.004, 0.012, 0.028$ and 0.04. b) Contour plots of $h = 0.01$, $\mathrm{Pe} = 10^8$ at $t = 0, 0.004, 0.012, 0.028$ and 0.04.

The next set of results in Figure 5.11 show the spreading liquid with $\mathrm{Pe} = 10$ and $\alpha = 8.0$. The perturbations are again damped and for large time near-planar spreading occurs. This is also clear in the temperature profiles in Figure 5.11(c)-(d), where the perturbations are damped for large time.

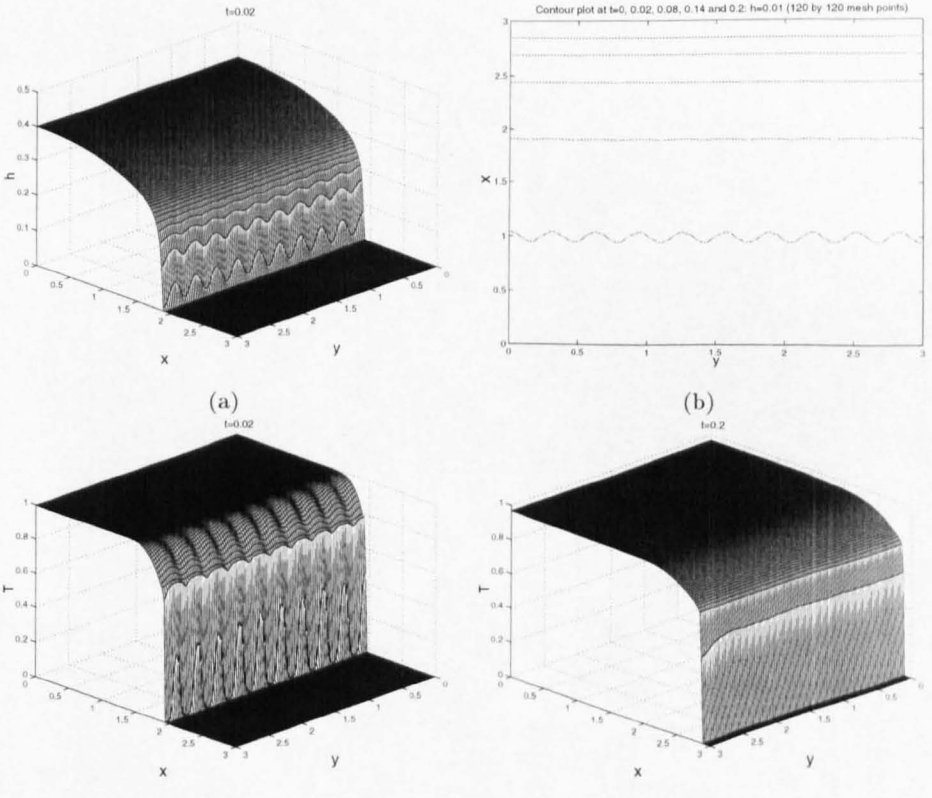

(a) (b)

(c) (d)

FIG. 5.11. Nonisothermal spreading: three dimensions with $\mathrm{Pe} = 10$, $\alpha = 8.0$ and $g_1 + g_2 = 0.5$. a) Free surface profile at $t = 0.04$ b) Contour plots of $h = 0.01$ at $t = 0, 0.02, 0.08, 0.14$ and 0.2. c) Temperature profile at $t = 0.02$ d) Temperature profile at $t = 0.2$.

Results for $\alpha = 3$ and $\mathrm{Pe} = 10^3$ are shown in Figure 5.12(a). The perturbations are seen to be rapidly damped. Increasing α to 3.5, Figure 5.12(b), shows the perturbations decaying. Note that here the mesh size is 120 by 120 over the spatial square mesh $[0,3] \times [0,3]$ and with $\Delta t = 10^{-4}$ over the time range $[0,3]$.

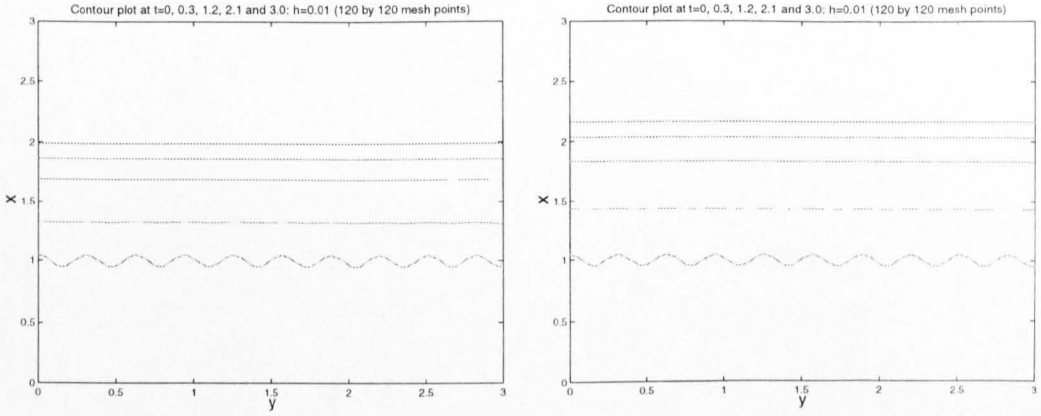

(a) (b)

FIG. 5.12. Nonisothermal spreading: three dimensions with $\mathrm{Pe} = 10^3$ and $g_1 + g_2 = 0.5$. a) Contour plots of $h = 0.01$, $\alpha = 3$ at $t = 0, 0.3, 1.2, 2.1$ and 3.0. b) Contour plots of $h = 0.01$, $\alpha = 3.5$ at $t = 0, 0.3, 1.2, 2.1$ and 3.0.

Setting $\alpha = 8$ and $\mathrm{Pe} = 10^3$, results for $\lambda = 10$ and $\lambda = 30$ are shown in Figure 5.13(a) and Figure 5.13(b), respectively. Increasing λ gives a related increase in the number of fingers developing, as expected.

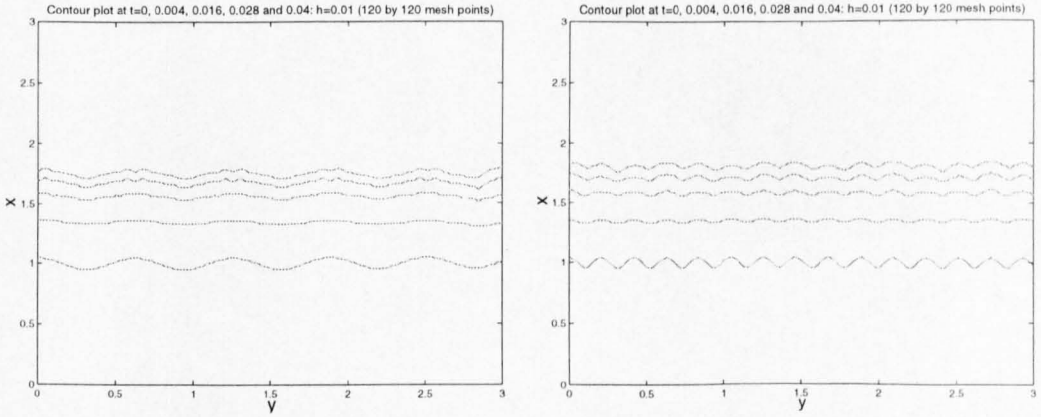

(a) (b)

FIG. 5.13. Nonisothermal spreading: three dimensions with $\alpha = 8$, $\mathrm{Pe} = 10^3$ and $g_1 + g_2 = 0.5$. Contour plots of $h = 0.01$, $t = 0, 0.004, 0.016, 0.028$ and 0.04. a) $\lambda = 10$. b) $\lambda = 30$.

Increasing the time range to $[0, 0.3]$ from $[0, 0.04]$ in Figure 5.13 gives the results in Figure 5.14, where the cooling of the liquid can be seen to retard the fingering growth.

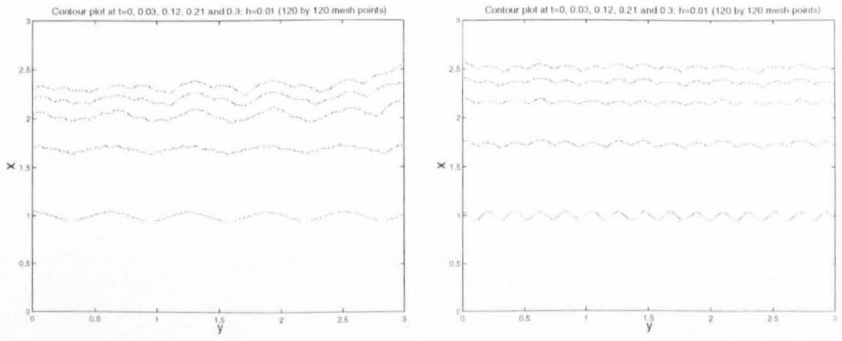

(a) (b)

FIG. 5.14. Nonisothermal spreading: three dimensions with $\alpha = 8$, $\mathrm{Pe} = 10^3$ and $g_1 + g_2 = 0.5$. Contour plots of $h = 0.01$, $t = 0, 0.004, 0.016, 0.028$ and 0.04. a) $\lambda = 10$. b) $\lambda = 30$.

5.4.2. *Axisymmetric spreading*

The following set of calculations has initial conditions for the height profile given by

$$h = (1 - x^2 - y^2)_+ + 10^{-6} \quad \text{at } t = 0. \tag{5.4.3}$$

The initial temperature of the droplet is unity and the boundary conditions (5.3.1)-(5.3.2) are applied at the boundary of the numerical domain. The following set of results has $\Delta t = 10^{-3}$ for the time range $[0, 30]$ and 100 by 100 mesh points in the $[0, 2] \times [0, 2]$ spatial domain. Starting off with the isothermal case, $\alpha = 0$, gives the results in Figures 5.15.

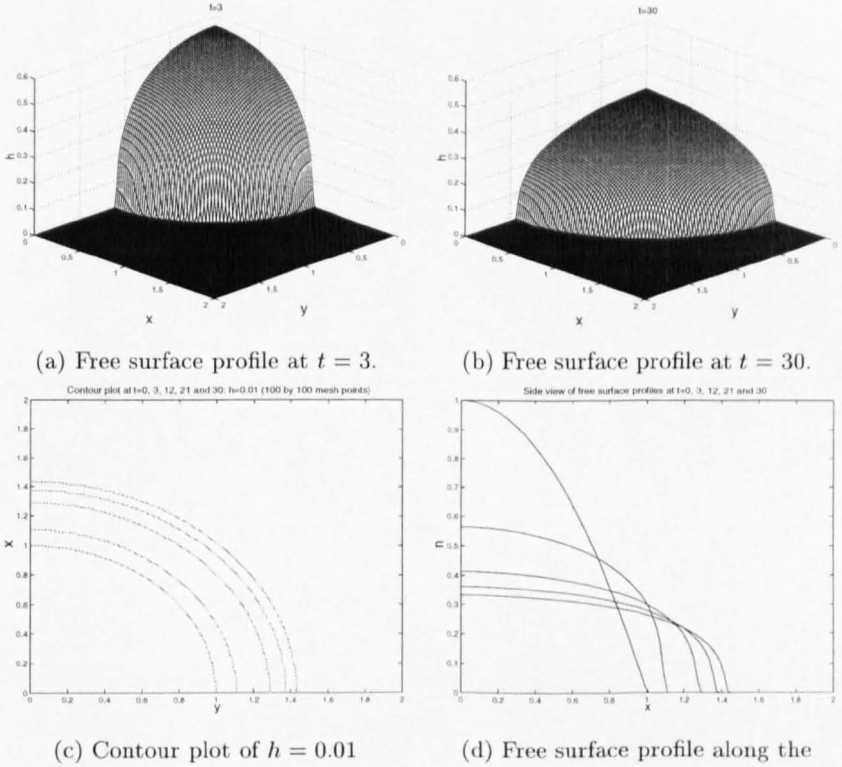

(a) Free surface profile at $t = 3$. (b) Free surface profile at $t = 30$.

(c) Contour plot of $h = 0.01$ (d) Free surface profile along the x-axis at $t = 0, 3, 12, 21, 30$.

FIG. 5.15. Isothermal spreading: $\alpha = 0$ with 100 by 100 mesh points.

The spreading satisfies $s \propto t^{0.124}$ for the front location and $h_{max} \propto t^{-0.24}$ for the maximum height. This is in good agreement with the similarity solutions for the axisymmetric case. The liquid is seen to spread radially, as in the contour plots in Figure 5.15(c). The free surface profile along the x-axis in Figure 5.15(d) show good visual agreement to the axisymmetric results in Chapter 4 (see Figure 4.27).

Introducing the thermal effects by setting $\alpha = 2$ and $\mathrm{Pe} = 10^6$ gives the results in Figure 5.16.

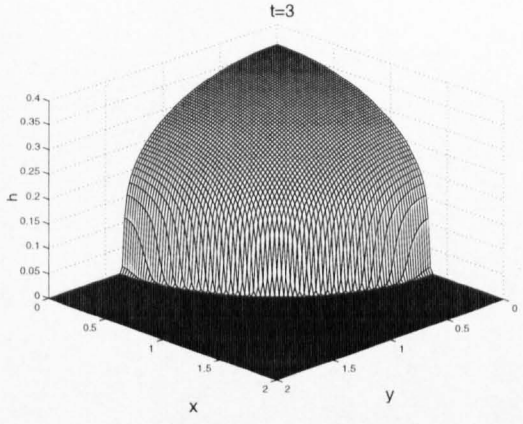

(a) Free surface profile at $t = 3$.

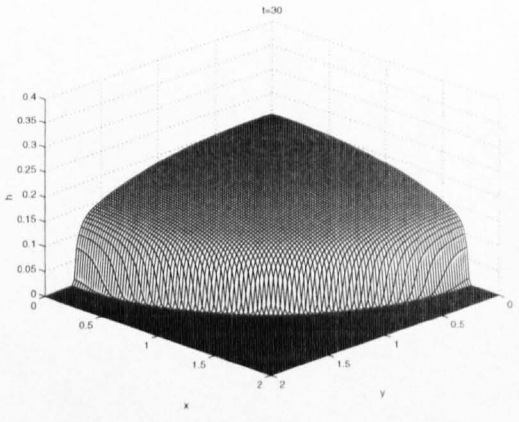

(b) Free surface profile at $t = 30$.

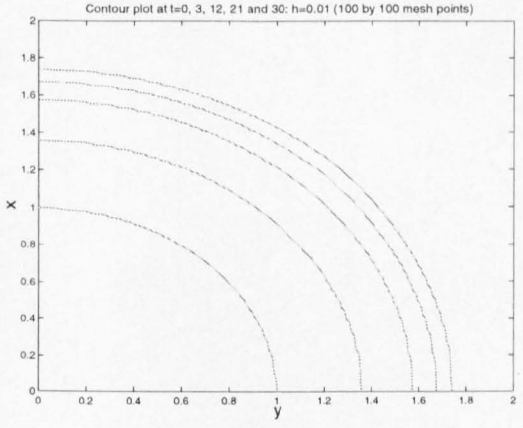

(c) Contour plot of $h = 0.01$

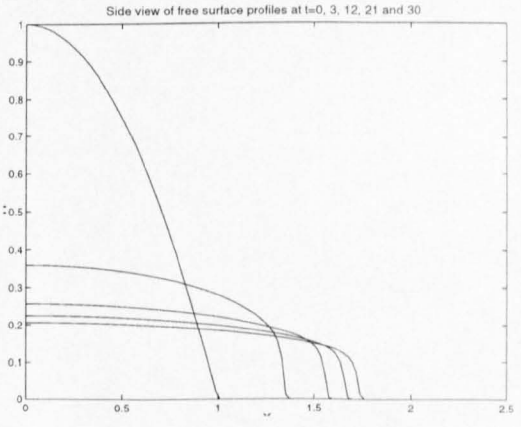

(d) Free surface profile along the x-axis at times $t = 0, 3, 12, 21$ and 30.

FIG. 5.16. Nonisothermal spreading: $\alpha = 2$, $\mathrm{Pe} = 10^6$ with 100 by 100 mesh points and $g_1 + g_2 = 0.5$.

The free surface profiles in Figure 5.16(d) show the steep flow front developing. The material again can be seen to be spreading radially, in good agreement with the axisymmetric results seen in Figure 4.31. Good agreement between the three-dimensional model and the results for radial symmetry for $\alpha = 2$ and $\mathrm{Pe} = 10^2$ is shown by Figures 5.17 and 4.34. The temperature profiles are again shown over the entire domain here, as opposed to being truncated at the flow front as in Chapter 4.

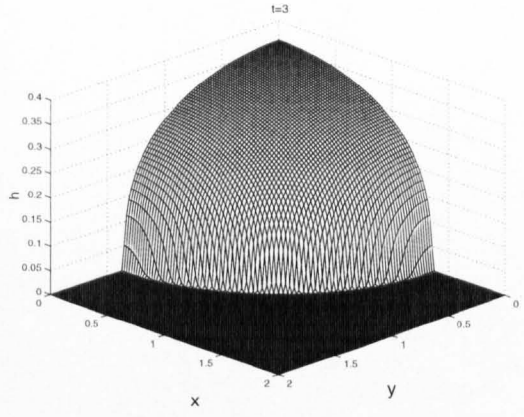

(a) Free surface profile at $t = 3$.

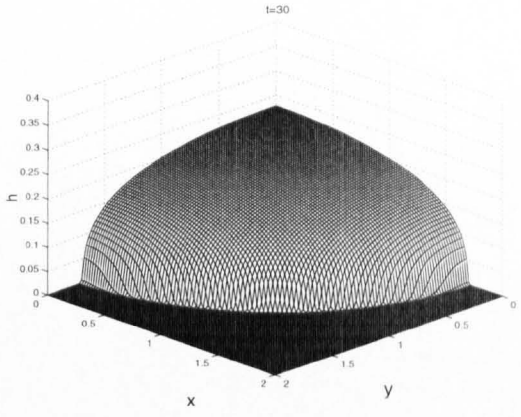

(b) Free surface profile at $t = 30$.

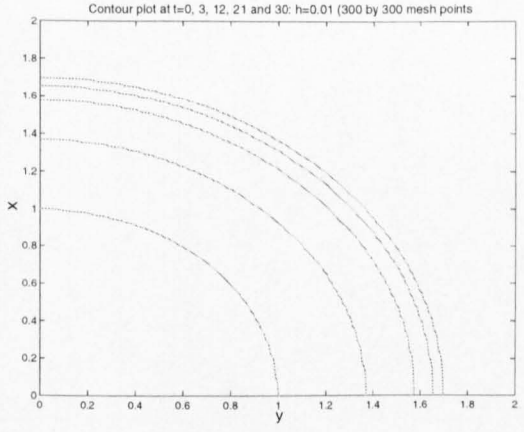

(c) Contour plot of $h = 0.01$

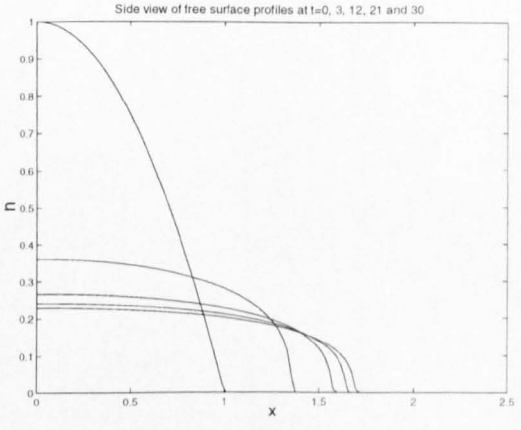

(d) Free surface profile along the x-axis at times $t = 0, 3, 12, 21$ and 30.

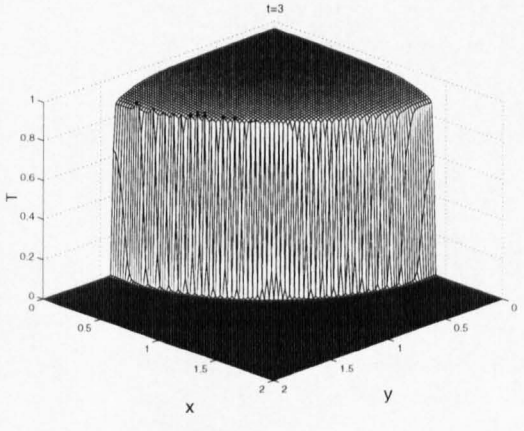

(e) Temperature profile at $t = 3$.

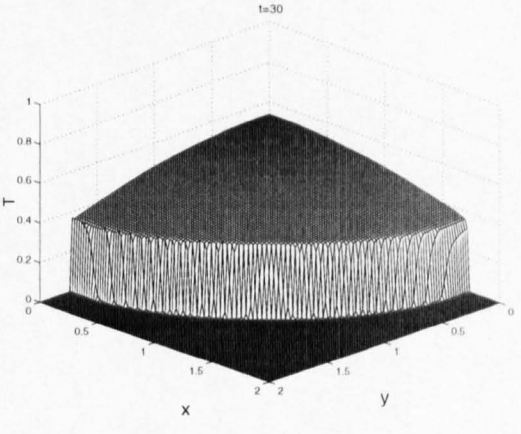

(f) Temperature profile at $t = 30$.

FIG. 5.17. Nonisothermal spreading: $\alpha = 2$, $\mathrm{Pe} = 10^2$ with 100 by 100 mesh points and $g_1 + g_2 = 0.5$.

Now we consider the more interesting case when there exists a strong coupling between the temperature and velocity fields. Results for $\mathrm{Pe} = 10^5$ are shown in Figures 5.18-5.19 for $\alpha = 5.9$.

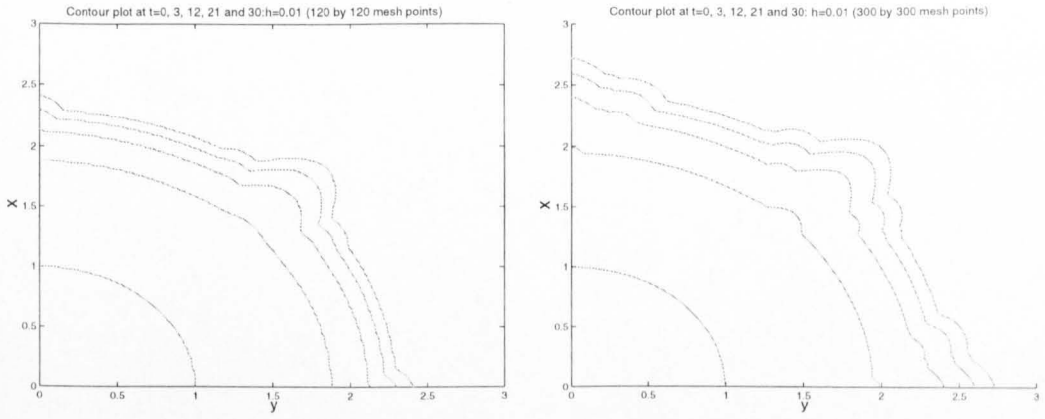

(a) (b)

FIG. 5.18. Nonisothermal spreading: three dimensions with $\mathrm{Pe} = 10^5$, $\alpha = 5.9$ and $g_1 + g_2 = 0.5$. Contour plots of $h = 0.01$ at $t = 3, 12, 21$ and 30. a) 120 by 120 mesh points. b) 300 by 300 mesh points

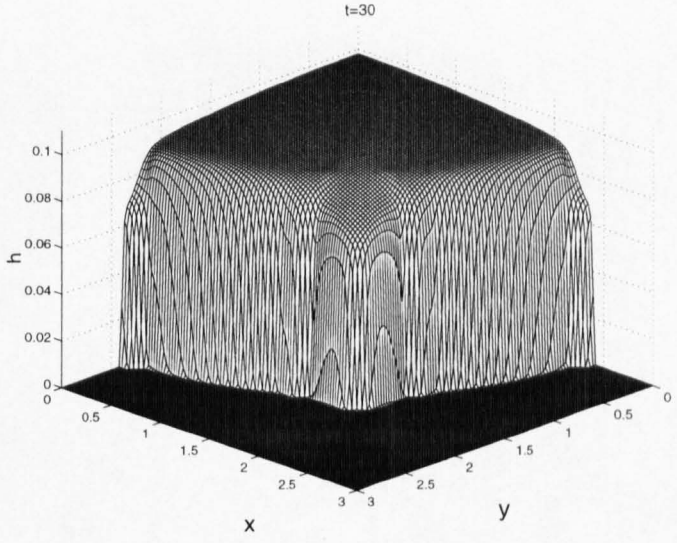

FIG. 5.19. Nonisothermal spreading: three dimensions with $\mathrm{Pe} = 10^5$, $\alpha = 5.9$ and $g_1 + g_2 = 0.5$. Free surface profile at $t = 30$ $h = 0.01$ at $t = 30$ with 120 by 120 mesh points.

The results in Figure 5.18 show the development of fingers produced by instabilities, the only perturbations to radial symmetry being introduced by the Cartesian mesh. Increasing the number of mesh points leads to more perturbations and subsequently more fingering. By contrast, the planar spreading results do not lead to a fingering morphology, unless introduced from the initial conditions because the Cartesian grid preserves the planar spreading. The free surface profile in Figure 5.19 is shown for the 120 by 120 mesh. Note that the finger is most prominent at an angular position of $\frac{\pi}{4}$; this is where the square mesh least represents the symmetry of the radial spreading.

The results shown in Figure 5.20 illustrate the effect of increasing the Peclet number. Figure 5.20(a) shows how the fingers are damped for sufficiently large time. Figure 5.20(b) shows the

fingering continuing to increase, the time not being sufficient to show the recovery of isothermal spreading which would require a very time consuming numerical run.

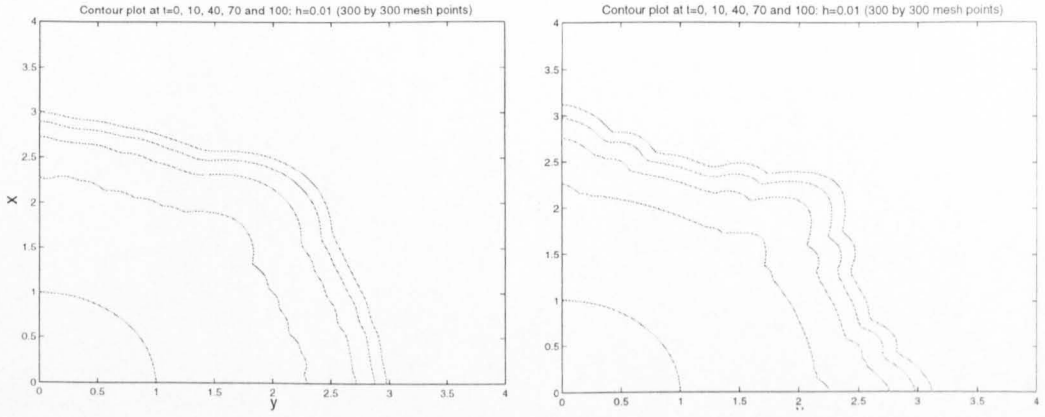

(a) (b)

FIG. 5.20. Nonisothermal spreading: three dimensions with $\alpha = 5.9$ and $g_1 + g_2 = 0.5$. Contour plots of $h = 0.01$ at $t = 0, 10, 40, 70$ and 100. a) $\mathrm{Pe} = 10^4$. b) $\mathrm{Pe} = 10^5$.

The above results introduced the perturbations from the mesh. The following results have the initial conditions

$$h = \left(1 - x^2 - y^2 + \varepsilon \cos\left(\lambda \arctan\left(\frac{y}{x}\right)\right)\right)_+ + 10^{-6} \quad \text{at } t = 0, \tag{5.4.4}$$

illustrated in Figure 5.21. Note that $\varepsilon = 0.05$ and $\lambda = 40$ are used for the following sets of results.

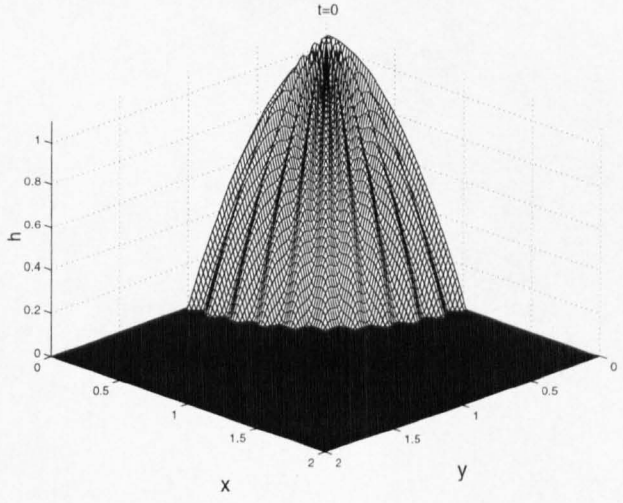

(a)

FIG. 5.21. Nonisothermal spreading: initial conditions, $\varepsilon = 0.05$ and $\lambda = 40$.

The first set of results, given in Figure 5.22, are for the isothermal case ($\alpha = 0$). The results show that the perturbations are damped out.

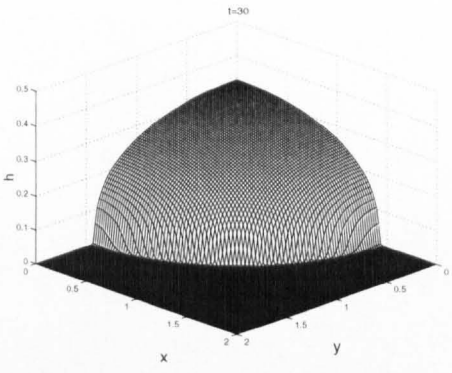

(a) Free surface profile at $t = 30$

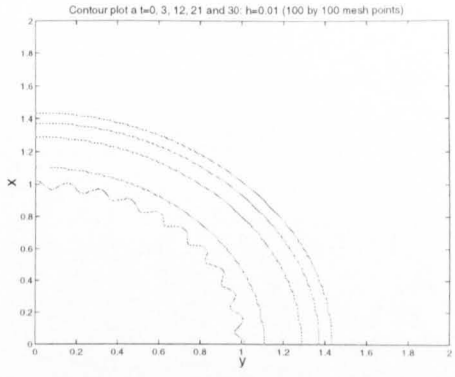

(b) Contour plot at $h = 0.01$.

FIG. 5.22. Isothermal spreading: $\alpha = 0$ with 100 by 100 mesh points.

The next set of results, with 120 by 120 mesh points over a $[0, 2] \times [0, 2]$ spatial domain with $\Delta t = 10^{-6}$, are shown in Figure 5.23. The small time scale is used because the diffusivity is initially very large and the results show fingering developing from the initial profile in Figure 5.21 with $\mathrm{Pe} = 10^3$ and $\alpha = 8.0$, which imply a large amount of cooling and a strong coupling between the temperature and velocity fields. The temperature profiles are clearly affected by the free surface perturbations, as in the planar spreading case, and the fingers are hot.

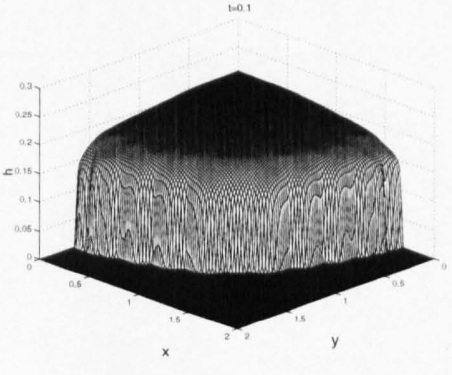

(a) Free surface profile at $t = 0.1$.

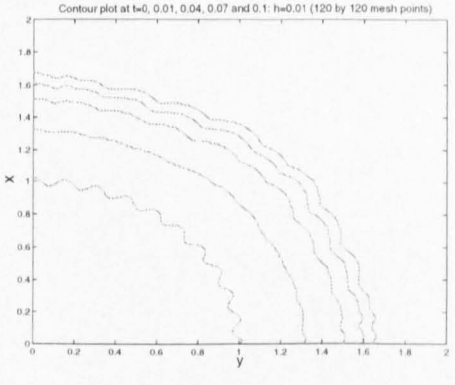

(b) Contour plots of $h = 0.01$ at $t = 0, 0.01, 0.04, 0.07$ and 0.1.

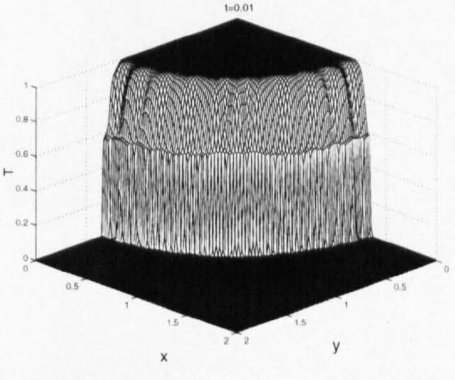

(c) Temperature profiles at $t = 0.01$.

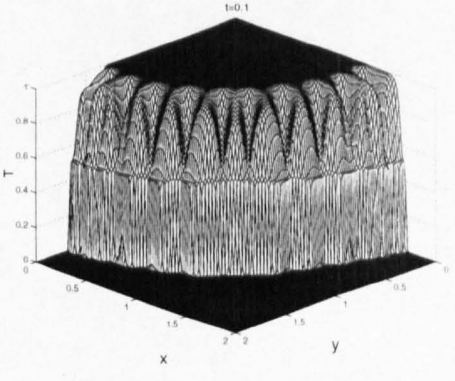

(d) Temperature profiles at $t = 0.1$.

FIG. 5.23. Nonisothermal spreading: three dimensions with $\mathrm{Pe} = 10^3$ $\alpha = 8.0$ and $g_1 + g_2 = 0.5$.

Increasing the time range to $[0, 5]$ and with 180 by 180 mesh points in the x and y-direction of size $[0, 3] \times [0, 3]$ gives the results in Figure 5.24. For large time the perturbations can be seen to be damped as the temperature tends to zero.

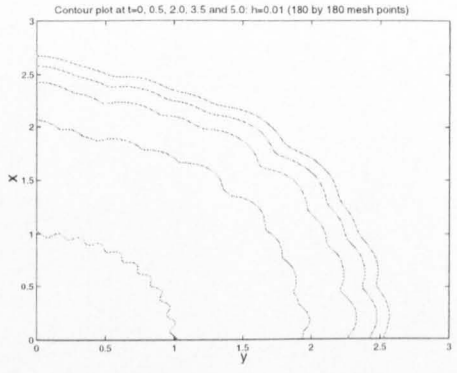

(a) Contour plots of $h = 0.01$ at $t = 0, 0.5, 2.0, 3.5$ and 5.0.

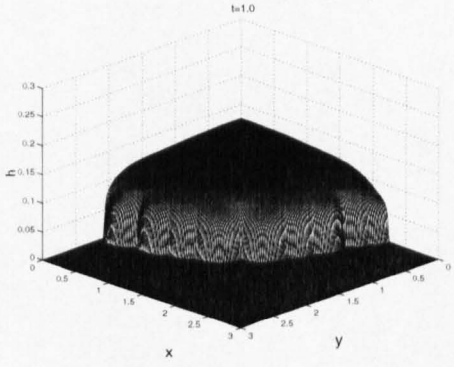

(b) Free surface profile at $t = 0.5$.

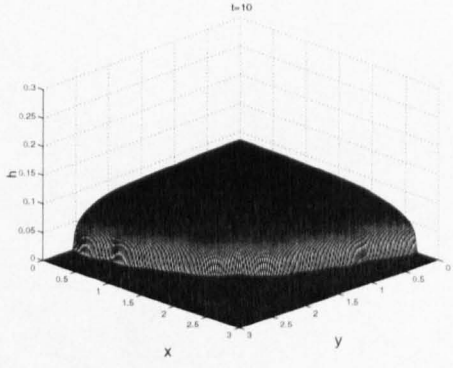

(c) Free surface profile at $t = 5.0$.

FIG. 5.24. Nonisothermal spreading: three dimensions with $\mathrm{Pe} = 10^3$, $\alpha = 8.0$ and $g_1 + g_2 = 0.5$.

The next set of results shows that decreasing α to 6 leads to a quicker suppression of the perturbations, see Figure 5.25.

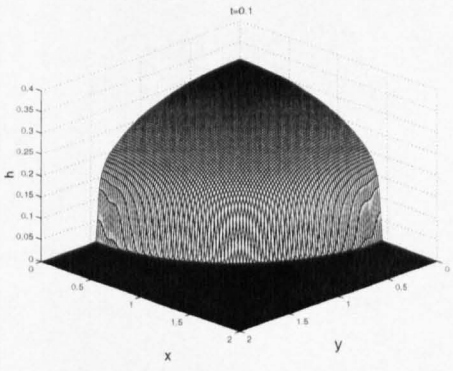

(a)

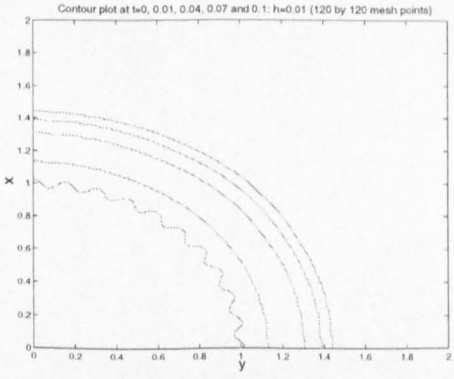

(b)

FIG. 5.25. Nonisothermal spreading: three dimensions with $\mathrm{Pe} = 10^3$, $\alpha = 6.0$ and $g_1 + g_2 = 0.5$. a) Free surface profile at $t = 0.1$ b) Contour plots of $h = 0.01$ at $t = 0, 0.01, 0.04, 0.07$ and 0.1.

The contour plots in Figure 5.26 show that with $\mathrm{Pe} = 10^5$ or $\mathrm{Pe} = 10^8$ and $\alpha = 8$ there are again no instabilities, the liquid spreading radially after a short transient. This implies that to get the instabilities, the liquid needs to lose heat (requiring Pe to be smaller) in order to produce a viscosity contrast along the front, enabling the development of the fingering morphology.

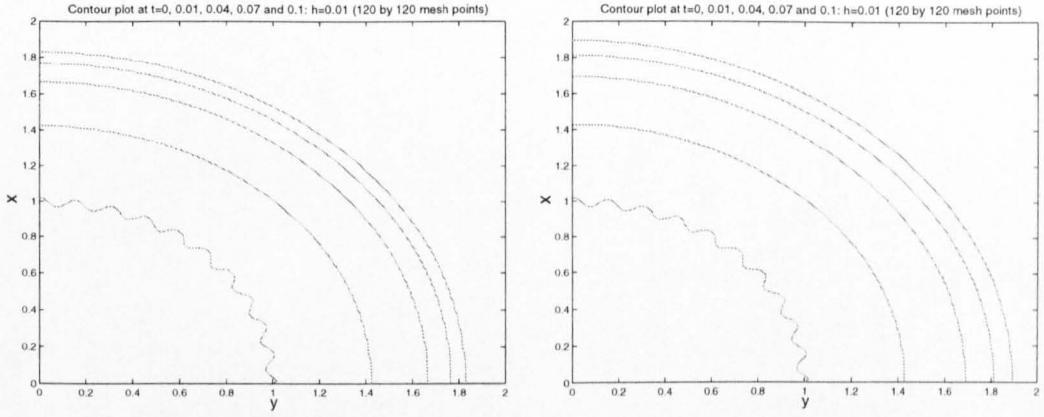

(a) (b)

FIG. 5.26. Nonisothermal spreading: three dimensions with $\alpha = 8.0$ and $g_1 + g_2 = 0.5$. a) Contour plots of $h = 0.01$, $\mathrm{Pe} = 10^5$ at $t = 0, 0.01, 0.04, 0.07$ and 0.1. b) Contour plots of $h = 0.01$, $\mathrm{Pe} = 10^8$ at $t = 0, 0.01, 0.04, 0.07$ and 0.1.

The effects of increasing the parameter λ is shown in Figure 5.27. As in the planar spreading results, increasing λ increases the number of fingers developing along the flow front. The results are shown with $\mathrm{Pe} = 10^3$ and $\alpha = 8.0$ in a 120 by 120 mesh with $\Delta t = 10^{-6}$. Increasing λ has a similar effect to increasing the number of mesh points (Figure 5.18), where there is a related increase in the number of fingers developing.

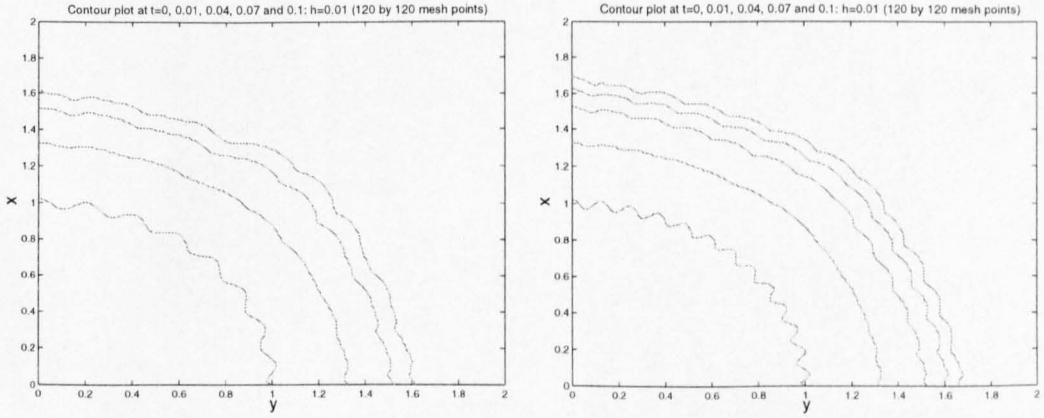

(a) (b)

FIG. 5.27. Nonisothermal spreading: three dimensions with $\mathrm{Pe} = 10^3$, $\alpha = 8.0$ and $g_1 + g_2 = 0.5$. Contour plots of $h = 0.01$ at $t = 0, 0.01, 0.04, 0.07$ and 0.1. a) $\lambda = 30$. b) $\lambda = 50$.

Increasing the time range from $[0, 0.1]$ as seen in Figure 5.27 to $[0, 0.3]$ gives the results in

Figure 5.28. The fingering is still seen to be developing with time; where there is not a sufficient amount of cooling to produce the isothermal case.

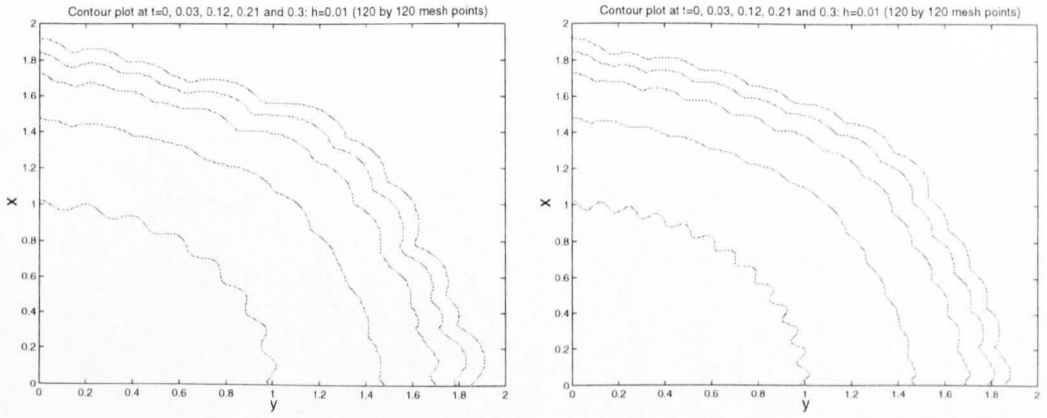

(a) (b)

FIG. 5.28. Nonisothermal spreading: three dimensions with $\mathrm{Pe} = 10^3$, $\alpha = 8.0$ and $g_1 + g_2 = 0.5$. Contour plots of $h = 0.01$ at $t = 0, 0.03, 0.12, 0.21$ and 0.3. a) $\lambda = 30$. b) $\lambda = 50$.

A parameter survey in (α,Pe) space seen in Figure 5.29 shows the region where the liquid material is most unstable. Increasing α, shows an increase in the range of Peclet values that can support the fingering growth. For large Peclet numbers, $\mathrm{Pe} > 10^8$, and $\mathrm{Pe} < 10$ the spreading is always stable since liquid is in an isothermal state. Note that for large time that the liquid temperature $T \to 0$ and results in a stable flow.

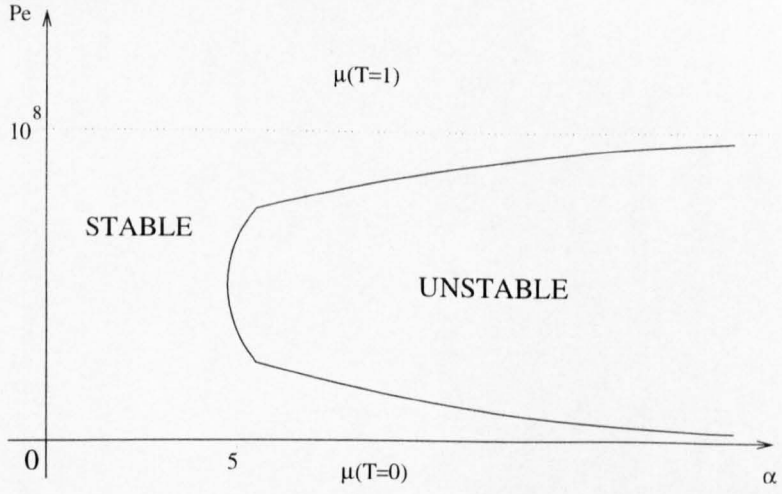

FIG. 5.29. Parameter survey of transient instabilities

5.5. Numerical Validation

The three-dimensional results show good agreement with the isothermal results in Chapter 4 (Figures 5.2(d) and 4.2 for planar spreading; Figures 5.15(d) and 4.27 for radial spreading) and agree with the similarity solutions. Including the thermal field, the results are again seen to agree

with the respective two-dimensional results in Chapter 4; see Figure 5.3 for example. This gives good confidence in the numerical schemes discussed in section 5.3.

The purpose of this section is to show that the fingering is mesh independent. The fingering is only prevalent when perturbations are introduced; for the planar spreading results the perturbations are only introduced by the initial conditions. The results in Figure 5.30 with $\mathrm{Pe} = 10^3$, $\alpha = 8.0$ and $\Delta t = 5 \times 10^{-6}$ show that the perurbations are dependent on the initial conditions and not the mesh. Figure 5.30(a) has 120 by 120 mesh points and Figure 5.30(b) has 160 by 160 mesh points.

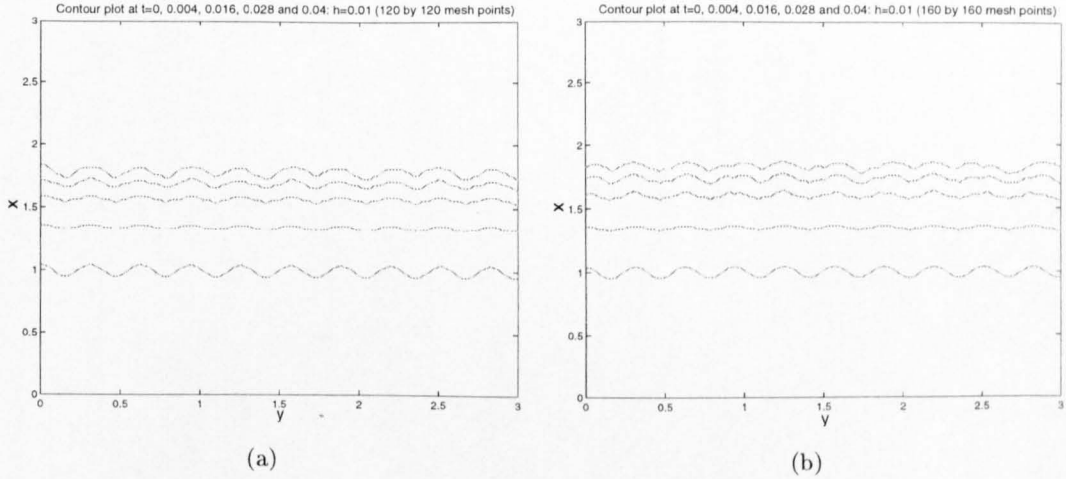

FIG. 5.30. Nonisothermal planar spreading: three dimensions with $\mathrm{Pe} = 10^3$, $\alpha = 8.0$ and $g_1 + g_2 = 0.5$ of contour plots of $h = 0.01$ at $t = 0, 0.004, 0.012, 0.028$ and 0.04. a) 120 by 120 mesh points. b) 160 by 160 mesh points.

This instability is also seen in Figures 5.13 and 5.27, where increasing the parameter λ increases the number of fingers developing along the flow front. Note that the results seen in Figure 5.18 (axisymmetric spreading) show that in the absence of initial perturbations, the development of fingers is produced by perturbations introduced by the anisotropic discretisation used by our numerical scheme.

5.6. Discussion

The results show that introducing perturbations along the flow front can cause the development of fingering. The fingering is shown to be mesh independent and dependent on the initial perturbations; hence the fingering is not a numerical instability. The fingering is shown to develop when there is a strong coupling between the velocity and temperature fields and a sufficient amount of cooling to produce a significant viscosity contrast along the flow front. When we have hotter liquid pushing against the cooler liquid near to the contact line, we have a situation in which less viscous liquid is displacing liquid that is more viscous. This is the physical basis on which Snyder & Tait (1998) postulated that the instability is analogous to the Saffman-Taylor fingering,

Saffman & Taylor (1958). For small time, the spreading is isothermal ($T = 1$) and this is also true for large time ($T = 0$). In between the two isothermal phases, instabilities arise when there exist a sufficiently steep viscosity gradient near the flow front.

CHAPTER SIX

Conclusion

6.1. Conclusion

In this thesis we have, by introducing a temperature-dependent viscosity, investigated the effect that a temperature field has on a non-isothermal gravity current of small aspect ratio spreading on a smooth horizontal substrate. Four temperature models have been considered, namely the heat source dominated model and the hot and cold substrate models in Chapter 2, the conduction limited model in Chapter 3 and the conduction dominated model in Chapters 4 and 5.

Inspite of the different temperature models considered, a widely occurring mechanism seen in nearly every model is the development of the steep flow front followed by a plateau. Physically this mechanism is caused by the accumulation at the flow front of cooled fluid transported along the top of the melt near where the flow is more mobile, see Stasiuk *et al.* (1993). The colder, more viscous fluid, at the front forms a barrier, forcing the height at the front to grow with time as hot, less viscous fluid continues to be fed in behind the front. The only temperature model not to show the plateauing is the hot and cold substrate temperature models in Chapter 2 which can be mapped to the isothermal spreading. The temperature in Chapter 3 varies in the vertical direction, whereas in Chapters 4 and 5 it is constant in the vertical direction. The isotherms shown in the experiments by Stasiuk *et al.* (1993) are seen to vary in the vertical direction, implying that the conduction limited model in Chapter 3 is the closest related model in this thesis.

Another theme seen in the later chapters (Chapters 3-5), relates to the fact that for small time (most noticeable with a large Peclet value), the spreading is seen to flow isothermally ($\mu = \mu(T = 1)$) and similarly for large time or with a small Peclet number, isothermal ($\mu = \mu(T = 0)$) spreading is again observed.

The most interesting results are probably those in the three-dimensional model in Chapter 5. The growth of fingers developing from the initial perturbations have a similar life span to that of the steep flow front seen in the earlier chapters. That is, as the fluid cools the fingers are seen to be suppressed, with the behaviour tending to the isothermal case ($\mu = \mu(T = 0)$). The steep flow front and plateauing are observed in the three-dimensional model, in agreement with the respective two-dimensional model. The fingering patterns seen in this thesis are caused by the viscosity gradients imposed near the flow front.

Aspects of this work in this thesis are to appear in King *et al.* (2000).

6.2. Further work

Possible extensions to the work in this thesis would include adding the third spatial dimension in Chapter 3, although would be computationally very time consuming. The temperature model in Chapters 4 and 5 could be extended to include the effects of viscous dissipation. Stability studies, non-thin film effects, chemical reaction effects and inertial effects could also be considered. Other possibilities could be to include into the formulation a non-horizontal substrate, as for example in López *et al.* (1996) (who also discuss surface tension effects) or introducing non-Newtonian effects into the model equations (as seen in Huang & Garcia (1998)).

The final extension we note is the subject current of work which develops further the hot substrate model first derived in Chapter 2, where an extra spatial dimension is now introduced and the substrate is assumed to have a variable temperature profile.

The governing non-dimensionalised temperature equation is derived from (5.2.46) on assuming $\epsilon^2 \ll 1$ (small aspect ratio) and $\epsilon^2 \mathrm{Pe} \ll 1$ (small reduced Peclet number). The temperature equation is thus given by

$$\frac{\partial^2 T}{\partial z^2} = 0 \tag{6.2.1}$$

with the boundary conditions $T = 0$ on the free surface and $T = T_b(x, y)$ on the substrate. The temperature equation can be easily solved using the boundary conditions to give

$$T = \frac{(h - z)T_b(x, y)}{h}. \tag{6.2.2}$$

The free surface evolution equation derived in the previous chapter in three-dimensions, (5.2.43), is given by

$$\frac{\partial h}{\partial t} = \frac{\partial}{\partial x}\left(D\frac{\partial h}{\partial x}\right) + \frac{\partial}{\partial y}\left(D\frac{\partial h}{\partial y}\right), \tag{6.2.3}$$

where

$$D = \int_0^h \frac{(z - h)^2}{\mu} dz. \tag{6.2.4}$$

The temperature equation, (6.2.2), is coupled to the free surface equation by the exponential non-dimensionalised viscosity law given by

$$\mu = \exp(-\alpha T), \tag{6.2.5}$$

where α is a positive constant. Substituting the viscosity law and temperature equation (6.2.2) into (6.2.4) gives the diffusivity as

$$D = \frac{h^3(\exp(\alpha T_b(x, y))(\alpha^2 T_b(x, y)^2 - 2\alpha T_b(x, y) + 2) - 2)}{\alpha^3 T_b(x, y)^3}. \tag{6.2.6}$$

This model is currently being investigated numerically by myself using similar numerical schemes to those discussed in Chapter 5.

APPENDICES

Appendix A. Nomenclature

The following lists the key notation used in this thesis.

x	horizontal spatial component
r	horizontal spatial component in polar coordinates
y	second horizontal spatial component (three-dimensional model)
z	vertical spatial component
u	horizontal velocity component
v	second horizontal velocity component (three-dimensional model)
w	vertical velocity component
t	time
T	temperature
h	free surface height
$\mu(T)$	Newtonian dynamic viscosity
k	thermal conductivity
ρ	density
p	pressure
c	specific heat
U_0	typical horizontal velocity scale
l_0	typical horizontal length scale
h_0	typical vertical length scale
μ_0	typical viscosity scale
ϵ	aspect ratio ($\epsilon = l_0/h_0$)
Pe	Peclet number (Pe = $\rho c U_0 l_0/k$)
Pe_r	reduced Peclet number ($\mathrm{Pe}_r = \epsilon^2 \mathrm{Pe}$)
Pr	Prandtl number (Pr = $c\mu_0/k$)
R	Reynolds number (R = $\rho U_0 l_0/\mu_0$)
ψ	stream function
Ψ	Stokes stream function
η	similarity variable
$\dot{q}$	heat source
s	flow front position

FIG. A.1. Nomenclature

Appendix B. Linearisation method

The isothermal equation governing the free surface, (2.2.1c), can be linearised, as shown for the general nonlinear diffusion equation in Richtmyer & Morton (1967). Equation (2.2.1c) can be written as,

$$\frac{\partial h}{\partial t} = \frac{1}{12}\frac{\partial^2 h^4}{\partial x^2}. \tag{B 1}$$

Denoting $h\left((i-1)\Delta x, n\Delta t\right)$ by h_i^n and using a Crank-Nicolson implicit scheme gives,

$$\frac{h_i^{n+1} - h_i^n}{\Delta t} = \frac{(h^4)_{i-1}^{n+1} - 2(h^4)_i^{n+1} + (h^4)_{j+1}^{n+1} + (h^4)_{i-1}^n - 2(h^4)_i^n + (h^4)_{j+1}^n}{24\Delta x^2} \tag{B 2}$$

This gives rise to nonlinear simultaneous equations, but a linear scheme is required. A suitable method is to approximate the $(h^4)_i^{n+1}$ by a linear scheme. This is done by time marching using Taylor's expansion of $(h^4)_i^{n+1}$ about the point (i, n), such that

$$(h^4)_i^{n+1} = (h^4)_i^n + \Delta t \left(\frac{\partial h^4}{\partial t}\right)_i^n + O(\Delta t^2). \tag{B 3}$$

Note that

$$\frac{\partial h^4}{\partial t} = 4h^3\frac{\partial h}{\partial t},$$

hence to $O(\Delta t)$

$$(h^4)_i^{n+1} = (h_i^4)^n + 4(h^3)_i^n(h_i^{n+1} - h_i^n). \tag{B 4}$$

Let $w_i = h_i^{n+1} - h_i^n$ and substitute (B 4) in (B 2) giving

$$\begin{aligned}\frac{w_i}{\Delta t} = \big[&(h^4)_{i-1}^n + 4(h^3)_{i-1}^n w_{i-1} - 2(h^4)_i^n - 8(h^3)_i^n w_i + (h^4)_{i+1}^n \\ &+4(h^3)_{i+1}^n w_{i+1} + (h^4)_{i-1}^n - 2(h^4)_i^n + (h^4)_{i+1}^n\big]/(24\Delta x^2).\end{aligned}$$

Rearranging gives,

$$-2r_x(h^3)_{i-1}^n w_{i-1} + (1 + 4r_x(h^3)_i^n)w_i - 2r_x(h^3)_{i+1}^n w_{i+1} = d_i^n, \tag{B 5}$$

where

$$d_i^n = r_x\left[(h^4)_{i-1}^n - 2(h^4)_i^n + (h^4)_{i+1}^n\right],$$

and $r_x = \frac{\Delta t}{12\Delta x^2}$. Equation (B 5) can be solved for ω using the Thomas algorithm taking the d_i^n as known. The equation $h_i^{n+1} = h_i^n + w_i$ completes the time step. Taking account of symmetry in the problem at $i = 1$ gives $h_{i+1} = h_{i-1}$ such that,

$$(1 + 4r_x(h^3)_i^n)w_i - 4r_x(h^3)_{i+1}^n w_{i+1} = d_i^n, \tag{B 6}$$

where

$$d_i^n = 2r_x\left[-(h^4)_i^n + (h^4)_{i+1}^n\right].$$

Implementing the above algorithm using FORTRAN 90 code gives the free surface profiles in Figure (B.2). Comparing the results with the NAG routine D03PCF shows four decimal places

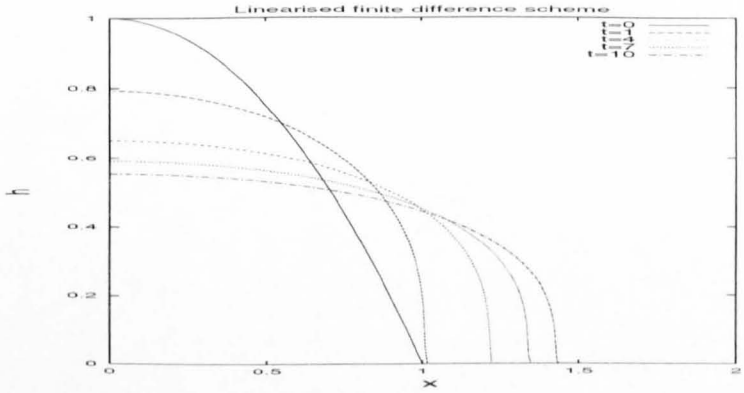

FIG. B.2. height profiles.

agreement with five hundred mesh points over the same range $0 \leq x \leq 3$ in both schemes. Note that NAG routine D03PCF is the updated NAG routine D03PGF.

Appendix C. Local truncation error analysis for the height profile finite difference scheme

In this appendix the local truncation error of the finite difference scheme governing the free surface is evaluated as shown in Smith (1985). The scheme (3.2.2) for the free surface can be written as,

$$\frac{h_i^{n+1}-h_i^n}{\Delta t} - \frac{1}{4\Delta x^2}\left[(h_{i+1}^{n+1}-h_i^{n+1})(D_{i+1}^{n+1}+D_i^{n+1}) - (h_i^{n+1}-h_{i-1}^{n+1})(D_i^{n+1}+D_{i-1}^{n+1})\right.$$
$$\left. + (h_{i+1}^{n}-h_i^{n})(D_{i+1}^{n}+D_i^{n}) - (h_i^{n+1}-h_{i-1}^{n+1})(D_i^{n+1}+D_{i-1}^{n+1})\right] = 0. \quad \text{(C 1)}$$

The following Taylor's expansions are substituted into (C 1).

$$h_i^{n+1} = h_i^n + \Delta t\left(\frac{\partial h}{\partial t}\right)_i^n + \frac{\Delta t^2}{2}\left(\frac{\partial^2 h}{\partial t^2}\right)_i^n + \frac{\Delta t^3}{6}\left(\frac{\partial^3 h}{\partial t^3}\right)_i^n + \cdots \quad \text{(C 2)}$$

$$h_{i\pm1}^{n+1} = h_i^n \pm \Delta x\left(\frac{\partial h}{\partial x}\right)_i^n + \Delta t\left(\frac{\partial h}{\partial t}\right)_i^n + \frac{\Delta x^2}{2}\left(\frac{\partial^2 h}{\partial x^2}\right)_i^n \pm \Delta x\Delta t\left(\frac{\partial^2 h}{\partial x\partial t}\right)_i^n + \frac{\Delta t^2}{2}\left(\frac{\partial^2 h}{\partial t^2}\right)_i^n$$
$$\pm \frac{\Delta x^3}{6}\left(\frac{\partial^3 h}{\partial x^3}\right)_i^n + \frac{\Delta x^2\Delta t}{2}\left(\frac{\partial^3 h}{\partial x^2\partial t}\right)_i^n \pm \frac{\Delta x\Delta t^2}{2}\left(\frac{\partial^3 h}{\partial x\partial t^2}\right)_i^n + \frac{\Delta t^3}{6}\left(\frac{\partial^3 h}{\partial t^3}\right)_i^n + \cdots \quad \text{(C 3)}$$

$$h_{i\pm1}^{n} = h_i^n \pm \Delta x\left(\frac{\partial h}{\partial x}\right)_i^n + \frac{\Delta x^2}{2}\left(\frac{\partial^2 h}{\partial x^2}\right)_i^n \pm \frac{\Delta x^3}{6}\left(\frac{\partial^3 h}{\partial x^3}\right)_i^n + \cdots \quad \text{(C 4)}$$

and can be similarly derived for D. Substituting the Taylor's expansions into the finite difference scheme gives

$$\left(\frac{\partial h}{\partial t}\right)_i^n - D_i^n\left(\frac{\partial^2 h}{\partial x^2}\right)_i^n - \left(\frac{\partial h}{\partial x}\right)_i^n\left(\frac{\partial D}{\partial x}\right)_i^n = 0 + O(\Delta x^2) + O(\Delta t). \quad \text{(C 5)}$$

Hence the truncation is $O(\Delta t)$ in time and $O(\Delta x^2)$ in space as expected. The principal part of the local truncation error is

$$\left(\frac{\Delta t}{2}\frac{\partial^2 h}{\partial t^2} - \frac{\Delta t}{2}\frac{\partial h}{\partial x}\frac{\partial^2 D}{\partial x\partial t} - \frac{\Delta t}{2}\frac{\partial^2 h}{\partial x\partial t}\frac{\partial D}{\partial x} - \frac{\Delta t}{2}D\frac{\partial^3 h}{\partial x^2\partial t}\right.$$

$$-\frac{\Delta x^2}{6}\frac{\partial h}{\partial x}\frac{\partial^3 D}{\partial x^3}-\frac{\Delta x^2}{4}\frac{\partial^2 h}{\partial x^2}\frac{\partial^2 D}{\partial x^2}-\frac{\Delta x^2}{6}\frac{\partial^3 h}{\partial x^3}\frac{\partial D}{\partial x}-\frac{\Delta x^2}{12}\frac{\partial^4 h}{\partial x^4}D\Bigg)\Bigg|_i^n. \tag{C 6}$$

Considering the explicit scheme for the free surface,

$$\frac{h_i^{n+1}-h_i^n}{\Delta t}-\frac{1}{2\Delta x^2}\left[(h_{i+1}^n-h_i^n)(D_{i+1}^n+D_i^n)-(h_i^n-h_{i-1}^n)(D_i^n+D_{i-1}^n)\right]=0, \tag{C 7}$$

gives the principal part of the local truncation error as

$$\left(\frac{\Delta t}{2}\frac{\partial^2 h}{\partial t^2}-\frac{\Delta x^2}{6}\frac{\partial h}{\partial x}\frac{\partial^3 D}{\partial x^3}-\frac{\Delta x^2}{4}\frac{\partial^2 h}{\partial x^2}\frac{\partial^2 D}{\partial x^2}-\frac{\Delta x^2}{6}\frac{\partial^3 h}{\partial x^3}\frac{\partial D}{\partial x}-\frac{\Delta x^2}{12}\frac{\partial^4 h}{\partial x^4}D\right)\Bigg|_i^n. \tag{C 8}$$

Considering an explicit scheme where the derivatives are discretised using standard central differences such that,

$$\frac{h_i^{n+1}-h_i^n}{\Delta t}-\frac{1}{2\Delta x^2}\left[(h_{i+2}^n-h_i^n)D_{i+1}-(h_i^n-h_{i-2}^n)D_{i-1}^n\right]=0. \tag{C 9}$$

This gives the principal part of the local truncation error as.

$$\left(\frac{\Delta t}{2}\frac{\partial^2 h}{\partial t^2}-\frac{\Delta x^2}{6}\frac{\partial h}{\partial x}\frac{\partial^3 D}{\partial x^3}-\frac{\Delta x^2}{2}\frac{\partial^2 h}{\partial x^2}\frac{\partial^2 D}{\partial x^2}-\frac{2\Delta x^2}{3}\frac{\partial^3 h}{\partial x^3}\frac{\partial D}{\partial x}-\frac{\Delta x^2}{3}\frac{\partial^4 h}{\partial x^4}D\right)\Bigg|_i^n. \tag{C 10}$$

Appendix D. Viscous dissipation

The energy equation governing the temperature evolution is

$$\rho c\left(\frac{\partial\theta}{\partial t}+u\frac{\partial\theta}{\partial x}+w\frac{\partial\theta}{\partial z}\right)=k\left(\frac{\partial^2\theta}{\partial x^2}+\frac{\partial^2\theta}{\partial z^2}\right)+\dot{q}+2\mu e_{ij}^2, \tag{D 1}$$

where c is the specific heat of the drop, k is the thermal conductivity, $\dot{q}$ is the strength of a heat source, θ is the temperature of the fluid, θ_s is the temperature on the substrate, θ_a is the ambient temperature and $2\mu e_{ij}^2$ is the viscous dissipation term. We define $\epsilon = h_0/l_0$ (the aspect ratio), where l_0 and h_0 are typical length scales in the x and z-directions respectively, U_0 to be a typical horizontal velocity scale and μ_0 to be a typical viscosity scale. The equations are non-dimensionalised by introducing

$$x=l_0x^*,\quad z=h_0z^*,\quad u=U_0u^*,\quad w=\epsilon U_0w^*,\quad \mu=\mu_0\mu^*,$$

$$T=\frac{\theta-\theta_1}{\Delta\theta},\quad \dot{q}=\frac{\Delta\theta}{h_0^2}\dot{q}^*,\quad t=\frac{l_0}{U_0}t^*,\quad \text{and}\quad p=\frac{U_0\mu_0l_0}{h_0^2}p^*. \tag{D 2}$$

The temperature is thus measured relative to θ_1 in units $\Delta\theta_1$ such that $\Delta\theta=\theta_i$ and $\theta_1=\theta_a=\theta_s$. Dropping the star notation for brevity, the above scales transform the energy equation to (the viscous dissipation being dealt with subsequently),

$$\epsilon^2\mathrm{Pe}\left\{\frac{\partial T}{\partial t}+u\frac{\partial T}{\partial x}+w\frac{\partial T}{\partial z}\right\}=\epsilon^2\frac{\partial^2T}{\partial x^2}+\frac{\partial^2T}{\partial z^2}+\dot{q}+\frac{2h_0^2\mu_0}{\Delta\theta k}\mu e_{ij}^2, \tag{D 3}$$

where the Prandtl number, Pe, is defined by

$$\mathrm{Pr}=\frac{c\mu_0}{k},$$

the Peclet number, Pe, by

$$\mathrm{Pe}=R\mathrm{Pr}=\frac{\rho cU_0l_0}{k}$$

and the Reynolds number, R, by

$$R = \frac{\rho U_0 l_0}{\mu_0}.$$

The extra terms caused by viscous dissipation of energy gives rise to

$$2\mu e_{ij}^2 = 2\mu(e_{11}^2 + e_{22}^2 + 2e_{12}^2), \tag{D 4}$$

where

$$e_{ij} = \frac{1}{2}\left(\frac{\partial u_i}{\partial x_j} + \frac{\partial u_j}{\partial x_i}\right). \tag{D 5}$$

Hence

$$2\mu e_{ij}^2 = 2\mu\left(\left(\frac{\partial u}{\partial x}\right)^2 + \left(\frac{\partial w}{\partial z}\right)^2 + \frac{1}{2}\left(\frac{\partial u}{\partial z} + \frac{\partial w}{\partial x}\right)^2\right) \tag{D 6}$$

Non-dimensionlising using the above scales and dropping the star notation gives

$$\frac{2U_0^2\epsilon^2\mu_0}{k\Delta\theta}\mu\left(\left(\frac{\partial u}{\partial x}\right)^2 + \left(\frac{\partial w}{\partial z}\right)^2 + \frac{1}{2}\left(\frac{1}{\epsilon^2}\left(\frac{\partial u}{\partial z}\right)^2 + h_0^2\left(\frac{\partial w}{\partial x}\right)^2 + 2\frac{\partial u}{\partial z}\frac{\partial w}{\partial x}\right)\right). \tag{D 7}$$

The leading order term is

$$\frac{U_0^2\mu_0}{k\Delta\theta}\mu\left(\frac{\partial u}{\partial z}\right)^2 \tag{D 8}$$

or

$$\mathrm{Br}\mu\left(\frac{\partial u}{\partial z}\right)^2, \tag{D 9}$$

where Br is the Brinkman number, defined by

$$\mathrm{Br} = \frac{U_0^2\mu_0}{k\Delta\theta}. \tag{D 10}$$

From (2.1.14) the Brinkman number is given by

$$\mathrm{Br} = \frac{\epsilon^2(\rho g)^2 h_0^4}{\mu_0\Delta\theta}. \tag{D 11}$$

The full energy equation can then be written as

$$\epsilon^2\mathrm{Pe}\left\{\frac{\partial T}{\partial t} + u\frac{\partial T}{\partial x} + w\frac{\partial T}{\partial z}\right\} = \epsilon^2\frac{\partial^2 T}{\partial x^2} + \frac{\partial^2 T}{\partial z^2} + \dot{q} + \mathrm{Br}\mu\left(\frac{\partial u}{\partial z}\right)^2. \tag{D 12}$$

REFERENCES

Acheson, D. J., 1990. *Elementary Fluid Dynamics*. Oxford University Press.

Allen, M. B., Herrera, I. & Pinder, G. F., 1988. *Numerical modelling in science and engineering*. John Wiley and Sons.

Balmforth, N. J., Burbidge, A. S., Craster, R. V., Salzig, J. & Shen, A., 2000. Visco-plastic modles of isothermal lava does. *J. Fluid Mech.* **403**, 37–65.

Barenblatt, G. I., 1952. On some unsteady motions of a liquid or gas in a porous medium. *Prikl. Mat. Mech.* **16**, 67–78.

Bercovici, D., 1994. A theoretical model of cooling viscous gravity currents with temperature-dependent viscosity. *Geophys. Res. Lett.* **21**, 1177–1180.

Bercovici, D. & Lin, J., 1996. A gravity current model of cooling mantle plume heads with temperature-dependent buoyancy and viscosity. *J. Geophys. Res.* **101** , 3291–3309.

Braun, R. J., Murray, B. T., Boettinger, W. J. & McFadden, G. B., 1995. Lubrication theory for reactive spreading of a thin drop. *Phys. Fluids* **7**, 1797–1810.

Davis, S. H., 1983. Contact-line problems in fluid mechanics. *J. Appl. Mech.* **50**, 977–982.

Davis, S. H. & Hocking, L. M., 1999. Spreading and imbibition of viscous liquid on a porous base. *Phys. Fluids* **11(1)**, 48–57.

Dussan, V. E. B., 1979. On the spreading of liquids on solid surfaces: static and dynamic contact lines. *Ann. Rev. Fluid Mech.* **11**, 371–400.

Ehrhard, P., 1993. Experiments on isothermal and non-isothermal spreading. *J. Fluid Mech.* **257**, 463–483.

Ehrhard, P., 1994. The spreading of hanging drops. *J. Coll. Inter. Sci.* **168(1)**, 242–246.

Ehrhard, P. & Davis, S. H., 1991. Non-isothermal spreading of liquid drops on horizontal plates. *J. Fluid Mech.* **229**, 365–388.

Farlow, S. J., 1982. *Partial differential equations for scientists and engineers*. John Wiley and Sons.

Fink, J. H. & Griffiths, R. W., 1990. Radial spreading of viscous-gravity currents with solidifying crust. *J. Fluid Mech.* **221**, 485–509.

Fink, J. H. & Griffiths, R. W., 1992. A laboratory analog study of the surface morphology of lava flows extruded from point and line sources. *J. Volc. Geotherm. Res.* **54**, 19–32.

Fink, J. H. & Griffiths, R. W., 1998. Morphology, eruption rates, and rheology of lava domes: Insights from laboratory models. *J. Geophys. Res.* **103**, 527–545.

Greenspan, H. P., 1978. On the motion of a small viscous droplet that wets a surface. *J. Fluid Mech.* **84**, 125–143.

Gregg, T. K. P. & Fink, J. H., 1995. Quantification of submarine lava-flow morphology through analog experiments. *J. Geol.* **23** , 73–76.

Griffiths, R. W. & Fink, J. H., 1997. Solidifying Bingham extrusions: a model for the growth of silicic lava domes. *J. Fluid Mech.* **347**, 13–36.

Guest, J. E., Kilburn, C. R. J., Pinkerton, H. & Duncan, A. M., 1987. The evolution of lava-flow fields: Observations of the 1981 and 1983 eruptions of Mount Etna, Sicily. *Bull. Volc.* **49**, 527–540.

Haley, P. J. & Miksis, M. J., 1991. The effect of the contact line on droplet spreading. *J. Fluid Mech.* **223**, 57–81.

Hallot, E., Stasiuk, M., Allan, S., Riley, D. & Sparks, R., 1994. *Experiments on solidification of viscous gravity currents*. Nuclear Electric Report.

Hocking, L. M., 1983. The spreading of a thin drop by gravity and capillary. *Q. J. Mech. appl. Math.* **36**, 55–69.

Homsy, G. M., 1987. Viscous fingering in porous media. *Ann. Rev. Fluid Mech.* **19**, 271–311.

Huang, X. & Garcia, M. H., 1998. A Herschel-Bulkley model for mud flow down a slope. *J. Fluid Mech.* **374**, 305–333.

Huppert, H. E., 1982a. Flow and instability of viscous gravity currents down a slope. *Nature* **300**, 427–429.

Huppert, H. E., 1982b. The propagation of two-dimensional and axisymmetric viscous gravity currents over a rigid horizontal surface. *J. Fluid Mech.* **121**, 43–48.

Huppert, H. E., 1986. The intrusion of fluid mechanics into geology. *J. Fluid Mech.* **173**, 557–594.

Huppert, H. E., Shepherd, J. B., Sigurdsson, H. & Sparks, R. S. J., 1982. On lava dome growth with application to the 1979 lava extrusion of the Soufriere of St. Vincent. *J. Volc. Geotherm. Res.* **14**, 199–222.

Huppert, H. E. & Woods, A. W., 1995. Gravity-driven flows in porous layers. *J. Fluid Mech.* **292**, 55–69.

Johnson, M. F. G., Schluter, R. A., Miksis, M. J. & Bankoff, S. G., 1999. Experimental study of rivulet formation on an inclined plate by fluorescent imaging. *J. Fluid Mech.* **394**, 339–354.

Kafoussias, N. G. & Williams, E. W., 1995. Thermal-diffusion and diffusion-thermo effects on mixed free forced convective and mass-transfer boundary-layer flow with temperature-dependent viscosity. *Int. J. Eng. Sci.* **33(9)**, 1369–1384.

King, J. R., 1990. Exact similarity solutions to some nonlinear diffusion equations. *J. Phys. A: Mathematics and General* **23** , 3681–3697.

King, J. R., Riley, D. S. & Sansom, A., 2000. Gravity currents with temperature-dependent viscosity. *To appear in CAMES* .

Lacey, A. A., Ockendon, J. R. & Tayler, A. B., 1982. Waiting time solutions of a nonlinear diffusion equation. *SIAM J. Appl. Math.* **42(6)**, 1252–1264.

Lister, J. R., 1992. Viscous flows down an inclined plane from point and line sources. *J. Fluid Mech.* **242**, 631–653.

Liu, K. F. & Mei, C. C., 1989. Slow spreading of a sheet of Bingham fluid on an inclined plane. *J. Fluid Mech.* **207**, 506–529.

López, J. & Miller, C. A., 1976. Spreading kinetics of liquid drops on solids. *J. Coll. Inter. Sci.* **56**, 460–468.

López, P. G., Bankoff, S. G. & Miksis, M. J., 1996. Non-isothermal spreading of a thin liquid film on an incline. *J. Fluid Mech.* **324**, 261–286.

Matar, O. K. & Trojan, S. M., 1999. The development of transient fingering patterns during the spreading of surfactant coated films. *Phys. Fluids* **11(11)**, 3232–3246.

McKinley, I. S., Wilson, S. K. & Duffy, B. R., 1999. Spin coating and air-jet blowing of thin viscous drops. *Phys. Fluids* **11(1)**, 30–47.

Mehta, K. N. & Sood, S., 1992. Transient free-convective flow with temperature-dependent viscosity in a fluid saturated porous-medium. *Int. J. Eng. Sci.* **30 (8)**, 1083–1087.

Mei, C. C., 1966. Nonlinear gravity waves in a thin sheet of viscous fluid. *J. Maths. and Phys.* **45**, 266–288.

Mitchell, A. R. & Griffiths, D. F., 1980. *The finite difference method in partial differential equations.* John Wiley and Sons.

Monaghan, J. J., Cas, R. A. F., Kos, A. & Hallworth, M., 1999. Gravity currents descending a ramp in a stratified tank. *J. Fluid Mech.* **379**, 39–70.

Moriarty, J. A., Schwartz, L. W. & Tuck, E. O., 1991. Unsteady spreading of thin films with small surface tension. *Phys. Fluids* **3(5)**, 733–742.

Morton, K. W. & Mayers, D. F., 1994. *Numerical Solutions of Partial Differential Equations.* Cambridge

Press.

Nakada, S. & Fujii, T., 1993. Preliminary report on the activity at Unzen Volcano (Japan) November 1990-November 1991: Dacite lava domes and pyroclastic flows. *J. Volc. Geotherm. Res.* **54**, 319–333.

Oron, A., Davis, S. H. & Bankoff, S. G., 1997. Long scale evolution of thin liquid films. *Rev. Mod. Phys.* **69**, 931–980.

Oron, A. & Peles, Y., 1998. Stabilization of thin liquid films by internal heat generation. *Phys. Fluids* **10**, 537–539.

Raznjevic, K., 1995. *Handbook of thermodynamic tables*. Begell House, 2 edn.

Reid, R. C., Prausnitz, J. M. & Poling, B. E., 1987. *The properties of gases and liquids*. McGraw Hill.

Richtmyer, R. D. & Morton, K. W., 1967. *Difference methods for initial-value problems*. John Wiley and Sons, 2 edn.

Ryan, M. P. & Blevins, J. Y. K., 1987. The viscosity of synthetic and natural silicate melts and glasses at high temperatures. *US Geol. Survey Bull.* **1764**, 1–563.

Saffman, P. G. & Taylor, G. I., 1958. The penetration of a fluid into a porous medium or Hele-Shaw cell containing a more viscous liquid. *Proc. R. Soc. Lond. A* **245**, 312–329.

Sakimoto, S. E. H. & Zuber, M. T., 1995. The spreading of variable-viscosity axisymmetric radial gravity currents: applications to the emplacement of Venusian 'pancake' domes. *J. Fluid Mech.* **301**, 65–77.

Schiaffino, S. & Sonin, A. A., 1997a. Motion and arrest of an advancing molten contact line on a cold solid of the smae material. *Phys. Fluids* **9(8)**, 2217–2226.

Schiaffino, S. & Sonin, A. A., 1997b. On the theory for the arrest of an advancing molten contact line on a cold solid of the same material. *Phys. Fluids* **9(8)**, 2277–2233.

Simpson, J. E., 1997. *Gravity Currents*. Cambridge University Press.

Smith, G. D., 1985. *Numerical solution of partial differential equations: finite difference methods*. Oxford University Press, 3 edn.

Smith, S. H., 1969. On initial value problems for the flow in a thin sheet of viscous liquid. *ZAMP* **20**, 556–560.

Snyder, D. & Tait, S., 1998. A flow-front instability in viscous gravity currents. *J. Fluid Mech.* **369**, 1–21.

Stasiuk, M. V. & Jaupart, C., 1997. lava flow shapes and dimensions as reflections of magma system conditions. *J. Volc. Geotherm. Res.* **78**, 31–50.

Stasiuk, M. V., Jaupart, C. & Sparks, R. S. J., 1993. Influence of cooling on lava-flow dynamics. *J. Geol.* **21**, 335–338.

Tanner, R. I., 1985. *Engineering Rheology*. Oxford University Press.

Wall, D. P. & Wilson, S. K., 1996. The linear stability of channel flow of fluid with temperature-dependent viscosity. *J. Fluid Mech.* **323**, 107–132.

Woods, A. W., 1998. Vaporizing gravity currents in a superheated porous medium. *J. Fluid Mech.* **377**, 151–168.

Wylie, J. J. & Lister, J. R., 1995. The effect of temperature-dependent viscosity on flow in a cooled channel with application to basaltic fissure eruptions. *J. Fluid Mech.* **305**, 239–261.

Wylie, J. J. & Lister, J. R., 1998. Stability of straining flow with surface cooling and temperature-dependent viscosity. *J. Fluid Mech.* **365**, 369–381.

Zhang, W. W. & Lister, J. R., 1999. Similarity solutions for van der Waals rupture of a thin film on a solid substrate. *Phys. Fluids* **11(9)**, 2454–2462.